PhD Thesis

Mingrui Zhao

Pinning down the origin of collective phenomena at the LHC

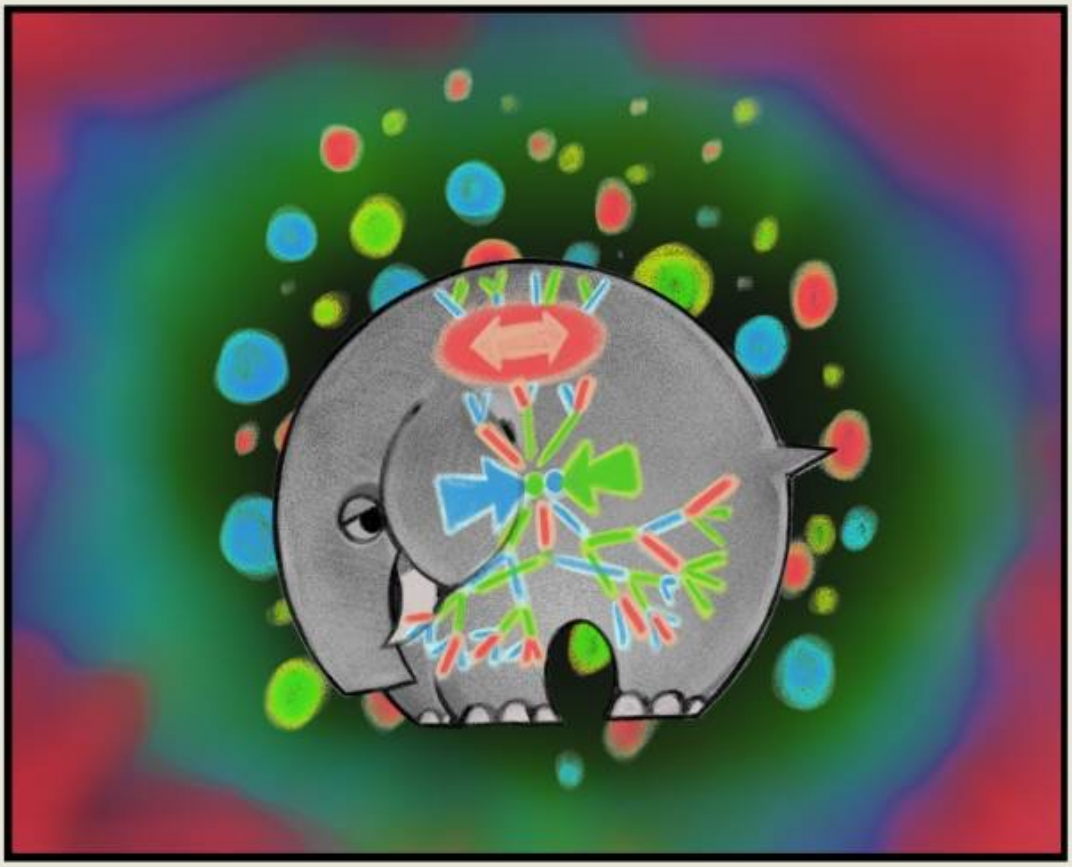

CERN-THESIS-2024-208
//2024

China Institute of Atomic Energy
University of Copenhagen

"*But one must ask every other man: Do you in all conscience believe that you can stand seeing mediocrity after mediocrity, year after year, climb beyond you, without becoming embittered and without coming to grief? Naturally, one always receives the answer: 'Of course, I live only for my "calling." ' Yet, I have found that only a few men could endure this situation without coming to grief.*"

Max Weber, *Science as a Vocation*

分类号_____ 密级_____

UDC_____

学 位 论 文

利用各向异性流
研究小对撞系统中的集体性起源

赵明锐

指导老师姓名 李笑梅, 研究员 中国原子能科学研究院

周铀, 副教授 哥本哈根大学

申请学位级别 博 士 专业名称 物理学

论文提交日期 _____ 论文答辩日期 _____

学位授予单位和日期 _____

答辩委员会主席 周书华

评阅人 周代翠，张晓明

2024 年 5 月

University of Copenhagen

PhD Thesis

Pinning down the origin of collective phenomena at the LHC

Author:
Mingrui Zhao

Supervisor:
Associate Professor You Zhou

High Energy Heavy-Ion Group
Niels Bohr Institute

UNIVERSITY OF COPENHAGEN

This PhD thesis has been submitted to the PhD School of the Faculty of Science, University of Copenhagen on 14-May-2024.

Abstract

The origin of Quark Gluon Plasma-like (QGP-like) phenomena within small collision systems has been a puzzle for researchers for over a decade. Throughout these years of investigation, the presence of collective effects has been confirmed. Moreover, numerous theoretical approaches have been attempted to describe these phenomena. Nonetheless, it has been determined that the phenomena cannot be adequately explained by simple mechanisms including either the initial or final stages alone.

Considering the complexity of the QGP-like phenomena in a small collision system, the best way to investigate the origin of the collectivity, or maybe the only possible way to pin down the origin of the collectivity, is to do the analysis with multi-observable analysis. In this thesis, the full Run 2 data sample with the ALICE detector at the LHC is used, providing the most precise measurements. Multiple observables are measured in pp, p–Pb, and Pb–Pb collisions. The measured observables include multiple particle correlations, cumulants, flow coefficients, symmetric cumulants, and correlations between flow and mean transverse momentum. Various methods for suppressing short-range correlations have been applied.

The measurements probe various mechanisms within the collisions. The initial stage of the collision is examined using flow coefficients v_n and nonlinear flow coefficients $v_{4,22}$ and $\chi_{4,22}$. Moreover, the event-by-event properties of the initial stage are assessed through measurements involving NSC(3,2), which address the initial eccentricity correlations. The initial size and shape correlation is investigated through the $\rho(v_2^2, [p_{\mathrm{T}}])$. The flow coefficients, the nonlinear flow $v_{4,22}$, and the NSC(4,2) are also influenced by the system's evolution. The $\rho_{4,22}$ addresses the event plane correlation. Observables such as $v_n\{2\}$ and $\chi_{4,22}$ have shown sensitivity to variations in the $|\Delta\eta|$ separation. Conversely, other observables like $c_2\{4\}$, $v_{4,22}$, and $\rho(v_2^2, [p_{\mathrm{T}}])$ are less sensitivity to non-flow contamination. The measurements impose constraints on the model and shed light on the system's origins, aiding in the building of a comprehensive model that describes the collective phenomenon in both large and small collision systems.

摘要

在小对撞系统中类 QGP 现象（集体效应）的起源是一个困扰了研究人员十多年的问题。在这些年的研究中，集体效应的存在已经得到确认。研究者尝试使用各种理论方法来描述这些现象。然而，研究发现，这些现象不能通过仅包含对撞初态效应或对撞末态效应的简单机制来解释。

考虑到小碰撞系统中类 QGP 现象的复杂性，研究集体性起源的最佳方式，或者可能是唯一可行的方式，就是进行多可观测量分析。这篇论文使用了大型强子对撞机的 ALICE 探测器几乎全部的 Run 2 数据样本，进行了最精确的测量，在 pp、p–Pb 和 Pb–Pb 碰撞中测量了多个可观测量。测量的可观测量包括多粒子关联、累积量、流系数、对称累积量以及流与平均横向动量之间的关联。同时，研究使用了各种方法来压低局部短程关联。

这些测量探究了对撞过程中的各种物理机制。对撞的初态效应可以通过流系数 v_n，非线性流系数 $v_{4,22}$ 以及 $\chi_{4,22}$ 进行探究。此外，对对称累积量 NSC(3,2) 的测量可以研究对撞初态的逐事件特征。这项测量表征了初态偏心性 $(\varepsilon_2, \varepsilon_3)$ 的关联。对 $\rho(v_2^2, [p_\mathrm{T}])$ 测量表征了初态大小和形状的关联性。流系数、非线性流 $v_{4,22}$ 和 NSC(4,2) 除了受到初态几何影响外，也受到系统演化效应的影响。对撞事件平面 (Ψ_2, Ψ_4) 的关联由观测量 $\rho_{4,22}$ 表征。诸如 $v_n\{2\}$ 和 $\chi_{4,22}$ 等可观测量表现出对赝快度间隔的敏感性。相反，其他可观测量如 $c_2\{4\}$、$v_{4,22}$ 和 $\rho(v_2^2, [p_\mathrm{T}])$ 对非流效应的敏感性较低。

测量结果表明，对于大多数可观测量，从大碰撞系统到小碰撞系统的过渡是平滑的，这表明产生这些可观测量的基本机制可能是相似的。然而，对于流系数 v_2（以及 $\langle\langle\cos(2\varphi_1 - 2\varphi_2)\rangle\rangle$ 和 $c_2\{2\}$），$\mathrm{cov}(v_2^2, [p_T])$，$c_k$，以及 $\rho(v_2^2, [p_T])$ 存在例外。在小碰撞系统和大碰撞系统之间，v_2 和 $\mathrm{cov}(v_2^2, [p_\mathrm{T}])$ 以及 $\rho(v_n^2, [p_\mathrm{T}])$ 的差异主要归因于在 Pb–Pb 碰撞中，初始几何形状源自核子的重叠区域，而在 pp 碰撞中，它们源自初态几何的涨落。对于 c_k，在低多重数环境中观察到三种碰撞系统的测量结果不同。这种差异可能归因于系统初始大小涨落的差异。

pp、p–Pb 和 Pb–Pb 碰撞的测量结果与不同的理论模型进行了比较。对于 pp 碰撞，比较了 PYTHIA 8、AMPT 以及来自 IP-Glasma + MUSIC + UrQMD 的计算。在 p–Pb 和 Pb–Pb 碰撞的情况下，测量结果与 AMPT 的运输模型预测以及 IP-Glasma + MUSIC + UrQMD 的流体动力学模型计算进行了比较。在许多情况下，基于少体相互作用的模型以及那些包含流体动力学演化的模型并不非常成功。从一个角度来看，初始几何形状的建模可能仍需要完善。此外，系统的实际演化是一个复杂的 QCD 过程，使用少体相互作用或流体动力学演化的模型可能都过于简化。

这些测量揭示了系统中集体性的起源，对理论模型施加了约束，将有助于构建一个模型从而全面地描述大小对撞系统中的集体现象。

Dansk resumé

Forståelsen af kvark-gluon plasma (Quark Gluon Plasma, QGP) lignende fænomener i små kollisionssystemer har været et mysterium for forskere i over ti år. Gennem årene har man bekræftet at der findes kollektive effekter i små kollisionssystemer, og man har forsøgt sig med flere teoretiske forklaringer, hidtil uden tilfredsstillende resultater. Det er dog påvist, at fænomenerne ikke kan forklares udelukkende ved simple mekanismer, der alene inkluderer systemets begyndelses- eller slutbetingelser.

Givet de quark-gluon-plasmalignende fænomeners kompleksitet i små kollisionssystemer tyder meget på at den bedste, og måske eneste, måde at undersøge dem på er gennem en såkaldte "multi-observabel" analyse. I dette studie vil al tilgængelig data fra LHC Run2 registreret med ALICE detektoren blive brugt til at give så præcise målinger, som det er muligt. Forskellige observerbare data bliver målt i både pp, p–Pb og Pb–Pb kollisionsdata. De relevante måledata inkluderer fler-partikel-korrelationer, kumulanter, flow-koefficienter, symmetriske kumulanter og korrelationer mellem flow og den gennemsnitlige transverse impuls. Flere metoder til at undertrykke non-flow korrelationer er blevet anvendt.

Målingerne er følsomme overfor forskellige mekanismer i partikelkollisionerne. Begyndelsesbetingelserne undersøges ved hjælp af flow-koefficienterne v_n og ikke-lineære flow koefficienter ($v_{4,22}$ og $\chi_{4,22}$). Begyndelsesbetingelsernes fluktuationer fra kollision til kollision involverer NSC(3,2), som er særlig følsom overfor korrelationer i excentricitet. Korrelationen imellem størrelsen og formen af QGP-fasen bliver undersøgt med $\rho(v_2^2, [p_\mathrm{T}])$. Flow-koefficienterne og de ikke-lineære flow-koefficienter $v_{4,22}$ samt NSC(4,2) bliver også påvirket af, hvordan kollisionssystemet udvikler sig efter den første kollision. Koefficienten $\rho_{4,22}$ er følsom overfor korrelationer imellem kollisionernes symmetriplan. $v_n\{2\}$ and $\chi_{4,22}$ har vist sig at være følsomme overfor de korrelerede partiklers adskillelse i pseudorapiditet, mens variablene $c_2\{4\}$, $v_{4,22}$ og $\rho(v_2^2, [p_\mathrm{T}])$ er mindre følsomme overfor Indflydelse af non-flow. Disse målinger kan hjælpe med til at afgrænse parametre i de eksisterende kollisionssystemmodeller og bestemme kilden til kollektive fænomener i relativistiske partikelkollisioner. De kan i sidste ende bidrage til at udvikle en komplet model, der kan beskrive disse fænomener i både små og store kollisionssystemer.

List of Publications

Papers and preprints

- Measurement of electroweak-boson production in Pb–Pb and p–Pb collisions at the LHC, Nucl.Part.Phys.Proc. 312-317 (2021) 22-26 (proceedings), Mingrui Zhao for ALICE collaboration
- Prospect for measurement of CP-violation phase ϕ_s study in the $B_s \to J/\psi\phi$ channel at a future Z factory, arXiv:2205.10565, Xiaomei Li, Manqi Ruan and Mingrui Zhao
- $W^{\pm}$-boson production in p–Pb collisions at $\sqrt{s_{\rm NN}} = 8.16$ TeV and Pb–Pb collisions at $\sqrt{s_{\rm NN}} = 5.02$ TeV, JHEP 05 (2023) 036, ALICE collaboration (as paper committee member)
- Jet charge identification in *ee*-*Z*-*qq* process at Z pole operation, arXiv:2306.14089, Hanhua Cui, Mingrui Zhao, Yuexin Wang, Hao Liang and Manqi Ruan
- Probe nuclear structure using the anisotropic flow at the Large Hadron Collider, EPJA 59 (2023) 279, Zhiyong Lu, Mingrui Zhao, Xiaomei Li, Jiangyong Jia and You Zhou
- Pinning down the origin of collectivity in small systems with ALICE, to be published at EPJ Web Conf. (proceedings), Mingrui Zhao for ALICE collaboration
- Exploring the nuclear structure with multiparticle azimuthal correlation at the LHC, in preparation (IRC review round 2), ALICE collaboration (as a paper committee member)
- Measurement of correlations between elliptic flow and mean transverse momentum in pp, p–Pb and Pb–Pb collisions at the LHC, in preparation (paper proposal approved), ALICE collaboration (as paper committee member)

Conference contributions

- Talk at the 14th Workshop on QCD Phase Transition and Relativistic Heavy-Ion Physics (QPT 2021), 28-Jul-2021, Study of nonlinear flow and symmetric cumulants in large and small systems
- Talk at the 7th-China LHC Physics Workshop (CLHCP 2021), 25-Nov-2021, Electroweak-boson production in p–Pb and Pb–Pb collisions at the LHC with ALICE
- Talk at the 13th Edition of The France China Particle Physics Laboratory Workshop (FCPPL), 16-Dec-2021, Electroweak-boson production in p–Pb and Pb–Pb collisions at the LHC with ALICE

- Talk at the Joint Workshop of the CEPC Physics, Software and New Detector Concept, 15-Apr-2022, CP measurement with $B_s \to J/\psi\phi$ process at the CEPC
- Poster at the XXIXth International Conference on Ultra-relativistic Nucleus-Nucleus Collisions (Quark Matter 2022), Measurement of flow harmonics, 06-Apr-2022, non-linear flow response and symmetric cumulants in large and small systems with ALICE
- Talk at the Joint Workshop of the CEPC Physics, Software and New Detector Concept in 2022, 24-May-2022, CP measurements with $B_s \to J/\psi\phi$
- Talk at the International Conference on High Energy Physics 2022 (ICHEP 2022), 07-Jul-2022, Electroweak-boson production from small to large collision systems with ALICE at the LHC
- Talk at the 2023 International Workshop on the High Energy Circular Electron Positron Collider, 24-Oct-2023, Study of TPC detector's distortion at e^+e^- collider
- Talk at the XXXth International Conference on Ultra-relativistic Nucleus-Nucleus Collisions (Quark Matter 2023), 05-Sep-2023, Pinning down the origin of collectivity in small systems with ALICE
- Talk at the XVI edition of the Workshop on Particle Correlations and Femtoscopy (WPCF 2023), 07-Nov-2023, Flow and transverse momentum fluctuations and correlations at ALICE
- Poster at the VII-th International Conference on the Initial Stages of High-Energy Nuclear Collisions (Initial Stages 2023), 20-Jun-2023, The opportunity of characterizing the nuclear deformation with the anisotropic flow at the LHC

Acknowledgements

I express my deepest gratitude to my supervisors, Xiaomei Li and You Zhou, whose guidance was indispensable in the completion of this thesis. My sincerely thanks go to my colleagues at the China Institute of Atomic Energy – Lei, Peiyu, Shihai, and Zhiyong – for their assistance both professionally and personally. Similarly, I am grateful to my colleagues at the Niels Bohr Institute – JJ, Ian, Børge, Christian, Kristjan, Emil, Debojit, Wenya, Mikkel, Anders and Yifan – for the helpful discussions with them.

I would also like to thank Jørgen, Panos and Korinna for reviewing the thesis and their valuable feedback.

Lastly, but most importantly, I would like to express gratitude to my parents for their support.

Contents

1 Starting from the chalk

For physicists, diving into the realm of philosophy, even when limited to scientific philosophy, can be dangerous. Lacking rigorous training in logical reasoning and the historical context of philosophy may lead the thinking or discussion to areas that have been extensively explored within the field of scientific philosophy. From a physicist's standpoint, engaging in philosophical discussions without delving into the details of physical theories can seem empty and superficial. Nevertheless, fundamental questions in physics and philosophy often serve as the initial motivation for some physicists to pursue scientific research, including me. In this chapter, I intend to elucidate concisely why the study of Quantum chromodynamics (QCD) matter droplets, which is the main object studied in this thesis, attracts reductionists and how their formation in small collision systems presents an excellent opportunity for in-depth study from a reductionist's perspective.

In 1992, Steven Weinberg published "Dreams of a Final Theory" [1], where he used chalk as an example to illustrate the concept of reductionism. He explained that every aspect of chalk, from its color, which is explained by electromagnetic theory, to its chemical composition, described by atomic theory, could ultimately be traced back to a "theory of everything"–the most advanced form of which is currently the Standard Model. In contrast, the concept of emergence, first brought to prominence by Anderson in his well-known 1972 paper "More is Different" [2], addresses that theories at one scale, such as condensed matter physics, do not directly emerge from more fundamental theories at a smaller scale. Instead, phenomena at different scales have their own unique properties, a concept known as emergentism. Both of the concepts, reductionism, and emergentism, are valid and do not conflict with each other, a view also agreed upon by Anderson himself.

In heavy-ion physics, "QCD condensed matter", the substance produced in heavy ion collisions, serves as the "chalk". In theory, QCD matter droplets are governed by the theory of everything, the Standard Model (SM). However, describing QCD matter droplets using the fundamental theory is exceedingly complex. The study of QCD matter require theories developed at the relevant scale, rather than limited to calculations from first-principle QCD.

As the collision system size decreases, such as in proton–proton collisions compared to lead–lead collisions, a similar "chalk" is formed [1]. The "chalk" produced in these smaller collision systems shares several properties with that created in lead–lead collisions. Prior

[1] Though it is uncertain whether the state produced is in equilibrium and can be adequately classified as "matter"

to the "discovery" of "chalk" in smaller systems, there was a minor effort to develop a unified model capable of coherently describing "chalk" in both collision systems. It was only after this "discovery" that the scales began to communicate more frequently, bridging the gap between the microscopic and macroscopic perspectives.

The goal of me, as a heavy-ion reductionist, is to establish a theory that seamlessly explains all aspects of QCD matter behavior at every energy scale and in every type of collision system, ideally showing how it relates to the Standard Model. While the latter may be too ambitious for the current era, the former is a feasible endeavor. To realize this goal, as an experimentalist, one must investigate a variety of observables across different collision systems, ranging from small to large. This process involves providing both inspiration and concrete data to inform and constrain theoretical models, a subject that this thesis will explore in depth.

2 Physics background

2.1 The standard model

2.1.1 The standard model of particle physics

All the phenomena in the universe are governed by the standard model [3–6] of particle physics, a gauge quantum field theory. In the standard model, there are three generations of fermions, which are the quarks and the leptons. The six quarks are up quark, down quark, charm quark, strange quark, bottom quark, and top quark. The six leptons are electron, electron neutrino, muon, muon neutrino, tau, and tau neutrino.

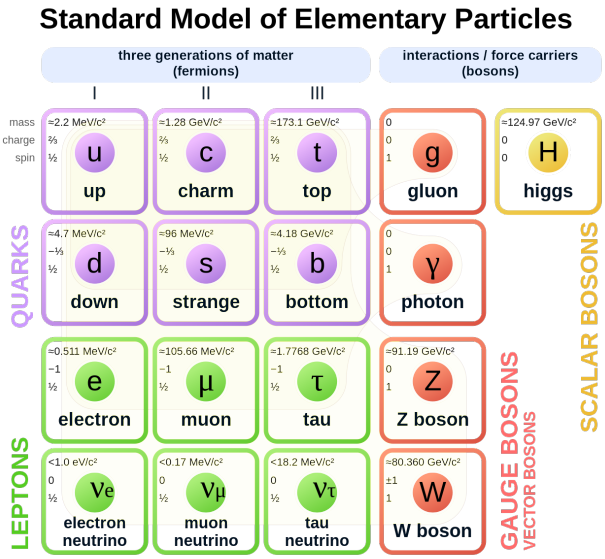

FIGURE 2.1: The standard model of particle physics. Figure taken from [7].

The interactions between the fermions are mediated by the gauge bosons. The gauge bosons are the photon, the gluon, the W boson, and the Z boson, carrying the electromagnetic, the strong, and the weak interactions, respectively.

The dynamics and kinematics of the theory, as well as the interactions between Standard Model particles, are governed by the Standard Model Lagrangian. The local

$SU(3)_C \times SU(2)_L \times U(1)_Y$ gauge symmetry constitutes the internal symmetry that defines the Standard Model Lagrangian. The Standard Model Lagrangian can be expressed as:

$$\mathcal{L} = \mathcal{L}_{\text{EW}} + \mathcal{L}_{\text{QCD}} + \mathcal{L}_{\text{Higgs}} + \mathcal{L}_{\text{Yukawa}}. \tag{2.1}$$

Here, $\mathcal{L}_{\text{EW}}$ and $\mathcal{L}_{\text{QCD}}$ represent two distinct gauge sectors, the electroweak sector and the Quantum Chromodynamics sector, respectively. The $\mathcal{L}_{\text{Higgs}}$ denotes the Higgs sector, and $\mathcal{L}_{\text{Yukawa}}$ encompasses the Yukawa couplings between the Higgs boson and fermions. Particle masses arise through the Higgs mechanism via spontaneous symmetry breaking of the electroweak symmetry. The Feynman diagram vertices of the Standard Model are summarized in figure 2.2.

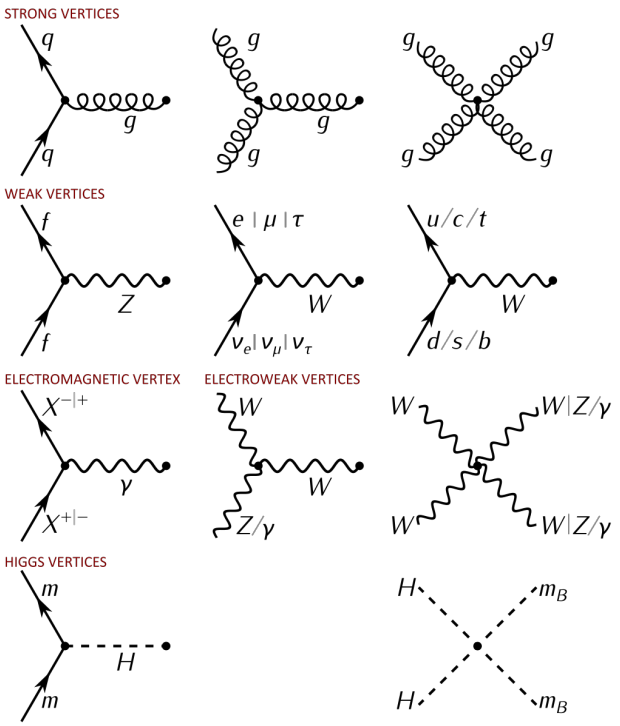

FIGURE 2.2: The Feynman diagram vertices of the standard model. Figure taken from [7].

2.1.2 The quantum chromodynamics

Quantum chromodynamics (QCD) is a piece of the standard model. It describes the strong interaction, the force that governs the interactions between quarks and gluons. Quarks and gluons are the fundamental constituents of nuclear matter, which is of primary

interest here. QCD is a non-Abelian gauge theory with the gauge group $SU(3)_{\mathrm{C}}$. The gauge bosons in this theory are gluons, while the matter fields are represented by quarks. The Lagrangian of QCD is expressed as follows [8]:

$$\mathcal{L}_{\mathrm{QCD}} = \sum_{f=1}^{N_f} \bar{\psi}_f (i\gamma^\mu D_\mu - m_f)\psi_f - \frac{1}{4} G^a_{\mu\nu} G^{a\mu\nu}, \tag{2.2}$$

where N_f is the number of flavors of quarks, ψ_f is the quark field, $D_\mu = \partial_\mu - i g_s G^a_\mu T^a$ is the covariant derivative, g_s is the strong coupling constant, $G^a_{\mu\nu}$ is the gluon field strength tensor, and T^a is the generator of the $SU(3)_{\mathrm{C}}$ group. The gluon field strength tensor is given by

$$G^a_{\mu\nu} = \partial_\mu G^a_\nu - \partial_\nu G^a_\mu + g_s f^{abc} G^b_\mu G^c_\nu, \tag{2.3}$$

where f^{abc} is the structure constant of the $SU(3)_{\mathrm{C}}$ group.

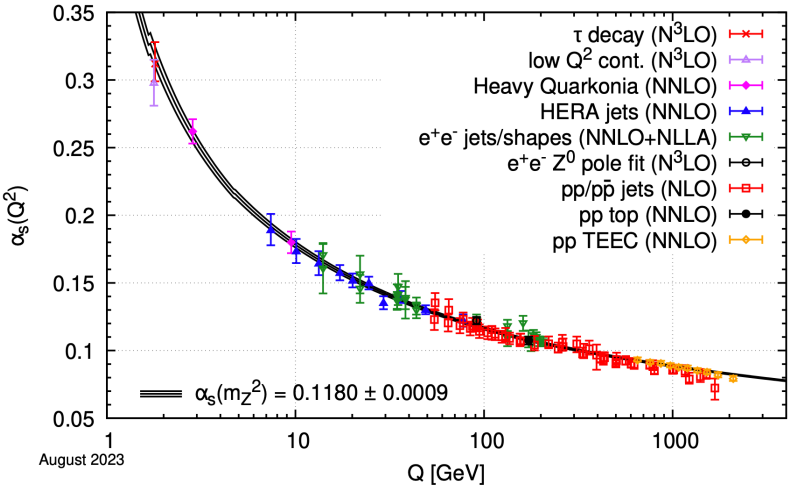

FIGURE 2.3: Summary of determinations of α_s as a function of the energy scale Q. Figure taken from [8].

Two very important features of QCD are asymptotic freedom [5, 9] and quark confinement. When the distance between the quarks becomes smaller, corresponding to a larger energy scale, the interactions between them weaken. Such a phenomenon is called asymptotic freedom. The dependence of the coupling constant with the energy scale is described by the beta-function, which is defined as

$$\frac{dg_s}{d\ln\mu} = \beta(g_s), \tag{2.4}$$

where μ is the renormalization scale. The beta-function is expressed as:

$$\beta(g_s) = -\beta_0 \frac{g_s^3}{16\pi^2}, \tag{2.5}$$

to the first order, with $\beta_0 = 11 - \frac{2}{3}N_f$. The $N_f = 6$ is the number of fermions. The negative sign of the beta-function indicates that the coupling constant decreases at higher energies, which is indicative of asymptotic freedom. The effective coupling constant is defined as

$$\alpha_s(Q^2) = \frac{g_s^2}{4\pi} = \frac{4\pi}{\beta_0 \log \frac{Q^2}{\Lambda_{\mathrm{QCD}}}}, \tag{2.6}$$

where Q is the energy scale and $\Lambda_{\mathrm{QCD}} \sim 300$ MeV is the QCD scale parameter depending on renormalization scheme. Equation 2.6 is validated experimentally and summarized in figure 2.3. The strong coupling constant α_s is approximately 0.1 at an energy scale of $Q \sim 100$ GeV, and the theory becomes strongly coupled at an energy scale of $Q \lesssim 1$ GeV. At high energies, quarks interact weakly, permitting the use of perturbative calculations.

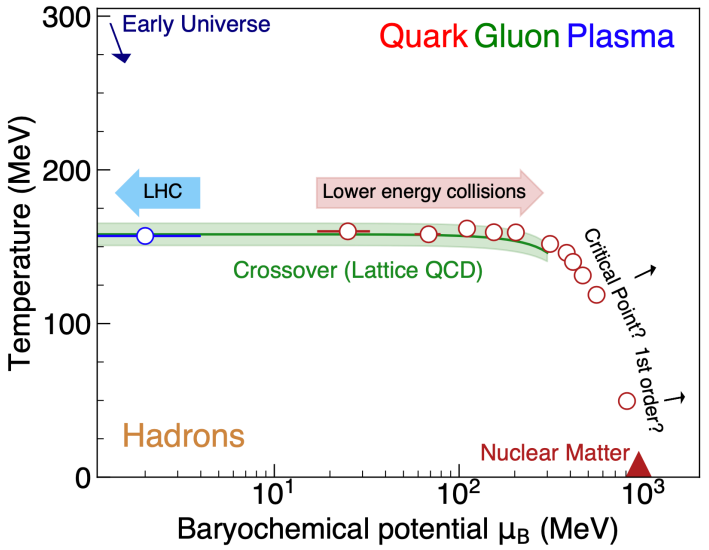

FIGURE 2.4: A schematic representation of the QCD phase diagram. Figure taken from [10].

At low energies, colored particles cannot exist in isolation, a phenomenon known as confinement. Quarks and gluons must bind together to form hadrons. The two primary types of hadrons are mesons (composed of one quark and one antiquark) and baryons (composed of three quarks). The phenomenon can be understood intuitionally. When the distance between quarks (and anti-quarks) increases, the force mediated by gluons does

not diminish but remains constant. Under extreme conditions, deconfinement can occur, leading to the formation of a state of matter called Quark-Gluon Plasma (QGP) [11]. As shown in the QCD phase diagram, figure 2.4, the QGP could exist when the temperature or the baryochemical potential (the baryochemical potential μ measures the imbalance between quark and anti-quark) is large. Experimentally, these conditions can be produced in heavy-ion collisions at the Relativistic Heavy Ion Collider (RICH) or the Large Hadron Collider (LHC), which will be discussed in the next section.

2.2 Heavy-ion collisions

2.2.1 Evolution of heavy-ion collisions

Deconfined QCD matter is predicted to be produced in heavy-ion collisions. Over the last three decades, a widely accepted framework for describing these collisions has developed [12]. This framework is illustrated in figure 2.5. Prior to the collision, the two nuclei are Lorentz contracted, resembling two pancake-like objects. These objects, characterized by the nuclei's wave functions, collide, initiating numerous QCD processes involving varying momentum transfers. Large momentum transfer QCD processes occur at the onset, succeeded by processes with lower momentum transfers. These interactions generate a multitude of partons, which deposit substantial energy and entropy within the small overlapping region of the nuclei. Initially, the system is not in equilibrium. The partons continue to interact, undergoing further processes with even smaller momentum transfers, resulting in softer partons. This thermalization process culminates in the formation of an equilibrated state known as the strongly interacting quark-gluon plasma.

The interactions among partons lead to the expansion and subsequent cooling of the system. As the density and temperature of the matter decrease, hadrons begin to form. The stop of changes in the matter's chemical composition is known as chemical freeze-out. During the chemical freeze-out, hadrons still interact with one another. However, as the matter continues to expand, these interactions stop at a stage referred to as kinetic freeze-out. Beyond this point, hadrons move freely without further interactions and are eventually detected by detectors.

2.2.2 Diagnostic tools

Many diagnostic tools are developed to study the properties of the matter created in heavy-ion collisions, providing information on the created matter at different stages of the collisions. These signatures or observables include the strangeness enhancement [13], the heavy flavor hadrons production, the jet quenching, and the anisotropic flow, etc. Some of them will be discussed in the following sections.

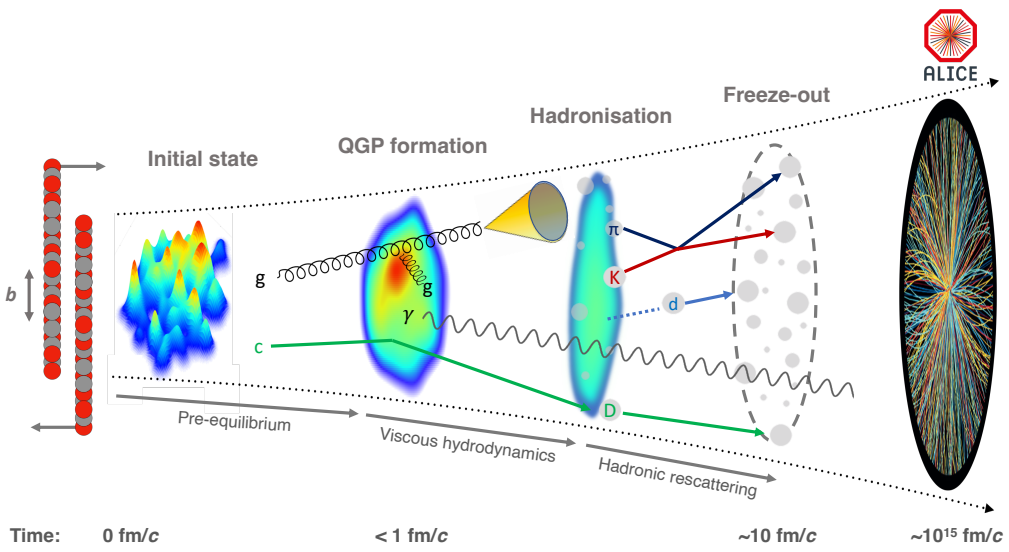

FIGURE 2.5: The evolution of heavy-ion collisions. Figure taken from [10].

Strangeness enhancement

Strangeness enhancement is an important indicator of deconfined matter formation and is regarded as one of the earliest proposed key signatures for the creation of the QGP [13–16]. When the temperature exceeds the mass of strange quarks, gluon fusion rapidly produces strange quark pairs. During hadronization, the enhancement of strange quarks leads to an enhanced production of strange hadrons. Figure 2.6 shows the hyperon-to-pion ratio in comparison to proton-proton collisions as measured by the ALICE and STAR experiments at the LHC and RHIC energy [17–24]. The particle Ξ ($\Xi^- = dss$) consists of two strange quarks, while the particle Ω ($\Omega^- = sss$) is a state with three strange quarks. The ratio of hyperons to pions in Pb–Pb collisions is higher than that in pp collisions. Furthermore, the difference in this ratio between Pb–Pb and pp collisions is much more pronounced for the Ω/π ratio than for the Ξ/π ratio. The measurements are consistent with the concept that strange quarks are produced abundantly in a medium whose temperature is higher than the mass of the strange quark.

Jet quenching

In heavy-ion collisions, the initial hard scattering of partons produces high-transverse momentum partons during the early stages of the collision. These highly energetic partons then propagate through QCD matter that is both high in temperature and density. As

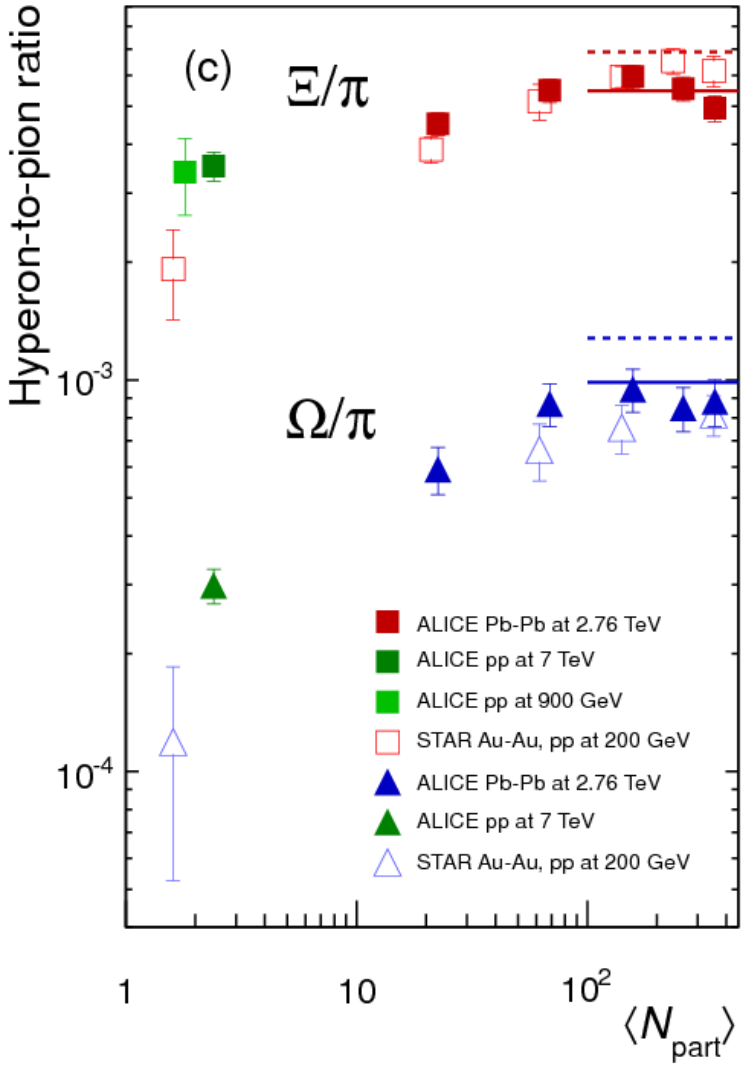

FIGURE 2.6: Hyperon-to-pion ratios as a function of $\langle N_{\mathrm{part}} \rangle$, for A–A and pp collisions at LHC and RHIC energies. Figure taken from [21].

a result, the partons interact with the medium, leading to energy loss primarily through radiative processes induced by the medium. This interaction modifies jet properties, such as jet energy, compared to scenarios where the medium is absent, a phenomenon known as jet quenching [25–28].

This modification could be quantified with many experimental techniques, including inclusive jet suppression, inter-jet correlations, and intra-jet distributions [29]. The inclusive jet suppression is quantified by the nuclear modification factor, denoted as R_{AA}. The R_{AA} is defined as

$$R_{\mathrm{AA}} = \frac{N_{\mathrm{AA}}}{N_{\mathrm{MB}} \langle T_{\mathrm{AA}} \rangle \sigma_{\mathrm{pp}}}, \tag{2.7}$$

where N_{AA} is the yield in the heavy-ion collisions, the N_{MB} is the corresponding number of minimum bias events, $\langle T_{\mathrm{AA}} \rangle$ is the average nuclear overlap function, and σ_{pp} is the cross-section of the production in the proton-proton collisions.

Figure 2.7 shows a measurement of the R_{AA} conducted by the ALICE experiment at 0-10% centrality. The R_{AA} is less than unity over a large range of kintematic region. The measurements support the idea that the jet loses energy as it travels through the hot, dense medium.

Heavy quarkonium suppression

The heavy quarkonium (such as the J/ψ and the Υ) are the bound states of the heavy quarks and anti-quarks. In the deconfined matter, due to the screening of the color charges of the heavy quarks and anti-quarks, the yield of the heavy quarkonium is suppressed compared to the superposition of the nucleon-nucleon collisions [31]. The dominant cause of the suppression can be viewed as dissociating the heavy quarkonium in the deconfined matter through interaction with the surrounding partons. The suppression of the heavy quarkonium is observed in many experiments. Figure 2.8 shows the nuclear modification factor of the J/ψ, measured by the ALICE experiment [32].

A deviation of R_{AA} from unity suggests that the system cannot be adequately described by a mere superposition of nucleon-nucleon collisions, suggesting the suppression of J/ψ production in Pb–Pb collisions. At LHC energies, the J/ψ production arises from a variety of mechanisms. In addition to the dissociation of J/ψ, the recombination of $c\bar{c}$ pairs [33], as well as the cold nuclear matter effects [34], can also play a significant role.

Anistropic flow

In heavy-ion collisions, the initial geometric asymmetry is transformed through interactions within the collectively expanding quark-gluon plasma into an anisotropic distribution of the final-state particles. This process effectively translates the spatial anisotropy of the early stages into observable momentum anisotropies among the emitted particles.

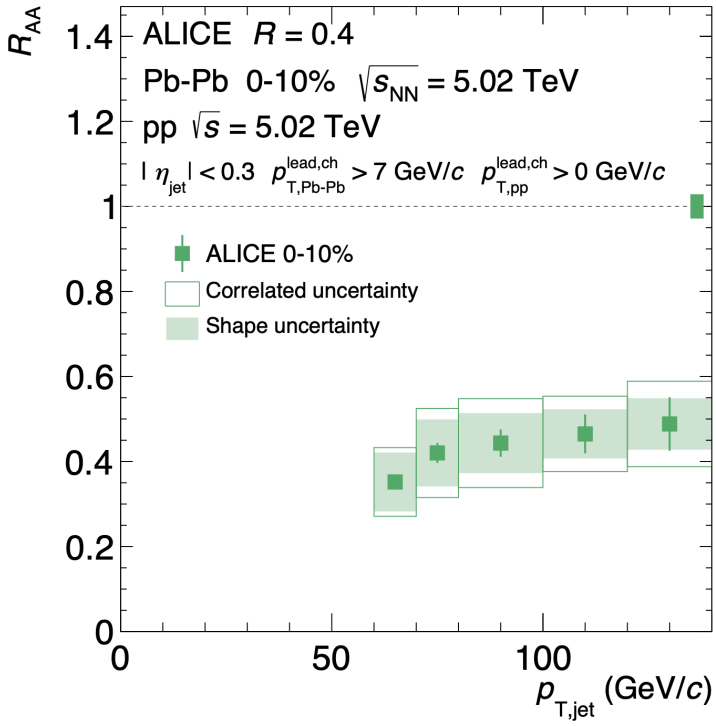

FIGURE 2.7: The nuclear modification factor of the jets, measured by the ALICE experiment. Figure taken from [30].

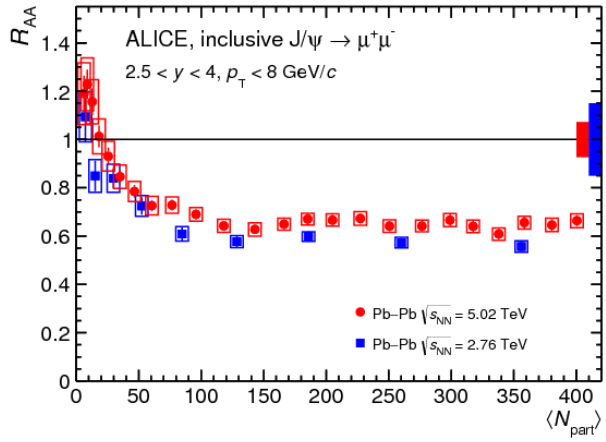

FIGURE 2.8: The nuclear modification factor of the J/ψ, measured by the ALICE experiment. Figure taken from [32]

Anisotropic flow [35, 36], quantifies the azimuthal anisotropy in the distribution of final-state particles. This distribution can be expressed as a Fourier series:

$$f(\varphi) = \frac{1}{2\pi}\left[1 + 2\sum_{n=1}^{\infty} v_n \cos[n(\varphi - \Psi_n)]\right], \tag{2.8}$$

where v_n represents the nth-order flow coefficient, and Ψ_n is the nth-order symmetry plane angle.

Figure 2.9 presents the measurements of the anisotropic flow coefficients v_2, v_3, and v_4 in Pb–Pb collisions taken by the ALICE experiment. The data shows an initial increase followed by a decrease in v_2 as centrality increases. Remarkably, this fluid has the lowest shear viscosity of any known substance, classifying it as a perfect liquid [37]. The shear viscosity is close to the lower bound of $\hbar/4\pi k_B$ predicted by the AdS/CFT [38].

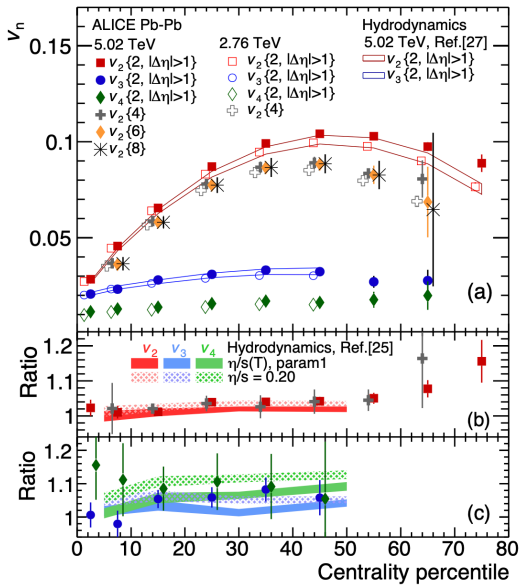

FIGURE 2.9: Anstropic flow coefficients v_2, v_3 and v_4 measured by ALICE collaboration in Pb–Pb collisions. Figure taken from [39].

The collectivity could also be characterized by the dihadron correlation [40, 41]. The correlation is proportional to the number of particle pairs within the kinematic region defined by $(\Delta\eta(= \eta_1 - \eta_2), \Delta\varphi(= \varphi_1 - \varphi_2))$. Here φ_1, η_1 and φ_2, η_2 represent the azimuthal angle and pseudorapidity of the two particles, respectively. Due to global collectivity, particles have a preferred direction of emission. Consequently, there is a higher likelihood that two particles will be emitted at closely aligned angles, resulting

in a ridge at $\Delta\varphi \sim 0$, regardless of their separation in $\Delta\eta$, as shown in the figure 2.10. Moreover, the peak observed at $\Delta\eta \sim 0, \Delta\varphi \sim 0$ is predominantly due to correlations between particles within the same jet.

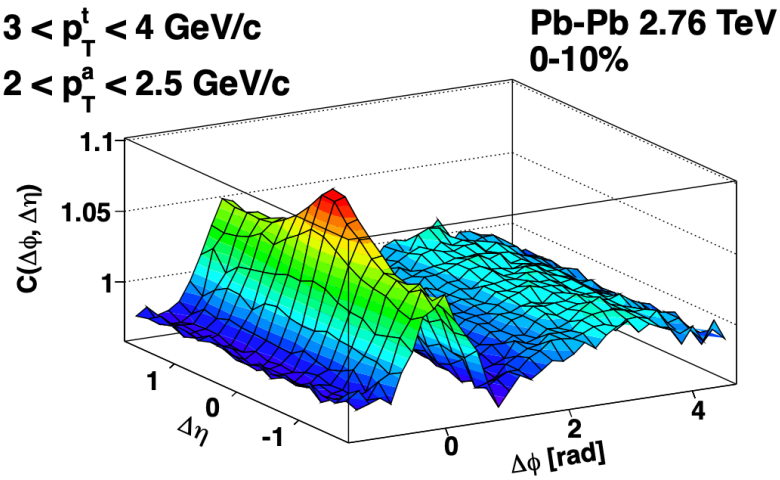

FIGURE 2.10: Dihadron correlation in Pb–Pb measured by the ALICE experiment. Figure taken from [41]

2.2.3 Theoretical tools

A variety of theoretical tools have been developed to simulate the processes involved in heavy-ion collisions, many of which will be discussed in this section. Lattice QCD [42–44] is a theory that describes the statistical properties of QCD matter, whereas other models are utilized to simulate the dynamic processes of the collision.

The state prior to the collisions is modeled using either the nucleon degree of freedom or the gluon degree of freedom. This is done through approaches like the Glauber model [45], the Kharzeev-Levin-Nardi (KLN) model [46–48], or the IP-Glasma model [49, 50]. In the early stages of the collision, hard parton scatterings are described using perturbative QCD [9]. However, perturbative QCD becomes inadequate for partons with low transverse momentum. The description of these low-momentum partons requires phenomenological models, such as the Lund string model. PYTHIA 8 [51, 52] is often used as a practical implementation of the Lund string model. Following the initial production of partons, they undergo rescattering. This leads to the thermalization of the system, which can be modeled using kinetic transport theories, such as the relativistic Boltzmann

equation [53, 54]. Once thermal equilibrium is achieved, hydrodynamics offers a macroscopic description of the system's evolution. On the other hand, the transport model, which is a microscopic approach, describes the evolution of the partonic system through the interaction of quasi-particles. In the final state, hadronic interactions are typically simulated using models such as UrQMD [55] and ART (A Relativistic Transport) [56] models.

Lattice QCD

Lattice QCD is a non-perturbative approach for solving QCD equations. It discretizes quark and gluon fields on a space-time lattice, allowing for the calculation of the thermodynamic properties of quark-gluon plasma.

Lattice QCD computations indicate that the transition from quark-gluon plasma to hadronic matter is a crossover at zero baryon chemical potential, meaning there is no distinct phase change. Instead, deconfined and confined phases can coexist. Furthermore, it has been demonstrated that at LHC energies, the energy density of the quark-gluon plasma does not reach the ideal gas limit. The partons within the plasma interact strongly, leading to the designation of this state as strongly interacting quark-gluon plasma (sQGP) [57].

Initial stage models

Various models have been developed to characterize the initial stage of heavy-ion collisions. The Glauber model [45], which is straightforward and widely used, describes the nucleus-nucleus interactions in terms of fundamental nucleon-nucleon interactions. Typically, the nucleon density distribution within nuclei is represented by a Woods-Saxon distribution, which accounts for the diffuse edge of the nucleus:

$$\rho(r) = \frac{\rho_0}{1 + \exp((r - R)/a)}, \tag{2.9}$$

where R is the radius of the nucleus, a is the diffuseness parameter, and ρ_0 is the central density. In heavy-ion collisions, it is often assumed that each nucleon follows a straight-line trajectory. Nuclear collisions can be viewed as a sequence of nucleon-nucleon collisions. The event-by-event fluctuation of the nucleon within the nuclei is modeled through the Monte-Carlo version of the models, called MC-Glauber.

The color glass condensate (CGC) [58] is a theoretical state of matter that emerges in the high-energy limit of QCD. It forms part of the wave function of a hadron, which overall is a color-neutral entity. The CGC concept posits that at high energies, the gluon density within a hadron becomes extremely high. In this dense environment, Bose-Einstein

condensation happens, and the gluons cannot be considered as independent particles. Instead, their collective behavior is described by a classical field. The CGC is significant for generating initial momentum anisotropy, crucial for understanding the early stages of heavy-ion collisions. The CGC is implemented with the KLN model. Additionaly, the Monte-Carlo version of the KLN model [46–48], the MC-KLN, considered the event-by-event fluctuation. Both the nucleon position fluctuations and the color charge fluctuations are considered in the IP-Glasma model, which is also based on the CGC framework. The initial Glasma fields are generated by using both the impact parameter-dependent saturation model (IP-Sat) [59] and the classical Yang-Mills theory [49, 50].

Relativistic hydrodynamics model chain

Relativistic hydrodynamics offers a macroscopic description of heavy-ion collisions grounded in the conservation laws of energy and momentum. For hydrodynamics to be applicable, the mean free path of the partons must be significantly smaller than the system's size, ensuring that interactions among partons are sufficiently frequent. Relativistic hydrodynamics has become a standard tool for describing the dynamics of heavy-ion collisions.

The fundamental equation of relativistic hydrodynamics is expressed as:

$$\begin{aligned} \partial_\mu T^{\mu\nu} &= 0, \\ \partial_\mu J^{\mu} &= 0, \end{aligned} \tag{2.10}$$

where $T^{\mu\nu}$ represents the energy-momentum tensor and J^{μ} is the net baryon charge current. The tensor $T^{\mu\nu}$ is defined by:

$$T^{\mu\nu} = (\epsilon + p + \Pi)u^{\mu}u^{\nu} - (p + \Pi)g^{\mu\nu} + \pi^{\mu\nu},$$

with ϵ denoting the energy density, p the pressure, u^{μ} the four-velocity of the fluid element, and $g^{\mu\nu}$ the metric tensor. The viscous effects are implemented in the shear stress tensor $\pi^{\mu\nu}$ and bulk pressure Π.

The initial condition and the equation of states are inputs of the relativistic hydrodynamic evolution. After the hydrodynamic evolution, particles are emitted from the fluid. The Cooper-Frye formula [60] is employed to transition from the fluid to a particle description. A typical relativistic hydrodynamics model chain is the IP-Glasma + MUSIC + UrQMD model [49, 50, 55]. As suggested by the name, the initial state of the collision is described by the IP-Glasma, as described in the previous part. The MUSIC model implements the relativistic viscous hydrodynamic simulation in 3+1 dimension. The hadronic afterburn is simulated with the UrQMD, a microscopic transport model describing the interaction between hadrons.

Few body interactions model chain

The evolution of the system in heavy-ion collisions can also be described by the transport models. These transport models describe the evolution of the system at a microscopic level, in contrast to hydrodynamics. They are also quasi-particle effective models in relation to QCD. One well-known transport model chain is the AMPT (A Multi-Phase Transport) model [61]. The AMPT model attempts to describe the entire process of heavy-ion collisions. In the AMPT, the quasi-particles are the nearly massless quarks. The initial state of the AMPT is determined by the HIJING model [62], which generates the strings and minijets. Subsequently, the strings and minijets undergo fragmentation into quark-antiquark pairs, a process referred to as the string melting mechanism. The interactions among the partons are then described using the ZPC (Zhang's Parton Cascade) model [63]. Quarks that are close together within phase space are combined into hadrons through the quark coalescence mechanism [64]. The interactions among the hadrons are characterized by the ART model. Another well-known transport model chain is the PACIAE [65]. Instead of using the HIJING initial condition as in AMPT, it uses PYTHIA 6 [66] to generate the initial partons. After that, the system undergoes a parton rescattering and hadronization. After that, a hadron rescattering happened.

2.3 Small collision systems

2.3.1 The surprise of the small collision systems

In the conventional understanding of heavy ion collisions, it was initially thought that quark-gluon plasma cannot form in smaller collision systems such as pp or p–Pb collisions. Nevertheless, in 2010, the CMS Collaboration presented measurements of dihadron collision [67], which suggested that a ridge structure is present in pp collisions, as illustrated in figure 2.11.

The peak at $(\Delta\eta \sim 0, \Delta\varphi \sim 0)$ primarily arises from particle pairs within the same jet, while the ridge at $\Delta\varphi \sim \pi$ is attributed to particles originating from back-to-back jets. Most importantly, the ridge observed at $\Delta\varphi \sim 0$ with a large $\Delta\eta$, as indicated by the red arrow in the plot, is typically considered a feature of long-range collectivity, as discussed in section 2.2.2. In Pb–Pb collisions, this long-range collectivity is usually interpreted as as a result of the formation of QGP. However, in pp collisions, this discovery was beyond the expectations of any existing theoretical model and is considered one of the most unexpected findings at the LHC.

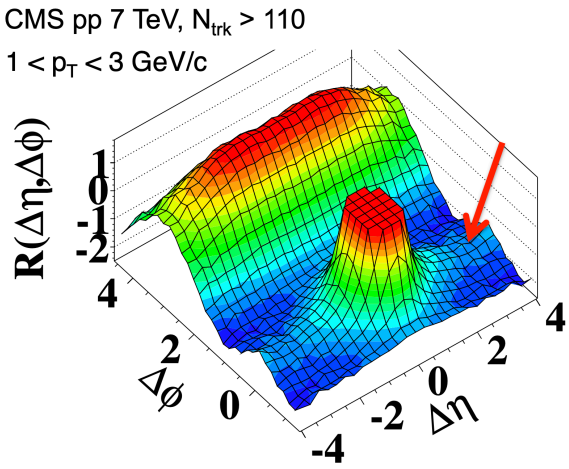

FIGURE 2.11: Dihadron correlation from CMS collaboration in pp collisions. Figure taken from [67].

2.3.2 Collectivity signatures

The signature is examined through subsequent analyses, a key one being the measurement of dihadron correlations in p–Pb collisions, conducted by the ALICE, ATLAS, and CMS collaborations [68–70]. Figure 2.12 displays the measurements in p–Pb collisions by the CMS collaboration. A pronounced near-side long-range structure is distinctly visible in the plot, confirming that global collectivity can also be observed in p–Pb collisions. Similar to the case in pp collisions, this ridge structure could not be explained by any intuitive model.

Flow observables are measured across both large (Pb–Pb, Xe–Xe) and small (p–Pb, pp) systems at the LHC by the ALICE, ATLAS, and CMS collaborations. Similarly, at RHIC, measurements are taken in large systems (Au–Au) and smaller collision systems (p–Au, d–Au, ^{3}He–Au) by the PHENIX and STAR experiments, as detailed in table 2.1. These flow observables offer insights into various aspects of the collision systems, including the initial stages, transport properties, and event-by-event characteristics, among others. The definitions and physical interpretations of these flow observables can be found in the references listed in the table 2.1.

Among the various analyses, the measurement of v_2 and v_3 by the PHENIX collaboration in p–Au, d–Au, and ^{3}He–Au collisions [74] stands out as particularly significant. The left plot in figure 2.13 presents the average system eccentricities as predicted by the MC-Glauber model. These eccentricities are determined by the projectile geometry at

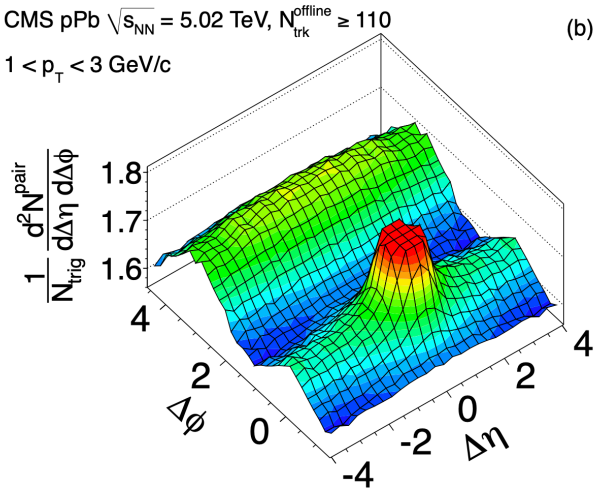

FIGURE 2.12: Dihadron correlation from CMS collaboration in p–Pb collisions at high multiplicity. Figure taken from [69].

TABLE 2.1: Collectivity observables are measured in both large and small collision systems. In this context, "A" denotes a heavy ion, which can be lead (Pb), xenon (Xe), or gold (Au).

Observable	A–A	p–A(d–A,^{3}He–A)	pp (high multiplicity)
Dihadron correlation	[41, 71]	[68–70]	[67, 68]
Anisotropic flow coefficients	[39, 72]	[72–75]	[72, 76]
Identified particle flow	[77]	[78, 79]	[80]
Multi-particle cumulants	[72, 81, 82]	[72, 82–86]	[72, 83, 84]
Decorrelation	[87–92]	[87, 88]	[92]
Nonlinear flow	[93–95]		
v_n-p_T correlation	[96, 97]	[96]	[98]
Flow magnitude correlation		[99–101]	[99, 100]
Flow magnitude fluctuation	[102]		
Event-plane correlation			
Event-by-Event v_n	[103, 104]		
High-p_T flow	[105, 106]	[107, 108]	[109, 110]
Charm flow	[111–114]	[115, 116]	[115, 117]
Bottom flow	[111, 118]	[119]	[117]

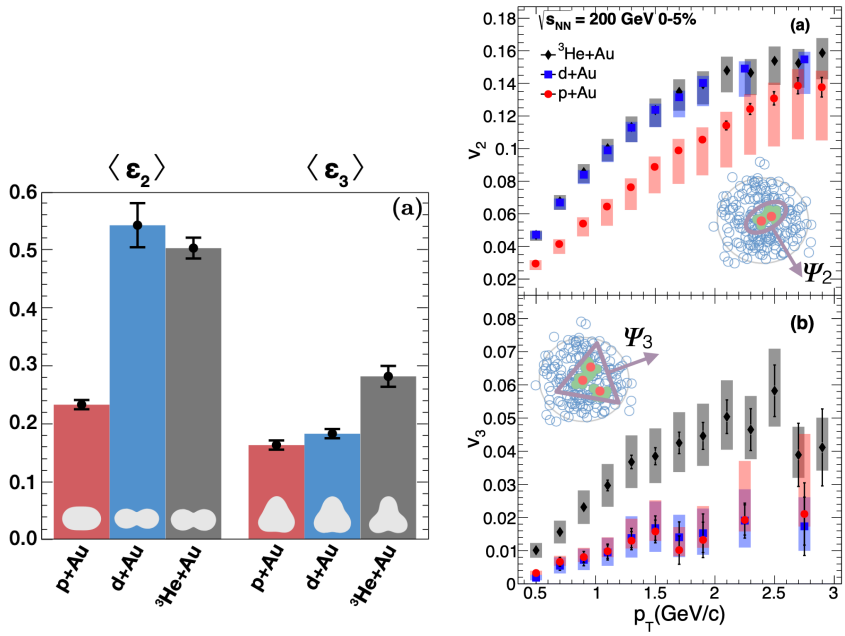

FIGURE 2.13: Left: ϵ_2 and ϵ_3 in p–Au, d–Au and ^{3}He–Au collisions, calculated with MC-Glauber model. Right: Measurement v_2 and v_3 conducted by the PHENIX collaboration in p–Au, d–Au and ^{3}He–Au collisions. Figures taken from [74].

the subnucleon level and are defined by the equation:

$$\epsilon_n = \frac{\sqrt{\langle r^n \cos(n\varphi)\rangle^2 + \langle r^n \sin(n\varphi)\rangle^2}}{\langle r^n \rangle}, \tag{2.11}$$

where the model predicts a order of $\varepsilon_2^{\text{p–Au}} < \varepsilon_2^{\text{d–Au}} \approx \varepsilon_2^{^3\text{He–Au}}$ and $\varepsilon_3^{\text{p–Au}} \approx \varepsilon_3^{\text{d–Au}} < \varepsilon_3^{^3\text{He–Au}}$. In heavy-ion collisions, the final state momentum anisotropy v_n is considered to be proportional to the initial spatial eccentricities. Additionally, the measurements, as in the right plot of figure 2.13, show an ordering of $v_2^{\text{p–Au}} < v_2^{\text{d–Au}} \approx v_2^{^3\text{He–Au}}$ and $v_3^{\text{p–Au}} \approx v_3^{\text{d–Au}} < v_3^{^3\text{He–Au}}$. It suggests that in p–Au, d–Au and ^{3}He–Au collisions, the final stage v_n values originate from a response to the initial geometry, highlighting the importance of subnucleon geometry in small systems.

Another intriguing measurements among the observables is the flow of identified hadrons, as investigated by the ALICE collaboration. In heavy-ion collisions, the interplay between radial and anisotropic flows induces a mass ordering effect in the flow patterns of identified particles within the low p_{T} region. Conversely, in the intermediate p_{T} region, the effects of baryon-meson grouping are evident and align with predictions from the

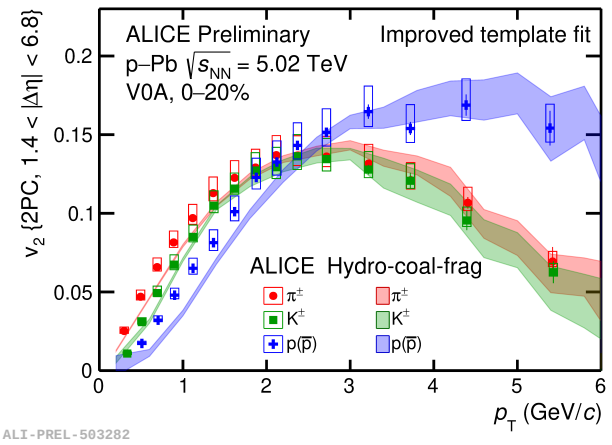

FIGURE 2.14: Identified particle flow in small collision systems. Figure taken from [120].

quark coalescence model. The flow of identified particles such as π, K, p, and Λ is measured in p–Pb collisions. These measurements use ultra-long-range azimuthal correlations and apply the template fit method to effectively minimize the contaminations of short-range few-particle correlations. The measurements confirm mass ordering at low-p_{T} and baryon-meson grouping at intermediate p_{T} in p–Pb collisions, as illustrated in figure 2.14. These findings support the presence of partonic collectivity in p–Pb collisions.

Furthermore, measurements have been conducted at even lower multiplicities in ultra-peripheral (UPC) [121, 122] electron-proton (ep) [123, 124], and electron-positron (ee) [125] collisions. Searches for near-side ridge yield in ee and ep collisions have been carried out using archived samples from the LEP ALEPH experiment and measured at the Belle experiment. No ridge structure was found in ep collisions. The measurements in ee collisions, shown in figure 2.15, reveal no near-side, long-range structure in these systems. However, when experiments are performed at high multiplicities, with $N_{\mathrm{trk}} > 50$, a subtle near-side long-range structure becomes slightly visible, as shown in the left plot of figure 2.16. The right plot of figure 2.16 illustrates the yield of associated tracks as a function of the azimuthal angle difference. A peak around $\Delta\varphi < 1$ is indicated, which failed to be described by the calculation with PYTHIA 8. A ridge structure in *ee* collision, if existing, indicates the collectivity may raise from the final state effects unrelated to the initial state. However, due to statistical limitations, it remains inconclusive whether a long-range structure truly exists.

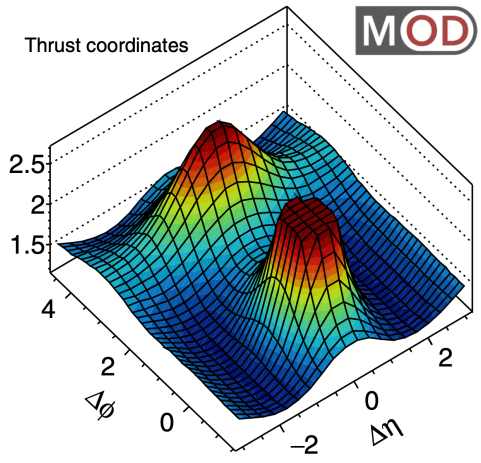

FIGURE 2.15: Dihadron correlation from ALEPH archived data in ee collisions. Figure taken from [125].

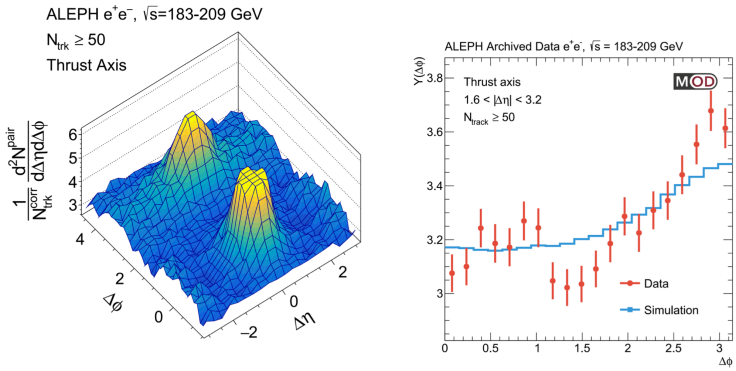

FIGURE 2.16: Dihadron correlation from ALEPH archived data in high multiplicity ee collisions. Figures taken from [125].

2.3.3 Other experimental evidence

Strangeness

Beyond collective dynamics, additional diagnostic tools are employed in small collision systems. The motivation for these studies is that if the collectivity observed in small collision systems originate from a fundamentally similar underlying mechanism as in the large collision systems, one would naturally expect to see some other QGP signatures, to some extent, in small collision systems as well. Strangeness enhancement, for instance, is also observed in small collision systems [126]. Figure 2.17 illustrates the ratio of strange hadrons to pions in pp, p–Pb, and Pb–Pb collisions as a function of multiplicity. In smaller systems like pp and p–Pb collisions, strangeness enhancement manifests as an increasing ratio of strange hadron production to pion yields with increasing charged particle multiplicity. Strange hadrons are more enhanced in events with high multiplicity. There appears to be a smooth transition from pp to p–Pb to Pb–Pb collisions. The trend is especially pronounced in multi-strange particles, suggesting that the enhancement is proportional to the strangeness content of the particles. Considering the presence of a hot, dense medium in small collision systems, events with higher multiplicity are expected to produce a larger number of strange quarks through gluon fusion, resulting in the observed multiplicity dependent yield ratio. The trend cannot be reproduced by the original PYTHIA 8 used in [126], as it does not show any dependence on centrality. However, by introducting the rope hadronization, PYTHIA 8 can effectively reproduce the trend [127].

Heavy flavour and jets

The measurement of heavy quarkonia in heavy-ion collisions probes the effects from a deconfined quark-gluon plasma, where mechanisms such as dissociation and recombination play significant roles. The yield ratio of bottomonium states $\Upsilon(2S)$ to $\Upsilon(1S)$ is particularly interesting to investigate because $\Upsilon(2S)$ is a excited state, and the two b quarks within $\Upsilon(2S)$ are less tightly bound compared to the ground state $\Upsilon(1S)$.

The CMS collaboration has measured the $\Upsilon(2S)$ to $\Upsilon(1S)$ yield ratio across pp, p–Pb, and Pb–Pb collisions [128]. As the charged tracks multiplicity increases, the $\Upsilon(2S)$ to $\Upsilon(1S)$ yield ratio is suppressed. The suppression observed in Pb–Pb collisions is primarily attributed to the dissociation through color screening, due to the presence of QGP [129]. Although the data is limited to certain multiplicity regions, the suppression exhibits a relatively smooth transition from pp to p–Pb to Pb–Pb collisions. These measurements suggest that medium effects on the Υ states become significant in pp and p–Pb collisions as the multiplicity increases, indicating the existence of the QGP droplet in small collision systems.

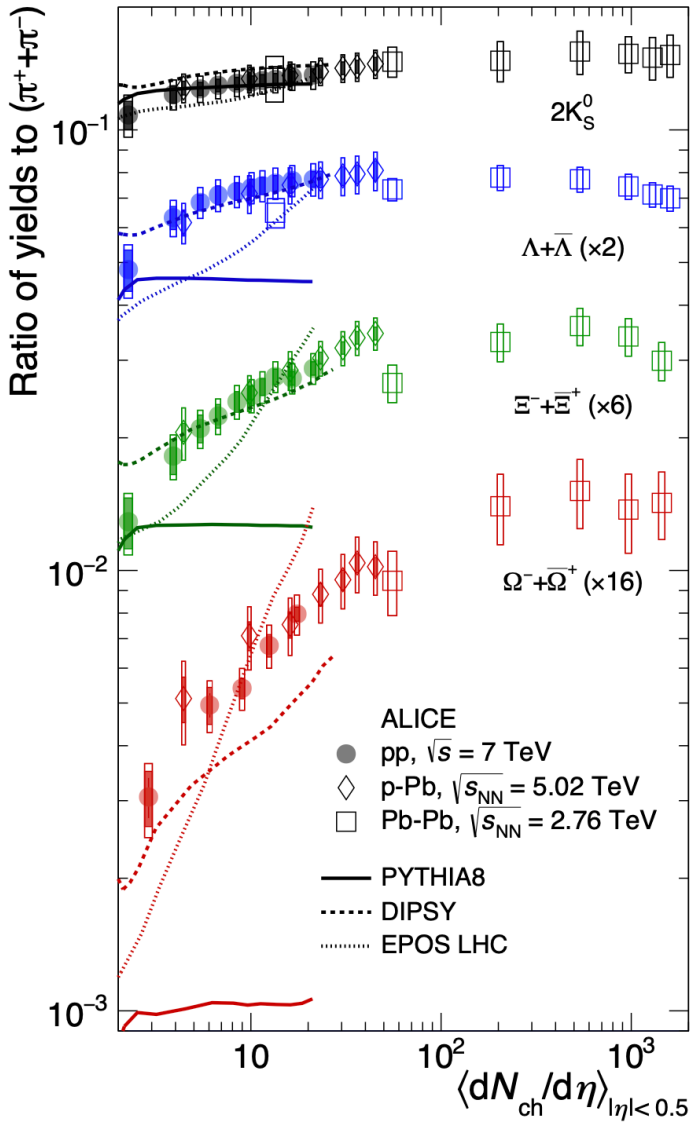

FIGURE 2.17: Yield ratios to pions as a function of $\langle dN_{\rm ch}/d\eta \rangle$ measured in $|y| < 0.5$ in pp, p–Pb and Pb–Pb collisions. Figure taken from [126].

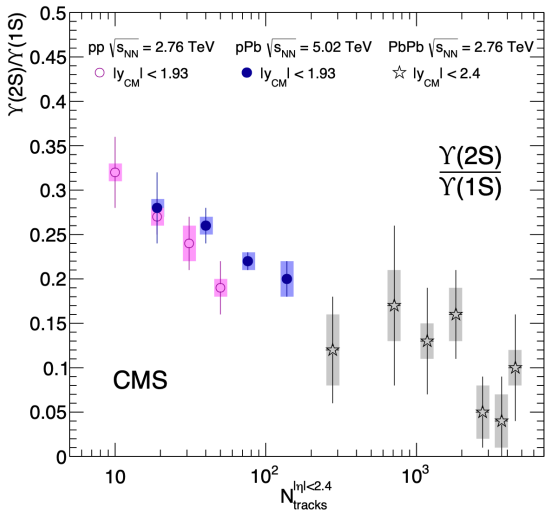

FIGURE 2.18: Single cross section ratios $\Upsilon(2S)/\Upsilon(1S)$ for $|y_{CM}| < 1.93$ versus charged-particle multiplicity measured in $|\eta| < 2.4$, for pp, p–Pb and Pb–Pb collisions. Figure taken from [128].

Another typical signature that usually indicates the presence of a hot, dense medium is jet quenching, as discussed in section 2.2.2, which has also been explored in small collision systems. However, unlike collective phenomena or strangeness enhancement, which show similarities in both large and small collision systems, jet quenching has not been observed in smaller systems [130–135]. One explanation for this is that the system is not sizeable enough to produce the energy loss required to cause jet quenching.

2.3.4 Theoretical overview

The emergence of long-range correlations and numerous indicators of medium effects in small collision systems raise important questions about the underlying mechanisms. It remains a subject of debate whether the observed collectivity in small systems arises from the same processes as in heavy-ion collisions. Since the observation of collective phenomena in small collision systems, considerable theoretical work has been undertaken. These models account for both initial and final state interactions. Initially, the profile of gluon hot spots within a proton is thought to generate the initial geometric eccentricity [49, 136]. Collectivity may also receive contributions from the color glass condensate, which introduces initial momentum anisotropy [49, 136]. The Lund string model suggests that collectivity can emerge from geometry by overlaping string. In the final stage, hydrodynamic models have proven highly successful in explaining many observables [50, 137, 138].

Simultaneously, transport models qualitatively agree with the data though there are some quantitative discrepancies compared to the experimental measurements [139]. However it is premature to conclude that it is unsuitable for modeling the collective behavior. In addition, collectivity can additionally manifest through hadronic rescattering in the final state [140]. Distinguishing the contributions from these various physical mechanisms is crucial for a comprehensive understanding of the dynamics at each stage of the collision.

2.3.5 Multi-observable analysis

As discussed in section 2.3.1, section 2.3.2 and section 2.3.3, the collective effects, which often referred to as QGP-like effects have been widely observed. Meanwhile, as discussed in section 2.3.4, various models are attempting to accurately describe the measurements. However, it has been discovered that the collective phenomena in small collision systems are complex, being influenced by factors such as initial stage effects, final stage effects, and short-range correlations. Attempting to attribute the collective phenomena to a single mechanism is an oversimplification and is not accurate.

Therefore, it is essential to examine the phenomena through a variety of observables. Although most observables cannot isolate a single physical mechanism, each one provides insight into different aspects of the phenomena, offering different sensitivity to the initial stages, system evolution, and hard scatterings. The flow coefficients v_n, cumulants c_n, symmetric cumulants $\mathrm{SC}(3,2), \mathrm{SC}(4,2)$, nonlinear flow observables $\rho_{4,22}, \chi_{4,22}, \rho_{4,22}$ and flow-mean transverse momentum correlations will be examined in the following sections, offering insights into the construction of models that describe the phenomena from the interplay from various physical aspects.

3 Anisotropic flow observables

3.1 Final state particle azimuthal distribution

Anisotropic flow [35, 36] was shortly introduced in section 2.2.2. The extended description is presented in this chapter. The azimuthal distribution of final particles in the transverse plane can be characterized using a Fourier series as equation 3.1:

$$f(\varphi) = \frac{1}{2\pi}\left[1 + 2\sum_{n=1}^{\infty} v_n \cos[n(\varphi - \Psi_n)]\right].$$

The distribution can also be written in a more compact form as:

$$f(\varphi) = \frac{1}{2\pi}\sum_{n=-\infty}^{+\infty} \overrightarrow{V_n}\, e^{-in\varphi}, \tag{3.1}$$

where $\overrightarrow{V_n}$ is the nth order flow-vector, defined as $\overrightarrow{V_n} = v_n\, e^{in\Psi_n}$. Its magnitude is v_n and its orientation is Ψ_n.

At mid-central heavy-ion collisions, due to the almond-like shape of the overlap region, with the hydrodynamic evolution from the initial stage to the final stage, the azimuthal distribution of the final particles exhibits anisotropy in the transverse plane, leading to a non-zero v_2. The nonvanishing higher-order flow harmonics coefficient v_3 arises from the initial fluctuations in geometry. Due to the quantum fluctuations in the initial state and transport development in the later stage, the symmetry plane Ψ_n and the flow coefficient v_n also fluctuate event-by-event [141]. The measurement of the flow harmonics coefficients and their fluctuations provide a powerful tool to study the initial geometry of the system and to constrain the viscosity to entropy density ratio of the QGP medium [142].

3.2 Multi-particle cumulants and flow coefficients

Precisely determining the symmetric plane is very challenging in experiments, if not impossible. The flow coefficient v_n can be obtained using the multi-particle cumulants technique, without knowing the symmetry planes [143, 144].

The two-particle flow harmonics coefficient v_n is defined as:

$$v_n\{2\} \equiv \sqrt{c_n\{2\}}, \tag{3.2}$$

where the two-particle cumulants $c_n\{2\}$ is a characteristic of the event-by-event distribution of v_n, defined as:

$$c_n\{2\} \equiv \langle v_2^2 \rangle. \tag{3.3}$$

The higher order multi-particle cumulants $c_n\{4\}$ and $c_n\{6\}$ are also the characteristics of the event-by-event distribution of v_n, defined as:

$$\begin{aligned} c_n\{4\} &\equiv \langle v_n^4 \rangle - 2\langle v_n^2 \rangle^2, \\ c_n\{6\} &\equiv \langle v_n^6 \rangle - 9\langle v_n^4 \rangle \langle v_n^2 \rangle + 12\langle v_n^2 \rangle^3. \end{aligned} \tag{3.4}$$

The corresponding multi-particle flow harmonics coefficients $v_n\{4\}$, $v_n\{6\}$ can be defined as:

$$\begin{aligned} v_n\{4\} &\equiv \sqrt[4]{-c_n\{4\}}, \\ v_n\{6\} &\equiv \sqrt[6]{\frac{1}{4} c_n\{6\}}. \end{aligned} \tag{3.5}$$

If the fluctuations of v_n are negligible and the non-flow correlations are absent, the different order multi-particle flow harmonics v_n are expected to be equal to each other:

$$v_n\{2\} = v_n\{4\} = v_n\{6\} = v_n. \tag{3.6}$$

If the distribution of v_n is Bessel-Gaussian, the mean and the standard deviation of v_n distributions can be approximated by the multi-particle flow harmonics $v_n\{m\}$ [141]:

$$\begin{aligned} v_n\{2\}^2 &\approx \bar{v}_n^2 + \sigma_{v_n}^2, \\ v_n\{4\}^2 &\approx \bar{v}_n^2 - \sigma_{v_n}^2. \end{aligned} \tag{3.7}$$

The following relation is approximately satisfied:

$$v_n\{4\} \approx v_n\{6\}. \tag{3.8}$$

Another significant advantage of using higher-order multi-particle flow harmonics coefficients is that they are less sensitive to few particle correlations, compared with the flow harmonics coefficients measured with two-particle cumulants.

3.3 Symmetric cumulants

The symmetric cumulants $\mathrm{SC}(m,n)$ [145], characterizing the correlations between v_m^2 and v_n^2, is defined as:

$$\mathrm{SC}(m,n) = \langle v_m^2 v_n^2 \rangle - \langle v_m^2 \rangle \langle v_n^2 \rangle \tag{3.9}$$

At mid-centrality heavy-ion collisions, where there is an almond-like shape of the overlap region, different even orders of flow harmonics (v_{2n}) are all expected to have a contribution from the initial geometry ellipticity ε_2. A positive correlation between v_2^2 and v_{2m}^2 is expected. The flow harmonic v_3 is proportional to the initial triangularity ε_3, which is driven by the fluctuations in the initial state. The correlation between v_2^2 and v_3^2 is expected to originate from the correlation between ε_2 and ε_3. Simulation shows that the ε_2 and ε_3 are anti-correlated, and thus the $\mathrm{SC}(3,2)$ is negative. It has been found that $\mathrm{SC}(m,n)$ exhibits a unique sensitivity to the initial conditions of the heavy-ion collisions [146]. It provides independent information on the properties of the QGP with respect to the information provided by the multi-particle cumulants.

The symmetric cumulants $\mathrm{SC}(m,n)$ can be normalized by the corresponding multi-particle flow harmonics $v_m\{2\}$ and $v_n\{2\}$, which is defined as:

$$\begin{aligned} \mathrm{NSC}(m,n) &\equiv \frac{\mathrm{SC}(m,n)}{\langle v_m^2 \rangle \langle v_n^2 \rangle} \\ &= \frac{\langle v_m^2 v_n^2 \rangle - \langle v_m^2 \rangle \langle v_n^2 \rangle}{\langle v_m^2 \rangle \langle v_n^2 \rangle} \end{aligned} \tag{3.10}$$

The normalization cancels the hydrodynamic response of the flow harmonics to the initial geometry fluctuations and makes the observable more sensitive to the initial conditions. The symmetric cumulants are also insensitive to few-particle correlations, which are strongly suppressed in four-particle cumulants [146].

3.4 Nonlinear flow mode

The low harmonics flow coefficients v_2 and v_3 are dominated by the linear response to the initial geometric eccentricities, i.e. $v_2 \propto \varepsilon_2$ and $v_3 \propto \varepsilon_3$. However, the higher harmonics flow v_4 is not only determined by the linear response to the initial geometry, but also the nonlinear response to the initial geometry, i.e.

$$V_4 = V_4^{\mathrm{L}} + V_4^{\mathrm{NL}} = V_4^{\mathrm{L}} + \chi_{4,22}(V_2)^2, \tag{3.11}$$

where V_4^{L} and V_4^{NL} are the linear and nonlinear response to the initial geometry, respectively.

If the nonlinear flow vector is independent of the linear flow vector, i.e. $V_4^{\rm L}$ and $V_4^{\rm NL}$ are orthogonal to each other, which has been confirmed by [94], the magnitude of the nonlinear part of V_4 could be measured with respect to the symmetry plane Ψ_2:

$$v_4^{\rm NL} = v_{4,22} = v_4\{\Psi_2\}. \tag{3.12}$$

The $v_4\{\Psi_2\}$ is defined as:

$$v_4\{\Psi_2\} = \frac{\Re\langle V_4^* V_2^2\rangle}{\sqrt{\langle V_2^{2*} V_2^2\rangle}} = \frac{v_4 v_2^2 \cos(4\Psi_4 - 4\Psi_2)}{\sqrt{\langle v_2^4\rangle}} \sim \langle v_4 \cos(4\Psi_4 - 4\Psi_2)\rangle. \tag{3.13}$$

The nonlinear coefficient $\chi_{4,22}$ could be obtained with

$$\chi_{4,22} = \frac{v_{4,22}}{\sqrt{\langle v_2^4\rangle}}. \tag{3.14}$$

The nonlinear flow harmonic $v_{4,22}$, combined with the measurement of low order flow harmonics v_2, reduces the dependence on the initial conditions and provides a direct measurement of the development of the anistropic flow from the initial geometry. The nonlinear contribution of V_4 can is also related to the positive sign of symmetric cumulants SC(4, 2) [147]. The nonlinear response coefficient is mostly determined at freeze-out [94], providing an unique opportunity to study this stage of the heavy-ion collisions. Another observable, $\rho_{4,22}$, defined as

$$\rho_{4,22} = \frac{v_{4,22}}{v_4\{2\}} \sim \langle \cos(4\Psi_4 - 4\Psi_2)\rangle, \tag{3.15}$$

charactering the correlation between different order flow symmetry planes.

3.5 $v_n^2 - [p_{\rm T}]$ correlation

The correlation between the average transverse momentum $p_{\rm T}$ and elliptic flow coefficient v_2^2 [148], is given by:

$$\rho(v_2^2, [p_{\rm T}]) = \frac{{\rm cov}(v_2^2, [p_{\rm T}])}{\sqrt{{\rm var}(v_2^2)}\sqrt{{\rm var}([p_{\rm T}])}}. \tag{3.16}$$

The square bracket in $[p_{\rm T}]$ denotes the average transverse momentum of charged particles in a given event. The v_2^2 is calculated using the 2-particle cumulant method. The ${\rm cov}(v_2^2, [p_{\rm T}])$ is the covariance between v_2^2 and $[p_{\rm T}]$, which is defined as:

$${\rm cov}(v_2^2, [p_{\rm T}]) = \langle v_2^2 \delta p_{\rm T}\rangle, \tag{3.17}$$

where $\delta p_T = [p_T] - \langle [p_T] \rangle$. The $\mathrm{var}(v_2^2)$ and $\mathrm{var}([p_T])$ are the variance of v_2^2 and $[p_T]$, which are defined as:

$$\mathrm{var}(v_2^2) = \langle v_2^4 \rangle - \langle v_2^2 \rangle^2, \tag{3.18}$$

$$\mathrm{var}([p_T]) = \langle \delta p_T^2 \rangle. \tag{3.19}$$

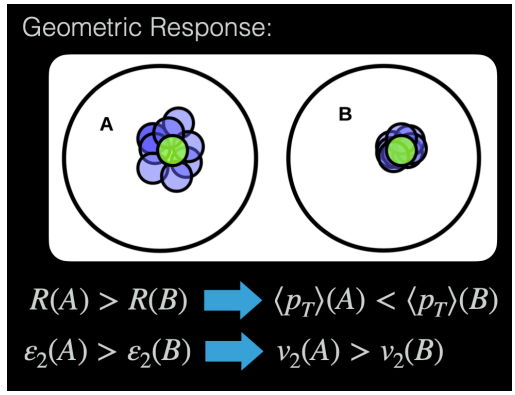

FIGURE 3.1: Sketch of how geometry affects the correlation between v_2 and $[p_T]$ in the case of a few participating nucleons. Figure taken from [149].

In heavy-ion collisions, the $[p_T]$ fluctuation is caused by the size fluctuation of the created fireball. The v_2^2 is determined by the initial geometry eccentricity ε_2^2. The measurement of $\rho(v_2^2, [p_T])$ in heavy-ion collisions is a probe of the initial state fluctuations, characterized by the correlation between the initial geometry eccentricity ε_2^2 and the size of the created fireball.

The geometric model depicted in figure 3.1 provides a straightforward visualization of the correlation in the case of few participating nucleons. When nucleons are compressed together, the resulting fireball is more compact. This compression correlates with an increase in the average transverse momentum. Consequently, the smaller size of the fireball leads to a reduction in v_2^2. Therefore, in such a case, the $\rho(v_2^2, [p_T])$ is expected to be negative.

4 Experimental setup

4.1 The Large Hadron Collider

The experimental analysis conducted in this thesis uses the data collected at the Large Hadron Collider (LHC) [150]. The LHC is the largest particle accelerator and it can accelerate particles to the highest energy in the whole world [150]. It is a circular accelerator with a circumference of 27 km. The LHC is the last in a series of accelerators in the CERN complex, which accelerate the particles to the desired energy, shown in figure 4.1. The LHC can accerate either protons or ions. For protons, the linear accelerator

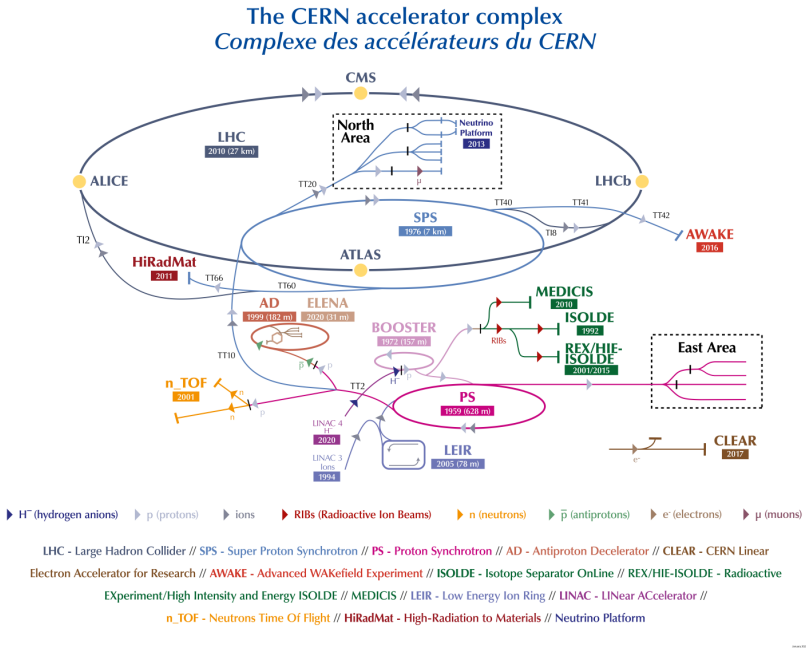

FIGURE 4.1: A schematic view of the LHC complex. Figure taken from [150].

Linac 2 first accelerates the beam to the energy of 50 MeV. Then, the beam accelerates to the energy of 1.4 GeV in the Booster. After that, the beam is injected into the Proton Synchrotron (PS), where the beam is accelerated to the energy of 25 GeV. The beam is then injected into the Super Proton Synchrotron (SPS), where the energy is raised to

450 GeV. Finally, the beam is injected into the LHC, accelerating to the desired energy. The LHC ring consists of two beam pipes in which the two beams circulate in opposite directions. The particles circulating in the LHC are grouped into bunches, with a bunch spacing of 25 ns for proton beams. Each proton bunch contains about 10^{11} protons, while each of the lead bunch contains about 7×10^7 lead ions.

The LHC started its operation in 2008. The first run of the LHC was from 2010 to 2013 (Run 1), and its second run (Run 2) was from 2015 to 2018. The third run (Run 3) started in 2022. The data used in this thesis is collected in the Run 2 period. At Run 2, the LHC is operated at a center of mass energy of 13 TeV for proton-proton collisions. At Run 2 period, the proton-lead collisions and lead-lead collisions are also conducted at the LHC.

One of the primary goal of the LHC is to search for the Higgs boson. Two general-purpose detectors, A Toroidal LHC ApparatuS (ATLAS) and Compact Muon Solenoid (CMS), are designed to search for the Higgs boson, which was discovered in 2012 by the two experiments. Many other physics topics are also studied at the LHC, such as the measurements of the standard model parameters, searching for dark matter, study of beyond the Standard Model physics, flavor physics and also the study of the quark-gluon plasma. To study fruitful physics topics besides the general-purpose detectors ATLAS and CMS, the Large Hadron Collider beauty (LHCb) experiment is designed for the study of flavor physics, and the A Large Ion Collider Experiment (ALICE) is designed to study the quark-gluon plasma.

4.2 ALICE detector

A Large Ion Collider Experiment (ALICE) is one of the large experiments at the LHC [151]. The ALICE detector is designed to study the quark-gluon plasma (QGP) created in heavy ion collisions. It is also the only detector at the LHC optimized for studying heavy ion collisions. Figure 4.2 shows the schematic view of the ALICE detector. The ALICE detector has two main parts: the central barrel and the muon spectrometer. The coverage of the central barrel is full azimuthal and $|\eta| < 0.9$. It is enclosed by a large solenoid magnet with a magnetic field of 0.5 T. The subdetectors of the central barrel include the Inner Tracking System (ITS) [152], the Time Projection Chamber (TPC) [153], the Time of Flight (TOF) detector [154], the Transition Radiation Detector (TRD) [155], the High Momentum Particle Identification Detector (HMPID) [156], the Photon Spectrometer (PHOS) [157], the Electromagnetic Calorimeter (EMCal) [158], the Di-jet Calorimeter (DCal) [159], the V0 detector [160], the T0 detector [161] and the Zero Degree Calorimeter (ZDC) [162]. Some of them will be introduced in the following sections.

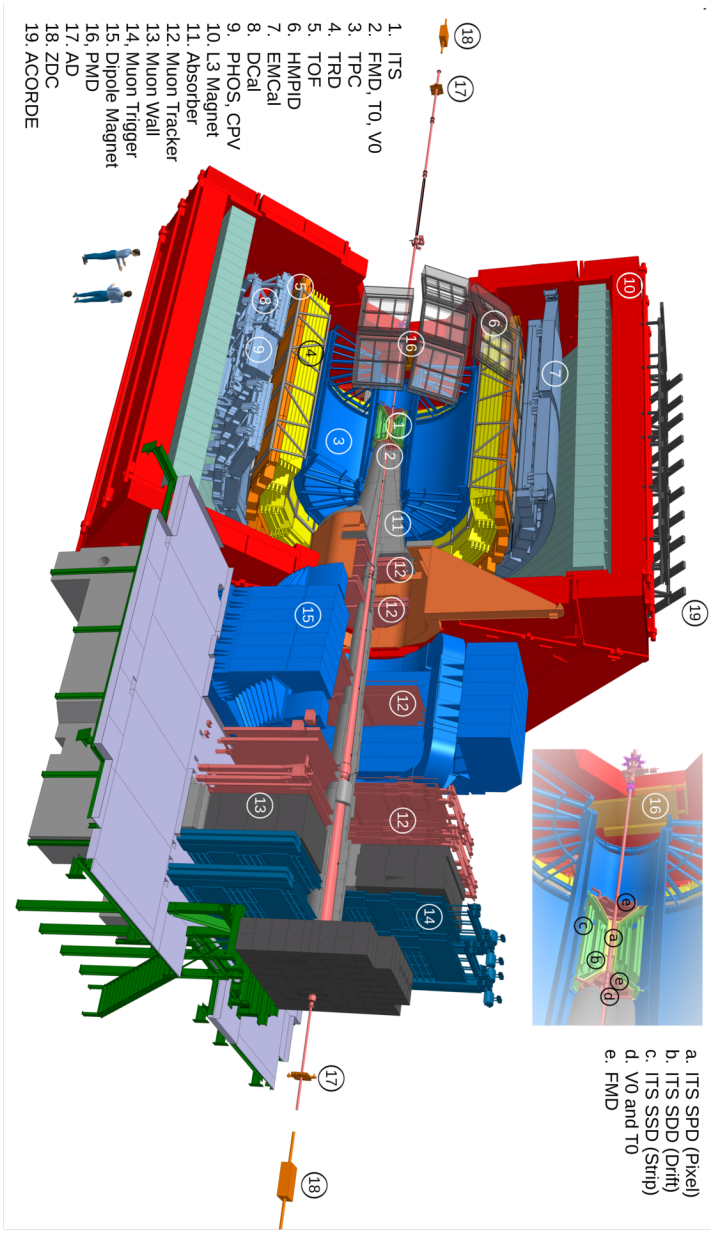

FIGURE 4.2: A schematic view of the ALICE detector during the LHC Run 2 period. Figure taken from [10].

The ALICE coordinate system is defined with the origin at the geometrical center of the ALICE detector [151].

The z-axis is oriented along the beam direction, pointing from the muon spectrometer to the central barrel. This means that the muon spectrometer is positioned at the negative end of z-axis. The x-axis is pointing toward the LHC ring's center. Meanwhile, the y-axis is pointing upwards.

4.2.1 Inner Tracking System

The Inner Tracking System (ITS) [152] is the innermost subdetector of the ALICE detector, designed to measure the vertex position of charged particles with high precision. It consists of six cylindrical layers of silicon detectors, divided into three different technologies. In the inner most layers, there are two layers of Silicon Pixel Detector (SPD). The middle layers are two layers of Silicon Drift Detector (SDD), and the outer layers are two layers of Silicon Strip Detector (SSD).

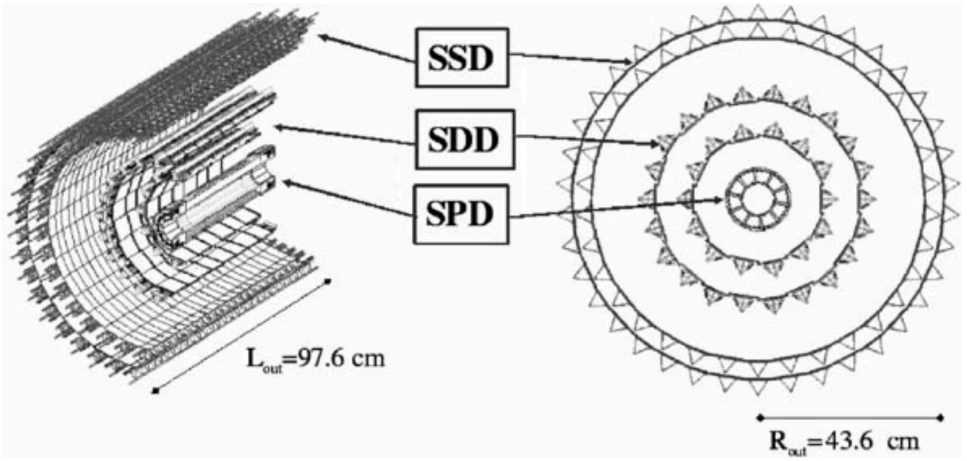

FIGURE 4.3: A schematic view of the ALICE inner tracking system. Figure taken from [163].

The SPD is located at the innermost layers of the ITS, with a radius of 3.9 cm and 7.6 cm. The spatial resolution of the SPD is about 12 μm in the transverse plane and 100 μm along the beam direction. The SDD is located at the middle layers of the ITS, with a radius of 15 cm and 23.9 cm. The outermost layers of the ITS are the SSD, with a radius of 38 cm and 43 cm. The spatial resolution of the SSD is about 20 μm in the transverse plane and 820 μm along the beam direction. With the hits from the SSD, the tracks reconstructed by the ITS can match those reconstructed by the TPC. The readout

of the SDD and SSD layers are analog, providing information on the energy loss of the charged particles. The particle identification can be performed by measuring $\mathrm{d}E/\mathrm{d}x$. The precise measurement of the vertex position and the particle trajectory enables the precise measurement of the distance of the closest approach (DCA) of the particle to the primary vertex. The DCA is used to identify the particles that are produced in the primary vertex.

4.2.2 Time Projection Chamber

The ALICE experiment uses the Time Projection Chamber (TPC) [153] as the main tracker. The TPC is a large cylindrical gas-filled detector with an inner and outer radius of 85 cm and 250 cm. The length of the TPC is 500 cm. A schematic view of the TPC is shown in Figure 4.4. The TPC is filled with a mixture of Ne-CO_2-N_2(90-10-5)

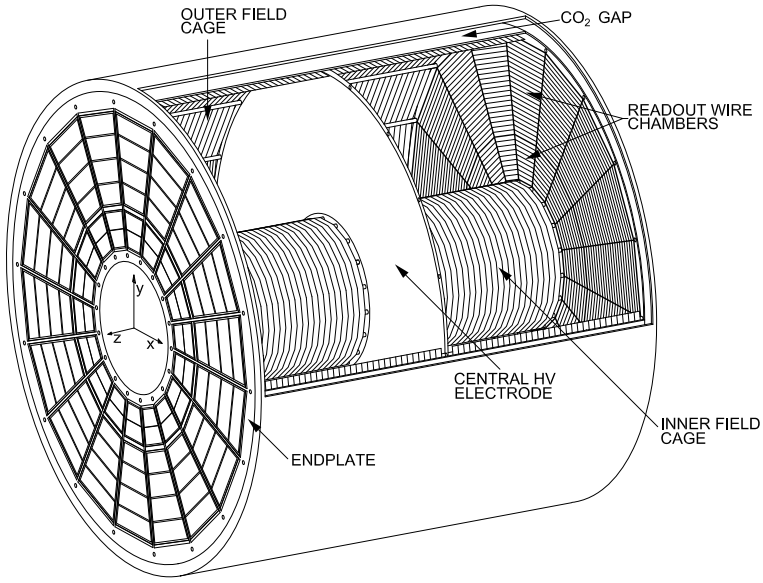

FIGURE 4.4: A schematic view of the ALICE Time Projection Chamber. Figure taken from [153].

gas. The sensitive volume of the TPC is immersed in a uniform electrostatic field of 400 V/cm, provided by the central electrode and the endplates. When a charged particle passes through the TPC, it ionizes the gas inside the volume. The electrons drift towards the endplates of the TPC under the influence of the electric field. The position of the hit in the transverse plane is measured by the position of the signal on the pads at the endplate. The $r-\phi$ resolution is about 1100 and 800 μm for the inner and outer radius of the TPC. The longitudinal position of the hit is measured by the time of the electron cloud arrival at the endplate. With the arrival time of the electrons and the drift velocity

of the electrons in the gas mixture, the longitudinal position of the hit can be determined with a resolution of 1100 to 1250 μm. With up to 159 space points for the reconstruction, the TPC provides a precise measurement of the particle momentum. Benefiting from the many layers, the TPC can measure the energy loss information of the charged particles at each layer. A precise $\mathrm{d}E/\mathrm{d}x$ measurement is obtained by combining the energy loss information along the particle trajectory. The particle identification could be performed according to the Bethe-Bloch curve, which differs for different particle masses.

4.2.3 Time of Flight

The Time of Flight (TOF) [154] detector, as its name indicates, is used to measure the time of the particle's arrival. The TOF detector is a large cylindrical detector with an inner and outer radius of 370 cm and 399 cm. It consists of 18 sectors in the azimuthal direction. Each sector consists of 5 modules in the z-direction. The 90 modules are built with Multi-gap Resistive Plate Chambers (MRPCs). The MRPCs are very fast detectors with the benefit of the high electrostatic field uniformly distributed in the gas volume. At such a high electrostatic field, the ionization electrons generated by the charged particles are immediately collected by the electrodes. The time resolution of the TOF detector reaches 40 ps. The flying time of the particle is determined by the time difference between the particle's arrival at the TOF detector and the collision time, which is determined by the T0 detector. Combined with the particle momentum measured by the TPC, the particle velocity and the particle mass can be determined. The information on the particle mass is used for particle identification.

4.2.4 T0 detector

The T0 detector [161] is a Cherenkov detector consisting of two arrays, T0A and T0C, located at the opposite side of the interaction point. The two arrays are located as close as possible to the beam pipe, covering the full azimuthal angle. When the charged particles pass through the quartz radiator, the Cherenkov photons are emitted and detected by the photomultiplier tubes (PMTs). The time resolution of the T0 detector is about 50 ps, providing the precise collision time of the event.

4.2.5 V0 detector

The V0 detector [160] is a plastic scintillator detector. It consists of two arrays, V0A and V0C, located at opposite sides of the interaction point. The V0A detector is located at the forward rapidity region at $z = 340$ cm, covering the pseudorapidity region of $2.8 < \eta < 5.1$. While the V0C detector is located at the backward rapidity region ($z = -90$ cm, $-3.7 < \eta < -1.7$), close to the muon spectrometer. The scintillator

molecules are excited by the charged particles passing through the scintillator, which emits photons that are detected by the PMTs. The signal strength of the PMTs is proportional to the number of charged particles passing through the scintillator. It is used for the centrality determination. As a solid-state detector, the V0 detector has a very good time resolution of 1 ns. If both V0A and V0C get a signal, and in coincidence with the beam bunch crossing, the event is triggered as a minimum bias event. The V0 detector is also used for the trigger of the high multiplicity events in pp collisions benefiting from the property that the charged particle multiplicity is proportional to the signal strength of the V0 detector.

4.3 Data collection

4.3.1 Trigger

Due to the high collision rate at the LHC, the ALICE detector can not read out all the events. The number of events that can be read out is limited by the readout time and the occupancy of the detectors.

The Central Trigger Processor (CTP) is the main part of the ALICE trigger system [164], used to decide whether to accept or reject the event. The CTP receives the signals from the subdetectors and makes the decision based on the trigger configuration. If the event is accepted, the CTP sends the trigger signal to the subdetectors to read out the data. There are three stages of trigger (L0, L1, and L2), with the increasing complexity and the increasing latency. The L0 trigger makes the decision within the time of 1.2 μs, while the L1 trigger provides a decision within the time of 6.5 μs. The fast response requirement prevents the L0 and L1 triggers from using all the information from the sub-detectors. After the preselection by the L0 and L1 trigger, the L2 trigger makes the decision within the time of 88 μs. After the three stages of trigger based on the information from the hardware, the High-Level Trigger (HLT) further selects the events of interest. It is the software trigger system, using the information based on the reconstructed data.

The so-called minimum bias trigger is defined to select the events with a coincidence of the signals from the V0 detector. The high multiplicity trigger is defined to select the events with an appropriate threshold of the signals from the V0 detector. For the LHC Run 2 period, about 3×10^9 minimum bias Pb–Pb events and 7×10^9 minimum bias p–Pb events were collected. For the pp collisions, about 2×10^{10} high-multiplicity triggered pp events were collected and 1×10^{10} minimum bias pp events were collected.

4.3.2 Reconstruction

The signal collected by the ALICE detector requires a series of reconstruction steps to be converted into the physical quantities analyzed in the physics analysis. The raw output signals from individual detectors are converted into digital signals. The digital signals with adjacent spatial and temporal information are grouped into clusters. The centers of the clusters are used to reconstruct the space points.

The space points are then classified into tracks with certain track-finding algorithms. Before the track finding, an estimation of the primary vertex (PV) is performed with the hits of SPD layers. Tracklets are constructed by combining the hits of the two layers of the SPD. The primary vertex is then estimated by finding the crossing point of most tracklets.

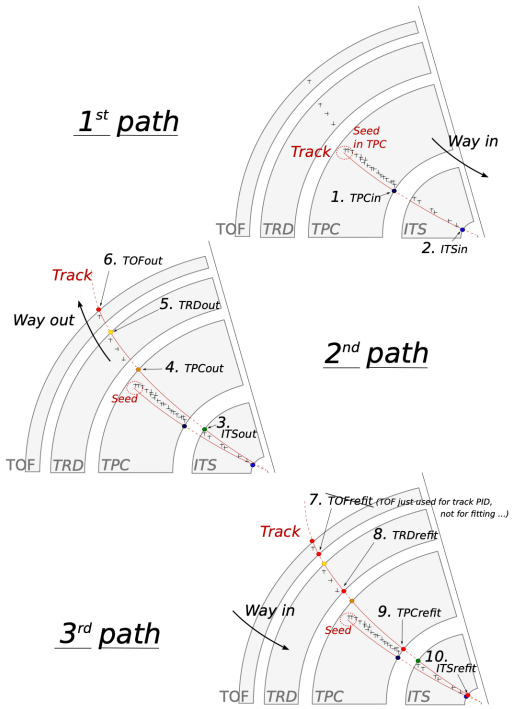

FIGURE 4.5: An illustration of the track reconstruction procedure. Figure taken from [165].

The track reconstruction procedure is illustrated in Figure 4.5. The track reconstruction algorithm starts from the outermost layer of the TPC, where the hit separation is the largest. It first uses the two outermost hits from the TPC as the seed of the track, constructing a track candidate. Then, the track candidate is propagated to the next layer of the TPC, where the hits are searched for the track candidate. The track parameters,

the necessary information for the track propagation, are determined by a track fitting procedure with the Kalman filter [166]. The Kalman filter considers the energy loss, multiple scattering, and the bending of the particle trajectory in the magnetic field. With the Kalman filter, the track parameters can be updated with the new space points in a continuous way. The track-finding procedure described above is repeated, and stopped at the innermost layer of the TPC. The track is then extrapolated to the ITS. The procedure is repeated in the ITS until all the possible hits are included in the track.

A second pass of the track finding is performed reversely from the innermost layer of the ITS in a similar procedure, ending at the TOF detector. In this procedure, the hits from the TRD and TOF are also included in the track finding.

Finally, the tracking procedure is repeated from the last hit, i.e., the outer wall of TOF towards the primary vertex. During the procedure, the track parameters are updated using the Kalman filter, called the track re-fitting. The primary vertex is then re-determined with the tracks reconstructed in the previous step.

The track reconstruction efficiency is about 90% for the tracks with $p_{\mathrm{T}} > 0.2$ GeV/c, benefiting from the large number of space points provided by the TPC. The relative momentum resolution could reach 1.5% when the track is reconstructed with the TPC and ITS.

5 Experimental analysis

This chapter presents the details of the experimental analysis. First, the dataset, along with the criteria for event and track selection, will be introduced. The detailed methodology for calculating the observables will then be introduced. Lastly, the approaches used to estimate statistical and systematic uncertainties will be described.

5.1 Dataset and selection

5.1.1 Dataset

The dataset used in this analysis was collected by ALICE during the LHC Run 2 periods. The data sample includes pp collisions at a center-of-mass energy of $\sqrt{s} = 13$ TeV collected in 2016, 2017, and 2018. Additionally, p–Pb collision data at center-of-mass energy per nucleon-nucleon pair $\sqrt{s_{\mathrm{NN}}} = 5.02$ TeV was collected in 2016. The Pb–Pb collision data at a center-of-mass energy per nucleon-nucleon pair $\sqrt{s_{\mathrm{NN}}} = 5.02$ TeV was collected in 2015 and 2018. The data sample encompasses nearly all of the LHC Run 2 data, enabling us to make the most precise measurements possible at ALICE.

5.1.2 Event selection

The data collected by the ALICE detector undergoes rigorous filtering and selection processes to ensure that the sample used in the analysis is of high quality and contains the most relevant physics information. This selection process includes both trigger selection and offline selection of events. The minimal bias trigger (MB) is used in p–Pb and Pb–Pb collisions. While in pp collisions, the High Multiplicity trigger (HM) is used, considering the flow signal is very small in pp collisions. The MB trigger is obtained through a coincidence of signals with the V0A and V0C in time. The amplitudes of the V0M are a sum of V0A and V0C signals, which is proportional to charged track multiplicity. The HM Trigger is designed to select events with a higher event activity among the all events. The HM Trigger is triggerd when the V0M signal is four to five times the average value observed in MB collisions, depending on the period of data collection. This effectively select the top 0.1% of MB events that has the highest particle multiplicity as measured by V0M.

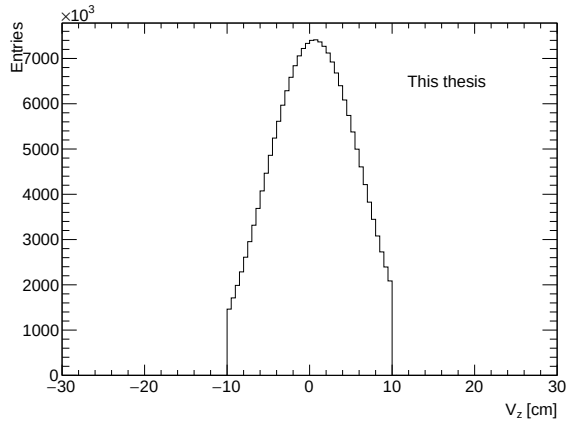

FIGURE 5.1: Distribution of V_z in 5.02 TeV Pb–Pb collisions after all the event cuts.

The positions of primary vertices are determined using signals recorded by the SPD. A vertex cut of $-10 < V_z < 10$ cm is implemented to reject events whose primary vertex is displaced significantly from the center of the detector. The example of primary vertex distribution in Pb–Pb collisions is plotted in figure 5.1.

5.1.3 Track selection

Selection criteria are applied to ensure the quality of the tracks. The default choice of tracks used in this analysis is global tracks. The global tracks require hits from both the Inner Tracking System (ITS) and the Time Projection Chamber (TPC), with a minimum requirement of 70 TPC clusters out of a total of 159. The maximum chi-squared (χ^2) value per TPC cluster should not exceed 2.5. Additionally, there must be at least one hit in the SPD detector, and the maximum χ^2 value per ITS cluster should not be larger than 3.6. A converged track fit is required during the final step of the track reconstruction procedure.

A criteria on the distance of closest approach (DCA) to the primary vertex is applied to reduce the tracks from secondary decays. The distance of the closest approach (DCA) in the longitudinal direction ($|\mathrm{DCA}_z|$) must be less than 2 cm. Additionally, the p_T distance of closest approach in the transverse plane cuts are $\mathrm{DCA}_{xy} < 7 \times (0.0026 + 0.005/p_\mathrm{T}^{1.01})$.

The general track cuts applied were as follows: $|\eta| < 0.8$, $0.2 < p_\mathrm{T} < 3.0$ GeV/c. The condition $|\eta| < 0.8$ ensures that the tracks are contained within the TPC acceptance coverage. The lower bound of the p_T selection is limited by the ability of the detector to confirm the curved tracks with a small radius could be reconstructed. The upper bound of p_T selection is to exclude particles from hard scattering, which is not the focus of

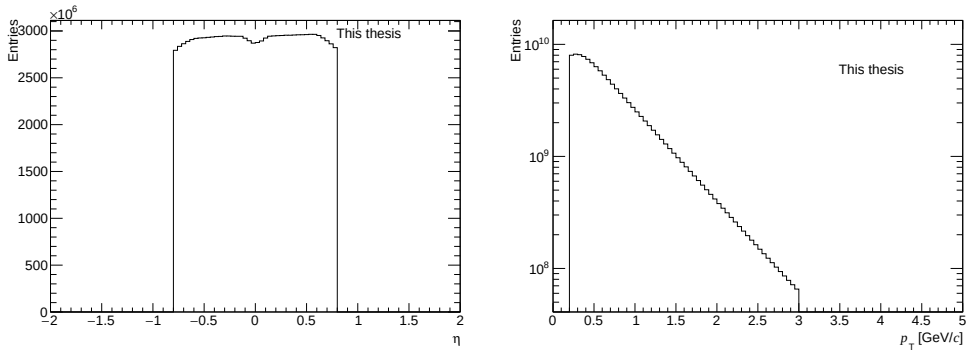

FIGURE 5.2: Distribution of pseudorapidity (left) and transverse-momentum (right) in 5.02 TeV Pb–Pb collisions, after all the event and track cuts.

this analysis. An example of pseudorapidity and transverse momentum distributions in Pb–Pb collisions are shown in figure 5.2.

5.2 Analysis procedure

Generally, the analysis procedure is structured as follows: events are first classified into event classes through their multiplicity, which is measured by taking into account the effects of the detector. The observables, to be described in the section 5.2.2, are measured for each event class. The flow observables are obtained in terms of multiple particle correlations, which are described in this section. The correlations include azimuthal correlations, transverse momentum correlations, and azimuthal-transverse momentum correlations. Calculating the multiple particle correlation usually requires multiple track loops, which are extremely CPU-heavy. The multiple azimuthal track loop is optimized to a single loop with the Q-cumulants method [143, 144], which will be discussed in section 5.2.3. In addition, the $v_2^2 - [p_{\mathrm{T}}]$ involving transverse momentum could not be simply expressed with the Q-cumulants method. Therefore, the expression of $v_2^2 - [p_{\mathrm{T}}]$ correlation in terms of track azimuthal angle and transverse momentum is specially discussed in section 5.2.4.

5.2.1 Event classification and multiplicity correction

The events are classified according to their charged tracks multiplicity in $0.2 < p_{\mathrm{T}} < 3$ GeV/c and $|\eta| < 0.8$. In the experiment, one can only obtain the reconstructed number of charged tracks, whereas the generated number of charged tracks could only be estimated. The generated number of charged tracks is estimated with an efficiency correction,

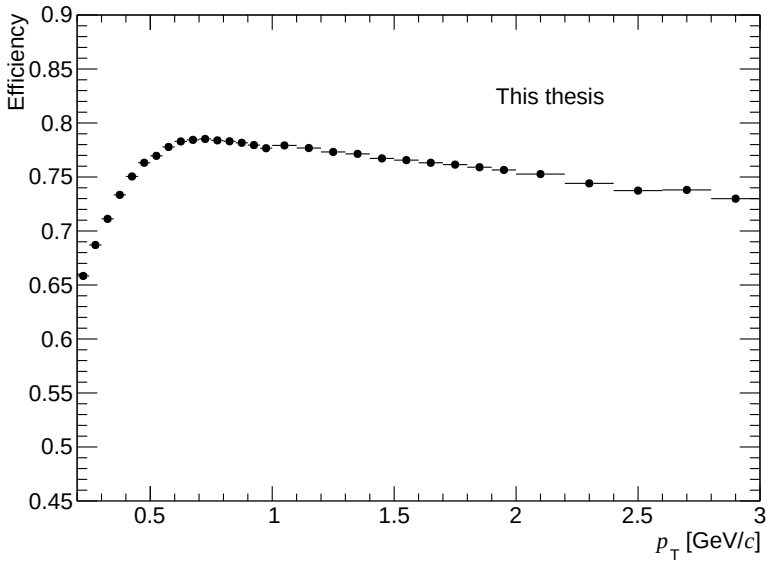

FIGURE 5.3: p_T-dependent efficiency in p–Pb collisions, calculated from DPMJET simulation. Efficiencies for pp and Pb–Pb collisions are obtained in a similar manner but are not shown here.

calculated by

$$N_{\rm ch}^{\rm gen} = \sum_{\rm trk} \frac{1}{{\rm eff}(p_{\rm T})}, \tag{5.1}$$

where the ${\rm eff}_{\rm trk}(p_{\rm T})$ is the $p_{\rm T}$ dependent tracking efficiency for each track, with the correction of feeddown. The efficiency is obtained from Monte Carlo simulation, defined as

$${\rm eff}(p_{\rm T}) = \frac{N_{\rm reco}(p_{\rm T})}{N_{\rm sim}(p_{\rm T})}, \tag{5.2}$$

where the $N_{\rm reco}$ and $N_{\rm sim}$ are the simulated and reconstructed number of tracks. In pp collisions, the PYTHIA 8 [51] generator is used in generating the events for efficiency estimation. While in p–Pb and Pb–Pb collisions, the DPMJET [167] and the HIJING [62] are considered.

The non-uniform efficiency is calculated from the Monte Carlo as the ratio of $p_{\rm T}$ distribution obtained from MC-reconstructed to $p_{\rm T}$ distribution from MC-truth data sample. MC-truth data sample contains only primary generated particles with positive or negative charge with the same kinematic cuts as are used in the real data analysis. The MC-reconstructed sample is obtained from the generated particles propagated through the detector using GEANT 4 [168] and then reconstructed using the same reconstruction procedure used in real data. An example of the efficiency plot is shown in figure 5.3.

FIGURE 5.4: Demostration of two-particle correlation without subevent, denoted as the standard method.

5.2.2 Formulation of observables

In this section, the details of measuring multi-particle azimuthal correlations, cumulants, flow coefficients, symmetric cumulants, and nonlinear flow observables will be presented. The explanation begins by expressing multi-particle azimuthal correlations through track loops that apply various suppression methods, without taking into account detector effects. The correction to the observables will be subsequently discussed. Finally, how the other observables are expressed with multi-particle azimuthal correlations will be discussed.

Two-particle azimuthal angle correlation

The multi-particle azimuthal angle correlations are first formulated without accounting for detector effects. The corrections for these effects in the multi-particle correlation expression will be addressed subsequently. The two-particle azimuthal angle correlation in an event is constructed as

$$\langle \cos(n(\varphi_1 - \varphi_2)) \rangle = \frac{1}{N_{\text{comb}}} \sum_{i \neq j} \cos(n(\varphi_i - \varphi_j)), \tag{5.3}$$

where φ_i and φ_j are the azimuthal angles of two particles. The left-hand side of the equation is a shorted form of the right-hand side. The variables φ_1 and φ_2 correspond to φ_i and φ_j, respectively, on the right-hand side of the equation 5.3. The variables i and j iterate over all pairs of tracks. The $N_{\text{comb}} = N_{\text{trk}}(N_{\text{trk}} - 1)$ represents the number of track combinations, where N_{trk} is the total number of tracks.

The two particles are taken from the range of $|\eta| < 0.8$ of the detector, as illustrated in figure 5.4. The approach of constructing the two-particle correlation using all track combinations is referred to as the standard method. This is to distinguish it from the subevent methods, which will be discussed subsequently.

The event-averaged two-particle azimuthal angle correlation is constructed as

$$\langle\langle\cos(n(\varphi_1-\varphi_2))\rangle\rangle = \frac{\sum_{i}^{\text{evt}} W_i\langle\cos(n(\varphi_1-\varphi_2))\rangle_i}{\sum_{i}^{\text{evt}} W_i}, \tag{5.4}$$

where i iterate over all the events, $\langle\cos(n(\varphi_1-\varphi_2))\rangle_i$ is the two-particle azimuthal angle correlation in one event defined in equation 5.3, and the W_i is the event weight, proportional to N_{comb}. The double angle bracket means the average of particle combinations and the average of events.

To suppress the effects of short-range particle correlations, the $|\Delta\eta|$ separation method, which is also called the two-subevent method, is used. When constructing the two-particle correlation, the particles are required to be chosen from specific η ranges, denoted as

$$\langle\cos(n(\varphi_1-\varphi_2))\rangle_{|\Delta\eta|>a} = \frac{1}{N_{\text{comb}}}\sum_{i,j}\cos(n(\varphi_i-\varphi_j)), \tag{5.5}$$

where a is the size of $|\Delta\eta|$ separation. The particle 1 is taken from the negative η region of the detector, i.e., $\eta_i < -a/2$ and the particle 2 is taken from the positive η region of the detector, i.e., $\eta_j > a/2$. Here the η_1 and η_2 are the pseudorapidity of particles 1 and 2, corresponding to the azimuthal angle φ_1 and φ_2, as illustrated in figure 5.5. The N_{comb} equal to N_1N_2 in this case, with N_1 the number of particles with $\eta_i < -a/2$ and N_2 the number of particles with $\eta_j > a/2$.

The event average for the two-particle correlation with $|\Delta\eta|$ separation takes the same procedure as the event average for the two-particle correlation with the standard method. Additionally, the event average procedure is the same and will not be repeated in the later discussions for the other multiparticle azimuthal angle correlation methods.

The $|\Delta\eta|$ separation method reduces the possibility that two particles originate from short-range correlations, such as fragmentations of the same jet or resonance decays. However, a notable limitation of this method is the significant reduction in statistics.

Additionally, two-particle correlations are used in constructing observables involving multiparticle correlations, such as $c_2\{4\}$ and $\text{SC}(m,n)$. The three-subevent method is used in constructing such observables. In this case, as a two-particle correlation, only two of the three subevents are used. Depending on the selected subevents among the three, the configuration is noted as $n_1|n_2|$, $n_1||n_2$, or $|n_1|n_2$. For instance, as shown in figure 5.6 the two-particle correlation with $n|-n|$ is constructed as

$$\langle\cos(n(\varphi_1-\varphi_2))\rangle_{n|-n|} = \frac{1}{N_{\text{comb}}}\sum_{i,j}\cos(n(\varphi_i-\varphi_j)), \tag{5.6}$$

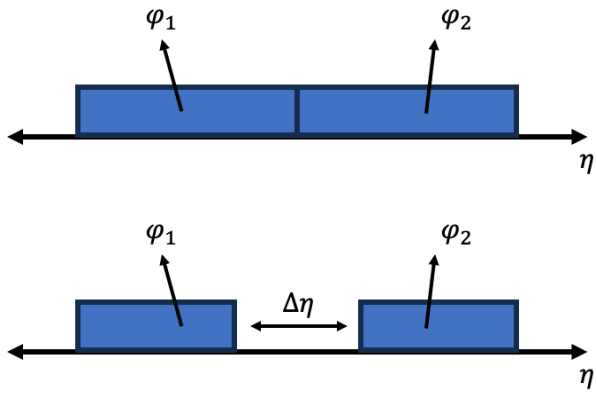

FIGURE 5.5: Demostration of two-particle correlation with two subevents.

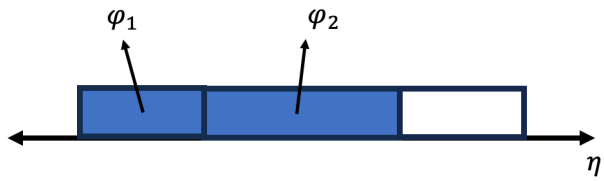

FIGURE 5.6: Demostration of two-particle correlation with two subevents, while the two subevents are selected to be the middle ($-0.4 < \eta < 0.4$) and left side ($-0.8 < \eta < -0.4$) of the detector.

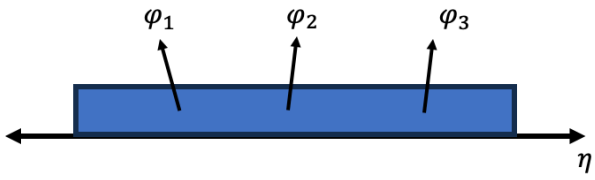

FIGURE 5.7: Demostration of three-particle correlation without subevent, denoted as the standard method.

where particle 1 is taken from the region of $\eta_i < -0.4$, and particle 2 is taken from the region of $-0.4 < \eta_j < 0.4$, as illustrated in figure 5.5.

Three-particle azimuthal angle correlation

Similarly, the 3-particle azimuthal angle correlation is constructed as

$$\langle \cos(n_1\varphi_1 + n_2\varphi_2 + n_3\varphi_3) \rangle = \frac{1}{N_{\text{comb}}} \sum_{i \neq j \neq k} \cos(n_1\varphi_i + n_2\varphi_j + n_3\varphi_k), \tag{5.7}$$

where φ_i, φ_j, and φ_k are the azimuthal angles of three particles. The three particles are taken from the full range of $|\eta| < 0.8$ of the detector, as illustrated in figure 5.7. The N_{comb} is the number of combinations, defined as $N_{\text{comb}} = N_{\text{trk}}(N_{\text{trk}} - 1)(N_{\text{trk}} - 2)$, with N_{trk} the number of tracks. The event-averaged three-particle azimuthal angle correlation is denoted as $\langle\langle \cos(n_1\varphi_1 + n_2\varphi_2 + n_3\varphi_3) \rangle\rangle$.

The subevent method can also be applied. In this case, the particles can be divided into two or three subevents. The pseudorapidity range defines the subevents. With two subevents, the three-particle correlation is denoted as

$$\langle\langle \cos(n_1\varphi_1 + n_2\varphi_2 + n_3\varphi_3) \rangle\rangle_{|\Delta\eta| > a}. \tag{5.8}$$

The formula will not be expanded, considering that the format of the equation is similar to previous equations. Instead, what is important is to address that the $|\Delta\eta| > a$ represents that $-0.8 < \eta_1 < -a/2, -0.8 < \eta_2 < -a/2$ and $a/2 < \eta_3 < 0.8$, where η_1, η_2 and η_3 are the pseudorapidity of particle 1, particle 2 and particle 3, corresponding to the azimuthal angle φ_1, φ_2 and φ_3, as illustrated in figure 5.8.

This analysis uses the three-subevent method in addition to the two-subevent method when calculating the multi-particle correlation. With three subevents, the three-particle correlation is noted as

$$\langle\langle \cos(n_1\varphi_1 + n_2\varphi_2 + n_3\varphi_3) \rangle\rangle_{n_1|n_2|n_3}, \tag{5.9}$$

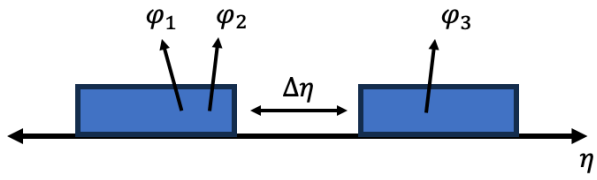

FIGURE 5.8: Demostration of three-particle correlation with two subevents.

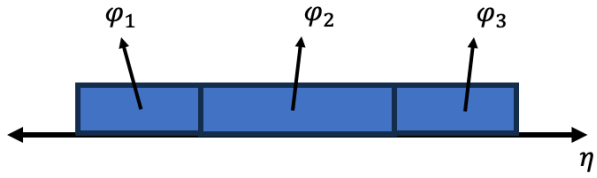

FIGURE 5.9: Demostration of three-particle correlation with three subevents.

where particles 1, 2 and 3 are taken from the left, middle, and right parts of the event. The order of harmonic n corresponding to the φ could be different. That means, the $n_1|n_2|n_3$ and $n_2|n_1|n_3$ ($n_1 \neq n_2$) are actually different configurations, as illustrated in figure 5.9.

Four-particle azimuthal angle correlation

The four-particle azimuthal angle correlation is noted as

$$\langle\langle\cos(n_1\varphi_1 + n_2\varphi_2 + n_3\varphi_3 + n_4\varphi_4)\rangle\rangle \tag{5.10}$$

Without using the sub-event, four particles are taken from the whole η region, called the standard method, as is illustrated in figure 5.10.

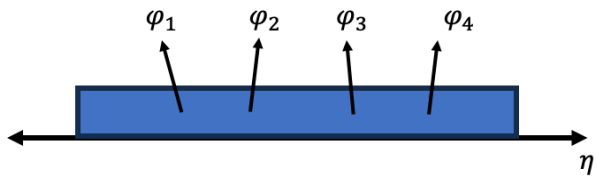

FIGURE 5.10: Demostration of four-particle correlation without subevents, denoted as the standard method.

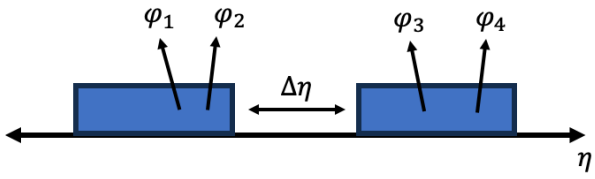

FIGURE 5.11: Demostration of four-particle correlation with two subevents.

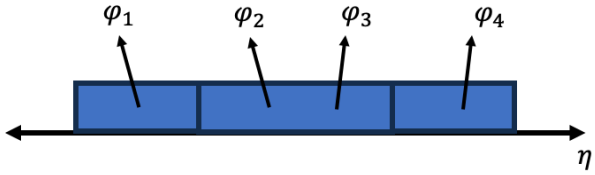

FIGURE 5.12: Demostration of four-particle correlation with three subevents.

The subevent method can also be applied. In this case, the particles can be divided into two or three subevents. The four-particle correlation with two subevents is noted as

$$\langle\langle\cos(n_1\varphi_1 + n_2\varphi_2 + n_3\varphi_3 + n_4\varphi_4)\rangle\rangle_{|\Delta\eta|>a} \tag{5.11}$$

Two particles are taken from the region of $\eta < -a/2$ and two others are taken from the region of $\eta > a/2$. The method is illustrated as in figure 5.12.

The three subevent method is also used for four-particle correlations, as illustrated in figure 5.11.

$$\langle\langle\cos(n_1\varphi_1 + n_2\varphi_2 + n_3\varphi_3 + n_4\varphi_4)\rangle\rangle_{n_1,n_2|n_3|n_4} \tag{5.12}$$

Here φ_1,φ_2,φ_3, and φ_4 are taken from different regions. There are a few choices; one can choose two particles from the left region of the detector, the middle region of the detector, or the right region. If the φ_1 and φ_2 is taken from the left region, φ_3 from middle and φ_4 from right, the configuration is labeled as $n_1, n_2|n_3|n_4$. The other configurations are labeled as $n_3|n_1, n_2|n_4$ and $n_3|n_4|n_1, n_2$, which manifest how the correlation is constructed through the notions themselves.

Non-uniform acceptance correction and efficiency correction

When accounting for detector inefficiency, the expression of multiple particle correlations requires a correction. This includes corrections for non-uniform acceptance and efficiency.

In some regions of φ, the number of tracks is less than the average due to the detector's inefficiency. This indicates that the particles are not uniformly distributed across φ when averaged over all events. Even from an isotropic source, the detected particles will exhibit a non-uniform distribution. Consequently, this introduces a bias in the measurement of multiparticle correlations.

To eliminate this bias, the expression for multiparticle correlation is corrected using a weight. For instance, the two-particle correlation formula (referenced as equation 5.3) is expressed as follows:

$$\langle\cos(n(\varphi_1 - \varphi_2))\rangle = \frac{1}{N_{\text{comb}}} \sum_{i \neq j} w_i w_j \cos(n(\varphi_i - \varphi_j)), \tag{5.13}$$

where w_i and w_j represent the effective number of particles corresponding to particles i and j, respectively, and the N_{comb} is modified from the $N_{\text{trk}}(N_{\text{trk}} - 1)$ in equation 5.3 to the effective number of combinations $N_{\text{comb}} = \sum_{i \neq j} w_i w_j$. The application of weight corrections to higher-order correlations is straightforward and will not be described here.

The procedure for obtaining the weights for non-uniform acceptance (NUA) utilizes the following method: One has to first extract the φ distribution in a (V_z, η) bin, where the V_z and η are vertex z position of the event and pseudorapidity of the track, respectively. Then one calculate weights as $w_i = w_i^{\text{A}} = N_{\text{max}}/N_i$, where N_{max} represents the maximum value within the φ distribution, and N_i denotes the value located in the ith bin of the φ distribution. Then, after applying the weights, the final φ distribution will be constant over the whole azimuth, as shown in figure 5.13.

The multi-particle correlation is dependent on the transverse momentum of the particles used in the formulation. As a result, the multiparticle correlation is also biased by the non-uniform efficiency in transverse momentum. Consequently, it is necessary to correct the measurements for inefficiencies originating from detector imperfections or losses during reconstruction, the same as the correction for non-uniform acceptance. For instance, the corrected two-particle correlation formula is represented as follows in equation 5.13, with $w_i = w_i^{\text{E}} = 1/\text{eff}(p_{\text{T}})$. This efficiency is the same one as the one obtained in section 5.2.1. By considering both efficiency and acceptance, the weight is determined by $w_i = w_i^{\text{A}} w_i^{\text{E}}$.

Cumulants expressed as multi-particle correlation

The two-particle cumulants $c_n\{2\}$ with the standard method is calculated as

$$c_n\{2\} = \langle\langle\cos(n(\varphi_1 - \varphi_2))\rangle\rangle. \tag{5.14}$$

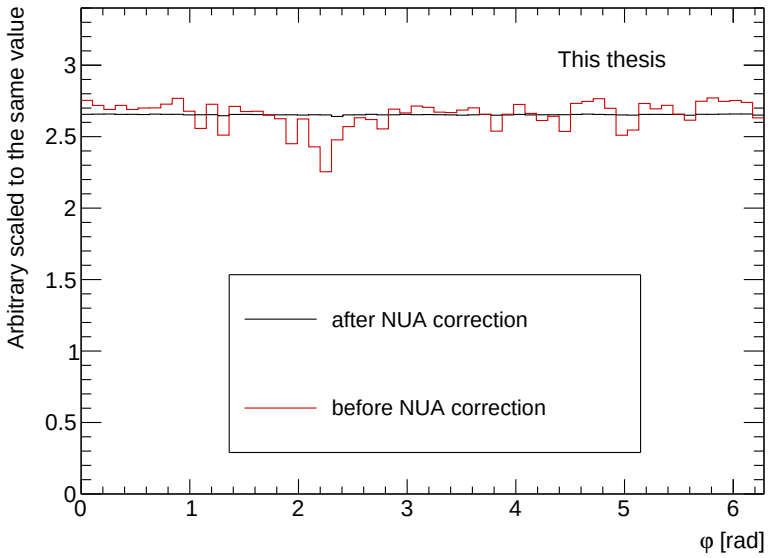

FIGURE 5.13: φ distribution after and before the non-uniform acceptance (NUA) correction.

With the η separation method, the the two-particle cumulants $c_n\{2, |\Delta\eta| > a\}$ is

$$c_n\{2, |\Delta\eta| > a\} = \langle\langle\cos(n(\varphi_1 - \varphi_2)\rangle\rangle_{|\Delta\eta|>a}. \tag{5.15}$$

The four-particle cumulant $c_2\{4\}$ is calculated as

$$\begin{aligned} c_2\{4\} &= \langle\langle\cos(2\varphi_1 + 2\varphi_2 - 2\varphi_3 - 2\varphi_4)\rangle\rangle \\ &- \langle\langle\cos(2\varphi_1 - 2\varphi_3)\rangle\rangle \langle\langle\cos(2\varphi_2 - 2\varphi_4)\rangle\rangle \\ &- \langle\langle\cos(2\varphi_1 - 2\varphi_4)\rangle\rangle \langle\langle\cos(2\varphi_2 - 2\varphi_3)\rangle\rangle \\ &= \langle\langle\cos(2\varphi_1 + 2\varphi_2 - 2\varphi_3 - 2\varphi_4)\rangle\rangle - 2\langle\langle\cos(2\varphi_1 - 2\varphi_3)\rangle\rangle^2 \end{aligned} \tag{5.16}$$

With η separation method, the four-particle cumulant is expressed as:

$$\begin{aligned} c_2\{4, |\Delta\eta| > a\} &= \langle\langle\cos(2\varphi_1 + 2\varphi_2 - 2\varphi_3 - 2\varphi_4)\rangle\rangle_{|\Delta\eta|>a} \\ &- 2\langle\langle\cos(2\varphi_1 - 2\varphi_3)\rangle\rangle^2_{|\Delta\eta|>a}. \end{aligned} \tag{5.17}$$

The $c_2\{4\}$ is also constructed with three-subevent methods. For the four-particle correlation with three-subevent methods, it takes two particles from the middle η region ($-0.4 < \eta < 0.4$) with harmonic coefficient 2, taking one particle from the left region ($\eta < -0.4$) with harmonic coefficient -2 and another particle from the right region ($\eta > 0.4$) with harmonic coefficient -2. In the $\langle\langle\cos(2\varphi_1 - 2\varphi_3)\rangle\rangle$ $\langle\langle\cos(2\varphi_2 - 2\varphi_4)\rangle\rangle$,

the term $\langle\langle\cos(2\varphi_1 - 2\varphi_3)\rangle\rangle$ should correlate the particle in the left region and particle in the middle region and $\langle\langle\cos(2\varphi_2 - 2\varphi_4)\rangle\rangle$ should correlate the particle in the middle region and particle in the right region, i.e.

$$\begin{aligned} c_2\{4\}_{-2|2,2|-2} &= \langle\langle\cos(2\varphi_1 + 2\varphi_2 - 2\varphi_3 - 2\varphi_4)\rangle\rangle_{-2|2,2|-2} \\ &- 2\,\langle\langle\cos(2\varphi_1 - 2\varphi_3)\rangle\rangle_{-2|2|}\,\langle\langle\cos(2\varphi_2 - 2\varphi_4)\rangle\rangle_{|2|-2}\,. \end{aligned} \tag{5.18}$$

Similarly, the other configurations are defined as

$$\begin{aligned} c_2\{4\}_{2,2|-2|-2} &= \langle\langle\cos(2\varphi_1 + 2\varphi_2 - 2\varphi_3 - 2\varphi_4)\rangle\rangle_{2,2|-2|-2} \\ &- 2\,\langle\langle\cos(2\varphi_1 - 2\varphi_3)\rangle\rangle_{2|-2|}\,\langle\langle\cos(2\varphi_2 - 2\varphi_4)\rangle\rangle_{2||-2} \end{aligned} \tag{5.19}$$

and

$$\begin{aligned} c_2\{4\}_{-2|-2|2,2} &= \langle\langle\cos(2\varphi_1 + 2\varphi_2 - 2\varphi_3 - 2\varphi_4)\rangle\rangle_{-2|-2|2,2} \\ &- 2\,\langle\langle\cos(2\varphi_1 - 2\varphi_3)\rangle\rangle_{2||-2}\,\langle\langle\cos(2\varphi_2 - 2\varphi_4)\rangle\rangle_{|2|-2}\,. \end{aligned} \tag{5.20}$$

The $v_n\{2\}$ and $v_2\{4\} = \sqrt[4]{-c_2\{4\}}$ has the corresponding configuration as $\sqrt{c_n\{2\}}$ and $\sqrt[4]{-c_2\{4\}}$, respectly. They are expressed as:

$$v_n\{2\} = \sqrt{\langle\langle\cos(n(\varphi_1 - \varphi_2)\rangle\rangle}, \tag{5.21}$$

$$v_n\{2, |\Delta\eta| > a\} = \sqrt{\langle\langle\cos(n(\varphi_1 - \varphi_2)\rangle\rangle_{|\Delta\eta|>a}}, \tag{5.22}$$

and

$$v_2\{4\} = \sqrt[4]{-c_2\{4\}}, \tag{5.23}$$

$$v_2\{4, |\Delta\eta| > a\} = \sqrt[4]{-c_2\{4, |\Delta\eta| > a\}}, \tag{5.24}$$

$$v_2\{4\}_{-2|2,2|-2} = \sqrt[4]{-c_2\{4\}_{-2|2,2|-2}}, \tag{5.25}$$

$$v_2\{4\}_{2,2|-2|-2} = \sqrt[4]{-c_2\{4\}_{2,2|-2|-2}}, \tag{5.26}$$

$$v_2\{4\}_{-2|-2|2,2} = \sqrt[4]{-c_2\{4\}_{-2|-2|2,2}}. \tag{5.27}$$

Symmetric cumulants

The symmetric cumulant is expanded as correlations as

$$\begin{aligned} \mathrm{SC}(m,n) &= \langle\langle\cos(m\varphi_1 + n\varphi_2 - m\varphi_3 - n\varphi_4)\rangle\rangle \\ &- \langle\langle\cos(m\varphi_1 - m\varphi_3)\rangle\rangle\,\langle\langle\cos(n\varphi_2 - n\varphi_4)\rangle\rangle\,. \end{aligned} \tag{5.28}$$

The SC(3,2) are measured with the standard method, η gap method, and three-subevent method, corresponding to the methods used for the four-particle correlations. Additionally, the two-particle correlation in the construction of the SC(3,2) should correspond to the four-particle correlation. For example, the SC(3,2) measured with η-gap method should be

$$\begin{aligned} \mathrm{SC}(3,2)_{|\Delta\eta|>a} &= \langle\langle\cos(3\varphi_1+2\varphi_2-3\varphi_3-2\varphi_4)\rangle\rangle_{|\Delta\eta|>a} \\ &- \langle\langle\cos(3\varphi_1-3\varphi_3)\rangle\rangle_{|\Delta\eta|>a}\,\langle\langle\cos(2\varphi_2-2\varphi_4)\rangle\rangle_{|\Delta\eta|>a}\,. \end{aligned} \tag{5.29}$$

While with the three-subevent methods, the SC(3,2) could be measured as

$$\begin{aligned} \mathrm{SC}(3,2)_{3,2|-3|-2} &= \langle\langle\cos(3\varphi_1+2\varphi_2-3\varphi_3-2\varphi_4)\rangle\rangle_{3,2|-3|-2} \\ &- \langle\langle\cos(3\varphi_1-3\varphi_3)\rangle\rangle_{3|-3|}\,\langle\langle\cos(2\varphi_2-2\varphi_4)\rangle\rangle_{2||-2}\,. \end{aligned} \tag{5.30}$$

Additionally, the other configurations are

$$\begin{aligned} \mathrm{SC}(3,2)_{-2|-3|3,2} &= \langle\langle\cos(3\varphi_1+2\varphi_2-3\varphi_3-2\varphi_4)\rangle\rangle_{-2|-3|3,2} \\ &- \langle\langle\cos(3\varphi_1-3\varphi_3)\rangle\rangle_{|-3|3}\,\langle\langle\cos(2\varphi_2-2\varphi_4)\rangle\rangle_{-2||2}\,, \end{aligned} \tag{5.31}$$

$$\begin{aligned} \mathrm{SC}(3,2)_{-3|3,2|-2} &= \langle\langle\cos(3\varphi_1+2\varphi_2-3\varphi_3-2\varphi_4)\rangle\rangle_{-3|3,2|-2} \\ &- \langle\langle\cos(3\varphi_1-3\varphi_3)\rangle\rangle_{-3|3|}\,\langle\langle\cos(2\varphi_2-2\varphi_4)\rangle\rangle_{|2|-2} \end{aligned} \tag{5.32}$$

$$\begin{aligned} \mathrm{SC}(3,2)_{-2|3,2|-3} &= \langle\langle\cos(3\varphi_1+2\varphi_2-3\varphi_3-2\varphi_4)\rangle\rangle_{-2|3,2|-3} \\ &- \langle\langle\cos(3\varphi_1-3\varphi_3)\rangle\rangle_{|3|-3}\,\langle\langle\cos(2\varphi_2-2\varphi_4)\rangle\rangle_{-2|2|} \end{aligned} \tag{5.33}$$

$$\begin{aligned} \mathrm{SC}(3,2)_{3,2|-2|-3} &= \langle\langle\cos(3\varphi_1+2\varphi_2-3\varphi_3-2\varphi_4)\rangle\rangle_{3,2|-2|-3} \\ &- \langle\langle\cos(3\varphi_1-3\varphi_3)\rangle\rangle_{3||-3}\,\langle\langle\cos(2\varphi_2-2\varphi_4)\rangle\rangle_{2|-2|} \end{aligned} \tag{5.34}$$

and

$$\begin{aligned} \mathrm{SC}(3,2)_{-3|-2|3,2} &= \langle\langle\cos(3\varphi_1+2\varphi_2-3\varphi_3-2\varphi_4)\rangle\rangle_{-3|-2|3,2} \\ &- \langle\langle\cos(3\varphi_1-3\varphi_3)\rangle\rangle_{-3||3}\,\langle\langle\cos(2\varphi_2-2\varphi_4)\rangle\rangle_{|-2|2}\,. \end{aligned} \tag{5.35}$$

The normalized observable NSC(3,2) is constructed with

$$\mathrm{NSC}(3,2) = \frac{\mathrm{SC}(3,2)}{v_3^2\{2\}v_2^2\{2\}},$$

where the NSC(3,2), the $v_3\{2\}$ and $v_2\{2\}$ are not required to apply the corresponding configuration, in order to suppress the effects from short-range correlation as possible.

The construction of SC(4,2) is totally same as SC(3,2), only replacing the third harmonic to the fourth harmonic.

Nonlinear flow mode

The $v_{4,22}$ is expressed as

$$v_{4,22} = \frac{\langle\langle\cos(4\varphi_1 - 2\varphi_2 - 2\varphi_3)\rangle\rangle}{\sqrt{\langle\langle\cos(2\varphi_1 + 2\varphi_2 - 2\varphi_3 - 2\varphi_4)\rangle\rangle}}. \tag{5.36}$$

They are the three particle correlation divided by the square root of four particle correlations. When calculating the correlation, for $v_{4,22}$, the harmonic coefficient 4 in numerator is corresponding to the 2,2 in denominator. Using the η gap method to calculate the three particle correlation, the particle associated with harmonic 4 is taken from the negative η region, and the other two particle are taken from the positive η region. This is called the configuration A, labeled as $\langle\langle\cos(4\varphi - 2\varphi - 2\varphi)\rangle\rangle_{|\Delta\eta|>a}$. The $v_{4,22}$ with η gap method is therefore constructed as

$$v_{4,22}(|\Delta\eta| > a) = \frac{\langle\langle\cos(4\varphi_1 - 2\varphi_2 - 2\varphi_3)\rangle\rangle_{|\Delta\eta|>a}}{\sqrt{\langle\langle\cos(2\varphi_1 + 2\varphi_2 - 2\varphi_3 - 2\varphi_4)\rangle\rangle}_{|\Delta\eta|>a}} \tag{5.37}$$

There is a square root in the denominator, and due to the statistical fluctuations, the four particle correlation could be negative in some of the multiplicity bin. Therefore, we first merge the three-particle correlation and four-particle correlation to large bin to avoid the fluctuation and then calculate the $v_{4,22}$.

The $v_{4,22}$ is also constructed with three-subevent method. It can take the particle associated with harmonic 4 from left region, and the other particles from middle and right region, i.e.

$$v_{4,22}(4|-2|-2) = \frac{\langle\langle\cos(4\varphi_1 - 2\varphi_2 - 2\varphi_3)\rangle\rangle_{4|-2|-2}}{\sqrt{\langle\langle\cos(2\varphi_1 + 2\varphi_2 - 2\varphi_3 - 2\varphi_4)\rangle\rangle}_{2,2|-2|-2}}, \tag{5.38}$$

and other configurations can be

$$v_{4,22}(-2|4|-2) = \frac{\langle\langle\cos(4\varphi_1 - 2\varphi_2 - 2\varphi_3)\rangle\rangle_{-2|4|-2}}{\sqrt{\langle\langle\cos(2\varphi_1 + 2\varphi_2 - 2\varphi_3 - 2\varphi_4)\rangle\rangle}_{-2|2,2|-2}}, \tag{5.39}$$

and

$$v_{4,22}(-2|-2|4) = \frac{\langle\langle\cos(4\varphi_1 - 2\varphi_2 - 2\varphi_3)\rangle\rangle_{-2|-2|4}}{\sqrt{\langle\langle\cos(2\varphi_1 + 2\varphi_2 - 2\varphi_3 - 2\varphi_4)\rangle\rangle}_{-2|-2|2,2}}. \tag{5.40}$$

The $\chi_{4,22}$ is constructed as

$$\chi_{4,22} = \frac{v_{4,22}}{\sqrt{v_2^4}} = \frac{\langle\langle\cos(4\varphi_1 - 2\varphi_2 - 2\varphi_3)\rangle\rangle}{\langle\langle\cos(2\varphi_1 + 2\varphi_2 - 2\varphi_3 - 2\varphi_4)\rangle\rangle}. \tag{5.41}$$

Similar as the $v_{4,22}$, with the two-subevent method, the $\chi_{4,22}$ is constructed as

$$\chi_{4,22}(|\Delta\eta| > a) = \frac{v_{4,22}}{\sqrt{v_2^4}} = \frac{\langle\langle\cos(4\varphi_1 - 2\varphi_2 - 2\varphi_3)\rangle\rangle_{|\Delta\eta|>a}}{\langle\langle\cos(2\varphi_1 + 2\varphi_2 - 2\varphi_3 - 2\varphi_4)\rangle\rangle_{|\Delta\eta|>a}}. \tag{5.42}$$

And with the three-subevent methods, they are constructed as

$$\chi_{4,22}(4|-2|-2) = \frac{\langle\langle\cos(4\varphi_1 - 2\varphi_2 - 2\varphi_3)\rangle\rangle_{4|-2|-2}}{\langle\langle\cos(2\varphi_1 + 2\varphi_2 - 2\varphi_3 - 2\varphi_4)\rangle\rangle_{2,2|-2|-2}}, \tag{5.43}$$

and

$$\chi_{4,22}(-2|4|-2) = \frac{\langle\langle\cos(4\varphi_1 - 2\varphi_2 - 2\varphi_3)\rangle\rangle_{-2|4|-2}}{\langle\langle\cos(2\varphi_1 + 2\varphi_2 - 2\varphi_3 - 2\varphi_4)\rangle\rangle_{-2|2,2|-2}}. \tag{5.44}$$

5.2.3 Q-cumulant method

The Q-cumulant method [143, 144] is designed to compute the m-particle correlation, changing the process from multiple particle track loops to a single-track loop, thereby significantly reducing CPU usage. The Q-cumulant is defined as

$$Q_{n,p} = \sum_i w_i^p \exp(in\varphi_i). \tag{5.45}$$

The Q-cumulant method could be used to calculate all correlations. For example, if one want to use the Q cumulant method to calculate the two-particle correlation, it can be expressed as:

$$\langle\cos(2\varphi_1 - 2\varphi_2)\rangle = \frac{Q_{n,1}^* Q_{n,1} - Q_{0,2}}{Q_{0,1}Q_{0,1} - Q_{0,2}}. \tag{5.46}$$

The $Q_{n,1}Q_{n,1}^*$ contains all the two-particle pairs, expaned as:

$$\begin{aligned} Q_{n,1}Q_{n,1}^* &= \sum_{i,j} w_i w_j \exp(in\varphi_1 - in\varphi_2) \\ &= \sum_{i\neq j} w_i w_j \exp(in\varphi_1 - in\varphi_2) + \sum_i w_i^2, \end{aligned} \tag{5.47}$$

where the i,j could take the same particles. If the same particle is taken, the $n\varphi_i - n\varphi_j = 0$ and thus $\exp(n\varphi_i - n\varphi_j) = 1$, which is called auto-correlation. With a subtraction of $Q_{0,2} = \sum_i w_i^2$, the $Q_{2,1}^* Q_{2,1} - Q_{0,2}$ represents the two particle correlation with different

particles. For the denominator, the $Q_{0,1}Q_{0,1}$ is the combination of all weight pairs, i.e.

$$Q_{0,1}Q_{0,1} = \sum_{i,j} w_i w_j = \sum_{i \neq j} w_i w_j + \sum_i w_i^2. \tag{5.48}$$

Similar the pairs with $i = j$ is removed through the substraction of $Q_{0,2}$.

The Q-cumulants method could also be used in the measurement of multi-particle correlations with $|\Delta\eta|$ separation. An example of two-particle correlation with η gap, obtained from Q-cumulants method is described as following. The Q vector is constructed with tracks in a subevent as

$$Q^A_{n,p} = \sum_i^{\eta_i < -a/2} w_i^p \exp(in\varphi_i), \tag{5.49}$$

where the i loop over tracks with $\eta < -a/2$. Another Q vector is constructed as

$$Q^B_{n,p} = \sum_i^{\eta_i > a/2} w_i^p \exp(in\varphi_i), \tag{5.50}$$

where the i loop over tracks with $\eta > a/2$. Therefore, the two-particle correlation could be expressed as

$$\langle \cos(n\varphi_1 - n\varphi_2) \rangle_{|\Delta\eta|>a} = \frac{Q^A_{n,1} Q^{B*}_{n,1}}{Q^A_{0,1} Q^B_{0,1}}. \tag{5.51}$$

Using the Q-cumulant method requires manually deriving the expressions for correlations represented by Q vectors. Moreover, as the order of the correlation increases, the expressions become more complex. The computation of these correlations as expressed through Q vectors is implemented by the Generic Framework [145], which enables the recursive calculation of high-order correlations and the integration of efficiency and acceptance corrections.

5.2.4 $v_n^2 - [p_\mathrm{T}]$ correlation

In this section, the observables involving the $v_n^2 - [p_\mathrm{T}]$ correlation is discussed. These observables includes the $\mathrm{cov}(v_2^2, [p_\mathrm{T}])$, $\sigma(v_2^2)$ and c_k.

The v_2^2 is measured with $|\Delta\eta| > a$ ($a = 0.8, 1.0, 1.2$) and $[p_\mathrm{T}]$ is measured in $|\eta| < 0.4$. The chosen kinematic region, as shown in the sketch (figure 5.14) automatically avoid auto-correlation in the calculation of $\mathrm{cov}(v_2^2, [p_\mathrm{T}])$, and provide a rejection of the short-range correlation in flow observables calculation.

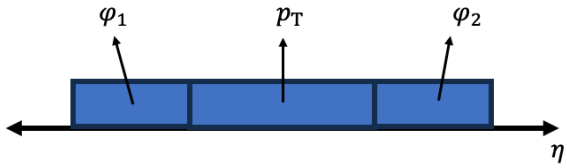

FIGURE 5.14: The sketch of the kinematic region for the $v_n^2 - [p_{\mathrm{T}}]$ correlation measurement.

Covariance between v_n^2 and $[p_{\mathrm{T}}]$

The covariance between v_n^2 and $[p_{\mathrm{T}}]$ is expressed as

$$\mathrm{cov}(v_2^2, [p_{\mathrm{T}}]) = \langle v_2^2 \delta p_{\mathrm{T}} \rangle = \langle v_2^2 [p_{\mathrm{T}}] \rangle - \langle v_2^2 \rangle \langle [p_{\mathrm{T}}] \rangle. \tag{5.52}$$

The $[p_{\mathrm{T}}]$ is the average in a single event (using a square bracket is a convention from the invention of this observable). Similar as the detector inefficiency correction to the multi-particle azimuthal correlations described in section 5.2.2, the weights are applied for these observables. The observables with the weights is expressed here as:

$$[p_{\mathrm{T}}] = \frac{\sum\limits_i w_i^{\mathrm{E}} p_{\mathrm{T}(i)}}{\sum\limits_i w_i^{\mathrm{E}}}, \tag{5.53}$$

where i loops over all the tracks in a given kinematic region ($|\eta| < 0.4, 0.2 < p_{\mathrm{T}} < 3$ GeV/c), and w_i is the weight of the track. It is noticed that the $[p_{\mathrm{T}}]$ is not affected by the non-uniform acceptance, and therefore does not require a correction.

The v_2^2 is calculated using the two-particle cumulant method, which is defined with the exact same expression as in equation 5.5. The same non-uniform acceptance and efficiency correction procedure as what is described in section 5.2.2 are applied to the measurements of v_2^2.

While averaging over all the events, the first term on the right hand of equation 5.52 is expressed as:

$$\langle v_2^2 [p_{\mathrm{T}}] \rangle = \frac{\sum\limits_i^{\mathrm{evt}} W_i v_{2(i)}^2 [p_{\mathrm{T}}]_i}{\sum\limits_i^{\mathrm{evt}} W_i}, \tag{5.54}$$

where the j loops over all the events. The event weight is a product of weight corresponding to the v_2^2 and the part corresponding to the $[p_{\mathrm{T}}]$, i.e., $W_i = W_v^{(i)} W_p^{(i)}$. The W_v is

constructed as:

$$W_v = \sum_{ij} w_i^{\mathrm{A}} w_i^{\mathrm{E}} w_j^{\mathrm{A}} w_j^{\mathrm{E}}, \tag{5.55}$$

and W_p is constructed as:

$$W_p = \sum_{i} w_i^{\mathrm{E}}. \tag{5.56}$$

The w_i^{A} and w_i^{E} are the non-uniform acceptance weight and the efficiency weight used in section 5.2.2.

The event averaged $\langle [p_{\mathrm{T}}] \rangle$ is calculated as:

$$\langle [p_{\mathrm{T}}] \rangle = \frac{\sum_{i}^{\mathrm{evt}} W_p^{(i)} [p_{\mathrm{T}}]_i}{\sum_{i}^{\mathrm{evt}} W_p^{(i)}}, \tag{5.57}$$

where the i loops over all the events in a given multiplicity bin.

It is important to address that in the calculation of $\langle v_2^2 \rangle$, the event weight is applied to each event, which is calculated as:

$$\langle v_2^2 \rangle = \frac{\sum_{i}^{\mathrm{evt}} W_p^{(i)} W_v^{(i)} v_{2(i)}^2}{\sum_{i}^{\mathrm{evt}} W_p^{(i)} W_v^{(i)}}, \tag{5.58}$$

The reason to apply W_p to the $\langle v_2^2 \rangle$ is that when we consider equation (3.17) with event weight correction, it becomes:

$$\begin{aligned} \mathrm{cov}(v_2^2, [p_{\mathrm{T}}]) &= \langle W_v W_p v_2^2 \delta p_{\mathrm{T}} \rangle = \big\langle W_v W_p v_2^2 ([p_{\mathrm{T}}] - \langle [p_{\mathrm{T}}] \rangle) \big\rangle \\ &= \langle W_v W_p v_2^2 [p_{\mathrm{T}}] \rangle - \langle W_v W_p v_2^2 \rangle \langle [p_{\mathrm{T}}] \rangle. \end{aligned} \tag{5.59}$$

Variance of v_2^2

The variance of the v_2^2 could be expressed with azimuthal correlation only, and therefore it could be calculated with the methods described in section 5.2.2. The square root of the variance of the v_2^2 is calculated as:

$$\begin{aligned} \sigma(v_2^2) &= \sqrt{\mathrm{var}(v_2^2)} \\ &= \sqrt{\langle\langle \cos(2\varphi_1 + 2\varphi_2 - 2\varphi_3 - 2\varphi_4) \rangle\rangle_{|\Delta\eta|>a} - \langle\langle \cos(2\varphi_1 - 2\varphi_3) \rangle\rangle^2_{|\Delta\eta|>a}}. \end{aligned} \tag{5.60}$$

Variance of $[p_{\mathrm{T}}]$

Applying the weights, in a single event, the variance of $[p_{\mathrm{T}}]$ is calculated as:

$$\delta p_{\mathrm{T}}^2 = \frac{\sum_{i \neq j} w_i^{\mathrm{E}} w_j^{\mathrm{E}} (p_{\mathrm{T}}^i - \langle [p_{\mathrm{T}}] \rangle)(p_{\mathrm{T}}^j - \langle [p_{\mathrm{T}}] \rangle)}{\sum_{i \neq j} w_i^{\mathrm{E}} w_j^{\mathrm{E}}}. \tag{5.61}$$

The term $\langle [p_{\mathrm{T}}] \rangle$ represents the event-averaged mean transverse momentum, as defined in equation 5.57. In principle, one should iterate over all events to determine $\langle [p_{\mathrm{T}}] \rangle$ before calculating the variance δp_{T}^2 within a single event. However, it will be shown that the term $\langle [p_{\mathrm{T}}] \rangle$ can be isolated by expanding equation 5.61. Therefore, iteration over all events is avoided.

Expanding the equation 5.61, the δp_{T}^2 is expressed as:

$$\delta p_{\mathrm{T}}^2 = [p_{\mathrm{T}}^2] - 2[p_{\mathrm{T}}]^w \langle [p_{\mathrm{T}}] \rangle + \langle [p_{\mathrm{T}}] \rangle^2, \tag{5.62}$$

where

$$[p_{\mathrm{T}}^2] = \frac{\sum_{i \neq j} w_i^{\mathrm{E}} w_j^{\mathrm{E}} p_{\mathrm{T}}^i p_{\mathrm{T}}^j}{\sum_{i \neq j} w_i^{\mathrm{E}} w_j^{\mathrm{E}}}, \tag{5.63}$$

and

$$[p_{\mathrm{T}}]^w = \frac{\sum_{i \neq j} w_i^{\mathrm{E}} w_j^{\mathrm{E}} p_{\mathrm{T}}^i}{\sum_{i \neq j} w_i^{\mathrm{E}} w_j^{\mathrm{E}}}. \tag{5.64}$$

The necessity for a nested loop can be avoided by reformulating equation 5.63 and equation 5.64 as

$$[p_{\mathrm{T}}^2] = \frac{(\sum_i w_i^{\mathrm{E}} p_{\mathrm{T}}^i)^2 - \sum_i (w_i^{\mathrm{E}} p_{\mathrm{T}}^i)^2}{(\sum_i w_i^{\mathrm{E}})^2 - \sum_i (w_i^{\mathrm{E}})^2}, \tag{5.65}$$

and

$$[p_{\mathrm{T}}]^w = \frac{(\sum_i w_i^{\mathrm{E}} p_{\mathrm{T}}^i)(\sum_i w_i^{\mathrm{E}}) - \sum_i ((w_i^{\mathrm{E}})^2 p_{\mathrm{T}}^i)}{(\sum_i w_i^{\mathrm{E}})^2 - \sum_i (w_i^{\mathrm{E}})^2}. \tag{5.66}$$

When averaging over all events, the weight is applied as:

$$\langle \delta p_{\mathrm{T}}^2 \rangle = \frac{\sum_i W_p^{(i)} (\delta p_{\mathrm{T}}^2)_i}{\sum_i W_p^{(i)}}, \tag{5.67}$$

where the i loops over all events. The W_p is constructed as:

$$W_p = (\sum_i w_i^{\mathrm{E}})^2 - \sum_i (w_i^{\mathrm{E}})^2. \tag{5.68}$$

5.3 Statistical uncertainty

The statistical uncertainty is generally calculated with the standard bootstrap method [169], which is a statistical resampling technique that samples a dataset with replacement to estimate the population of a random variable.

In the bootstrap method used in this analysis, the entire data sample is divided into 30 sub-samples. Then, 30 sub-samples are randomly selected with replacements from the full dataset. Each sub-sample may be selected multiple times. The 30 newly selected sub-samples are then combined to form a single sample. This process is repeated for 100 times to create 100 new resampled dataset. For each of the 100 samples, the observables are calculated. The standard deviation of the observables across the 100 samples is computed and used as the measure of statistical uncertainty. An example of the procedure is shown in figure 5.15, showing the $\langle\langle\cos(2(\varphi_1 - \varphi_2))\rangle\rangle$ at $\langle N_{\mathrm{ch}}\rangle = 426$. The histogram shows the distribution of $\langle\langle\cos(2(\varphi_1 - \varphi_2))\rangle\rangle$ calculated with the 100 resampled dataset. The red point with the uncertainty shows the results measured with the entire sample, and the uncertainty is from the standard deviation of the observables measured with the resampled set, calculated with

$$\sigma(x) = \sqrt{\frac{(x_i - \bar{x})^2}{100 \times (100 - 1)}}, \tag{5.69}$$

with $\bar{x} = \sum_i x_i/100$ and x_i the measured observable $\langle\langle\cos(2(\varphi_1 - \varphi_2))\rangle\rangle$ in the ith resampled set.

The bootstrap method automatically addresses the correlation between different observables. However, a potential drawback of this method is the statistical instability of the observables. For instance, the measured $c_2\{4\}$ may turn out positive in some sub-samples due to statistical fluctuations, even though the measurement is negative for the entire sample. In such cases, the uncertainty of $c_2\{4\}$ is determined using the bootstrap method, and the uncertainty of $v_2\{4\} = \sqrt[4]{-c_2\{4\}}$ is subsequently calculated through error propagation.

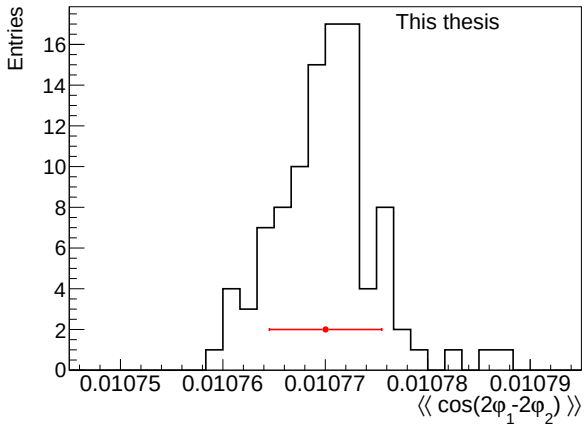

FIGURE 5.15: Example of the $\langle\langle\cos(2(\varphi_1 - \varphi_2))\rangle\rangle$ at $\langle N_{\mathrm{ch}}\rangle = 426$ from 5.02 TeV Pb–Pb collisions. The histogram shows the distribution of $\langle\langle\cos(2(\varphi_1 - \varphi_2))\rangle\rangle$ calculated with the 100 resampled dataset. The red point with the uncertainty shows the results measured with the entire sample, and the uncertainty is from the standard deviation of the observables measured with the resampled set.

5.4 Systematic uncertainties

Systematic uncertainties represent the deviation between the measured result and its true value, assuming an infinitely large dataset. These uncertainties stem from imperfections in experimental conditions. In all results, systematic uncertainties were assessed by implementing stricter criteria for event and particle selection.

The systematic uncertainty associated with event selection was probed by altering the cut-off for the primary vertex's position along the beam direction, denoted as $|V_z|$. This was achieved by varying the cut from $|V_z| < 10$ cm to $|V_z| < 7$ cm. Additionally, variations in track selection were examined. Instead of using the global tracks (identified by filter bit 96), as described in section 5.1.3, hybrid tracks (identified by filter bit 768) were utilized, which uses different track types with different track qualities. The minimum required number of TPC clusters was increased from 70 to 80. Furthermore, the cut for DCA_z was tightened from 2 cm to 1 cm. The DCA_{xy} cut is varied from $\mathrm{DCA}_{xy} < 7 \times (0.0026 + 0.005/p_{\mathrm{T}}^{1.01})$ to $\mathrm{DCA}_{xy} < 4 \times (0.0026 + 0.005/p_{\mathrm{T}}^{1.01})$, donated as a change from 7 σ to 4 σ. Each of these modifications was implemented individually to assess their impact.

For each variation of the selection criteria, appropriate non-uniform acceptance and non-uniform efficiency corrections are implemented. When the track cuts are modified, the recalculated track multiplicity is determined using the default cuts. As a result, the x-axis correction remains consistent for both the default and varied results. Figure 5.16 shows

TABLE 5.1: Summary of the systematics with variation.

Variable	Default cuts	Varied cuts
$\|V_z\|$	10 cm	7 cm
Track type	Global track (FB96)	Hybrid track (FB768)
N_{TPC} Clusters	70	80
$\|\mathrm{DCA}_z\|$	2 cm	1 cm
$\|\mathrm{DCA}_{xy}\|$	7 σ	4 σ

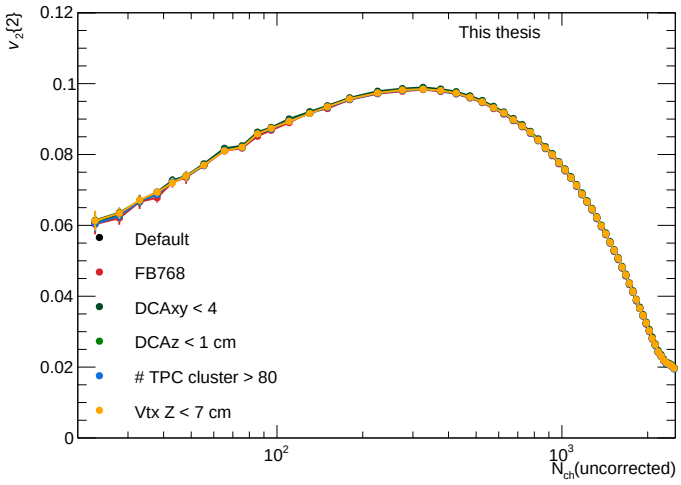

FIGURE 5.16: Comparision between default results and the results with varied cuts for $v_2\{2\}$ in 5.02 TeV Pb–Pb collisions.

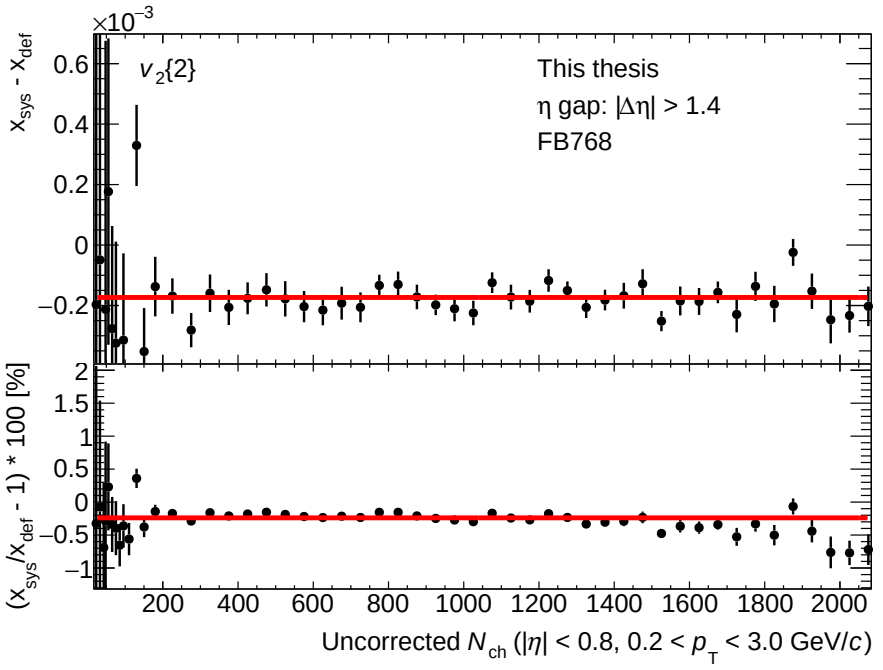

FIGURE 5.17: Ratio and difference of $v_2\{2\}$ between the results with default cut and cut varying the global track to hybrid track in 5.02 TeV Pb–Pb collisions.

the default results and the results with varied cuts for $v_2\{2\}$, as an example. The ratio of the results obtained under the default cut and the varied cut and the difference between them is calculated, as shown in figure 5.17. These differences are firstly smoothed with a constant function or first-order polynomial function to avoid any bin-by-bin statistical fluctuation. The maximum difference evaluated with the different smoothing methods is taken as the estimated systematics for this check. The fitted results yield an absolute uncertainty of 1.73×10^{-4} and a relative uncertainty of 0.239%. The $|0.239\% \times v_2\{2\}|$ and $|1.73 \times 10^{-4}|$ are compared bin-by-bin and the maximum of them is taken as the systematic uncertainty.

A Barlow check [170] is also performed for each observable and cut change. The Barlow n_σ is

$$n_\sigma = \frac{x_{\text{def}} - x_{\text{sys}}}{\sqrt{\sigma^2_{\text{def}} \pm \sigma^2_{\text{sys}}}},$$

where "+" sign is used when the sample with default and varied cuts are statistically independent. Conversely, if the sample with varied cuts is a subset of the sample with the default cut, then the "−" sign is used.

If the measurement remains unbiased by any variations in the selection criteria, then

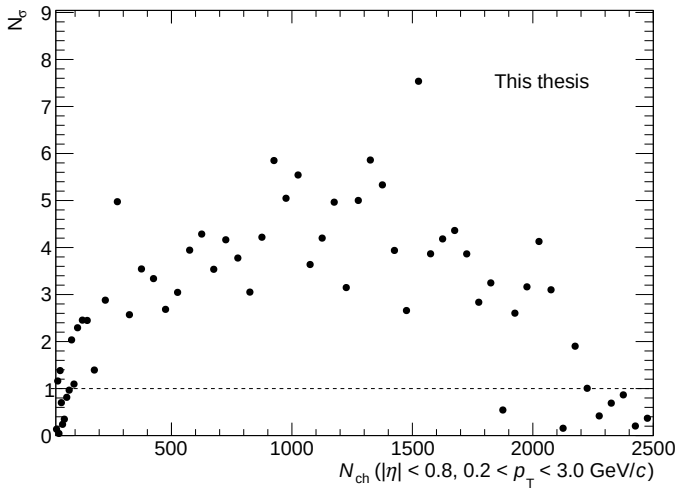

FIGURE 5.18: Barlow n_σ for $v_2\{2\}$ by changing the global tracks to hybrid tracks, from 5.02 TeV Pb–Pb collisions.

n_σ will approximately follow a Gaussian distribution with a mean of 0 and a standard deviation of 1. If the most of the data points are with $|n_\sigma| > 1$, the source of the systematic uncertainty is regarded as statistically significant, which will be taken into account in the total systematics. Figure 5.18 shows an example of the Barlow n_σ of $v_2\{2\}$ in Pb–Pb collisions when changing from global tracks to hybrid tracks. The quantity of data points exceeding 1 significantly is larger than 30% (the proportion corresponding to 1σ) of the total data points. This indicates that the variation from global to hybrid tracks is statistically significant and should, therefore, be accepted as a source of systematic uncertainty.

The total systematic uncertainty are calculated as the quadratic sum of these individual sources.

6 Results and discussion

This chapter presents and discusses the measurements of various flow observables, including multi-particle azimuthal correlations, cumulants, flow harmonics, symmetric cumulants, and nonlinear flow observables, in pp, p–Pb and Pb–Pb collisions at the LHC. In section 6.1, the focus is on multi-particle azimuthal correlations, the foundational components for constructing flow observables. Subsequently, section 6.2 delves into the discussion of cumulants, followed by the examination of flow harmonics derived from these cumulants. The characteristics of symmetric cumulants and the observables describing the nonlinear flow mode are presented and discussed in separate sections, specifically in section 6.4 and section 6.5. Finally, the correlations between the flow and the mean transverse momentum are explored in 6.6.

The results obtained using different non-flow suppression methods are presented and discussed in each section, alongside comparisons with the non-flow calculations from the PYTHIA 8 [51] model, considered one of the most reliable models available for describing hard scattering. Various non-flow suppression methods are examined, and the measurements demonstrating the most effective non-flow suppression are selected for comparison with the state-of-the-art hydrodynamics model IP-Glasma + MUSIC + UrQMD [171] calculations, where non-flow effects are negligible. At the same time, the significance of the results obtained with different non-flow suppression methods should not be underestimated. Observables with different $|\Delta\eta|$ separations probe different correlation lengths in addition to their role as benchmarks for selecting results with minimal non-flow contamination. This provides an opportunity for an apples-to-apples comparison between models with few-body interactions, such as PYTHIA 8 and AMPT [61], to investigate the different mechanisms in these models, which exhibit varying sensitivity to different correlation lengths.

6.1 Multi-particle correlations

Multi-particle correlations serve as the fundamental elements for calculating various flow observables. They are also the foundation for discussing flow signals and non-flow contamination in other flow observables.

Perspective: Flow and non-flow Before examining specific observables, it is beneficial to discuss the concepts of flow and non-flow. The terms "flow" and "non-flow" may vary in meaning depending on the context or among different physicists.

One perspective treats flow as a phenomenon where the particles detected in a given collision event are independently governed by an underlying probability distribution, a concept commonly assumed within the hydrodynamic framework [172]. A crucial yet frequently overlooked aspect is the necessity for the system to exhibit an infinite number of degrees of freedom, which leads to the assumption of independence. The requirement for an infinite number of degrees of freedom is met in hydrodynamic models, as they are classical field theory. Given an underlying probability distribution, the intrinsic flow coefficients v_n and flow symmetry plane Ψ_n exist on an event-by-event basis. This perspective supports the concept of flow fluctuations and flow correlations. Conversely, non-flow encompasses any phenomena that violate the assumption of independent particle emission, typically associated with jet correlations or the cascading decay of particles.

Another perspective considers flow as the global collectivity of multiple particles, particularly the long-range collectivity. Imagine a system where two particles are emitted back-to-back due to energy-momentum conservation. As the system evolves, multiple daughter particles are emitted in a cascade, and these particles interact with one another. In the final state, an azimuthal anisotropy could be observed. In this case, if multiple particles are produced within a pair of back-to-back jets and are distributed over a wide range within the jet cone, the observed behavior of the jet correlation is considered to be flow effects. Only correlations that are short-range or involve fewer particles will be regarded as non-flow effects.

It is worth mentioning that the two perspectives converge in large collision systems. This is because the assumption of independence is approximately satisfied, and the correlation becomes global. Whereas, in small collision systems, the flow and non-flow effects may be distinguished differently according to the two perspectives. This clarification is not merely a trivial exercise in semantics. It is particularly important when explaining the underlying physics of flow observables. For example, from the second perspective on flow, the $c_2\{4\}$ with a positive value is not strange at all. In contrast, from the first perspective, a positive $c_2\{4\}$ occurs only if the flow fluctuation is considerably large compared with the average flow coefficient. In this thesis, the term "flow" refers to a global, long-range, multi-particle correlation that assumes particles are emitted independently. "Non-flow" refers to short-range correlations, correlations involving a few particles, or any other effects breaking the

independence assumption depending on the context, provided it does not introduce ambiguity. If needed, "short-range correlation" or "few particle correlation" is explicitly used instead of "non-flow" to avoid confusion.

6.1.1 Two-particle correlations

Figure 6.1 displays the multiplicity-dependent two-particle correlations for the second, third, and fourth harmonics in Pb–Pb collisions at $\sqrt{s_{\rm NN}} = 5.02$ TeV. The measurements employ the standard method as well as the two-subevent methods with pseudorapidity separation ranging from $|\Delta\eta| > 0$ to $|\Delta\eta| > 1.4$. The two-particle correlations between particles from the left (or right) side of the detector, specifically $\eta < -0.4$ (or $\eta > 0.4$), and particles from the middle of the detector, i.e., $-0.4 < \eta < 0.4$, are also presented, denoted as 2|-2| (see sketch in figure 6.1). The subevent methods are extensively discussed in chapter 5. As the $|\Delta\eta|$ increases, the correlations between the two particles exhibit a monotonic decrease for $\langle\langle\cos(2\varphi_1 - 2\varphi_2)\rangle\rangle$, $\langle\langle\cos(3\varphi_1 - 3\varphi_2)\rangle\rangle$, and $\langle\langle\cos(4\varphi_1 - 4\varphi_2)\rangle\rangle$. At high multiplicity ($N_{ch} \gtrsim 1000$), where the collective expansion of the system dominates the correlations, the relative differences between the standard methods and the subevent methods are minor. However, in the low multiplicity region, where the number of charged tracks is less than a few hundred, the magnitude of the two-particle correlations undergoes a significant change with different $|\Delta\eta|$ separations suppression methods. The suppression is more pronounced in regions of lower multiplicity. The dramatic change in the measurements with different $|\Delta\eta|$ is because of the effective suppression of the short-range correlations. Even with the application of the maximum achievable pseudorapidity separation ($|\Delta\eta| > 1.4$) within the ALICE TPC acceptance, the two-particle correlation does not saturate, indicating the persistence of short-range correlation effects in the low multiplicity region. At low multiplicity, i.e., $N_{\rm ch} \lesssim 80$, the two-particle correlation with the standard method exhibits a decrease with the increasing multiplicity. This decreasing trend diminishes when the $|\Delta\eta|$ separation increases. A noticeable increase with increasing $N_{\rm ch}$ in $\langle\langle\cos(2\varphi_1 - 2\varphi_2)\rangle\rangle$ becomes evident with the largest gap ($|\Delta\eta| > 1.4$), and this similar pattern is observed for $\langle\langle\cos(3\varphi_1 - \varphi_2)\rangle\rangle$ and $\langle\langle\cos(4\varphi_1 - \varphi_2)\rangle\rangle$.

The two-particle correlation is equivalent to the two-particle cumulants, i.e., $c_n\{2\} = \langle\langle\cos(n(\varphi_1 - \varphi_2))\rangle\rangle$. Without the presence of non-flow, the $c_n\{2\}$ measures the $\langle v_n^2\rangle$. The variation in $c_2\{2\}$ with respect to the $N_{\rm ch}$ mainly stems from the changing overlap geometry of the colliding nuclei in Pb–Pb. As collisions change from central to mid-central, corresponding to a decreasing of $N_{\rm ch}$ in Pb–Pb collisions, the overlap region changes from a round to a diamond-like shape. As the $N_{\rm ch}$ increases, the value of $c_2\{2\}$ decreases. This is because the system becomes less dense, leading to less frequent hadronic interactions. With a further decreases in $N_{\rm ch}$, the number of participating nucleons is very small, and the overlap geometry is predominantly determined by the fluctuating

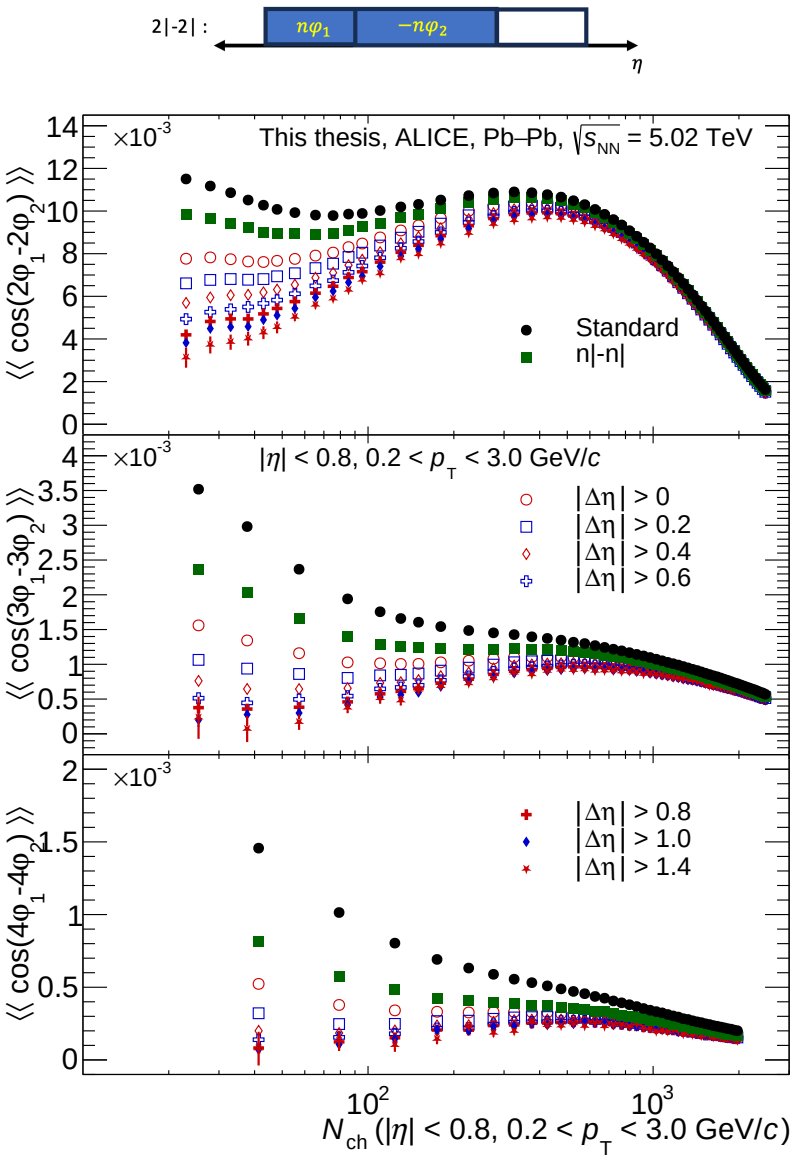

FIGURE 6.1: Measurements of two-particle correlations of second, third, and fourth harmonics $(\langle\langle\cos(2(\varphi_1 - \varphi_2))\rangle\rangle, \langle\langle\cos(3(\varphi_1 - \varphi_2))\rangle\rangle, \langle\langle\cos(4(\varphi_1 - \varphi_2))\rangle\rangle)$ as a function of multiplicity in Pb–Pb collisions. The correlations are measured with the standard method and the pseudorapidity separation methods.

positions of the participating nuclei. This initial spatial anisotropy is ultimately converted into momentum anisotropy, leading to the observed pattern in $\langle\langle\cos(n\varphi_1 - n\varphi_2)\rangle\rangle$. If the system is dominated by the short-range few particle correlations, the $\langle\langle\cos(n\varphi_1 - n\varphi_2)\rangle\rangle$ is expected to scale as $1/N_{\rm ch}$ [173]. When the $|\Delta\eta|$ separation is not sufficient, the non-flow effects could be significant. The interplay of these flow and non-flow effects results in the trend of $\langle\langle\cos(n\varphi_1 - n\varphi_2)\rangle\rangle$ first decreases, followed by a less steep decrease, and potentially even an increase, as the multiplicity increases, in the region where $N_{\rm ch} \lesssim 300$.

Figures 6.2 and 6.3 present the measurement of $\langle\langle\cos(2\varphi_1 - 2\varphi_2)\rangle\rangle$, $\langle\langle\cos(3\varphi_1 - 3\varphi_2)\rangle\rangle$, and $\langle\langle\cos(4\varphi_1 - 4\varphi_2)\rangle\rangle$ as a function of multiplicity in p–Pb and pp collisions, respectively. The non-flow suppression method is applied in the same configurations as in Pb–Pb collisions. Similar to the Pb–Pb collision at low multiplicity, the two-particle correlations in small collision systems undergo significant changes when a larger $|\Delta\eta|$ is applied. Notably, the two-particle correlation in the three-subevent method with 2|-2| (see the sketch in figre 6.1) yields the second-largest correlation, surpassed only by the standard method that does not suppress non-flow effects well. This configuration 2|-2| employs the same separation length as $|\Delta\eta| > 0$ but involves fewer pairs in the correlation. Additionally, the η region used for the configuration 2|-2| ($-0.8 < \eta < 0.4$) is smaller than the $|\Delta\eta| > 0$ ($-0.8 < \eta < 0.8$), and the averaged $|\Delta\eta|$ is shorter in 2|-2|, resulting in a larger correlation than $|\Delta\eta| > 0$.

In p–Pb and pp collisions, a declining trend with respect to the increasing of multiplicity is observed for $\langle\langle\cos(n\varphi_1 - n\varphi_2)\rangle\rangle$ using the standard method. With a larger $|\Delta\eta|$, the decreasing trend weakens in both pp and p–Pb collisions. Similar to low-multiplicity Pb–Pb collisions, the two-particle correlations in pp and p–Pb do not reach saturation, even with the largest possible $|\Delta\eta|$ separation. It suggests that some remaining short-range correlations persist in the measured two-particle correlations.

The assumption that the $\langle\langle\cos(n\varphi_1 - n\varphi_2)\rangle\rangle$ measures the event averaged $\langle v_n^2\rangle$ may not be valid in small collision systems. Nevertheless, by comparing results from small and large collision systems, some indications can be inferred. The correlation's dependence on the multiplicity is weak in small collision systems. Because, in pp and p–Pb collisions, the wounded nucleons do not generate a strong initial geometric eccentricity. Additionally, the decreasing trends with increasing $N_{\rm ch}$ for $\langle\langle\cos(n\varphi_1 - n\varphi_2)\rangle\rangle$ with the standard method observed in small collision systems could be attributed to an interplay between non-flow effects, scaled by $1/N_{\rm ch}$, alongside flow effects. The trend exhibits a steeper decrease with increasing $N_{\rm ch}$ in p–Pb collisions than in pp collisions, which may be attributed to the usage of a high-multiplicity trigger in pp collisions.

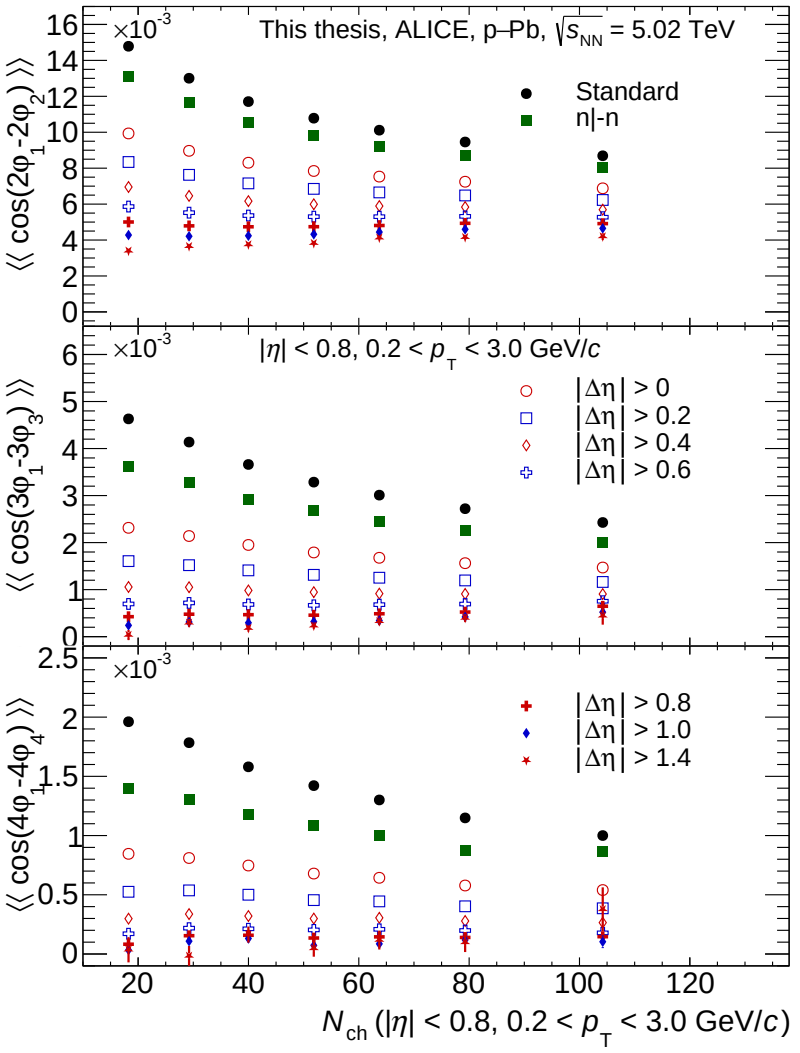

FIGURE 6.2: Measurements of two-particle correlations of second, third, and fourth harmonics ($\langle\langle\cos(2\varphi_1 - 2\varphi_2)\rangle\rangle$, $\langle\langle\cos(3\varphi_1 - 3\varphi_2)\rangle\rangle$, $\langle\langle\cos(4\varphi_1 - 4\varphi_2)\rangle\rangle$) as a function of multiplicity in p–Pb collisions. The correlations are measured with the standard method and the pseudorapidity separation method.

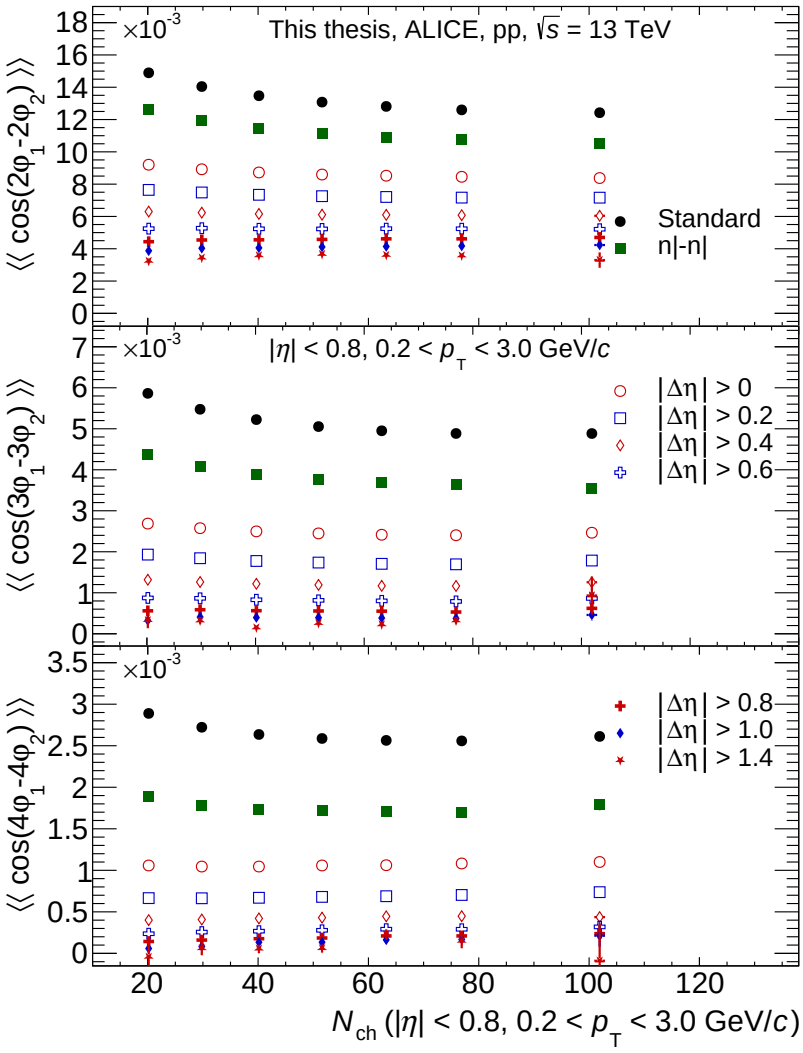

FIGURE 6.3: Measurements of two-particle correlations of second, third, and fourth harmonics ($\langle\langle\cos(2\varphi_1-2\varphi_2)\rangle\rangle$, $\langle\langle\cos(3\varphi_1-3\varphi_2)\rangle\rangle$, $\langle\langle\cos(4\varphi_1-4\varphi_2)\rangle\rangle\rangle$ as a function of multiplicity in pp collisions. The correlations are measured with the standard method and the pseudorapidity separation method.

Perspective: Contributions to two-particle correlation Two-particle correlations can be factorized more easily than multi-particle correlations. The following discussion will explore the contributions of global collectivity and jet phenomena to two-particle correlations. This analysis employs a simple model that assumes particles follow a pattern of global expansion, supplemented by the presence of a pair of back-to-back jets.

The two-particle correlations can be factorized by a weighted sum of few particle short-range correlations, few particle long-range correlations, and global particle correlations. The correlation $\langle\langle\cos(n(\varphi_1-\varphi_2))\rangle\rangle$ is shortened as c_n here. The dominant contribution of the particle short-range correlation is the correlation of particles from the same jet, while the main source of the few-particle long-range correlation is the two-particle correlations from a pair of back-to-back jets. The other particle pairs are considered global correlations. The two particles from the same jet usually have small $|\Delta\eta|$ and $|\Delta\varphi|$. The two particles from back-to-back jets usually have a $|\Delta\varphi|$ around π, while the $\Delta\eta$ of the two particles are quite arbitrary.

Denoting the short-range correlations, few particle long-range correlations, and global particle correlations as "S", "L" and "G" respectively, the two-particle correlations can be factorized as

$$c_n = f_S c_{nS} + f_L c_{nL} + f_G c_{nG} \tag{6.1}$$

where f with the corresponding subscript is the ratio between the number of particle pairs from a correlation source and the number of total particle pairs. Therefore, $f_S + f_L + f_G = 1$. The factor f is the same for different orders of harmonics. It is naively expected that the c_{nS} is around $\cos(0) = 1$, while the c_{nL} are different for different order of harmonics. The c_{2L} and c_{4L} are around $\cos(2\pi) = \cos(4\pi) = 1$, while the c_{3L} is around $\cos(3\pi) = -1$. It provides an intuitive expectation for the two-particle correlations from back-to-back jets, and the observed positive c_3 is explained as a global collectivity.

Figure 6.4 shows the measurement of two-particle correlations for the second, third, and fourth harmonics in pp collisions as well as the comparison to the PYTHIA 8 [52] calculation. The PYTHIA 8 calculation is based on Monash tunning [51]. In addition, a mimic of the ALICE V0M high multiplicity trigger, which is described in section 4.3.1, is applied. The model calculation is compared with the measurements using standard configuration and the two-subevent methods with $|\Delta\eta| > 0$, $|\Delta\eta| > 0.8$ and $|\Delta\eta| > 1.4$. The jet contribution predominantly causes the non-zero two-particle correlations in the PYTHIA 8 calculations. The ordering of results with different $|\Delta\eta|$ separations observed

in the PYTHIA 8 calculations is the same as in the measurements. The PYTHIA 8 calculations show slight decreasing trends with respect to multiplicity, substantially underestimate the measurements for $\langle\langle\cos(2(\varphi_1-\varphi_2))\rangle\rangle$ for every $|\Delta\eta|$ separation. It shows that PYTHIA 8 cannot accurately describe short-range correlation measurements, and it also fails to mimic long-range correlations in its calculations. For $\langle\langle\cos(3(\varphi_1-\varphi_2))\rangle\rangle$, with $|\Delta\eta| > 1.4$, the sign of the observable is negative in PYTHIA 8, whilst it is positive in measurement. PYTHIA 8 also underestimates $\langle\langle\cos(4(\varphi_1-\varphi_2))\rangle\rangle$ in the standard method. However, when employing a larger $|\Delta\eta|$, the PYTHIA 8 calculation is able to reproduce $\langle\langle\cos(4(\varphi_1-\varphi_2))\rangle\rangle$ with high accuracy. Given that the same pairs of particles are utilized to measure different harmonics of $\langle\langle\cos(n(\varphi_1-\varphi_2))\rangle\rangle$, it's important to note that while $\langle\langle\cos(4(\varphi_1-\varphi_2))\rangle\rangle$ may accurately yield the observed long-range ($|\Delta\eta| > 1.4$) correlation, the fundamental mechanism in data and calculation might be different, considering the incorrect sign prediction for $\langle\langle\cos(3(\varphi_1-\varphi_2))\rangle\rangle$.

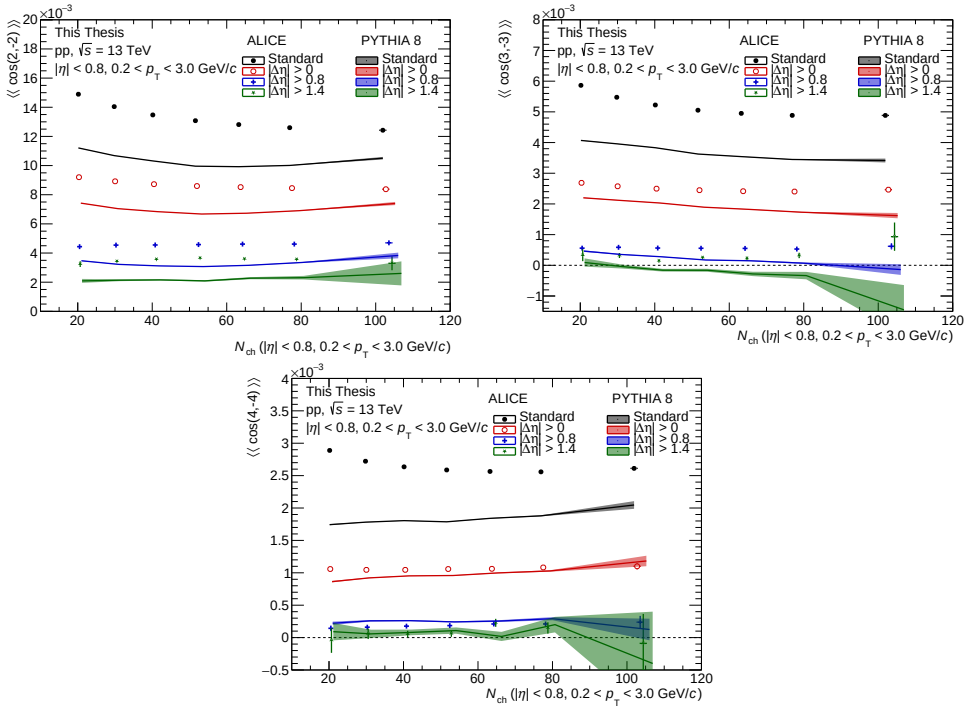

FIGURE 6.4: Calculations of two-particle correlations of second, third, and fourth harmonics ($\langle\langle\cos(2(\varphi_1-\varphi_2))\rangle\rangle$, $\langle\langle\cos(3(\varphi_1-\varphi_2))\rangle\rangle$, $\langle\langle\cos(4(\varphi_1-\varphi_2))\rangle\rangle$) as a function of multiplicity in pp collisions from PYTHIA 8 [52], compared with the measurements.

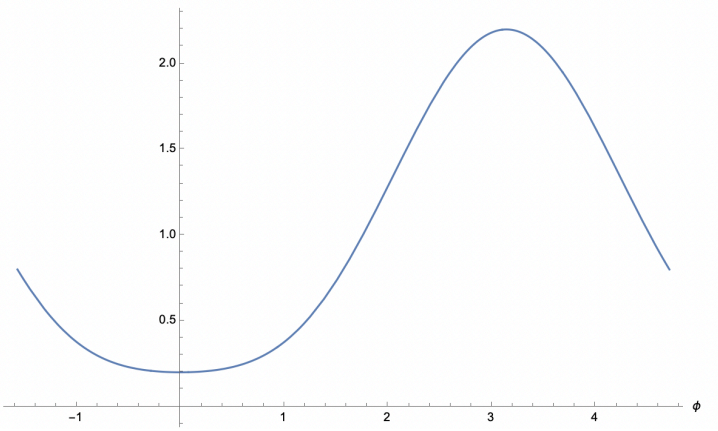

FIGURE 6.5: Shape of $1 - 1\cos(\Delta\varphi) + 0.1\cos(2\Delta\varphi)$.

Perspective: Contributions to two-particle correlation (continue) However, the statement of $c_{2L} \approx 1, c_{4L} \approx 1$ and $c_{3L} \approx -1$ is not always correct. The shape $1 - 1\cos(\Delta\varphi) + 0.1\cos(2\Delta\varphi)$ (see figure 6.5) mimic a properties of $\Delta\varphi$ distribution of particles from the back-to-back jets, which has a peak at π. However, the c_3 from this distribution is 0 rather than around -1.

Therefore, one should not directly link a negative c_3 (which is the case in PYTHIA 8) to the back-to-back jets. Additionally, although the back-to-back jet always contributes to the measured correlation and can not be removed through the $|\Delta\eta|$ separation method, it is not suitable to claim that any observable is contaminated by the back-to-back jets.

6.1.2 Three and four-particle correlations

Figure 6.6 and 6.7 presents a three-particle correlations of mixed harmonics $\langle\langle\cos(4\varphi_1 - 2\varphi_2 - 2\varphi_3)\rangle\rangle$, measured in large and small collision systems. These correlations are essential components in the measurement of nonlinear flow response observables such as $v_{4,22}$, $\chi_{4,22}$, and $\rho_{4,22}$, defined in chapter 3. The results with varying $|\Delta\eta|$ are presented. In addition, three-subevent methods are also employed. As shown in figure 6.6, the $\langle\langle\cos(4\varphi_1 - 2\varphi_2 - 2\varphi_3)\rangle\rangle$ exhibits an initial increase and subsequent decrease with the increasing multiplicity in Pb–Pb collisions. This pattern is consistent across results using various $|\Delta\eta|$ separations. Distinctions between the measurements with different $|\Delta\eta|$ separation methods are obvious at low multiplicities ($N_{\mathrm{ch}} \lesssim 1000$), while these differences diminish at higher multiplicities ($N_{\mathrm{ch}} \gtrsim 1000$). The three-particle correlation shows a

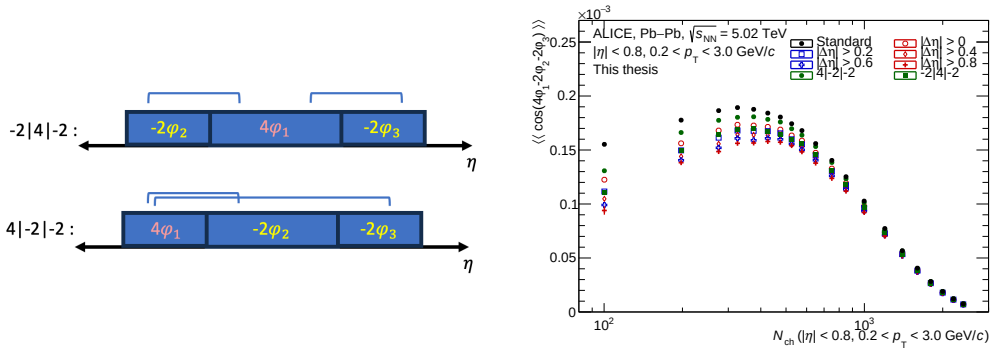

FIGURE 6.6: Measurements of three-particle correlations of mixed harmonics $\langle\langle\cos(4\varphi_1 - 2\varphi_2 - 2\varphi_3)\rangle\rangle$ as a function of multiplicity in Pb–Pb collisions. The correlations are measured with the standard method, the pseudorapidity separation methods, and the three-subevent methods.

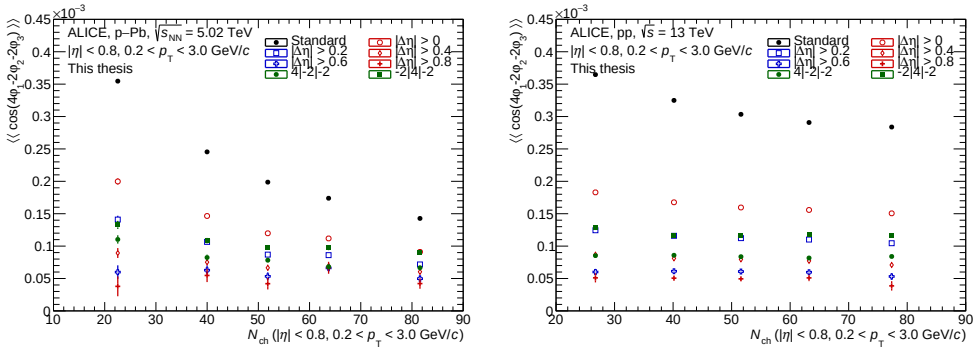

FIGURE 6.7: Measurements of three-particle correlations of mixed harmonics $\langle\langle\cos(4\varphi_1 - 2\varphi_2 - 2\varphi_3)\rangle\rangle$ in p–Pb and pp collisions. The correlations are measured with the standard method, the pseudorapidity separation method, and the three-subevent method.

monotonic decrease with an increasing $|\Delta\eta|$ separation. Among the three-subevent methods, the measurement with $-2|4|-2$ configuration (see the sketch in figure 6.6) has the second largest results in magnitude, only smaller than the results using the standard configuration. The measurement with the $4|-2|-2$ method (see sketch in figure 6.6) exhibits a correlation of magnitude similar to that observed for $|\Delta\eta| > 0.2$. Considering the two three-subevent method configurations, the $-2|4|-2$ method has two short-range correlations, while the $4|-2|-2$ method has one short-range and one long-range correlation. The three-subevent method has a shorter-range correlation than the two-subevent methods with a large $|\Delta\eta|$ separation, while the three-subevent method is less influenced by the back-to-back jets.

In both p–Pb and pp collisions, the standard method shows a decreasing pattern with

respect to the increasing multiplicity for $\langle\langle\cos(4\varphi_1 - 2\varphi_2 - 2\varphi_3)\rangle\rangle$. In pp collisions, this decrease becomes barely noticeable beyond $|\Delta\eta| > 0.2$. Conversely, in p–Pb collisions, the decreasing trend persists even at $|\Delta\eta| > 0.2$. In both collision systems, an increase in $|\Delta\eta|$ consistently leads to a reduction in $\langle\langle\cos(4\varphi_1 - 2\varphi_2 - 2\varphi_3)\rangle\rangle$. The results from the three-subevent configuration with $-2|4|-2$ are larger than magnitude than that with $4|-2|-2$ configuration, consistent with what has been seen in Pb–Pb collisions. This difference between the results of the two different configurations arises from the fact that the $-2|4|-2$ configuration encompasses two short-range correlations, whereas the $4|-2|-2$ configuration includes one short-range correlation and one long-range correlation.

The observable $\langle\langle\cos(4\varphi_1-2\varphi_2-2\varphi_2)\rangle\rangle$ measures the $\langle v_4 v_2^2 \cos(4(\Psi_4-\Psi_2))\rangle$, encoding the information of both the magnitude of flow and the correlation between flow symmetry planes. In large collision systems, such as Pb–Pb collisions, transitioning from low to high multiplicity, corresponding to moving from peripheral to central collisions, the event plane correlation is getting smaller. This will be elaborated upon in section 6.5.2. Additionally, the flow coefficients v_4 and v_2 decrease as the multiplicity $N_{\rm ch}$ increases from approximately 100 to 2000. The v_4 and v_2 are observables connected to the measurements of $\langle\langle\cos(2(\varphi_1-\varphi_2))\rangle\rangle$ and $\langle\langle\cos(4(\varphi_1-\varphi_2))\rangle\rangle$. The contributions of symmetry plane correlation and flow magnitude together give rise to the observed trend of $\langle\langle\cos(4\varphi_1-2\varphi_2-2\varphi_3)\rangle\rangle$ in Pb–Pb collisions. Using the standard method, the observed decreasing trend with increasing $N_{\rm ch}$ in small collision systems may also be attributed to non-flow correlations. Notably, a more pronounced decreasing trend is observed in p–Pb collisions compared to pp collisions, similar as the patterns noted in $\langle\langle\cos(n(\varphi_1 - \varphi_2))\rangle\rangle$ measurements, explained as a stronger non-flow effects in p–Pb than pp collisions. The weak dependence of $\langle\langle\cos(4\varphi_1 - 2\varphi_2 - 2\varphi_3)\rangle\rangle$ on multiplicity suggests that the correlation between flow angles Ψ_2 and Ψ_4 is not strongly influenced by multiplicity. This will be further explored through the analysis of $\rho_{4,22}$.

The comparison between $\langle\langle\cos(4\varphi_1 - 2\varphi_2 - 2\varphi_3)\rangle\rangle$ measurements in pp collisions and the PYTHIA 8 [52] calculations is shown in figure 6.8. The PYTHIA 8 calculations underestimate the measurements obtained using the standard method. Furthermore, even when employing the three sub-event method 4|-2|-2 or the two sub-event methods, PYTHIA 8 still underestimates the measurements for $\langle\langle\cos(4\varphi_1-2\varphi_2-2\varphi_3)\rangle\rangle$, suggesting that it is insufficient for mimic long-range three-particle correlations, which may arise from flow effects in data.

The correlation observed among four particles may originate from the pairwise correlation of two particles within the group, or it could stem from a non-factorizable correlation involving all four particles. The four-particle correlation $\langle\langle\cos(2\varphi_1 + 2\varphi_2 - 2\varphi_3 - 2\varphi_4)\rangle\rangle$ encode the information of two-particle correlation $\langle\langle\cos(2(\varphi_1 - \varphi_2))\rangle\rangle$ and the genuine four-particle correlations. It also serves as the denominator of the $v_{4,22}$, $\chi_{4,22}$ and $\rho_{4,22}$.

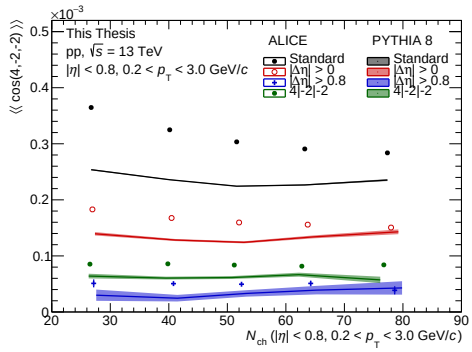

FIGURE 6.8: Calculations of three-particle correlations of mixed harmonics $\langle\langle\cos(4\varphi_1 - 2\varphi_2 - 2\varphi_3)\rangle\rangle$ as a function of multiplicity in pp collisions with PYTHIA 8 [52], compared with the measurements.

The $\langle\langle\cos(3\varphi_1 + 2\varphi_2 - 3\varphi_1 - 2\varphi_2)\rangle\rangle$ and $\langle\langle\cos(4\varphi_1 + 2\varphi_2 - 4\varphi_3 - 2\varphi_4)\rangle\rangle$ are ingredients to obtain the symmetric cumulants SC(3,2) and SC(4,2), respectively.

The four-particle correlations are measured in Pb–Pb collisions with the standard and pseudorapidity separation methods as well as the three-subevent methods. The measurements are shown in figure 6.9. Using the standard method, the $\langle\langle\cos(2\varphi_1 + 2\varphi_2 - 2\varphi_1 - 2\varphi_2)\rangle\rangle$, $\langle\langle\cos(3\varphi_1 + 2\varphi_2 - 3\varphi_1 - 2\varphi_2)\rangle\rangle$, and $\langle\langle\cos(4\varphi_1 + 2\varphi_2 - 4\varphi_3 - 2\varphi_4)\rangle\rangle$ all exhibit decreasing values with the increase of N_{ch} within the region of low multiplicity ($N_{\mathrm{ch}} \lesssim 100$). Additionally, the curve descends sharply at high multiplicities ($N_{\mathrm{ch}} \gtrsim 300$). The observables decrease as the $|\Delta\eta|$ increases, consistent with the trends observed in all previous two and three-particle correlations. It is interesting to note that the results from different three-subevent configurations are quite different. Selecting two particles from the central region of the detector results in two short-range correlations, leading to the highest level of non-flow contamination compared to other three-subevent configurations. Additionally, it's observed that the measurements with the $3,2|-3|-2$ (or $4,2|-4|-2$) configuration (see sketch in figure 6.9) are significantly larger than the results with $3,2|-2|-3$ (or $4,2|-2|-4$) configuration due to the higher sensitivity of high harmonics to the short-range correlations.

The measurement is also conducted in small collision systems of p–Pb and pp collisions as shown in figure 6.10. A decreasing trend of $\langle\langle\cos(2\varphi_1 + 2\varphi_2 - 2\varphi_3 - 2\varphi_4)\rangle\rangle$ with the standard method is observed in p–Pb and pp collisions. With larger $|\Delta\eta|$ separation, the decreasing trend becomes weaker compared with the standard method in p–Pb and pp collisions. The difference between the standard and the pseudorapidity separation methods is more significant than in Pb–Pb collisions because the non-flow effects are much larger in small collision systems. The measurements reveal an ordering of various three-subevent configurations, resembling the patterns observed in Pb–Pb collisions. For

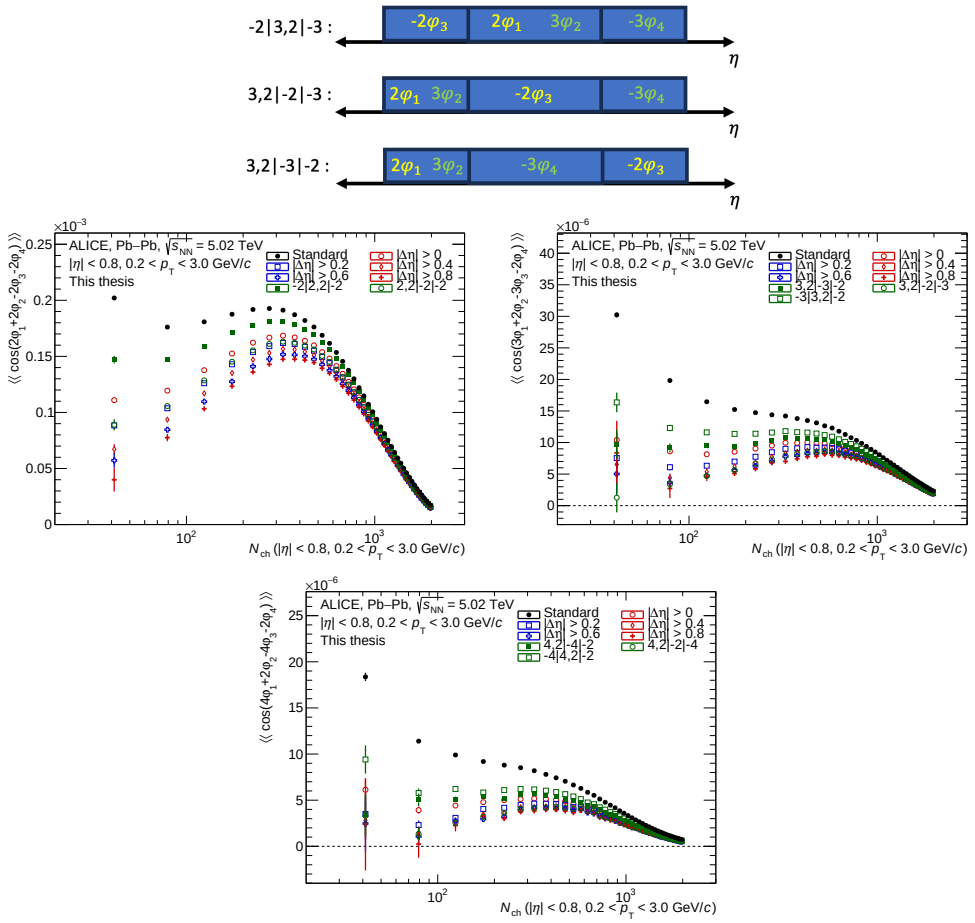

FIGURE 6.9: Measurements of four-particle correlations $\langle\langle\cos(2\varphi_1 - 2\varphi_2 + 2\varphi_3 - 2\varphi_4)\rangle\rangle$, $\langle\langle\cos(3\varphi_1 + 2\varphi_2 - 3\varphi_3 - 2\varphi_4)\rangle\rangle$, and $\langle\langle\cos(4\varphi_1 + 2\varphi_2 - 4\varphi_3 - 2\varphi_4)\rangle\rangle$ as a function of multiplicity in Pb–Pb collisions. The correlations are measured with the standard method, the pseudorapidity separation methods, and the three-subevent methods.

$\langle\langle\cos(3\varphi_1 + 2\varphi_2 - 3\varphi_3 - 2\varphi_4)\rangle\rangle$ and $\langle\langle\cos(4\varphi_1 + 2\varphi_2 - 4\varphi_3 - 2\varphi_4)\rangle\rangle$, the observed pattern is similar as $\langle\langle\cos(2\varphi_1 + 2\varphi_2 - 2\varphi_3 - 2\varphi_4)\rangle\rangle$. Both observables exhibit a decreasing trend with respect to the increasing of multiplicity in both p–Pb and pp collision systems with the standard method. When applying $|\Delta\eta|$ separation, the correlation decreases monotonically. Substantial deviations between the different three sub-event methods can be observed. The measurements with $3,2| - 2| - 3$ (or $4,2| - 2| - 4$) configuration demonstrate the least contamination from short-range correlations, for the same reasons explained as in Pb–Pb collisions.

The four-particle correlation $\langle\langle\cos(n\varphi_1 + m\varphi_2 - n\varphi_3 - m\varphi_4)\rangle\rangle$, measures the $\langle v_n^2 v_m^2\rangle$

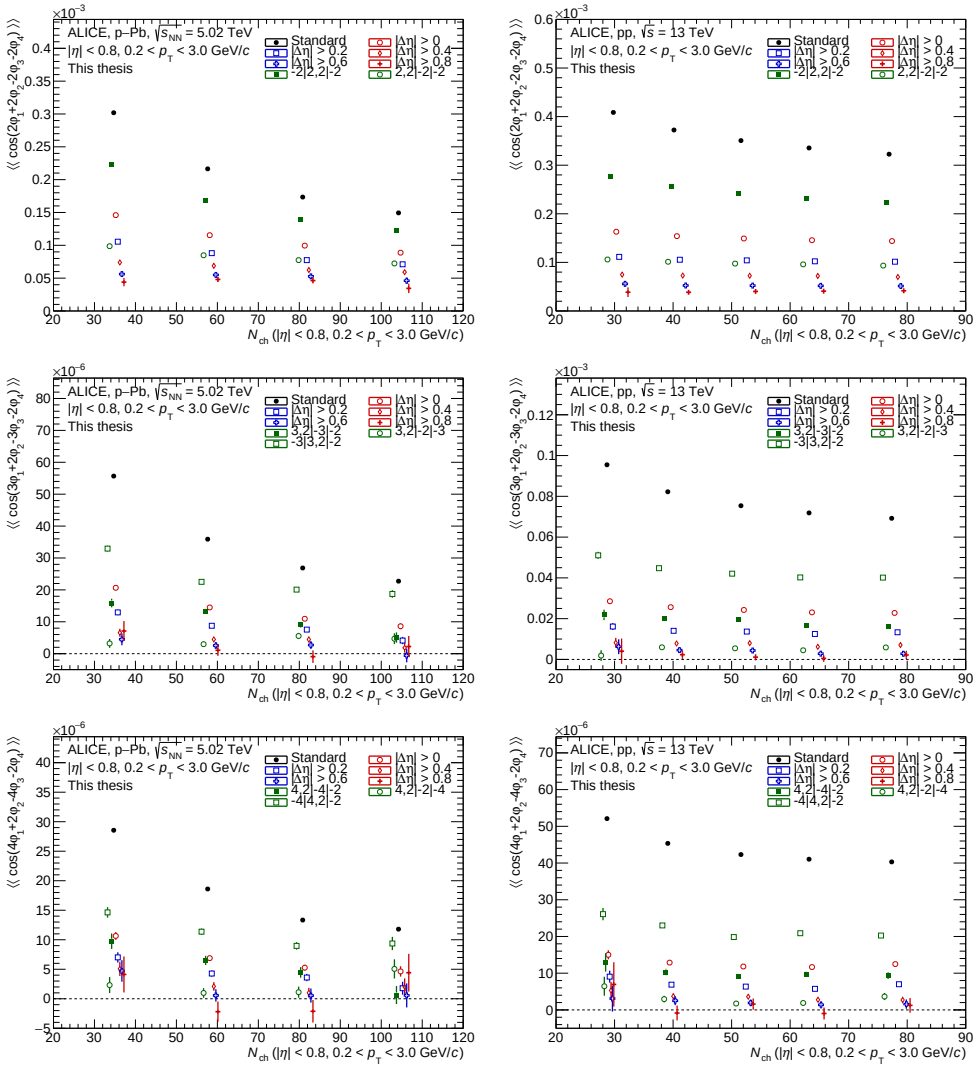

FIGURE 6.10: Measurements of four-particle correlations $\langle\langle\cos(2\varphi_1 - 2\varphi_2 + 2\varphi_3 - 2\varphi_4)\rangle\rangle$, $\langle\langle\cos(3\varphi_1 + 2\varphi_2 - 3\varphi_3 - 2\varphi_4)\rangle\rangle$ and $\langle\langle\cos(4\varphi_1 + 2\varphi_2 - 4\varphi_3 - 2\varphi_4)\rangle\rangle$ as a function of multiplicity in p–Pb (left), pp (right) collisions. The correlations are measured with the standard method and the pseudorapidity separation methods, as well as the three-subevent methods.

when flow is the dominant factor. With a substantial $|\Delta\eta|$ separation, i.e., $|\Delta\eta| > 0.8$, is applied, the four-particle correlation initially increases and then decreases with respect to the multiplicity. Additionally, the observed trend using the standard method, without any non-flow suppression, is an interplay between the flow and short-range correlation effects. In pp and p–Pb collisions, the observable's multiplicity dependence is weak when

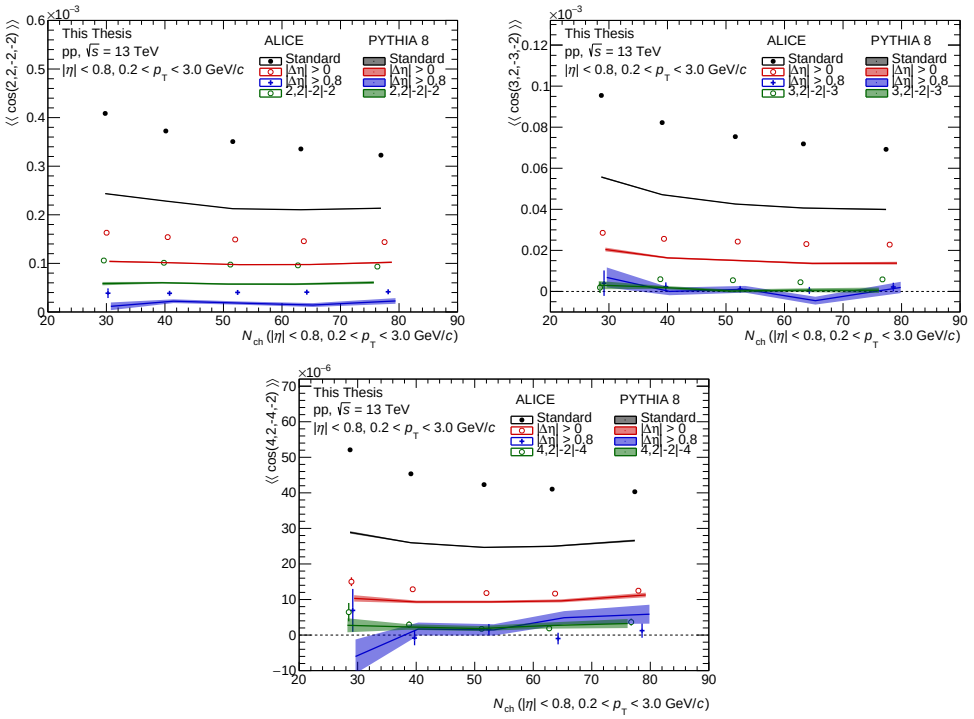

FIGURE 6.11: Calculation of four particle correlations $\langle\langle\cos(2\varphi_1 - 2\varphi_2 + 2\varphi_3 - 2\varphi_4)\rangle\rangle$, $\langle\langle\cos(3\varphi_1 + 2\varphi_2 - 3\varphi_3 - 2\varphi_4)\rangle\rangle$, $\langle\langle\cos(4\varphi_1 + 2\varphi_2 - 4\varphi_3 - 2\varphi_4)\rangle\rangle$ as a function of multiplicity in pp collisions with the PYTHIA 8 [52], compared with the measurements.

the pseudorapidity gap is large ($|\Delta\eta| > 0.8$). The initial geometry profile does not change much when changing the multiplicity, which was previously confirmed through the study of two-particle correlations. With the additional measurements of four-particle correlations, it indicates that the geometry fluctuation is also insensitive to the changing of multiplicity.

The four-particle correlations are examined using PYTHIA 8 [52] calculation and compared with the measurements for various analysis methods. These methods include the standard method, $|\Delta\eta| > 0$, $|\Delta\eta| > 0.8$, and the three-subevent method with configurations $2, 2|-2|-2$ (or $3, 2|-2|-3$, or $4, 2|-2|-4$). The selected three-subevent method is considered the least sensitive to the short-range correlations among the different three-subevent configurations. The comparison is shown in figure 6.11. PYTHIA 8 successfully mimics the changing trend of multiple particle correlations when different analysis methods are applied, including the standard methods, variations in $|\Delta\eta|$, and the three-subevent methods. Upon comparing the calculation with the measurements, it becomes evident that for $\langle\langle\cos(2\varphi_1 + 2\varphi_2 - 2\varphi_3 - 2\varphi_4)\rangle\rangle$, PYTHIA 8 fails to describe the measurements for any configuration. Similarly, this model has the challenge to reproduce most of

the measurements for $\langle\langle\cos(3\varphi_1+2\varphi_2-3\varphi_3-2\varphi_4)\rangle\rangle$ and $\langle\langle\cos(4\varphi_1+2\varphi_2-4\varphi_3-2\varphi_4)\rangle\rangle$. Relatively better agreement is observed with $|\Delta\eta|>0.8$ for $\langle\langle\cos(3\varphi_1+2\varphi_2-3\varphi_3-2\varphi_4)\rangle\rangle$ and $\langle\langle\cos(4\varphi_1+2\varphi_2-4\varphi_3-2\varphi_4)\rangle\rangle$, as well as for $\langle\langle\cos(4\varphi_1+2\varphi_2-4\varphi_3-2\varphi_4)\rangle\rangle$ with the three-subevent method. The agreements between the PYTHIA 8 calculation and measurements with $|\Delta\eta|>0.8$ could be attributed to the fact that both the measurements and calculation are close to zero.

6.2 Cumulants

The two-particle cumulants have identical values as the two-particle correlations, illustrated in figure 6.1, figure 6.3 and figure 6.2 in section 6.1. Further insights into the physics of the two-particle cumulants were also provided and will not be reiterated here.

Figure 6.12 and 6.13 presents the measurement of second harmonic four-particle cumulants $c_2\{4\}$ in large system (Pb–Pb) and small systems (p–Pb, pp) collisions. $c_2\{4\}$ is generally less influenced by non-flow effects, compared with the two-particle cumulants, due to its implementation involving four particles, where few particle correlation effects cancel out in genuine four-particle correlations. The measurements are presented using the standard method and different $|\Delta\eta|$ separations. The three-subevent method is also applied to the measurement.

In Pb–Pb collisions, as shown in figure 6.12, results from all the methods exhibit a comparable magnitude. Regardless of the non-flow suppression method, all data points consistently maintain a negative value. With all the different configurations, the $c_2\{4\}$ always first decrease and then increase with the multiplicity increasing. With the increasing of $|\Delta\eta|$, the changing of the $c_2\{4\}$ is not obvious, indicating the $c_2\{4\}$ is not sensitive to the non-flow effects. Even with the standard procedure, which is believed to contain most few-particle correlation effects, $c_2\{4\}$ is negative at the lowest multiplicity. The data point with the standard method at the most peripheral bin is close to zero. Whilst with implementing the $\Delta\eta$ separation or with the three subevent methods, a clear deviation from zero emerges.

Notable differences could be seen in p–Pb and pp collisions among the standard, various $|\Delta\eta|$, and the three-subevent methods, as shown in figure 6.13. In p–Pb collisions, the $c_2\{4\}$ with standard method shows a transition from positive to negative with increased multiplicity. With an increase of the $|\Delta\eta|$, the value of $c_2\{4\}$ becomes smaller. The results for $|\Delta\eta|>0, |\Delta\eta|>0.2$ and $|\Delta\eta|>0.4$ in the lowest N_{ch} bin are positive but consistent with zero within the uncertainty. However, due to the fluctuation, no monotonous dependence of the $|\Delta\eta|$ separation can be observed in the three subevent methods. The decreasing trend with the increasing N_{ch} is present for $|\Delta\eta|>0$, $|\Delta\eta|>0.2$ and $|\Delta\eta|>0.4$. This decreasing trend for $|\Delta\eta|>0.8$ is also observable but the uncertainty is relatively

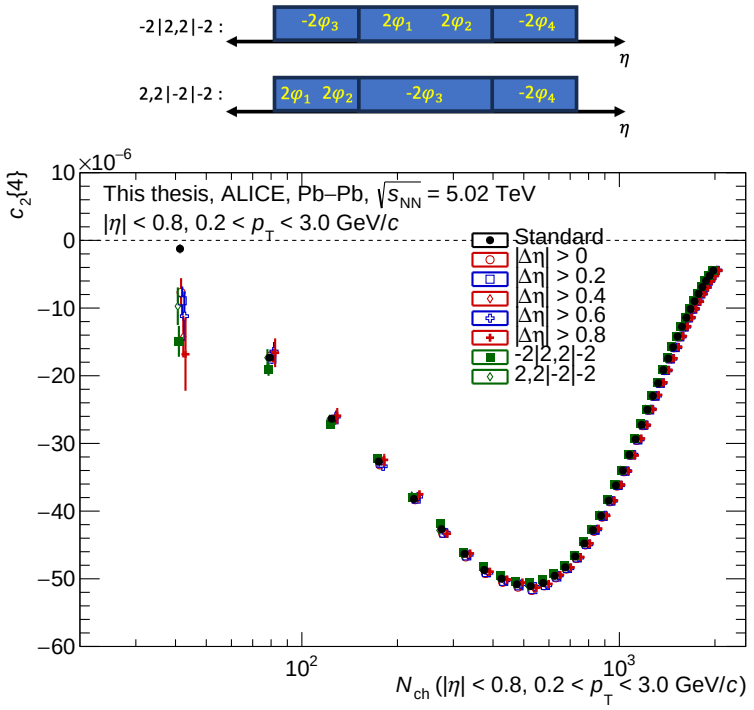

FIGURE 6.12: Measurements of $c_2\{4\}$ as a function of multiplicity in Pb–Pb collisions. The standard method, $|\Delta\eta|$ separation methods, and three-subevent methods are used. The x-axis is shifted for visibility.

large. The $c_2\{4\}$ with the $2,2|-2|-2$ is smaller than the $-2|2,2|-2$, except for the points with the largest multiplicity. Both of them are negative expect for the point of $2,2|-2|-2$, which could also just be leviated because of the statistical fluctuation. In pp collisions, The $c_2\{4\}$ with the standard method exhibits a decreasing trend with the increasing of $N_{\rm ch}$, which diminishes with larger $|\Delta\eta|$ ($|\Delta\eta| > 0.2$). The standard method yields a positive value for $c_2\{4\}$, but as $|\Delta\eta|$ increases, it turns to a negative value. With the $|\Delta\eta| > 0$, the decreasing trend could still be observed. While with further increasing of the $|\Delta\eta|$ separation such as $|\Delta\eta| > 0.2$, the multiplicity dependence of the $c_2\{4\}$ is weak. At the same time, all the data points for $|\Delta\eta| > 0.2$ are negative. Generally, an ordering of $c_2\{4, \text{Standard}\} > c_2\{4, |\Delta\eta| > 0\} > c_2\{4, |\Delta\eta| > 0.2\} > c_2\{4, |\Delta\eta| > 0.4\} > c_2\{4, |\Delta\eta| > 0.6\}$ could be concluded, with a few exception which might be caused by the statistical fluctuation. Both of the two three subevent configurations ($2,2|-2|-2$ and $-2|2,2|-2$) of $c_2\{4\}$ are negative regardless of the multiplicity. And neither of the two configuration shows a strong multiplicity dependence. The two different subevent configurations of $c_2\{4\}$ are clearly distinct from each other in pp collisions. The configuration

$2,2|-2|-2$ is with one long-range correlation and one short-range correlation. This configuration is less affected by the short-range correlations compared with the $-2|2,2|-2$, which contains two short-range correlations. The $c_2\{4\}$ with the three subevent method $2,2|-2|-2$ is smaller compared with the $-2|2,2|-2$.

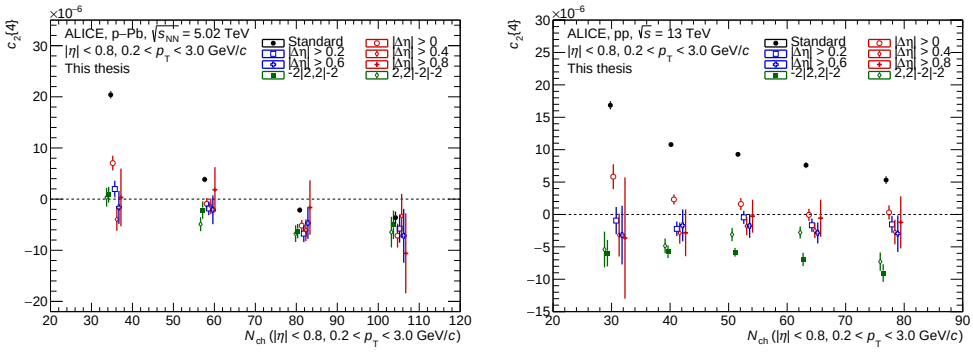

FIGURE 6.13: Measurements of $c_2\{4\}$ as a function of multiplicity in p–Pb (left) and pp (right) collisions. The standard method, $|\Delta\eta|$ separation methods, and three-subevent methods are used. The x-axis is shifted for visibility.

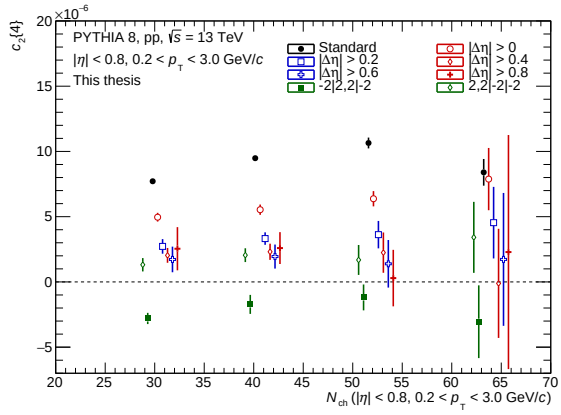

FIGURE 6.14: Calculation of $c_2\{4\}$ as a function of multiplicity in pp with PYTHIA 8 [52]. The standard method, $|\Delta\eta|$ separation methods, and three-subevent methods are used. The x-axis is shifted for visibility.

The $c_2\{4\}$ is calculated with the PYTHIA 8 [52] in pp collisions, as shown in figure 6.14. It is to check whether this state-of-the-art non-flow model could well describe the measurements. Additionally, it is interesting to see whether the differences of $c_2\{4\}$ with different $|\Delta\eta|$ separations could also be mimiced by the calculation from PYTHIA 8. In PYTHIA 8, there are only a few particle correlations. After subtracting the short-range

correlations, the $c_2\{4\}$ represents the remaining longer-range few particle correlations. Similar to the data, the $c_2\{4\}$ decreases with the increasing $|\Delta\eta|$. Even with the largest $|\Delta\eta|$ separation of $|\Delta\eta| > 0.8$, shown in figure 6.14, no significant signature of negative $c_2\{4\}$ is observed in the model calculation. The effect of the non-flow subtraction method should not be judged by the criteria of the smallest absolute value of the $c_2\{4\}$ or smallest $c_2\{4\}$. Selecting the results according to whether they introduce short or long correlation is preferred, since the longer range correlation is usually more interesting.

In a flow dominant collision system, the $c_2\{4\}$ measures $\langle v_2^4\rangle - 2\langle v_2^2\rangle^2$, and it can also be expressed as $-(\langle v_2\rangle^2 - \sigma_v^2)^2$ when the event-by-event v_2 follow a Bessel-Gaussian distribution and when the σ_v is small compared to the averaged $\langle v_2\rangle$ [141]. In non-central Pb–Pb collision systems where elliptic flow fluctuations are minor compared to the elliptic flow v_2 itself, $c_2\{4\}$ can be approximated as $\langle -v_2^4\rangle$ if only the leading term is considered. Therefore, in Pb–Pb collisions, the $c_2\{4\}$ decreases and then increases with the increasing number of charged tracks. According to the formula $c_2\{4\} = -(\langle v_2\rangle^2 - \sigma_v^2)^2$, the value of $c_2\{4\}$ is naturally negative. However, this expression may not hold in certain scenarios. For instance, a positive $c_2\{4\}$ can occur in systems characterized by few-particle correlations. Yet, it's important to note that few-particle correlations do not always result in a positive $c_2\{4\}$, as observed in the PYTHIA 8 calculation. Another potential cause for the deviation from this relationship is significant flow fluctuations, which could also lead to a positive $c_2\{4\}$ [174].

6.3 Flow coefficients

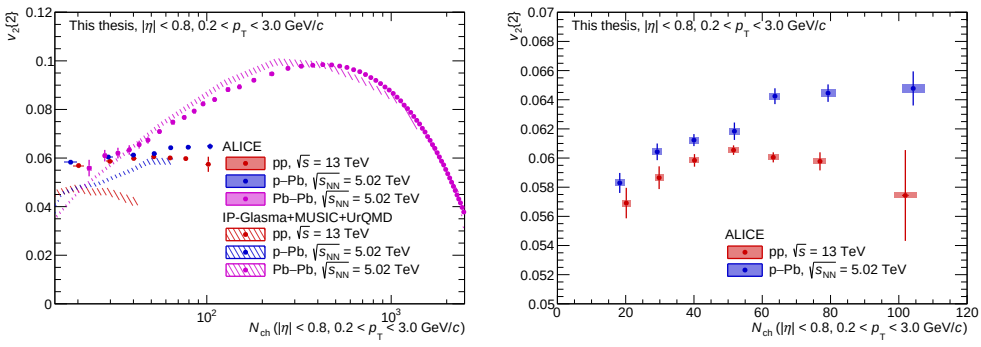

FIGURE 6.15: Left: Measurements of $v_2\{2\}$ as a function of multiplicity in pp, p–Pb and Pb–Pb collisions. The measurements are compared with the IP-Glasma + MUSIC + UrQMD [49] calculation. Right plot: zoom in on the measurements in pp and p–Pb collisions.

The second-order flow coefficients with two-particle cumulants methods, i.e., $v_n\{2\} = \sqrt{c_n\{2\}}$ are measured in pp, p–Pb, and Pb–Pb collisions as a function of the multiplicity, shown in figure 6.15. The separation of $|\Delta\eta| > 1.4$ is used for the measurements. The comparison with PYTHIA 8 [52] calculation for $\langle\langle\cos(2\varphi_1 - 2\varphi_2)\rangle\rangle$, as shown in figure 6.4, already suggests the measurement can not be solely explained by the non-flow effects modeled in PYTHIA 8. In Pb-Pb collisions, the data points firstly increase and then decrease with the increasing of $N_{\rm ch}$, attributed to the emergence of geometric effects. In small collision systems, the multiplicity dependence of $v_2\{2\}$ in both pp and p-Pb collisions is considerably weaker compared to that observed in Pb–Pb collisions. A notable deviation between data in pp and Pb–Pb becomes evident at approximately $N_{\rm ch} > 50$. The same deviation is also observed between the measurements in p–Pb and Pb–Pb collisions at $N_{\rm ch} \gtrsim 50$. In pp and p–Pb collisions the $v_2\{2\}$ originates from the fluctuation of the color field from the initial stage, while in Pb–Pb collision, the $v_2\{2\}$ originates from the overall shape of the overlapping region of the two nuclei.

When zooming in on the results from p–Pb and pp collisions, a clear deviation can be observed between pp and p–Pb results. Moreover, the previously observed increasing behavior of $v_2\{2\}$ in a previous study [72] is absent when more data is used in pp collisions. Instead, the following trend appears: the $v_2\{2\}$ firstly increase and then decrease with respect to the increasing multiplicity. In p–Pb collisions, there is an observed increase in $v_2\{2\}$ with respect to the multiplicity. These distinctions between the pp and p–Pb systems suggest potential differences in the fluctuating initial geometry or initial momentum correlation across different collision systems.

The hybrid hydrodynamic model, IP-Glasma + MUSIC + UrQMD [49], provides a qualitative agreement with the Pb–Pb results. In pp and p–Pb collisions, the IP-Glasma + MUSIC + UrQMD calculations are limited to a relatively low multiplicity region. The hydrodynamics calculations underestimates the $v_2\{2\}$ measurements in both of the small collision systems. The increasing trend in the model is more pronounced than what has been measured in p–Pb collisions. Additionally, the hydrodynamics model predicts a declining trend with increasing $N_{\rm ch}$, different from the measurements in pp collisions.

The measurements of the third order flow coefficient with two-particle correlation methods $v_3\{2\}$ in pp, p–Pb, and Pb–Pb collisions are shown in figure 6.16. The measurements are conducted with $|\Delta\eta| > 1.4$, altered from the previous analysis [72] with $|\Delta\eta| > 1.0$, aimed at minimizing potential bias from short-range correlations. In Pb–Pb collisions, the $v_3\{2\}$ initially increase, and then decrease with the increasing of multiplicity, in agreement with the trend of ϵ_3 predicted from Glauber [45] and KLN [175, 176] models. Meanwhile, there is no pronounced multiplicity dependence in pp collisions, while an increasing trend is seen in p–Pb collisions. The IP-Glasma + MUSIC + UrQMD model qualitatively reproduces the measurements in Pb–Pb collisions, however the model

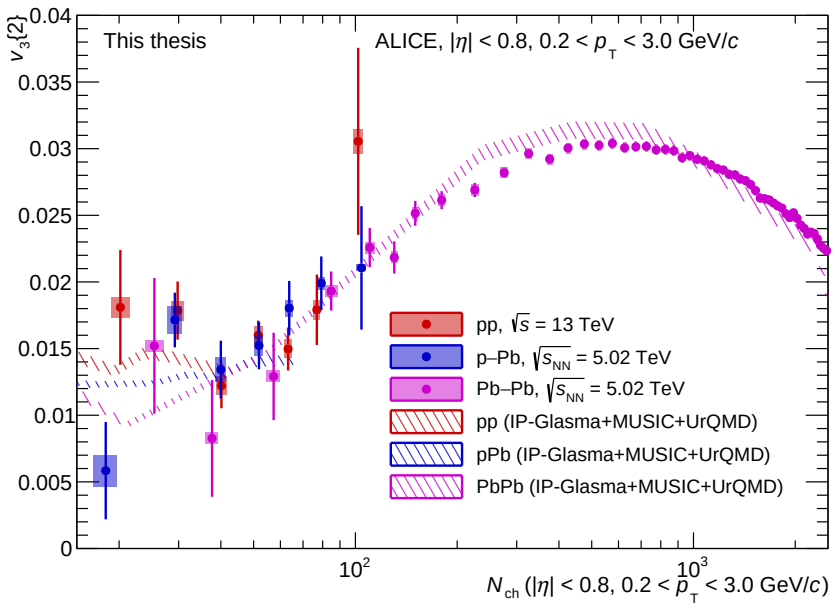

FIGURE 6.16: Measurements of $v_3\{2\}$ as a function of multiplicity in pp, p–Pb and Pb–Pb collisions. The measurements are compared with the IP-Glasma + MUSIC + UrQMD [49] calculation.

only works approximately in p–Pb and pp collisions.

The measurement of $v_4\{2\}$ is presented in figure 6.17, showing a trend that first increase and then decrease with the increasing of N_{ch} in Pb–Pb collisions. The measurements in Pb–Pb could be well reproduced by the IP-Glasma + MUSIC + UrQMD [49] calculation over a wide multiplicity region from roughly 50 to 2500. The multiplicity dependence of $v_4\{2\}$ is not evident due to the substantial uncertainty in p–Pb collisions. The IP-Glasma + MUSIC + UrQMD calculation approximately reproduces both the magnitude of $v_4\{2\}$. In pp collisions, the measurements show a clear increasing trend as multiplicity increases. The hydrodynamics model underestimates $v_2\{2\}$ while overestimating $v_4\{2\}$ in pp collisions, indicating that the data and model discrepancy cannot be simply resolved by tuning transport coefficients. This inconsistency may be linked to the nonlinear contribution from ϵ_2, which will be further discussed in section 6.5.

The flow coefficients with the four-particle cumulants method $v_2\{4\}$ is shown in figure 6.18 and compared with the results from $v_2\{2\}$. The current understanding of non-flow subtraction suggests that when employing the configuration of $2, 2|-2|-2$, there is one short-range correlation and one long-range correlation; the non-flow contamination is minimal among the two different three subevent configurations. In all three collision systems, $v_2\{4\}$ consistently shows a smaller magnitude compared to $v_2\{2\}$. In Pb–Pb

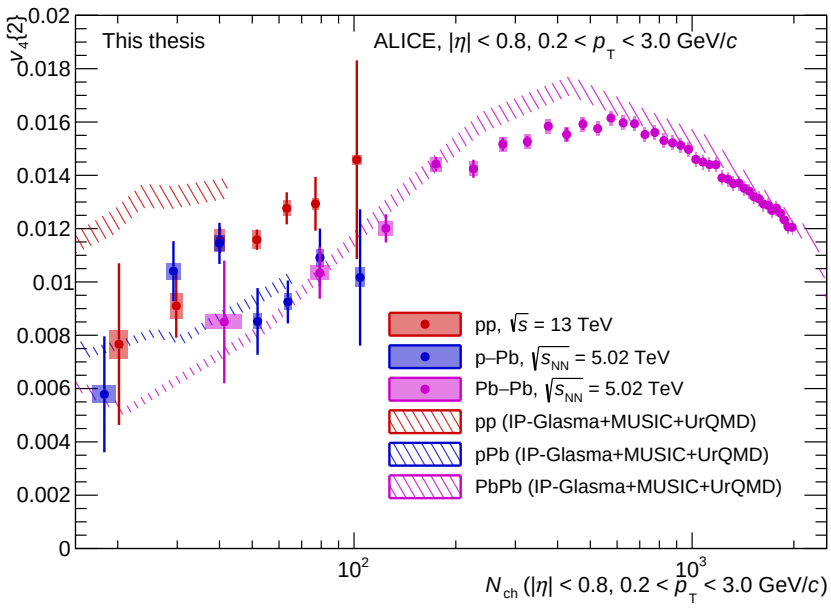

FIGURE 6.17: Measurements of $v_4\{2\}$ as a function of multiplicity in pp, p–Pb and Pb–Pb collisions. The measurements are compared with the IP-Glasma + MUSIC + UrQMD [49] calculation.

collisions, difference between $v_2\{4\}$ and $v_2\{2\}$ is attributed to the fluctuations of v_2. The observed smaller $v_2\{4\}$ compared with the $v_2\{2\}$ in small collision systems also indicates a possibility that the flow fluctuations cause $v_2\{4\}$ to be smaller than $v_2\{2\}$.

The $v_2\{6\}$ is also measured in pp collisions, compared with $v_2\{2\}$ and $v_2\{4\}$. Due to the limited statistics, only the standard method, without any suppression of short-range correlation, is used. The measurements are also plotted in figure 6.18. The $v_2\{6\}$ is also expected to be smaller than $v_2\{2\}$ in a flow dominant system. While in this measurement, the magnitudes of $v_2\{2\}$ and $v_2\{6\}$ are approximately the same. The $v_2\{6\} < v_2\{4\}$ is usually interpreted as a sign of non-Gaussianity in the v_2 distribution, as noted in [177]. However, what is observed in this analysis is a $v_2\{6\} > v_2\{4\}$. The best explanation for the observation might be the influence of short-range correlations.

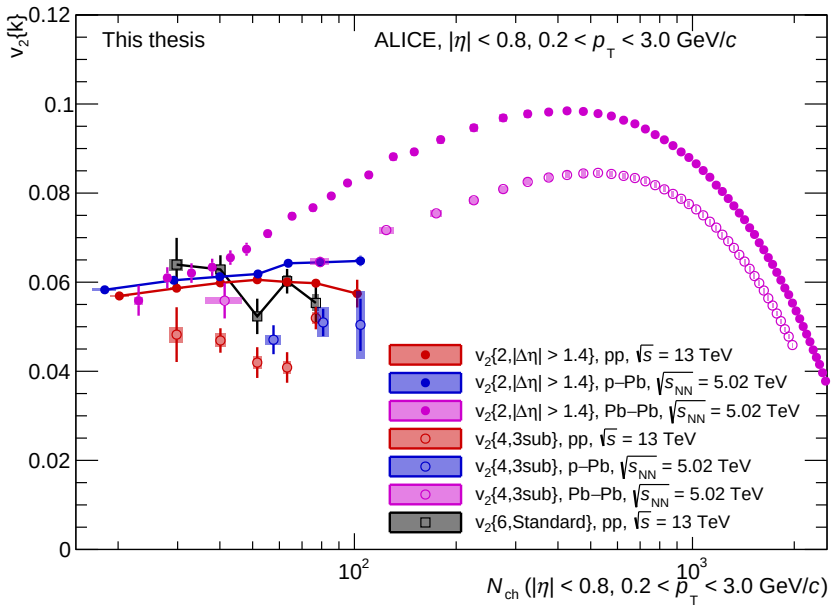

FIGURE 6.18: Measurements of $v_2\{2\}$ and $v_2\{4\}$ as a function of multiplicity in pp, p–Pb and Pb–Pb collisions, and $v_2\{6\}$ as a function of multiplicity in pp collisions.

6.4 Summeric cumulants

6.4.1 SC(3,2)

The symmetric cumulants SC(3,2) are measured in Pb–Pb collisions and small collision systems shown in figure 6.19, 6.20 and 6.21, respectively. By construction, symmetric cumulants further suppress the effect of a few particle correlations.

As shown in figure 6.19, in Pb–Pb collisions, the SC(3,2) using the standard methodology is positive at the lowest multiplicity points. However, as the event multiplicity increases, the SC(3,2) transitions towards negative values, initially decreasing before rising again with higher multiplicities. At the highest multiplicity region, the SC(3,2) tends towards zero. This trend persists even with an increase in $|\Delta\eta|$ separation. Notably, results obtained with $|\Delta\eta|$ separation are consistently smaller across all multiplicities compared to those obtained using standard methods. Nevertheless, even with a substantial $|\Delta\eta|$ separation ($|\Delta\eta| > 0.8$), positive SC(3,2) values are observed at the very low multiplicity regions. As shown in the figure 6.20, similar trends emerge when utilizing the three-subevent approach. The results decrease as the multiplicity increases, and it then increases before reaching zero at high multiplicities. Notably, the three-subevent methods

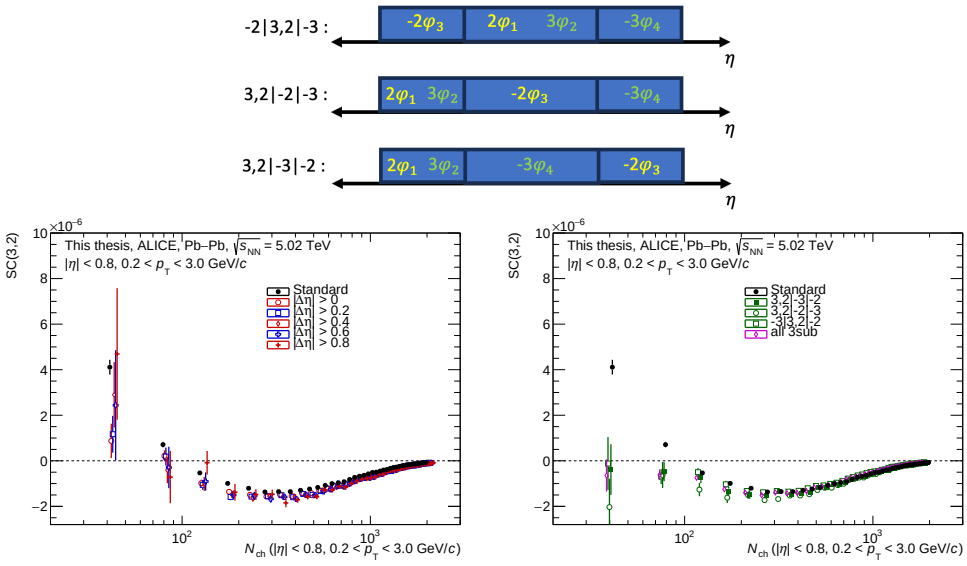

FIGURE 6.19: Measurements of SC(3,2) as a function of multiplicity in Pb–Pb collisions. The measurements with standard methods and different $|\Delta\eta|$ separation methods are presented in the left plot. The measurements with standard methods and different three-sub event configurations are presented in the right plot.

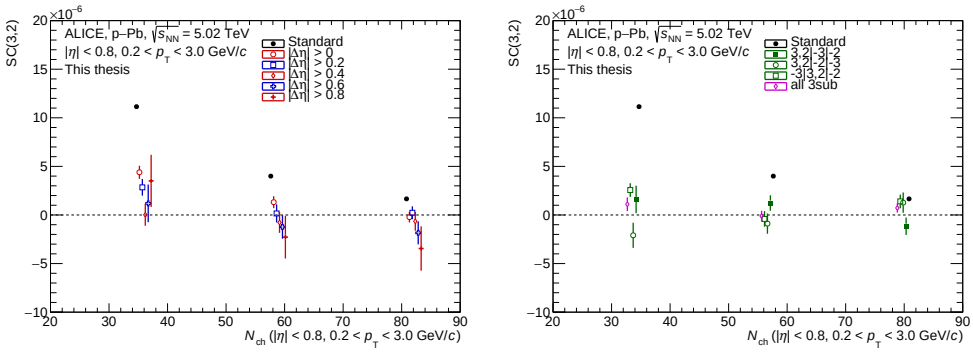

FIGURE 6.20: Measurements of SC(3,2) as a function of multiplicity in p–Pb collisions. The measurements with standard methods and different $|\Delta\eta|$ separation methods are presented in the left plots. The measurements with standard methods and different three-subevent configurations are presented in the right plots.

can yield negative values at the outermost peripheral region. In p–Pb collisions, with the limit of statistics, only a few data points could be obtained for each non-flow suppression configuration. With the standard method, the SC(3,2) is positive, and it decreases to zero with increasing multiplicity. While with the increase of $|\Delta\eta|$, the SC(3,2) becomes smaller.

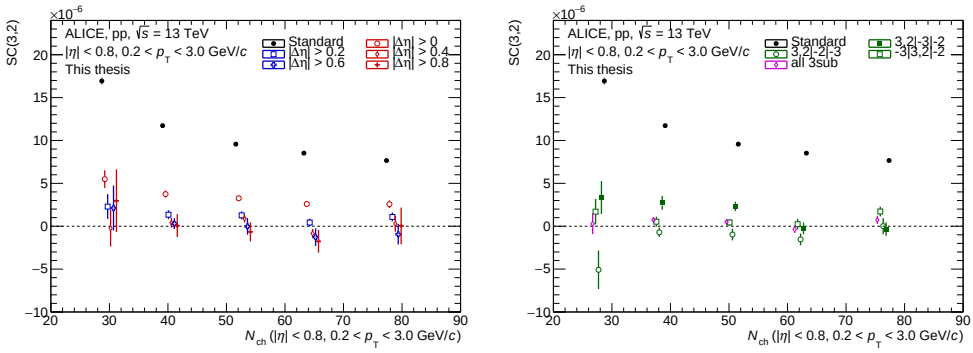

FIGURE 6.21: Measurements of SC(3,2) as a function of multiplicity in pp collisions. The measurements with standard methods and different $|\Delta\eta|$ separation methods are presented in the left plots. The measurements with standard methods and different three-subevent configurations are presented in the right plots.

For $|\Delta\eta| > 0$ and $|\Delta\eta| > 0.2$, the data points at the smallest multiplicity are positive while the other the SC(3,2) is measured to be negative at higher multiplicity for $|\Delta\eta| > 0$ and $|\Delta\eta| > 0.2$. The results using the three-subevent methods are close to zero. In pp collisions, one shows a more obvious sensitivity to applying the $|\Delta\eta|$ separation or using three subevent methods, compared with the Pb–Pb collisions, as shown in figure 6.21. With the standard methods, the SC(3,2) are large and decrease with increasing multiplicity. This behavior is believed to be due to the contamination from the short-range correlations. With an increase of $|\Delta\eta|$, the SC(3,2) is getting smaller, and the monotonic decrease trend with the increasing of multiplicity is less obvious. With $|\Delta\eta| > 0.2$ or a larger $|\Delta\eta|$, the SC(3,2) does not show an obvious multiplicity dependency. In addition, the measurements with three different subevent methods show systematic differences between each other. The $3,2|-2|-3$ configuration is considered to exhibit minimal effect from short-range correlations. This approach includes a long-range correlation among particles associated with the third-order harmonic and a short-range correlation among particles associated with the second-order harmonic. The configuration $-3|3,2|-2$ includes two short-range correlations. As for the $3,2|-3|-2$, it contains one short-range correlation and one long-range correlation, but the long-range correlation is associated with the second-order harmonic.

The SC(3,2) calculated in pp collisions with the PYTHIA 8 [52] model is shown in figure 6.22. The PYTHIA 8 could mimic the behavior of the decreasing SC(3,2) with the increase of the $|\Delta\eta|$. It is also noticed that with the three-subevent configuration $3,2|-2|-3$, the calculation with PYTHIA 8 is negative. The observation of negative SC(3,2) in PYTHIA 8 suggests that the same sign of SC(3,2) in large and small collisions may not represents a same origin in the two collision systems.

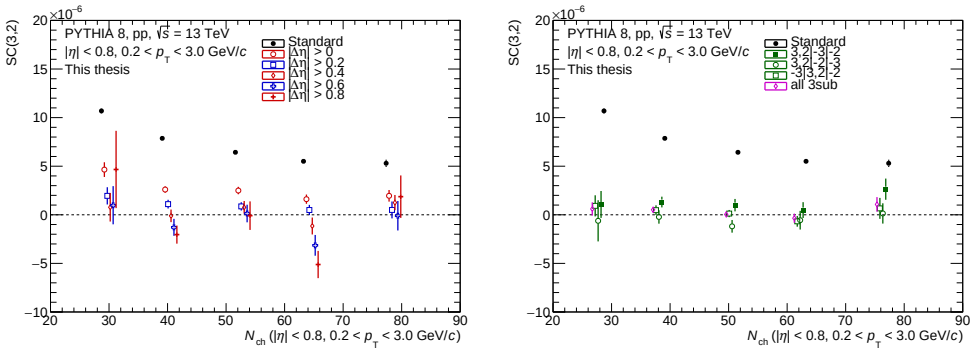

FIGURE 6.22: Calculations of SC(3,2) as a function of multiplicity in pp collisions with PYTHIA 8 [52]. The calculations are with standard methods, different $|\Delta\eta|$ separation methods, and different three-subevent configurations.

The symmetric cumulants SC(3,2) are compared with the hydrodynamical model IP-Glasma + MUSIC + UrQMD [49], as displayed in figure 6.23 (top). The measurements use the combined results from the three three-subevent method configurations, in order to reduce the statistical uncertainty and to be consistent with the previous study [72]. In both the pp and p–Pb collisions, the measurements do not show clear centrality dependence. Most of the data points are positive with a few consistent with zero within the uncertainty. In Pb-Pb collisions, the symmetric cumulants, the covariance between the v_2^2 and v_3^2, are well consistent with the predictions of the hydrodynamical model. This suggests that both the correlation between ellipticity and triangularity, which originates from nuclei position fluctuations, and the transport properties in large collision systems can be well modeled. The first data point with lowest multiplicity deviates from the trend of going zero at low multiplicity. The hydrodynamic model, IP-Glasma + MUSIC + UrQMD, predicts a very small SC(3,2) in pp and p–Pb collisions, which is consistent with zero. This suggests that within the model, the initial eccentricity covariance $\mathrm{cov}(\varepsilon_2^2, \varepsilon_3^2)$ is either negligible or the covariance diffuses during the hydrodynamic evolution of the system. Another factor contributing to the small SC(3,2) could be the tiny absolute fluctuations in v_2^2 or v_3^2 on an event-by-event basis. It is worth clarifying that, even if the absolute fluctuations of v_n^2 are small, the relative fluctuations in comparison to v_n^2 themselves could still be substantial.

To reduce the impact of variations in v_n^2, the normalized symmetric cumulants are investigated. The normalized symmetric cumulants, i.e., symmetric cumulants normalized with $\langle v_2^2 \rangle$ and $\langle v_3^2 \rangle$, are also compared with theoretical calculation, presented in the right plot of figure 6.23 (bottom). The normalized symmetric cumulants NSC(3,2) are predicted to be less sensitive to the details of the hydrodynamic evolution of the system,

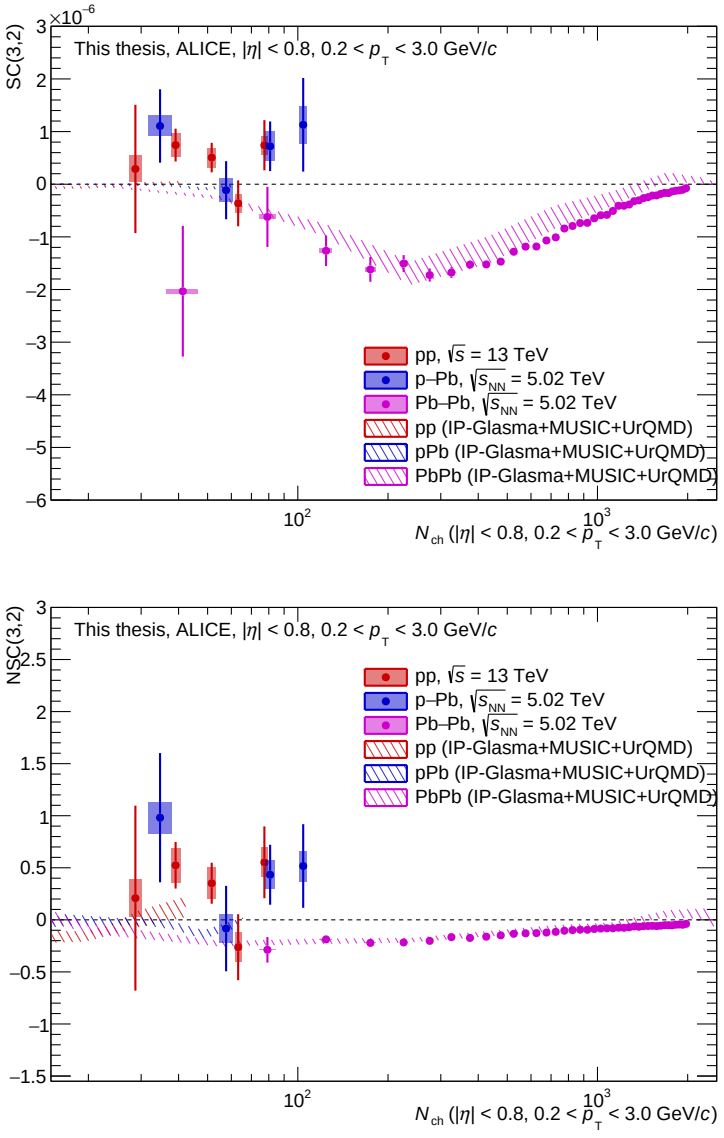

FIGURE 6.23: Symmetric cumulants SC(3,2) (top) and normalized symmetric cumulants NSC(3,2) (bottom) in pp, p–Pb and Pb–Pb collisions, compared with the IP-Glasma + MUSIC + UrQMD [49] calculation.

in contrast to the symmetric cumulants. To be consistent with the study in [72], the SC(3,2) with a combination of the three-subevent configuration is used as the numerator and the $v_2\{2, |\Delta\eta| > 1.4\}$, $v_3\{2, |\Delta\eta| > 1.0\}$ are used in the denominator.

In Pb–Pb collisions, the normalized symmetric cumulant NSC(3,2) shows an increase from approximately -0.3 to 0, corresponding to an increase in the number of charged

tracks from about 80 to 2000. Furthermore, the IP-Glasma + MUSIC + UrQMD [49] model provides an accurate description of the NSC(3,2), effectively capturing the covariance between the ε_2^2 and ε_3^2. Consequently, this agreement reduces the possibility of an accidental correlation between theoretical predictions and measurements in SC(3,2), which is affected by both the initial geometric correlation between the second and third orders of eccentricity and the evolution of the hydrodynamic system. In pp and p–Pb collisions, the observed normalized symmetric cumulants NSC(3,2) are notably large when compared to the peak value measured in Pb–Pb collisions. Intuitively, the initial geometric profile arises from a fluctuating color field. If the initial energy or entropy deposition fluctuations are pronounced, the eccentricities could be quite random. Therefore a weak correlation between various orders of eccentricities is anticipated. Thus, the pronounced negative NSC(3,2) could be attributed to the initial geometry without significant event-by-event fluctuations or the presence of an alternative underlying mechanism. Another consideration is that the system may not be driven by flow but by finite particle correlations.

A pronounced positive NSC(3,2) indicates a strong correlation between the system eccentricity ε_2^2 and ε_3^2.

6.4.2 SC(4,2)

The symmetric cumulants SC(4,2) are measured in both large and small collision systems, as shown in figure 6.24, 6.25 and 6.26. In Pb–Pb collisions, within the range of $N_{\mathrm{ch}} \gtrsim 100$, the value initially rises before declining with the increasing multiplicity. Notably, with the standard method, the first data point in the peripheral Pb–Pb measurement stands out significantly compared to subsequent points. As the $|\Delta\eta|$ separation increases, the SC(4,2) lowers, suggesting that the large value of this point at the lowest multiplicity with the standard method is because of short-range correlation contamination. With all the methods, except for the first point at the lowest multiplicity, the SC(4,2) first increases with increasing multiplicity and then goes down, approaching zero at N_{ch} around 2000. With the enlargement of the $|\Delta\eta|$ separation, the SC(4,2) gets smaller for the presented multiplicity range. The SC(4,2) with all three subevent methods is smaller than the measurements with standard methods. The differences between the measurements with different three-subevent choices are evident. This suggests that the short-range correlation is non-negligible with using the three-subevent methods. In p–Pb collisions, SC(4,2) displays a decreasing trend with the standard methods as shown in figure 6.25. With the increasing of $|\Delta\eta|$, the observable seems to decrease, the same as the pattern that will be shown in pp collisions, while the uncertainties are large. No significant deviation from the three subevent methods could be observed. Similarly as in p–Pb collisions, the measurements with the standard analysis method show a declining trend in pp collisions,

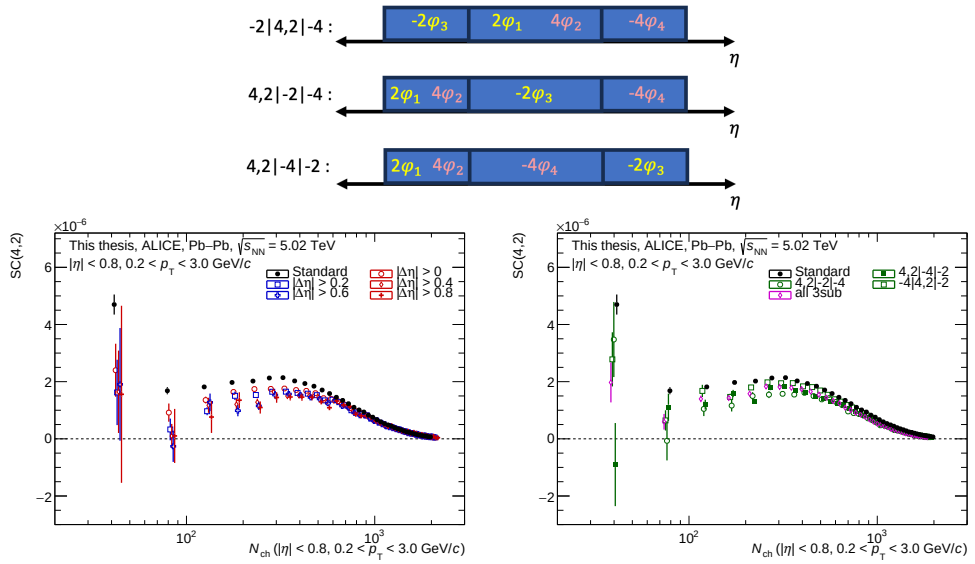

FIGURE 6.24: Measurements of SC(4,2) as a function of multiplicity in Pb–Pb collisions. The measurements with standard methods and different $|\Delta\eta|$ separation methods are presented in the left plot. The measurements with standard methods and different three-subevent configurations are presented in the right plot.

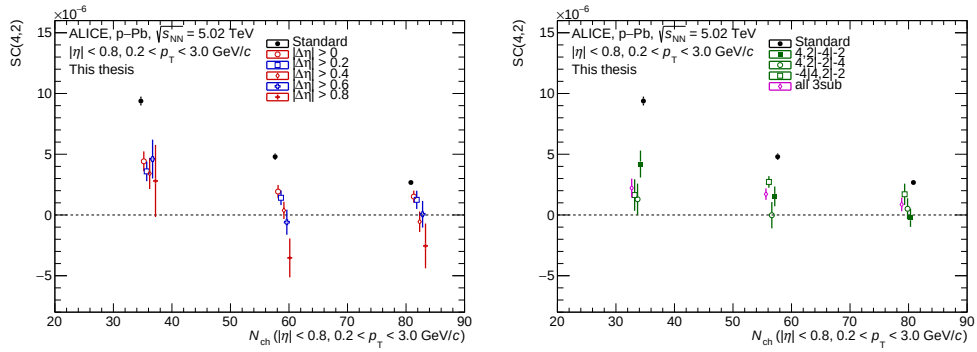

FIGURE 6.25: Measurements of SC(4,2) as a function of multiplicity in p–Pb collisions. The measurements with standard methods and different $|\Delta\eta|$ separation methods are presented in the left plots. The measurements with standard methods and different three-subevent configurations are presented in the right plots.

which becomes less evident with an increasing $|\Delta\eta|$ separation as shown in figure 6.26. The magnitude of the SC(4,2) in pp collisions is much larger than that in p–Pb collisions. Additionally, with the increase of $|\Delta\eta|$, the SC(4,2) decreases monotonously. For all configurations, SC(4,2) is either positive or consistent with zero. The measurements with

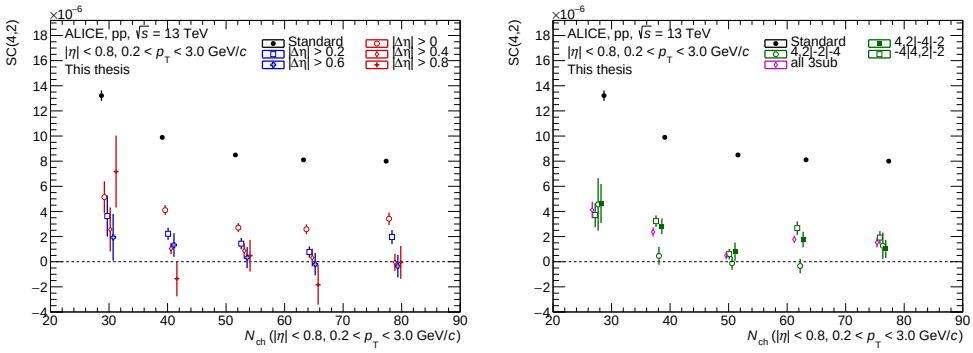

FIGURE 6.26: Measurements of SC(4,2) as a function of multiplicity in pp collisions. The measurements with standard methods and different $|\Delta\eta|$ separation methods are presented in the left plots. The measurements with standard methods and different three-subevent configurations are presented in the right plots.

different three subevent configurations in pp collisions exhibit significant discrepancies. The $4,2|-4|-2$ and $-4|4,2|-2$ configurations notably deviate substantially from zero, whereas the $4,2|-2|-4$ configuration aligns closely with zero. Similar to the SC(3,2), the measurements of SC(4,2) with $4,2|-2|-4$ contain a long-range correlation associated with fourth-order harmonics and a short-range correlation associated with second-order harmonics. This configuration is considered to suffer the least short-range correlation among the three different three subevent methods.

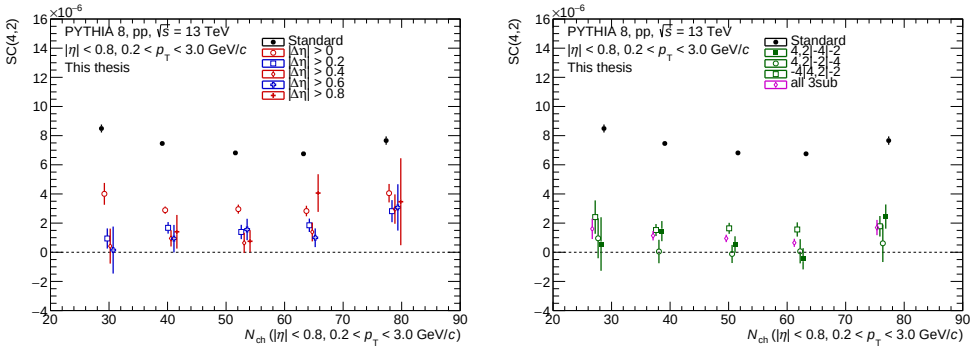

FIGURE 6.27: Calculations of SC(4,2) as a function of multiplicity in pp collisions with PYTHIA 8 [52]. The calculations are with standard methods, different $|\Delta\eta|$ separation methods, and different three-subevent configurations.

The symmetric cumulant SC(4,2) in pp collisions is calculated with the PYTHIA 8 [52] model. Unlike the data, where SC(4,2) measurements exhibit a decreasing trend with the standard method, PYTHIA 8 results indicate a relatively flat trend with increasing

multiplicity. Moreover, enlarging the $|\Delta\eta|$ leads to smaller SC(4,2) values, which could be monitored through the data points with the lowest $N_{\rm ch}$, where the uncertainty is relatively small. No clear difference between the results of three different three-subevent methods can be seen with current uncertainty.

The measurements of symmetric cumulants SC(4,2) are compared with the hydrodynamics model IP-Glasma + MUSIC + UrQMD [49] calculations, as illustrated in figure 6.28 in pp, p–Pb and Pb–Pb collisions. The measurements presented in the plot use the results with the combined three-subevent methods, the same as what is used in [72]. In a flow-driven system, the SC(4,2) measures the covariance between the v_2^2 and v_4^2. In Pb–Pb collisions, the SC(4,2) is close to zero at central collisions where the multiplicity is large ($N_{\rm ch} \sim 2000$), rising at mid-centrality ($N_{\rm ch} \sim 300$) and going down at the peripheral region ($N_{\rm ch} \lesssim 300$). The exception is that at very low multiplicity, the data point shows large SC(4,2), but with very large statistical uncertainty. In Pb–Pb collisions, the theoretical calculation with IP-Glasma + MUSIC + UrQMD agrees well with the data curve. The measurements in pp and p–Pb collision are positive and decrease with the increasing $N_{\rm ch}$. On the contrary, in the case of pp and p–Pb collisions, the IP-Glasma + MUSIC + UrQMD calculation shows symmetric cumulants nearing zero, indicating a small covariance between v_2^2 and v_4^2. The smaller values of symmetric cumulants may arise from the small variance of v_2^2 or v_4^2. To understand the underlying physics behind it, the investigation of NSC(4,2) is necessary.

The NSC(4,2) is measured in pp, p–Pb, and Pb–Pb collisions, shown in figure 6.28 (bottom). To obtain the NSC(4,2), the SC(4,2) values are further normalized by v_2^2 and v_4^2, using the $|\Delta\eta| > 1.4$ for v_2^2 and $|\Delta\eta| > 1.0$ for v_4^2. In Pb–Pb collisions, the NSC(4,2) values show a gradual increase from approximately $N_{\rm ch} \sim 2000$ to $N_{\rm ch} \sim 100$, in contrast to SC(4,2), which reaches its peak at around $N_{\rm ch} \sim 300$. The NSC(4,2) measures the correlation between the v_4^2 and v_2^2, where the v_4^2 has a contribution from a linear and a nonlinear part. If the linear contribution dominates, the NSC(4,2) has a major contribution from the correlation between ε_2^2 and ε_4^2[1]. While if the nonlinear flow dominates, or if the v_4^L is independent to the v_2, the NSC(4,2) is approximately $\rho_{4,22}^2(\langle v_2^6\rangle/(\langle v_2^4\rangle\langle v_2^2\rangle)-1)$ [147]. The $\rho_{4,22}$ characterize the event-plane correlation, whose measurements will be presented and discussed in the later sections. And the $\langle v_2^6\rangle/(\langle v_2^4\rangle\langle v_2^2\rangle) - 1 = {\rm cov}(v_2^4, v_2^2)/(\langle v_2^4\rangle\langle v_2^2\rangle)$, which is always positive by definition. The IP-Glasma + MUSIC + UrQMD [49] well described the NSC(4,2) in Pb–Pb collisions at a multiplicity of $N_{\rm ch} \gtrsim 100$ and above. In pp and p–Pb collisions, NSC(4,2) in both pp and p–Pb collisions are larger than zero but with large uncertainties. As just discussed in Pb–Pb collisions, the large positive NSC(4,2) could be explained by a contribution from the nonlinear flow. The IP-Glasma + MUSIC + UrQMD underestimates the measurements, indicating an underestimate from nonlinear

[1] Exactly speaking, it should use cumulant-defined anisotropy coefficient ε' [178] rather than ε

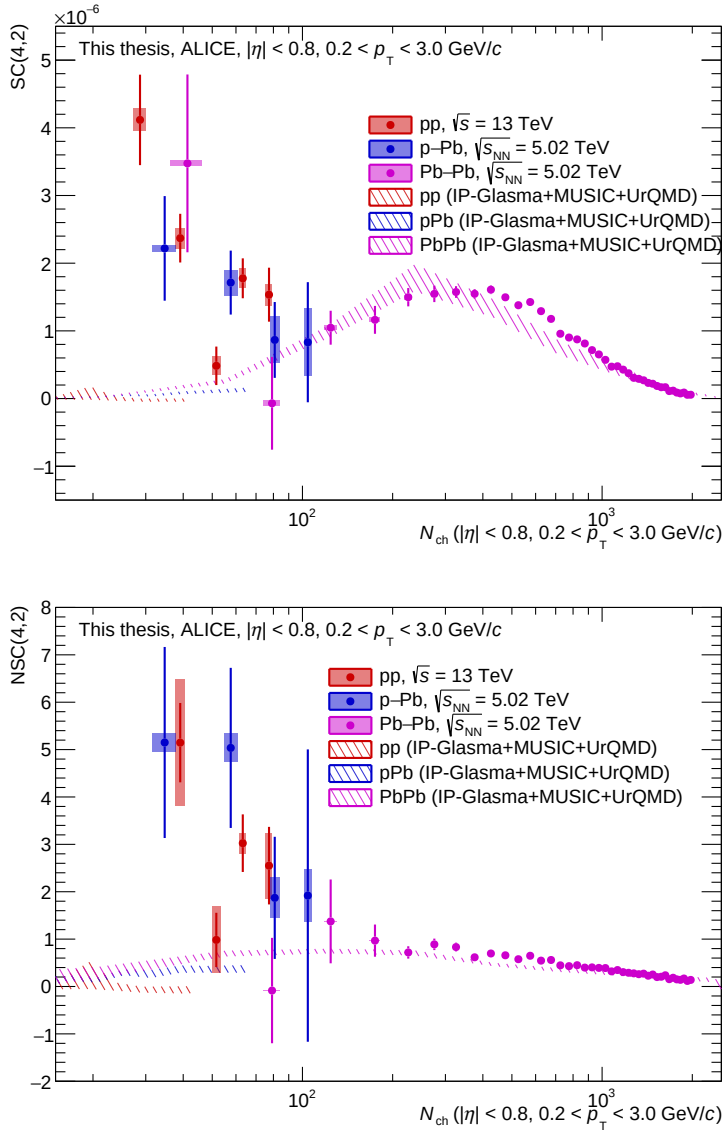

FIGURE 6.28: Measurements of symmetric cumulants SC(4,2) (top) and normalized symmetric cumulants NSC(4,2) (bottom) as a function of multiplicity in pp, p–Pb and Pb–Pb collisions, compared with the IP-Glasma + MUSIC + UrQMD [49] calculation.

flow, which will be further verified through the nonlinear flow measurements in the later section.

6.5 Non-linear flow response

6.5.1 $v_{4,22}$

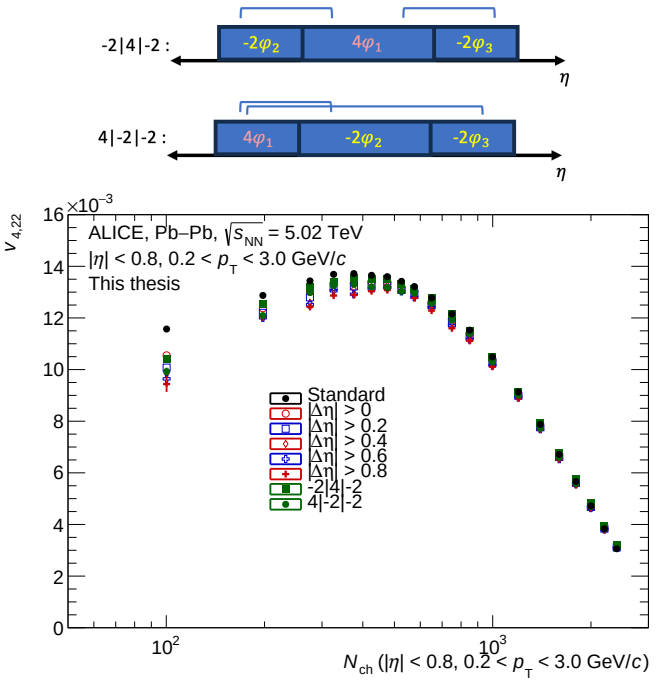

FIGURE 6.29: Measurements of $v_{4,22}$ as a function of multiplicity in Pb–Pb collisions. The standard method, $|\Delta\eta|$ separation methods, and three-subevent methods are used.

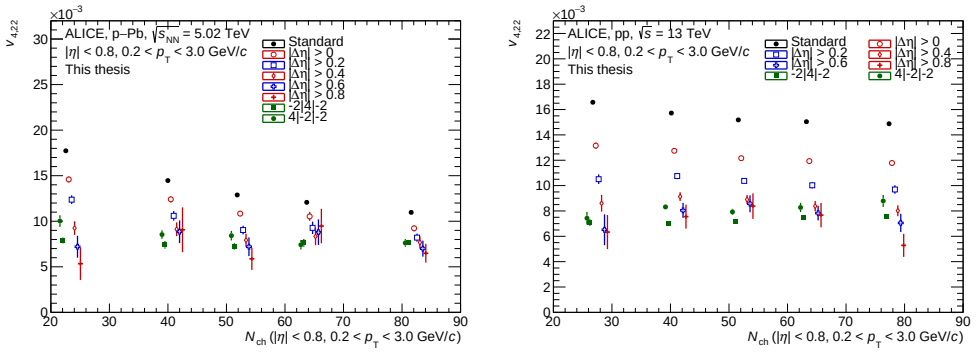

FIGURE 6.30: Measurements of $v_{4,22}$ as a function of multiplicity in p–Pb (left) and pp (right) collisions. The standard method, $|\Delta\eta|$ separation methods, and three-subevent methods are used. The x-axis is shifted for visibility.

The non-linear flow coefficients $v_{4,22}$ is measured as a function of multiplicity in Pb–Pb, p–Pb and pp collisions, as shown in figure 6.29 and figure 6.30. In Pb–Pb collisions, this observable initially increases with the increasing multiplicity before decreasing. Results obtained through different $|\Delta\eta|$ separation methods are well consistent, suggesting that the observable is not very sensitive to non-flow contamination for the region dominated by flow. In p–Pb collisions, the $v_{4,22}$ with the standard method is the largest and decreases with increasing multiplicity. With the increasing $|\Delta\eta|$ separation, the $v_{4,22}$ becomes smaller, and the results show a weak to no dependence on $N_{\rm ch}$. In pp collisions, the value of $v_{4,22}$ is notably large with the standard method. However, as the $|\Delta\eta|$ separation increases, $v_{4,22}$ decreases. Till a $|\Delta\eta| > 1.0$, this decreasing trend does not saturate. The measurements with $|\Delta\eta| > 1.0$ are consistent with the results with various three-subevent methods within the statistical uncertainty, though a systematic difference between the measurements of the two different three-subevent configurations is observed.

The behavior of the $v_{4,22}$ with increasing of $|\Delta\eta|$ can more or less be mimicked by the non-flow model, as displayed in figure 6.31, which is unexpected. Non-flow effects cannot account for this behavior, as PYTHIA 8 [52] calculation fails to accurately describe $\langle\langle\cos(4\varphi_1 - 2\varphi_2 - 2\varphi_3)\rangle\rangle$ or $\langle\langle\cos(2\varphi_1 + 2\varphi_2 - 2\varphi_3 - 2\varphi_4)\rangle\rangle$, suggesting that the agreement between $v_{4,22} = \langle\langle\cos(4\varphi_1 - 2\varphi_2 - 2\varphi_3)\rangle\rangle / \sqrt{\langle\langle\cos(2\varphi_1 + 2\varphi_2 - 2\varphi_3 - 2\varphi_4)\rangle\rangle}$ in measurements and calculation could be coincidental.

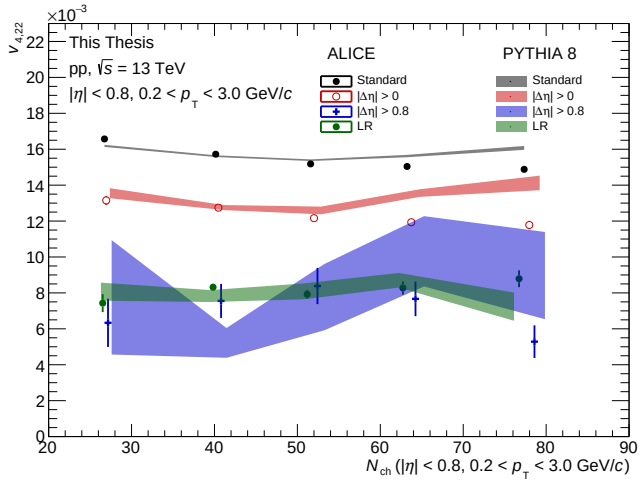

FIGURE 6.31: Calculation of $v_{4,22}$ as a function of multiplicity in pp collisions with the PYTHIA 8 [52] calculation, compared with the measurements.

The non-linear flow coefficients $v_{4,22}$ are compared with the calculation from the hydrodynamics model, IP-Glasma + MUSIC + UrQMD [49], shown in figure 6.32. The

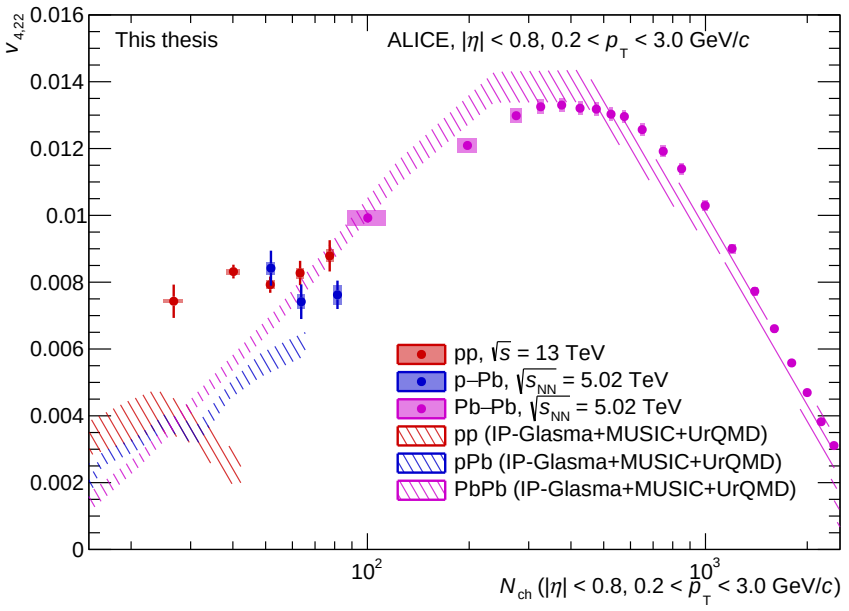

FIGURE 6.32: Measurements of $v_{4,22}$ as a function of multiplicity in pp, p–Pb and Pb–Pb collisions. The measurements are compared with the IP-Glasma + MUSIC + UrQMD [49] calculation.

coefficient $v_{4,22}$ quantifies the fourth-order flow, originating from the initial eccentricity ϵ_2^2. A pattern where it initially increases and then decreases as the multiplicity $N_{\rm ch}$ increases is observed. This behavior is connected to the multiplicity dependence of both v_2^2 and $\chi_{4,22}$, with the latter primarily influenced by the initial stages of the system. The hydrodynamics could qualitatively describe the measurements in Pb–Pb collisions. Whether it can provide a good description for the $\chi_{4,22}$ will be discussed later. In pp and p–Pb collision systems, the non-linear flow coefficient $v_{4,22}$ does not show an obvious multiplicity dependence. The magnitudes of $v_{4,22}$ in pp and p–Pb collisions are similar to that observed in Pb–Pb collisions for a similar multiplicity region. This measurements indicate a similar system evolution across collision systems because the similar magnitudes of $v_2\{2\}$ are already observed in pp, p–Pb and low multiplicity Pb–Pb collisions. The IP-Glasma + MUSIC + UrQMD model tends to underestimate the measurement of $v_{4,22}$ in pp collisions. In p–Pb collisions, the model exhibits an increasing trend, which is not seen in the measurements. Notably, at the highest multiplicity with $N_{\rm ch} \sim 65$, the model calculations are slightly lower than the measurements. Furthermore, in pp collisions, based on the earlier finding that the IP-Glasma + MUSIC + UrQMD model overestimates $v_4\{2\}$ shown in figure 6.17, it suggests that the linear components of v_4 are not accurately reproduced with IP-Glasma + MUSIC + UrQMD. This implies that the

initial conditions of the model require additional refinement.

6.5.2 $\rho_{4,22}$

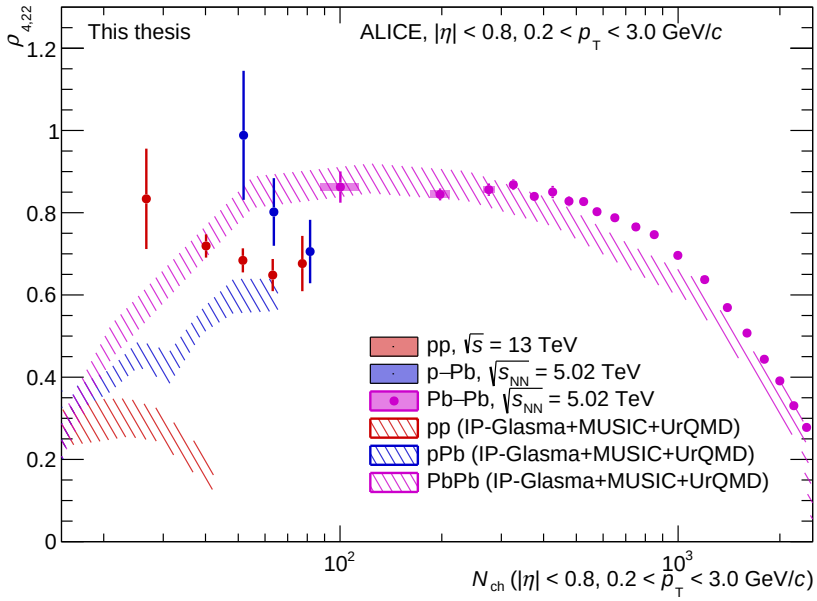

FIGURE 6.33: Measurements of $\rho_{4,22}$ as a function of cmultiplicity in pp, p–Pb and Pb–Pb collisions. The measurements are compared with the IP-Glasma + MUSIC + UrQMD [49] calculation.

The $\rho_{4,22}$ measurements have been performed in pp, p–Pb, and Pb–Pb collisions and are compared with the hydrodynamical model IP-Glasma + MUSIC + UrQMD [49] calculations, as shown in figure 6.33. A three-subevent configuration of 4|-2|-2 for $v_{4,22}$ and two-subevent $|\Delta\eta| > 1.0$ for $v_4\{2\}$ is chosen to compute $\rho_{4,22}$, attributing to a compromise between statistical precision and contamination on short-range correlation effects. The $\rho_{4,22} \approx \langle\cos(4(\Psi_4 - \Psi_2))\rangle$ represents a correlation between the flow symmetry planes in a flow-driven system. It is expected that the value will be large when the difference between Ψ_2 and Ψ_4 is small and has small fluctuation on an event-by-event basis. In Pb–Pb collisions, $\rho_{4,22}$ keeps approximately constant from $N_{\rm ch} \sim 100$ to $N_{\rm ch} \sim 300$, after which it begins to decline. By an $N_{\rm ch} \sim 2000$, $\rho_{4,22}$ decreases to approximately 0.3. The observed trend suggests that in central collisions, the system becomes isotropic, leading to a more random orientation of Ψ_2 and Ψ_4. Consequently, the correlations between the Ψ_2 and Ψ_4 tend to diminish. At the multiplicity region of $N_{\rm ch} > 100$ in Pb–Pb collisions, the calculation agrees with the measurements fairly well. In p–Pb collisions, the three data

points are of similar magnitude compared with low multiplicity Pb–Pb collisions within the uncertainty. In pp collisions, the $\rho_{4,22}$ show a decreasing trend with the increasing multiplicity. At the lowest multiplicity bin, the $\rho_{4,22}$ hold a similar magnitude as in the Pb–Pb collisions, while at high multiplicity region in pp collisions, the magnitude is evidently smaller than the platform in low multiplicity Pb–Pb collisions. From an initutive view point, if the expansion of the system is influenced by various sources, the orientation of the flow vector may become more random, suggesting a weaker correlation between Ψ_2 and Ψ_4. Conversely, a strong correlation between Ψ_2 and Ψ_4 implies that the system's expansion is likely dominated by a single source. It is also worth noticing that the IP-Glasma + MUSIC + UrQMD underestimates the $\rho_{4,22}$ in pp collisions, which is agree with that the IP-Glasma + MUSIC + UrQMD also underestimates NSC(4,2).

6.5.3 $\chi_{4,22}$

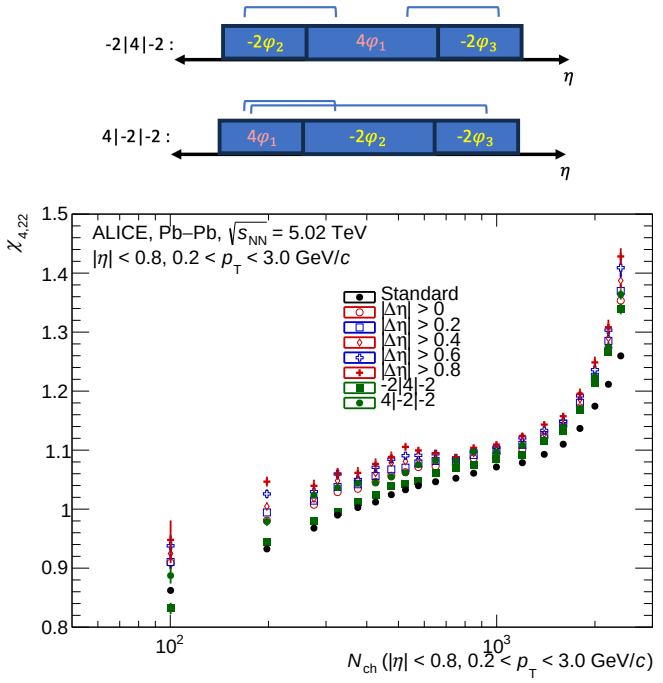

FIGURE 6.34: Measurements of $\chi_{4,22}$ as a function of multiplicity in Pb–Pb collisions. The standard method, $|\Delta\eta|$ separation methods, and three-subevent methods are used.

The multiplicity dependence of the $\chi_{4,22}$, measured with different non-flow suppression methods in pp, p–Pb and Pb–Pb collisions, are presented in figure 6.34 and figure 6.35. In Pb–Pb collisions, the $\chi_{4,22}$ with standard methods gradually rises from around 0.85 to

around 1.25 at the largest multiplicity region ($N_{\mathrm{ch}} \sim 2000$). The results from different $|\Delta\eta|$ separation methods are not compatible with each other. With the increase of the $|\Delta\eta|$, the $\chi_{4,22}$ becomes larger. The measurements with the two different three-subevent configurations show clear deviations. Additionally, they deviate clearly from the standard method that does not apply any suppression of short-range correlations.

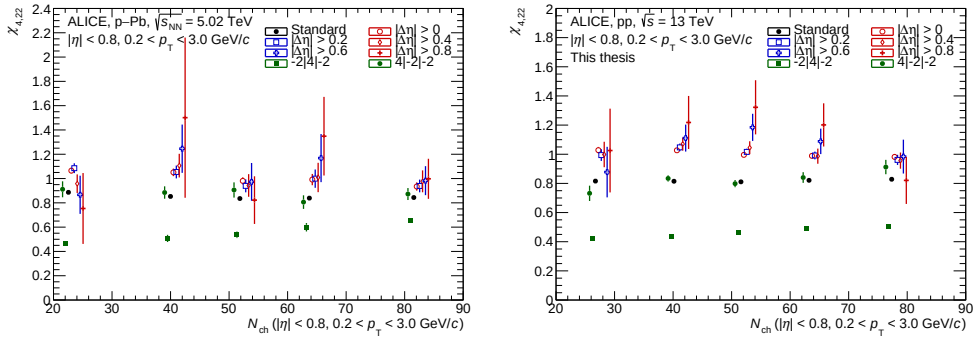

FIGURE 6.35: Measurements of $\chi_{4,22}$ as a function of multiplicity in p–Pb (left) and pp (right) collisions. The standard method, $|\Delta\eta|$ separation methods, and three-subevent methods are used.

In p–Pb and pp collisions, with the increasing of the $|\Delta\eta|$ separation, the $\chi_{4,22}$ generally becomes larger. When applying the three-subevent methods with the $2,2|-2|-2$ that is regarded to have one short-range correlation and one long-range correlation with an ability to suppress the non-flow, the $\chi_{4,22}$ is compatible with the standard method. With another three-subevent configuration $(-2|2,2|-2)$, which is regarded as suffering dramatically from the short-range correlation contamination, the $\chi_{4,22}$ is measured to be small compared with the standard configuration. The results show that $\chi_{4,22}$ is very sensitive to the choice of $|\Delta\eta|$ separation, which reflects its sensitivity to the short-range correlation effects.

The variation of $\chi_{4,22}$ observed with different three-subevent methods is also seen in the calculation from PYTHIA 8 [52]. The three-subevent method with the configuration 2|2|-2,-2, is once again consistent with the results with the standard method. A larger pseudorapidity separation results in an increased $\chi_{4,22}$. However, the measurements employing any pseudorapidity gap method do not agree with the calculations from any of the three-subevent methods. This study suggests that the three-subevent methods incorporate significant short-range correlations in the $\chi_{4,22}$ measurements. Therefore, utilizing the widest possible $|\Delta\eta|$ separation is essential.

The $\chi_{4,22}$ in pp, p–Pb and Pb–Pb collisions with the largest possible $|\Delta\eta|$ separation is presented in figure 6.37. It is noted that, in Pb–Pb collisions, $\chi_{4,22}$ modestly decreases from highest multiplicity to $N_{\mathrm{ch}} \sim 1000$ and then remains almost constant from $N_{\mathrm{ch}} \sim$

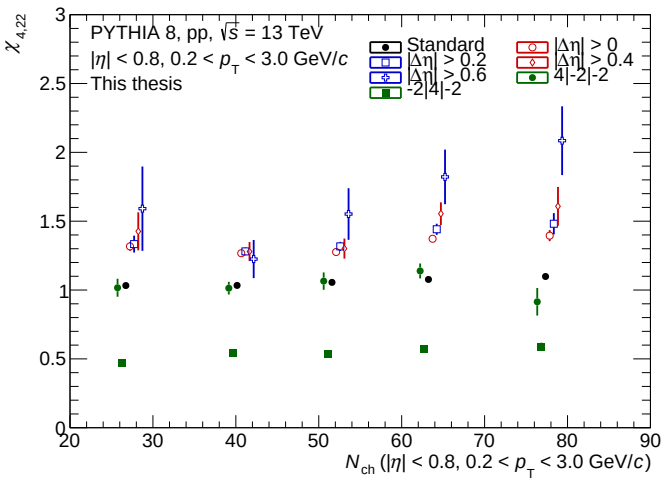

FIGURE 6.36: Calculation of $\chi_{4,22}$ as a function of multiplicity in pp collisions with PYTHIA 8 [52], with standard methods, different $|\Delta\eta|$ separation method, and different three-sub event configurations.

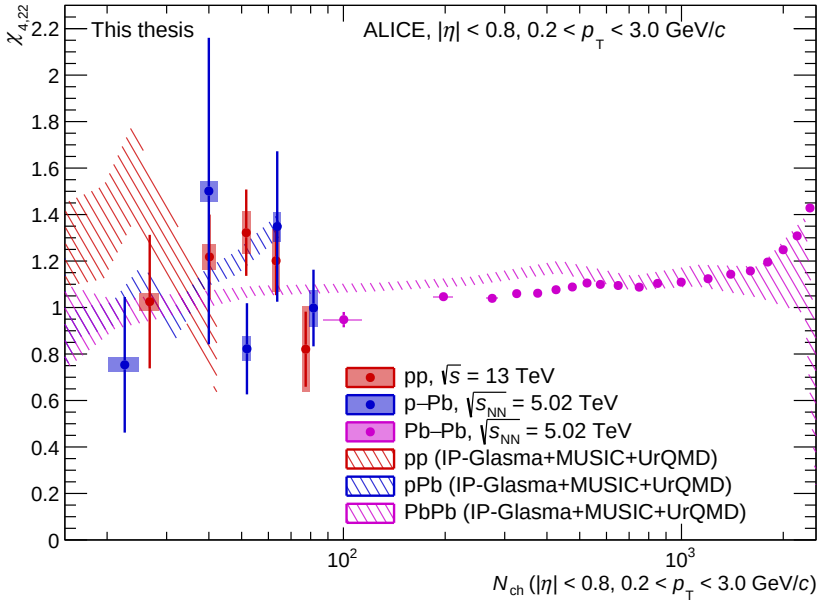

FIGURE 6.37: Measurements of $\chi_{4,22}$ measured as a function of multiplicity in pp, p–Pb and Pb–Pb collisions. The measurements are compared with the IP-Glasma + MUSIC + UrQMD [49] calculation.

1000 to the region of $N_{\rm ch} \sim 100$. Consequently, the trend of $v_{4,22}$ (in figure 6.32),

which is an initial increase followed by a decrease with increasing multiplicity, is primarily attributed to the rise of v_2 from low multiplicity to high multiplicity rather than a variation in the non-linear mode coefficient. In pp and p–Pb collisions, no obvious multiplicity dependency could be confirmed. They are consistent with the $\chi_{4,22}$ in $N_{\rm ch} \lesssim 1000$ of Pb–Pb collisions with a large uncertainty. The measurements are compared with the IP-Glasma + MUSIC + UrQMD [49] calculations. In Pb–Pb collisions, both the $\chi_{4,22}$ and the $v_{4,22}$ can be well reproduced with the IP-Glasma + MUSIC + UrQMD, suggesting that the model is good at modeling both the initial condition together with the system evolution in Pb–Pb collisions. In addition, the calculation from IP-Glasma + MUSIC + UrQMD also agrees with the measurements in pp and p–Pb collisions. However, the relatively small discrepancy between the data and experimental results does not necessarily suggest the excellence of the initial condition modeling, as changes to the initial conditions only lead to minor variations in $\chi_{4,22}$ [94].

6.6 Flow-transverse momentum correlations

6.6.1 $\mathrm{cov}(v_2^2, [p_{\rm T}])$

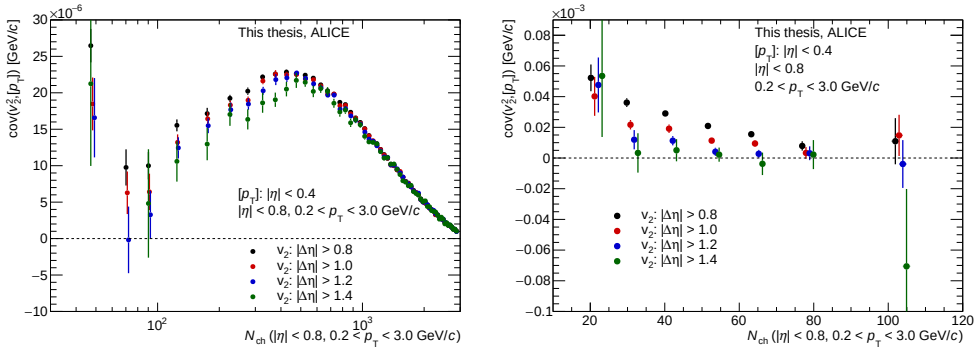

FIGURE 6.38: Measurements of $\mathrm{cov}(v_2^2, [p_{\rm T}])$ as a function of multiplicity in Pb–Pb (left) and pp (right) collisions. The measurements are with different $|\Delta\eta|$ separation to obtain the v_2^2.

The covariance between v_2^2 and $[p_{\rm T}]$, denoted as $\mathrm{cov}(v_2^2, [p_{\rm T}])$, has been measured in Pb–Pb collisions and pp collisions with different $|\Delta\eta|$ separations, as shown in figure 6.38. The measurement are with a fixed region ($|\eta| < 0.4$) to measure $[p_{\rm T}]$, and a varying region ($|\Delta\eta| > 0.8, 1.0, 1.2, 1.4$) to measure the v_2^2. In Pb–Pb collisions, for $N_{\rm ch} \lesssim 500$, the $\mathrm{cov}(v_2^2, [p_{\rm T}])$ is found to decrease monotonously with the increasing $|\Delta\eta|$. While at a higher multiplicity region, the $\mathrm{cov}(v_2^2, [p_{\rm T}])$ is not sensitive to the $|\Delta\eta|$. With all the $|\Delta\eta|$ separations, the $\mathrm{cov}(v_2^2, [p_{\rm T}])$ show a consistent trend: it initially decreases, then increases,

and ultimately decreases again as the multiplicity increases in Pb–Pb collisions. In pp collisions, the $\mathrm{cov}(v_2^2, [p_\mathrm{T}])$ has been measured with the same $|\Delta\eta|$ seperation methods as the what has been done in Pb–Pb collisions. The covariance $\mathrm{cov}(v_2^2, [p_\mathrm{T}])$ decreases monotonously with the increasing the $|\Delta\eta|$. With the $|\Delta\eta| > 0.8$, $|\Delta\eta| > 1.0$ or $|\Delta\eta| > 1.2$, the measurements show a decreasing trend with the increasing N_ch. While with the $|\Delta\eta| > 1.4$, given the small value of the convariance and the large uncertainty, it is not possible to draw a definitive conclusion regarding the multiplicity dependency. With the increasing $|\Delta\eta|$, the contribution from the short-range correlation decreases. The covariance could become smaller with the suppression of the short-range correlation effects. The examination of how the covariance changes with variations in $|\Delta\eta|$ separation in p–Pb collisions has not been conducted due to insufficient data.

Despite the presence of non-negligible short-range correlations, measurements with $|\Delta\eta| > 0.8$ are used in model comparisons and subsequent calculations of $\rho(v_2^2, [p_\mathrm{T}])$. This is due to the fact that measurements with $|\Delta\eta| > 0.8$ has the least statistical uncertainty. Furthermore, it will be demonstrated later that $\rho(v_2^2, [p_\mathrm{T}])$ is not significantly affected by the short-range correlations. The comparisons of $\mathrm{cov}(v_2^2, [p_\mathrm{T}])$ in pp, p–Pb, and Pb–Pb collisions are shown in figure 6.39. The results in figure 6.39 are all obtained with $|\Delta\eta| > 0.8$ for calculating v_2^2 and $|\eta| < 0.4$ for calculating $[p_\mathrm{T}]$. In pp collisions, $\mathrm{cov}(v_2^2, [p_\mathrm{T}])$ decreases monotonically with an increasing number of charged tracks, but the results remain positive even at the highest multiplicity. This monotonically decreasing trend with increasing N_ch is also observed in p–Pb collisions. However, in p–Pb collisions, $\mathrm{cov}(v_2^2, [p_\mathrm{T}])$ is measured to be negative at the highest multiplicity ($N_\mathrm{ch} \sim 130$), although the possibility of it being non-negative cannot be excluded due to large uncertainties. In Pb–Pb collisions, $\mathrm{cov}(v_2^2, [p_\mathrm{T}])$ initially decreases and then increases with the increasing multiplicity. At low multiplicities ($N_\mathrm{ch} \lesssim 70$), the data points for pp, p–Pb, and Pb–Pb collision systems overlap with each other. Starting with a number of charged tracks approximately $N_{ch} \sim 70$, the observed covariance in small and large collision systems appears to diverge. This may be due to the fact that in small collision systems, the initial geometry consistently originates from fluctuations, irrespective of multiplicity. In contrast, in Pb–Pb collisions within regions of high multiplicity, the initial geometry is shaped by the overlapping geometry of the wounded nucleons.

The measurements are compared with the theoretical model calculation from PYTHIA 8 [52, 179], AMPT [61, 179] and hydrodynamics model IP-Glasma + MUSIC + UrQMD [49, 180], as shown in figure 6.39 (right) and figure 6.40. As shown in figure 6.39 (right), in Pb–Pb collisions, the AMPT calculation shows a same positive sign as the measurements. The trend seen in the AMPT calculation initially shows a decrease, followed by an increase, with the increasing N_ch. This pattern is same as the trend observed in the data. However, the magnitude of the $\mathrm{cov}(v_2^2, [p_\mathrm{T}])$ is overestimated by the AMPT calculation.

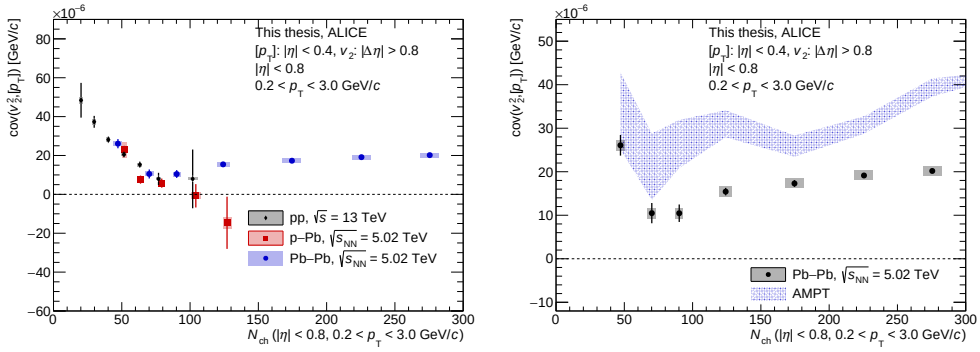

FIGURE 6.39: Left: Measurements of $\mathrm{cov}(v_2^2, [p_T])$ as a function of multiplicity in pp, p–Pb and Pb–Pb collisions. Right: Measurements of $\mathrm{cov}(v_2^2, [p_T])$ in Pb–Pb collisions, compared with AMPT [61, 179] calculation.

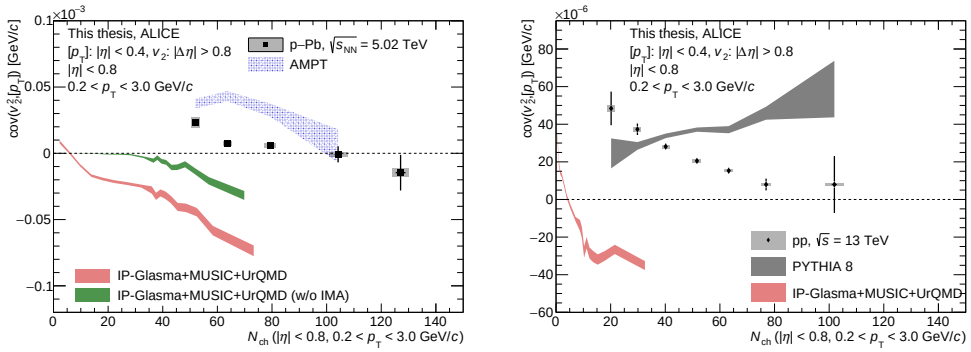

FIGURE 6.40: Measurements of $\mathrm{cov}(v_2^2, [p_T])$ as a function of multiplicity in p–Pb (left), pp (right) collisions, compared with PYTHIA 8 [52, 179], AMPT [61, 179] and IP-Glasma + MUSIC + UrQMD [49, 180] calculations.

The deviation between the measurements and calculation could attribute to multiple reason, including the insufficient modeling of initial geometry or transport processes. In p–Pb collisions, the measurements are compared with the AMPT model calculation as well as the IP-Glasma + MUSIC + UrQMD calculation, as shown in figure 6.40 (left). A decreasing trend with increasing multiplicity is obtained from the AMPT model calculation. However, similar as the the calculation in Pb–Pb collisions, the AMPT calculation in p–Pb collision also overestimate the measurements. Calculations using the IP-Glasma + MUSIC + UrQMD model, neither with or without the initial momentum anisotropy contributed from the CGC, can accurately describe the measurements, failing to even capture the correct sign of $\mathrm{cov}(v_2^2, [p_T])$ in p–Pb collisions. As shown in figure 6.40 (right), in pp collisions, the measurements are compared with the PYTHIA 8 and the IP-Glasma +

MUSIC + UrQMD calculations. The calculation from the PYTHIA 8 shows an increasing trend with the increasing N_{ch}, which is contradictory to the measurements, where the $\mathrm{cov}(v_2^2, p_{\mathrm{T}})$ decreases with the increasing multiplicity. This disagreements suggest the explanation of the measurements with only a non-flow mechanism is not enough. Additionally, the measurements are compared with the IP-Glasma + MUSIC + UrQMD calculations in pp collisions, incorporating the initial momentum anisotropy arising from the CGC effects. This model fails to even capture the correct sign of $\mathrm{cov}(v_2^2, p_{\mathrm{T}})$ in pp collisions. The difficulty in describing the measurements could stem from either an incorrect relative contribution of the CGC and hydrodynamic components, or a lack of consideration for non-flow short-range contributions. It is also possible that this deviation between calculations and measurements comes from an inadequate modeling of the initial geometry. To properly understand the reasons behind the poor modeling of these measurements, a flow + jets hybrid model will be beneficial.

6.6.2 c_k

The dynamic fluctuation of $[p_{\mathrm{T}}]$ measured in pp, p–Pb, and Pb–Pb collisions, with respect to multiplicity within $|\eta| < 0.4$, is illustrated in the figure 6.41 (left). The observable c_k is one of the components used in the calculation of $\rho(v_n^2, [p_{\mathrm{T}}])$, and it characterizes the fluctuation in system size [181]. Across all three collision systems, the c_k exhibit a decreasing trend with the increasing of number of charged tracks. Notably, an ordering of $c_k(\mathrm{pp}) > c_k(\mathrm{p–Pb}) > c_k(\mathrm{Pb–Pb})$ is seen, similar as the observation in [182]. This ranking differs from most flow observables, which usually exhibit a smooth transition across different collision systems. This indicates the initial size fluctuations are different among the three collision systems under the same multiplicity.

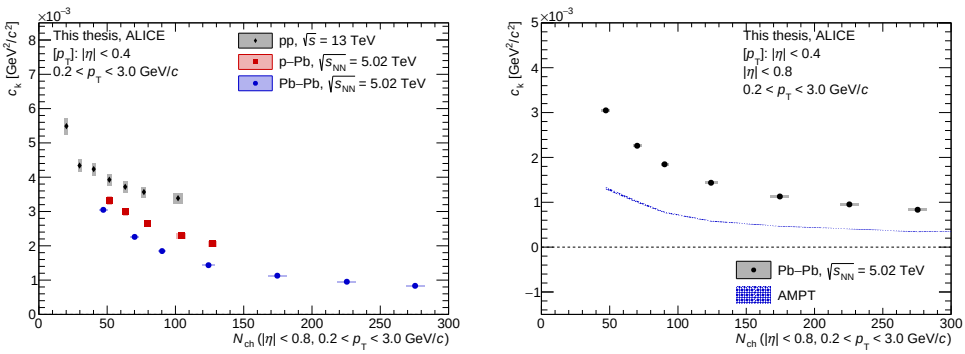

FIGURE 6.41: Left: Measurements of c_k as a function of multiplicity in pp, p–Pb and Pb–Pb collisions. Right: Measurements of c_k as a function of multiplicity in Pb–Pb collisions, compared with the AMPT [61, 179] calculation.

In Pb–Pb collisions, the c_k measurements are compared with the calculation from the AMPT [61, 179] model, as shown in the right plot of figure 6.41. Despite that similar decreasing trends are observed in both the measurements and the AMPT model calculations, the AMPT results significantly underestimates the measurements. In figure 6.42, the measurements are compared with various models calculatinos in small collision systems. The left panel shows the comparison in p–Pb collisions, and the right panel shows the comparison in pp collisions. In p–Pb collisions, the AMPT prediction exhibits a decreasing trend, but it appears much flatter compared to the measurement, which shows a steeper decline. Additionally, the AMPT model underestimates the measurements, similar to its prediction in Pb–Pb collisions. Furthermore, comparisons are made between the measurements and a hydrodynamical model calculations. Notably, the c_k calculations obtained with and without initial momentum anisotropy differ significantly. However, neither of the model with initial momentum anisotropy nor without it accurately describes the measurements. In pp collisions, PYTHIA 8 [52, 179] calculation exhibits a similar decreasing trend as the measurements, except for the first data point at the lowest N_{ch}, where it overestimates the measurement. On the other hand, the IP-Glasma + MUSIC + UrQMD [49, 180] model predicts an increase from $N_{\mathrm{ch}} \sim 0$ to $N_{\mathrm{ch}} \sim 10$. For $N_{\mathrm{ch}} > 10$, with a increase in N_{ch}, the c_k decreases. This model substantially underestimates the measured c_k.

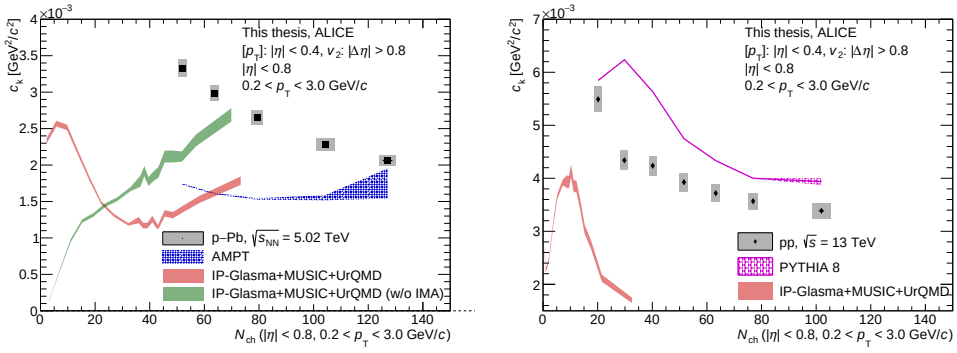

FIGURE 6.42: Measurements of c_k as a function of multiplicity in p–Pb (left) and pp (right) collisions, compared with PYTHIA 8 [52, 179], AMPT [61, 179] and IP-Glasma + MUSIC + UrQMD [49, 180] calculations.

6.6.3 $\sigma(v_2^2)$

The measurements of v_2^2 fluctuations var(v_2^2), with different $|\Delta\eta|$ separations performed in Pb–Pb and pp collisions are shown in figure 6.43. In Pb–Pb collisions, a decreasing of var(v_2^2) with increasing of $|\Delta\eta|$ could be clearly monitored at $N_{ch} \lesssim 500$. In pp collisions,

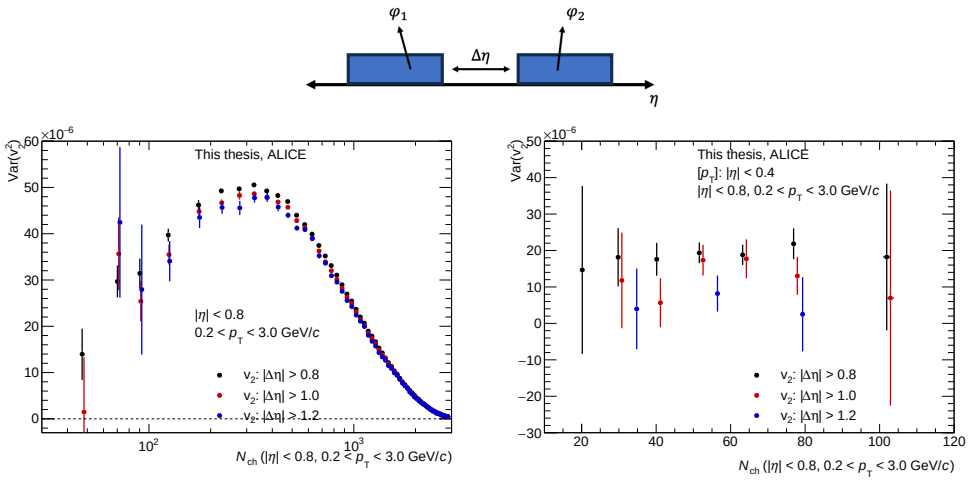

FIGURE 6.43: Measurements of $\mathrm{var}(v_2^2)$ as a function of multiplicity with different $|\Delta\eta|$ in Pb–Pb (left) and pp (right) collisinos.

despite the large uncertainties, a decrease in the measurements can be observed as the $|\Delta\eta|$ increases. The measurements of the $\mathrm{var}(v_2^2)$ with varying $|\Delta\eta|$ in p–Pb collisions has not been conducted due to insufficient data.

For the same reasons as the case of $\mathrm{cov}(v_2^2, [p_\mathrm{T}])$, the measurements with $|\Delta\eta| > 0.8$ are selected for model comparison and the subsequent calculation of $\rho(v_2^2, [p_\mathrm{T}])$. The measurement of $\sigma(v_2^2) = \sqrt{\mathrm{var}(v_2^2)}$ in pp, p–Pb, and Pb–Pb collisions are shown in figure 6.44 (left). In pp collisions, $\sigma(v_2^2)$ does not show a clear dependence on multiplicity. In p–Pb collisions, $\sigma(v_2^2)$ decreases with increasing N_ch, although with sizeable statistical uncertainties. Conversely, in Pb–Pb collisions, $\sigma(v_2^2)$ increases with the number of charged tracks. The fluctuations in v_2^2 across pp, p–Pb, and Pb–Pb collisions are of comparable magnitude within the uncertainty for $N_\mathrm{ch} < 100$. However, an increasing trend in Pb–Pb collisions is observed with the increasing N_ch.

The measurements are compared with the calculations from theoretical models PYTHIA 8 [52, 179] and AMPT [61, 179], along with a hydrodynamics model calculation, in the Pb–Pb collisions as shown in figure 6.44 (right), and in p–Pb and pp collisions in figure 6.45. In Pb–Pb collisions, the AMPT calculation well described the trend, and only slightly overestimates the measurements. In p–Pb collisions, the AMPT calculation is also able to reproduce the measurements, exhibiting a similar flat trend as the data, with only a slight overestimation of the measurements. The $\sigma(v_2^2)$ calculation from the IP-Glasma + MUSIC + UrQMD [49, 180] model is limited to $N_\mathrm{ch} \lesssim 80$. The $\sigma(v_2^2)$ calculation from IP-Glasma + MUSIC + UrQMD model without the initial momentum anisotropy from the CGC starts from zero at very low multiplicity regions. As the number of charged particles increases, $\sigma(v_2^2)$ also increases, as shown in figure 6.45 (left). For the calculations

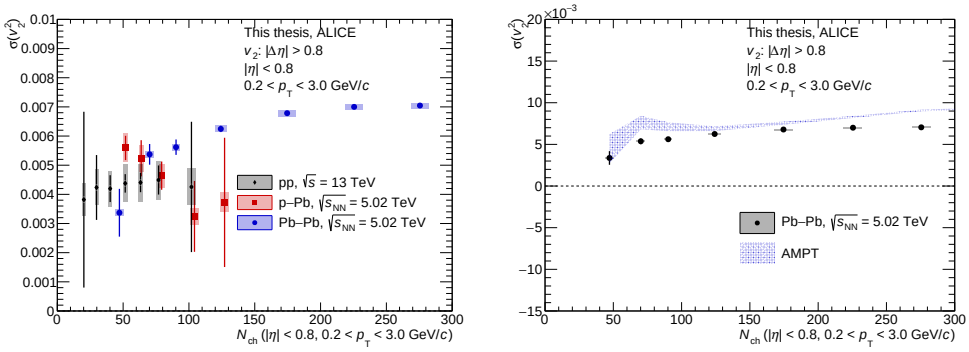

FIGURE 6.44: Left: Measurements of $\sigma(v_2^2)$ as a function of multiplicity in pp, p–Pb and Pb–Pb collisions. Right: Measurements of $\sigma(v_2^2)$ as a function of multiplicity in Pb–Pb collisions compared with AMPT [61, 179] calculation.

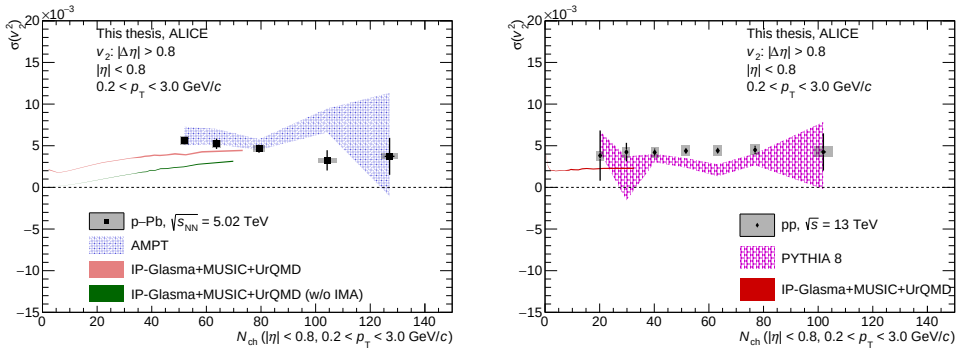

FIGURE 6.45: Measurements of $\sigma(v_2^2)$ as a function of multiplicity in p–Pb (left) and pp (right) collisions, compared with the PYTHIA 8 [52, 179], AMPT [61, 179] and IP-Glasma + MUSIC + UrQMD [49, 180] calculations.

with the initial momentum anisotropy, $\sigma(v_2^2)$ begins at a positive value when $N_{ch} \sim 0$, and gradually increases as a function of multiplicity. At the multiplicity region where the measurements and calculations are both available ($50 \lesssim N_{\rm ch} \lesssim 70$), both the IP-Glasma + MUSIC + UrQMD with and without the initial momentum anisotropy underestimate $\sigma(v_2^2)$. The prediction with the initial momentum anisotropy aligns more closely with the measurement. However, it's worth noting that with an increase in $|\Delta\eta|$, $\sigma(v_2^2)$ is expected to decrease, if the variation in $\sigma(v_2^2)$ with varying $|\Delta\eta|$ is the same in p–Pb as in pp and Pb–Pb collisions. Similar to p–Pb collisions, the hydrodynamic model calculations are not available at high multiplicity regions. Within the region where theory calculations and measurements are available, the model calculation underestimates $\sigma(v_2^2)$. However, as

suggested in figure 6.43, an increase in $|\Delta\eta|$ is expected to result in a smaller $\mathrm{var}(v_2^2)$. Consequently, $\sigma(v_2^2)$ is also expected to decrease. This suggests that the agreement between the measurements and the IP-Glasma + MUSIC + UrQMD prediction might improve with further suppression of short-range correlations. Unfortunately, due to limitations in statistics, obtaining valid results with a larger $|\Delta\eta|$ separation is challenging. Calculations with PYTHIA 8 employ the same $|\Delta\eta|$ as the measurements. The weak multiplicity dependence of the measurements could be well reproduced by the PYTHIA 8 calculation. The calculation from PYTHIA 8 is only slightly underestimating the data points.

6.6.4 $\rho(v_2^2, [p_\mathrm{T}])$

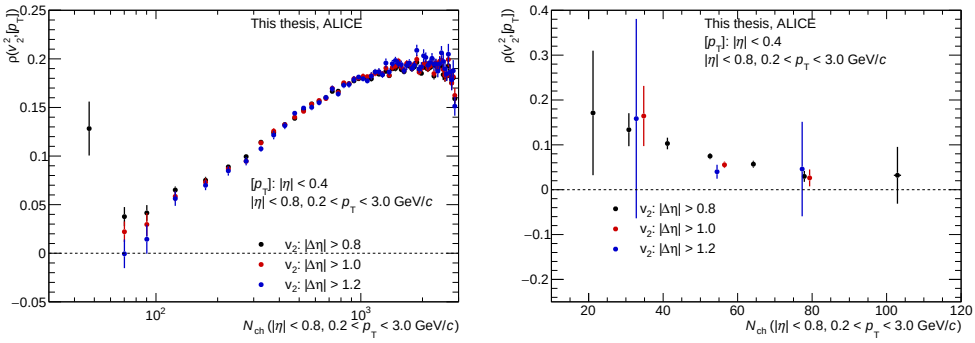

FIGURE 6.46: Measurements of $\rho(v_2^2, [p_\mathrm{T}])$ as a function of multiplicity in Pb–Pb (left) and pp (right) collisions. The measurements are with different $|\Delta\eta|$ separation to obtain the v_2^2.

The Pearson correlation coefficients, $\rho(v_2^2, [p_\mathrm{T}])$, have been measured in Pb–Pb and pp collisions using various pseudorapidity separation $|\Delta\eta|$, as shown in figure 6.46. In Pb–Pb collisions, it is observed that the measurements do not exhibit a significant change when varying the $|\Delta\eta|$ separation throughout the entire range of multiplicity. For pp collisions, as shown in figure 6.46 (right), despite a relatively large uncertainty, the change in $\rho(v_2^2, [p_\mathrm{T}])$ with an increase in $|\Delta\eta|$ is not significant, especially when compared to the situations of $\mathrm{cov}(v_2^2, [p_\mathrm{T}])$ or $\mathrm{var}(v_2^2)$, shown in figure 6.38 and 6.43. It is concluded that the effects of short-range correlations are mainly cancelled out in both the numerator and denominator when determining $\rho(v_2^2, [p_\mathrm{T}])$ results.

Given that the $\rho(v_2^2, [p_\mathrm{T}])$ shows weak sensitivity to the variation of pseudorapidity separation $|\Delta\eta|$, and in order to maximize the precision, $|\Delta\eta| > 0.8$ is used for the final results and subsequent physics discussions. The measurements from pp, p–Pb, and Pb–Pb collisions are shown in figure 6.47. The measured correlations are within the range of -0.1 to 0.2, suggesting a relatively weak correlation strength between v_2^2 and $[p_\mathrm{T}]$ in the low multiplicity region ($N_\mathrm{ch} \lesssim 200$). Upon normalization with $\sigma(v_2^2)$ and $\sqrt{c_k}$,

the trend of $\rho(v_n^2, [p_T])$ remains similar to the results of $\mathrm{cov}(v_2^2, [p_T])$. In both two small collision systems, pp and p–Pb collisions, there is a evident decrease in $\rho(v_2^2, [p_T])$ with the increasing multiplicity. In Pb–Pb collisions, the correlation coefficient $\rho(v_2^2, [p_T])$ exhibits an initial decrease followed by an increase with the increasing N_{ch}, similar as the behavior observed in $\mathrm{cov}(v_2^2, [p_T])$ shown in figure 6.39. For low multiplicities, i.e., $N_{ch} \lesssim 70$, the $\rho(v_n^2, [p_T])$ values in pp and p–Pb collisions are consistent with each other. Meanwhile, for the Pb–Pb collisions in the low multiplicity region, the data points also align with the measurements from pp and p–Pb collisions. Similar as the $\mathrm{cov}(v_2^2, [p_T])$, the agreement could be explained as follows: At very low multiplicities, i.e., $N_{\mathrm{ch}} \lesssim 70$, the initial stages of all three collision systems are all originates from fluctuations of the initial energy or entropy deposition. Consequently, the initial shape and size correlation across the three different collision systems could be similar. For Pb–Pb collisions in high multiplicity region, the geometry effects stemming from the overlapping region of the colliding nuclei gradually become more significant, and thus a non-monotonic trend is evident in Pb–Pb collision systems.

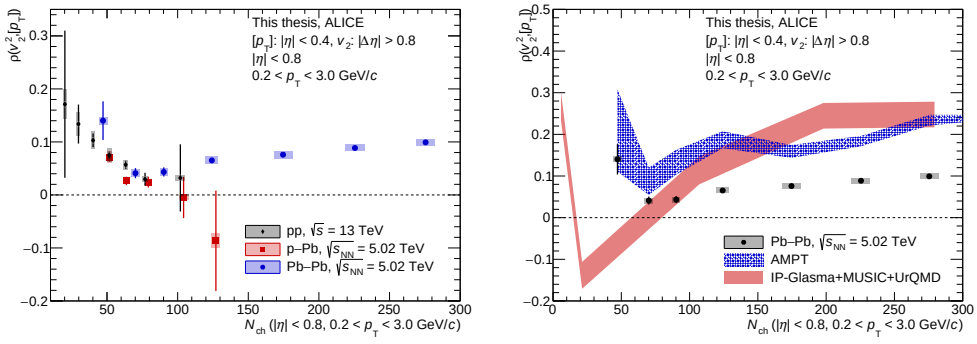

FIGURE 6.47: Left: Measurements of $\rho(v_2^2, [p_T])$ as a function of multiplicity in pp, p–Pb and Pb–Pb collisions. Right: Measurements of $\rho(v_2^2, [p_T])$ as a function of multiplicity in Pb–Pb collisions, compared with the AMPT [61, 179] and IP-Glasma + MUSIC + UrQMD [49, 180] calculations.

The measurements are compared with the calculation from AMPT [61, 179], and IP-Glasma + MUSIC + UrQMD model [49, 180], as shown in the right plot of figure 6.47 for Pb–Pb collisions, and in the figure 6.48 for small collision systems. Additionally, in pp collisions the measurement is also compared with the PYTHIA 8 calculation as shown in figure 6.48 (right). In Pb–Pb collisions, both the calculations from IP-Glasma + MUSIC + UrQMD model and from the AMPT model show a non-monotic behaviour. It should be addressed that the non-monotic trend is firstly predicted by the hydrodynamical model. Then the similar trend is observed in data and finally the behaviour is observed in AMPT calculation. In p–Pb collisions, as shown in figure 6.48, the hydrodynamics model fails

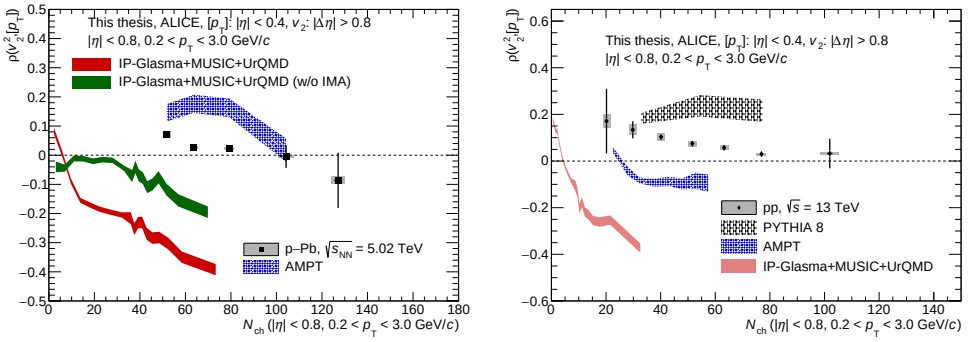

FIGURE 6.48: Measurements of $\rho(v_2^2, [p_T])$ in p–Pb (left) and pp (right) collisions, compared with the PYTHIA 8 [52, 179], AMPT [61, 179] and IP-Glasma + MUSIC + UrQMD [49, 180] calculations.

to accurately capture the measurements, whether with or without the initial momentum anisotropy from the CGC. Without the CGC effects, the model predicts negative correlations for the entire multiplicity region. However, when incorporating the initial momentum anisotropy from CGC effects, a positive correlation emerges at very low multiplicities, turning the results to positive for $N_{ch} \lesssim 10$. Nonetheless, in the region where both the measurements and calculations are available, the signs of the measurements and IP-Glasma + MUSIC + UrQMD calculation are opposite. In contrast, the AMPT calculation in p–Pb collisions exhibits better agreement with the measurements, as shown in figure 6.48 (left). The AMPT calculation give a positive correlation $\rho(v_2^2, [p_T])$ in p–Pb collisions, decreasing with increasing multiplicity, which aligns with the observed trends in the measurements, only slightly overestimating the measurements. Similar as in p–Pb, in pp collisions, the IP-Glasma + MUSIC + UrQMD model calculation is positive at very low multiplicities, decreasing with increasing multiplicity. As the multiplicity rises from $N_{\mathrm{ch}} \lesssim 10$ to high multiplicities, the $\rho(v_n^2, [p_T])$ turns to negative values. Similarly, the AMPT model in pp collisions also predicts a positive correlation at low multiplicities for $N_{ch} \sim 20$. As the multiplicity increases, this correlation shifts to a negative value. In contrast, the PYTHIA 8 model provides a positive correlation in pp collisions, which can be attributed to the contribution of jets. Intuitively, when an event has a greater contribution from jets, it leads to an increase in both the mean transverse momentum and the azimuthal anisotropy, thereby creating a positive correlation. However, PYTHIA 8 does not align with the observed trends in the measurements. Whether or not PYTHIA 8 calculation can successfully describe the $\rho(v_2^2, [p_T])$, the results cannot be solely explained by non-flow effects since PYTHIA 8 fails to model both the numerator and the denominator of $\rho(v_2^2, [p_T])$, as previously discussed. Unlike the decreasing trend observed in the data, there is no clear dependence on multiplicity observed for $\rho(v_n^2, [p_T])$ in PYTHIA 8.

Similar to the discussion on $\mathrm{cov}(v_2^2, [p_\mathrm{T}])$, adequately incorporating the jet contribution into the hydrodynamical model may be crucial for accurately describing the correlation between flow and mean transverse momentum.

7 Summary

The origin of QGP-like phenomena within small collision systems has been a puzzle for researchers for over a decade. Throughout these years of investigation, the presence of collective effects, as discussed in Chapter 2, has been confirmed. Moreover, as detailed in Chapter 2, numerous theoretical approaches have been attempted to describe these phenomena. Nonetheless, it has been determined that the phenomena cannot be adequately explained by simple mechanisms, including the initial or final stages.

Considering the complexity of the QGP-like phenomena in a small collision system, the best way to investigate the origin of the collectivity, or maybe the only possible way to pin down the origin of the collectivity, is to analyze with multi-observable analysis. This thesis uses the full Run 2 data sample with the ALICE detector at the LHC, providing the most precise measurements using the method described in Chapter 5.

Chapter 6 presents the results of measurements in pp, p–Pb, and Pb–Pb collisions. The measured observables include multiple particle correlations, cumulants, flow coefficients, symmetric cumulants, and correlations between flow and mean transverse momentum. Various methods for suppressing short-range correlations have been applied.

The measurements probe various mechanisms within the collisions. The initial stage of the collision is examined using flow coefficients v_n and nonlinear flow coefficients $v_{4,22}$ and $\chi_{4,22}$. Moreover, the event-by-event properties of the initial stage are assessed through measurements involving NSC(3,2), which address the initial eccentric correlations. The initial size and shape correlation is investigated through the $\rho(v_2^2, [p_{\mathrm{T}}])$. The flow coefficients, the nonlinear flow $v_{4,22}$, and the NSC(4,2) is also influenced by the system's evolution. The $\rho_{4,22}$ addresses the event plane correlation. Observables such as $v_n\{2\}$ and $\chi_{4,22}$ have shown sensitivity to variations in the η gap. Conversely, other observables like $c_2\{4\}$, $v_{4,22}$, and $\rho(v_2^2, [p_T])$ are less sensitivity to non-flow contamination. The main physics carried by each of the observable is summarized in the table 7.1.

The measurements indicate that for most observables, the transition from large to small collision systems is smooth, suggesting the underlying mechanism to generate these observables could be similar. However, exceptions are noted for the flow coefficient v_2 (as well as $\langle\langle\cos(2(\varphi_1-\varphi_2))\rangle\rangle$ and c_2), the $\mathrm{cov}(v_2^2, [p_{\mathrm{T}}])$, the c_k, and the correlation $\rho(v_2^2, [p_{\mathrm{T}}])$. The discrepancies in v_2 and $\mathrm{cov}(v_2^2, [p_T])$, as well as $\rho(v_2^2, [p_T])$, between small and large collision systems, are predominantly attributed to that in Pb–Pb the initial geometry originates from the overlap region of the wounded nucleon, while in pp collisions, they originate from the fluctuating color fields. As for the c_k, it is observed that even at low

Table 7.1: Summary of observables

Observable	Physics message
v_n	Initial stage. System evolution.
SC(3, 2)	Initial eccentricity correlation. System evolution.
NSC(3, 2)	Initial eccentricity correlation.
SC(4, 2)	Initial eccentricity correlation. Nonlinear contribution to v_4.
NSC(4, 2)	Initial eccentricity correlation. Nonlinear contribution to v_4.
$v_{4,22}$	Initial stage. System evolution.
$\chi_{4,22}$	Initial stage.
$\rho_{4,22}$	Event plane correlations.
$\mathrm{cov}(v_2^2, [p_\mathrm{T}])$	Initial size-shape correlation.
c_k	Initial size fluctuation.
$\sigma(v_2^2)$	Initial shape fluctuation.
$\rho(v_2^2, [p_\mathrm{T}])$	Initial size-shape correlation.

multiplicities, the measurements are different across the three collision systems. This discrepancy may be attributable to differences in the initial size fluctuations.

The measurements from pp, p–Pb, and Pb–Pb collisions are compared with different theoretical models. For pp collisions, comparisons are made with PYTHIA 8, AMPT, and calculations from IP-Glasma + MUSIC + UrQMD. In the case of p–Pb and Pb–Pb collisions, the measurements are compared with the transport model predictions from AMPT and the hydrodynamic model calculations from IP-Glasma + MUSIC + UrQMD. In many instances, models based on few-body interactions, as well as those incorporating hydrodynamic evolution, are not very successful. From one perspective, the modeling of the initial geometry may still require refinement. Furthermore, the system's evolution in reality is a complex QCD process, and the models that use either few-body interactions or hydrodynamic evolution could potentially be oversimplified.

The measurements impose constraints on the model and shed light on the system's origins, aiding in the building of a comprehensive model that describes the collective phenomenon in both large and small collision systems. For certain observables, such as SC(3,2), additional statistical data is necessary to derive more definitive conclusions regarding the physical interpretations they may offer. Moreover, the high-multiplicity trigger often faces criticism for its challenging mimic in theoretical models, making a direct comparison between experiment measurement and theoretical predictions. These will be taken into account in upcoming measurements during LHC Run 3.

Appendices

A Preliminary results

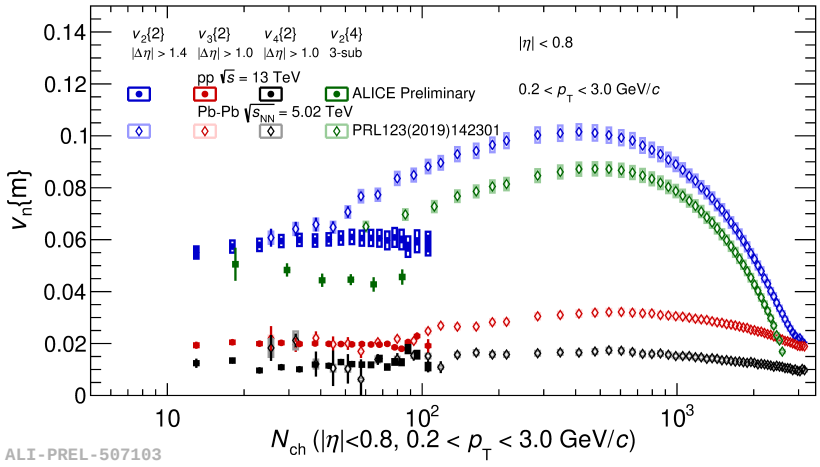

FIGURE A.1: Measurements of $v_n\{m\}$ as a function of multiplicity in pp collisions. Figure taken from [183].

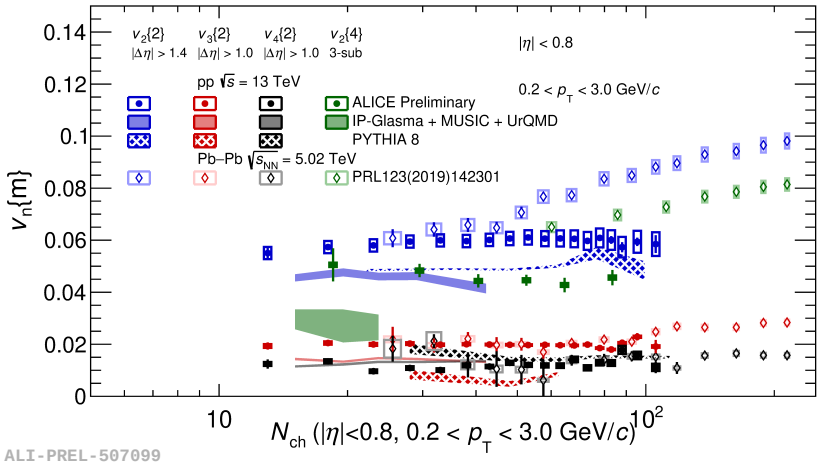

FIGURE A.2: Measurements of $v_n\{m\}$ as a function of multiplicity in pp collisions (zoomed in to low multiplicity region). Figure taken from [183].

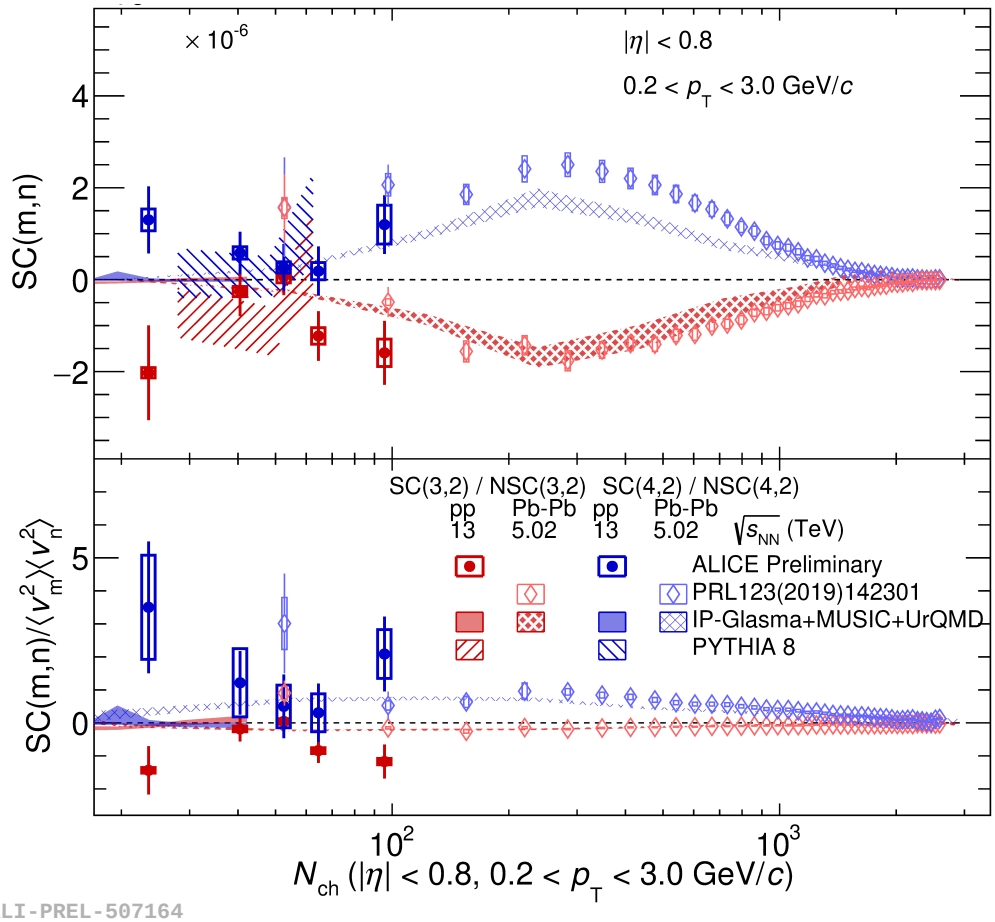

FIGURE A.3: Measurements of $v_n\{m\}$ as a function of multiplicity in pp collisions. Figure taken from [183].

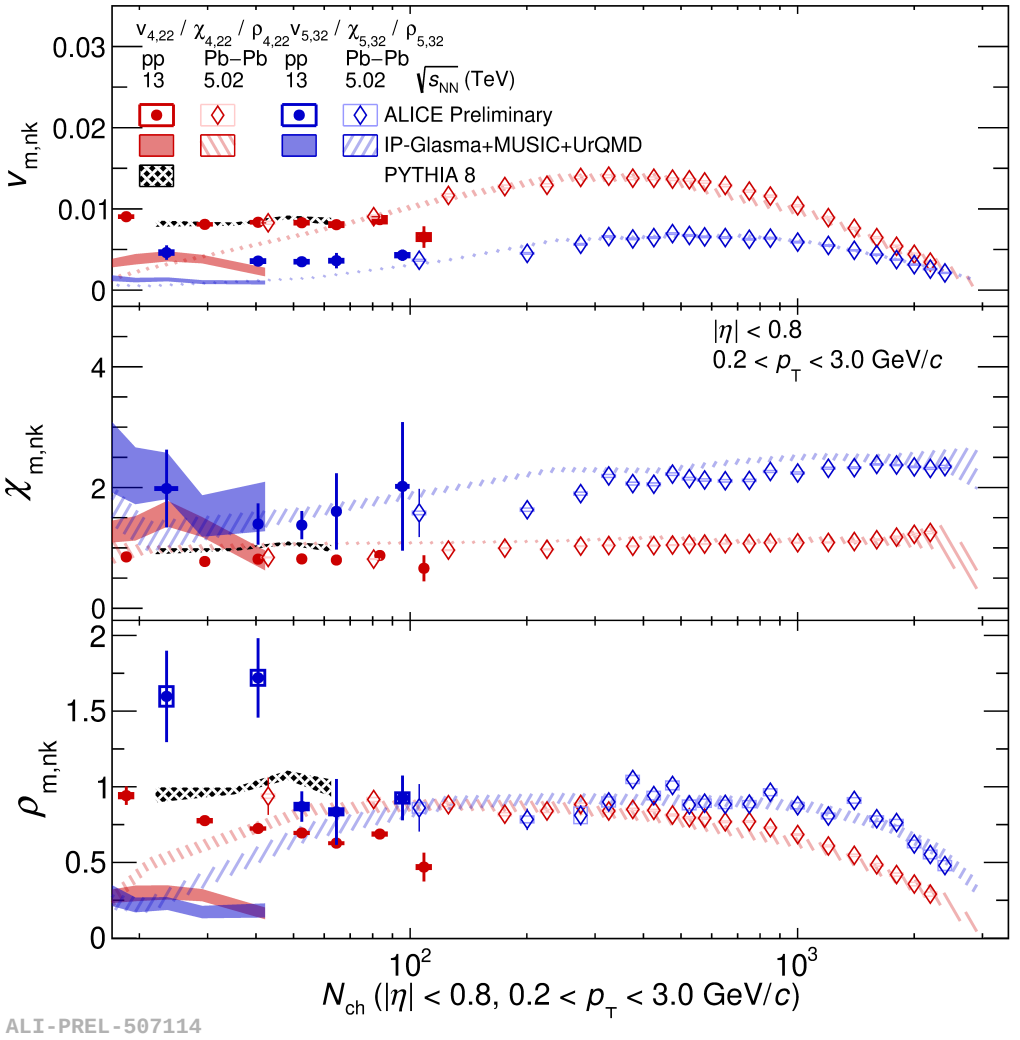

FIGURE A.4: Measurements of nonlinear flow as a function of multiplicity in pp collisions. Figure taken from [183].

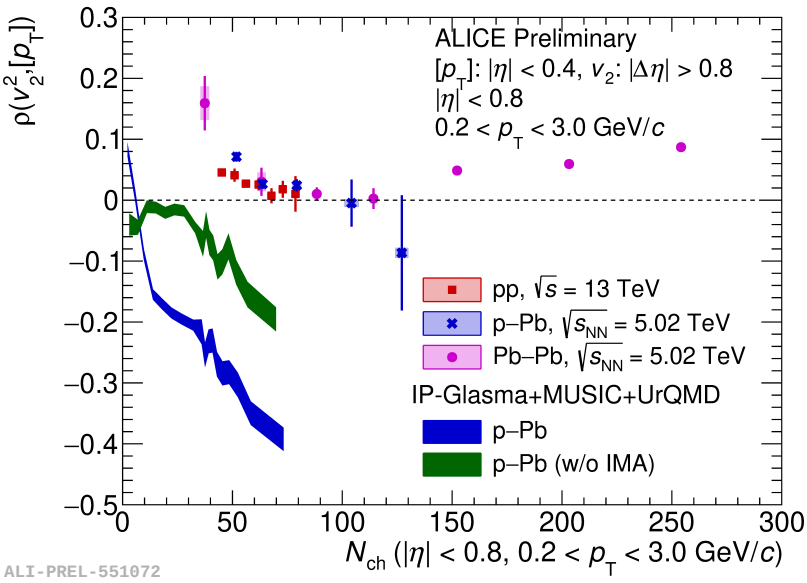

FIGURE A.5: Correlation of charged-particle v_2^2 and $[p_T]$ in Pb–Pb, p–Pb and pp collisions. Figure taken from [184].

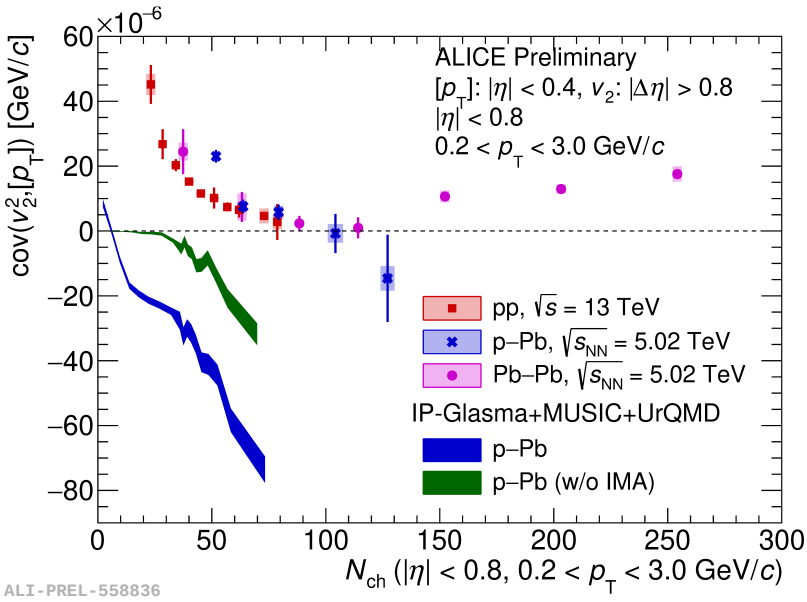

FIGURE A.6: Covariance of charged-particle v_2^2 and $[p_T]$ in Pb–Pb, p–Pb and pp collisions. Figure taken from [184].

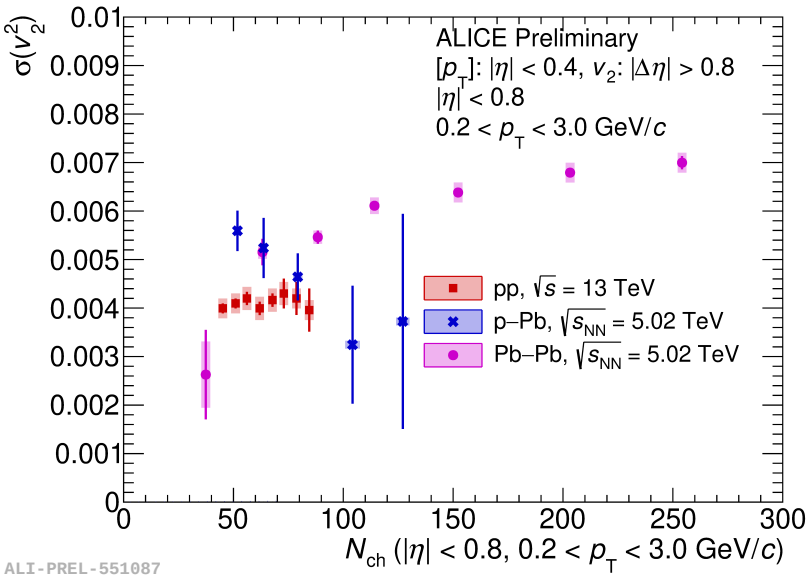

FIGURE A.7: v_2^2 fluctuations as a function of charged-particle multiplicity in Pb–Pb, p–Pb and pp collisions [184].

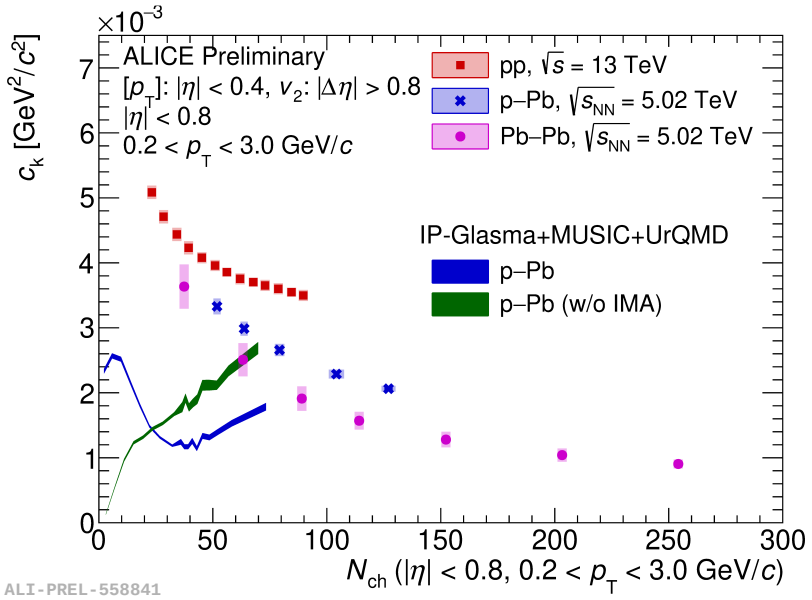

FIGURE A.8: Dynamic [p_T] fluctuations as a function of charged-particle multiplicity in Pb–Pb, p–Pb and pp collisions. [184].

B $W^{\pm}$ boson production

In this thesis, the primary focus is investigating the origins of collectivity through anisotropic flow observables. There have also been numerous attempts to pinning the origins of collectivity using hard scattering, as outlined in section 2.3.3. To understand the QGP-like effects using hard scattering, precise measurements of the nuclear parton distribution function are crucial. During my master's program, I focused on measuring the production of the $W^{\pm}$ boson in Pb–Pb collisions, with the majority of the analysis being conducted at that time. This work was extended into my Ph.D. studies and finalized in a publication [185] in 2023. The following section provides a brief overview of the analysis procedure and summarizes the key findings.

B.1 Data samples and analysis strategy

The $W^{\pm}$ boson production cross-section measured in this study is derived from a sample of Pb–Pb collisions at a nucleon-nucleon center-of-mass energy of $\sqrt{s_{\mathrm{NN}}} = 5.02$ TeV. The data were collected in the forward rapidity region $2.5 < y < 4$.

Neutrinos produced in the final state of $W^{\pm}$ boson decays cannot be detected. Instead, $W^{\pm}$ boson candidates are extracted from the single muon transverse momentum spectrum using a template fitting method. The $W^{\pm}$ and $W^{\pm}$ boson templates are generated using the POWHEG framework, followed by a simulation of their propagation through the ALICE detector. Muons originating from heavy-flavor decays are modeled using the p_{T} and y distributions calculated by FONLL [186]. For Pb–Pb collisions, the heavy-flavor decay muon spectrum is adjusted by the nuclear modification factor R_{AA}. The final yield is determined after applying an efficiency correction. figure B.1.

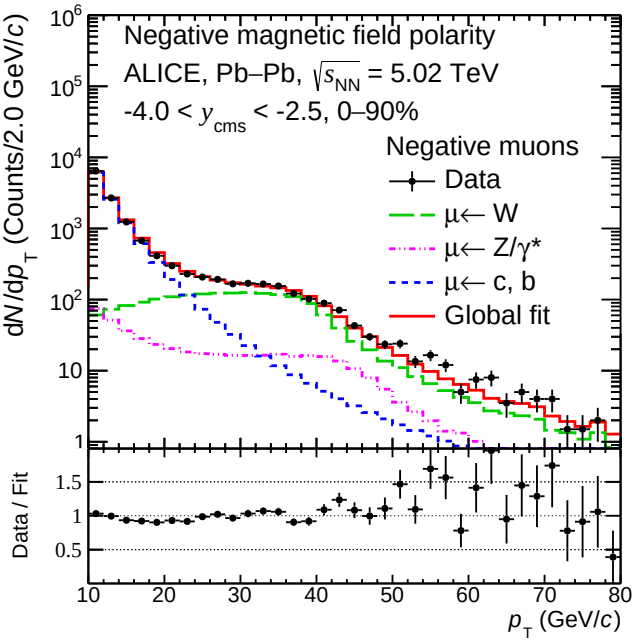

FIGURE B.1: Example of extraction of the $W^{\pm}$ signals. The figure is taken from [185].

B.2 Results

Figure B.2 shows the cross section for $W^{\pm}$ bosons, and the charge asymmetry. The charge asymmetry is defined as

$$A_{\mathrm{ch}} = \frac{N_{\mu^+ \leftarrow W^+} - N_{\mu^- \leftarrow W^-}}{N_{\mu^+ \leftarrow W^+} + N_{\mu^- \leftarrow W^-}}.$$

The MCFM+CT14 [187, 188] theoretical calculation without the nuclear modification overestimates the $W^{\pm}$ yields. The measurements are compatible with calculations that include the nPDFs using different models for $W^{\pm}$. With the nuclear modification, the central value of the prediction is closer to the measurements but the uncertainties are larger.

The normalized yields are measured as a function of centrality as presented in figure B.3. The $W^{\pm}$ measurements are compared with the HG-PYTHIA [189] prediction, which includes biases due to event selection and geometry that cause supression in peripheral region. Considering the large uncertainty, no centrality dependence is observed in the measurements.

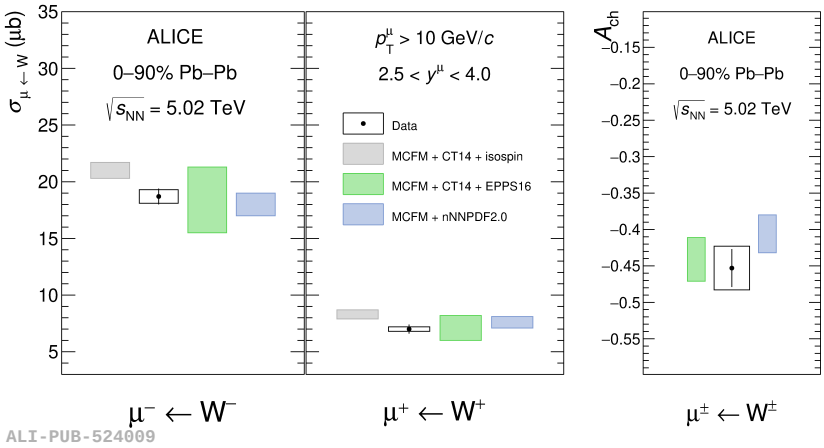

FIGURE B.2: Cross section and charge asymmetry of $W^\pm$ (right) in Pb–Pb collisions. The figure is taken from [185].

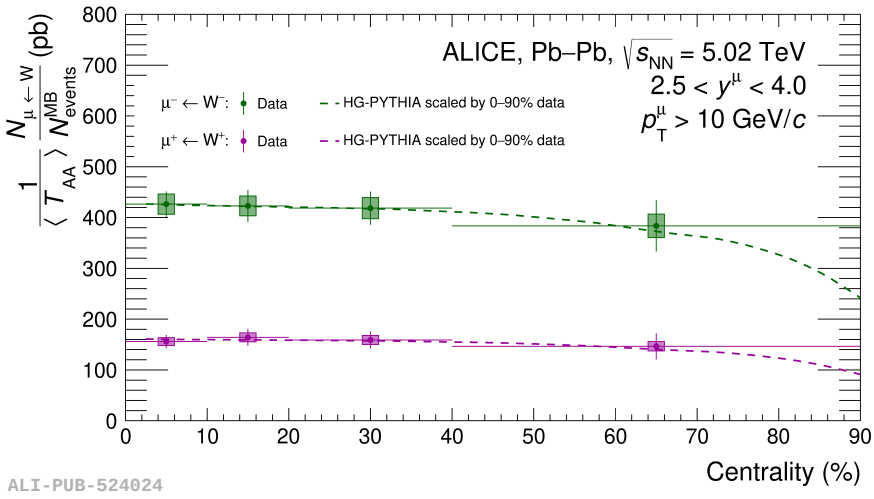

FIGURE B.3: Normalized yield of $W^\pm$ in Pb–Pb collisions as a function of centrality. The figure is taken from [185].

C Probe nuclear structure

The significance of nuclear structure has been increasingly acknowledged by the community in studies over recent years.

The following sections presents our study of nuclear structure in Xe–Xe collisions with the AMPT. On one hand, this study pioneers the investigation of nuclear structure through flow measurements at the LHC, providing a framework for potential future research into nuclear structure of oxygen-oxygen (O–O) collisions. It is expected that the role of nuclear structure will become even more important in upcoming oxygen-oxygen collisions at the LHC. It is important that oxygen is a medium-sized nucleus, significantly larger than a proton yet considerably smaller than lead or xenon. Therefore, the investigation of flow phenomena in O–O collisions is of great importance in pinning down the origin of collectivity across small to large systems in future research. On the other hand, understanding the nuclear structure in Xe–Xe collisions is important itself for identifying the origins of collective phenomena, considering that Xe–Xe collisions often serve as the reference systems for such studies.

C.1 Analysis procedure

The density profile of Xe is described by Woods-Saxon distribution:

$$\begin{aligned} \rho(r,\theta,\phi) &= \frac{\rho_0}{1+e^{[r-R(\theta,\phi)]/a_0}}, \\ R(\theta,\phi) &= R_0(1+\beta_2[\cos\gamma Y_{2,0}+\sin\gamma Y_{2,2}]), \end{aligned} \tag{C.1}$$

where a_0 represents the nuclear diffuseness and R_0 represents the radius. The β_2 is the quadrupole deformation parameters and the γ is the triaxial deformation parameter.

In this study, simulation samples of Xe–Xe collisions with varying parameters a_0, β_2, and γ using the AMPT model was generated. Various flow observables, introduced in chapter 3, are calculated using these samples. These observables include cumulants, flow coefficients, symmetric cumulants, and nonlinear flow modes.

C.2 Results

The complete list of results can be found in [190]. As an example of the findings, the calculation of $v_2\{2\}$ and $v_3\{2\}$ for different β_2 and γ is presented in figure C.1. The

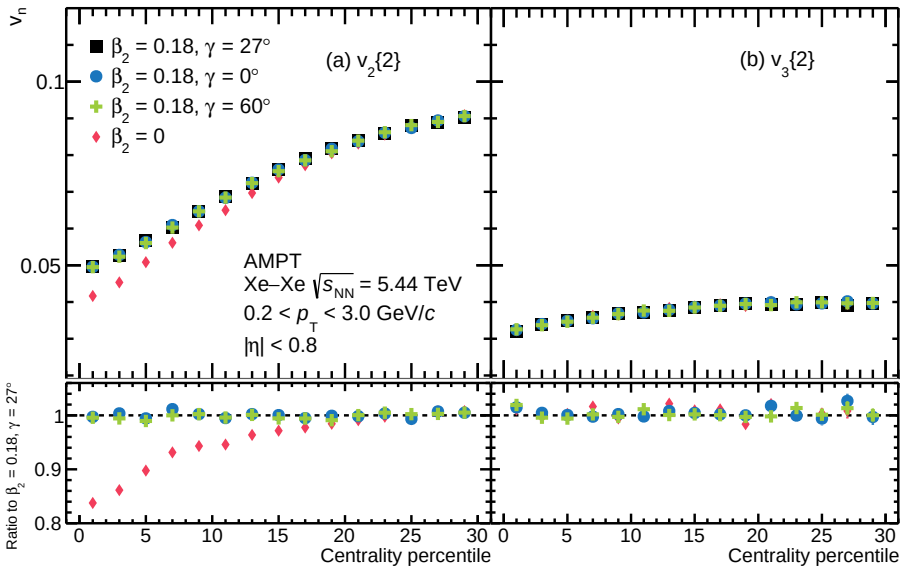

FIGURE C.1: Calculation of $v_2\{2\}$ and $v_3\{2\}$ as a function of centrality in Xe–Xe collisions with varying β_2 and γ with AMPT.

analysis revealed that $v_2\{2\}$ is sensitive to changes in β_2 but is less affected by variations in γ. In contrast, $v_3\{2\}$ is found to be insensitive to both β_2 and γ.

This study also finds that the observables $v_{4,22}$, $\chi_{4,22}$, and NSC$(3,2)$ are sensitive to β_2. Interestingly, none of the flow observables examined in this study are sensitive to γ. This insensitivity is important because another study [191] has shown that observables such as $\rho(v_2^2, [p_T])$ are sensitive to both β_2 and γ. It is only by combining $\rho(v_2^2, [p_T])$ with observables that are insensitive to β_2 that one can constrain both parameters, β_2 and γ.

Bibliography

[1] Steven Weinberg. *Dreams of a final theory: The Search for the fundamental laws of nature*. 1992.

[2] Philip W Anderson. "More Is Different: Broken symmetry and the nature of the hierarchical structure of science." *Science* 177 (1972).

[3] S. L. Glashow. "Partial Symmetries of Weak Interactions". *Nucl. Phys.* 22 (1961). DOI: 10.1016/0029-5582(61)90469-2.

[4] Steven Weinberg. "A Model of Leptons". *Phys. Rev. Lett.* 19 (1967). DOI: 10.1103/PhysRevLett.19.1264.

[5] David J. Gross and Frank Wilczek. "Ultraviolet Behavior of Nonabelian Gauge Theories". *Phys. Rev. Lett.* 30 (1973). DOI: 10.1103/PhysRevLett.30.1343.

[6] Peter W. Higgs. "Broken Symmetries and the Masses of Gauge Bosons". *Phys. Rev. Lett.* 13 (1964). DOI: 10.1103/PhysRevLett.13.508.

[7] Wikipedia contributors. *Standard Model — Wikipedia, The Free Encyclopedia*. [Online; accessed 20-Mar-2024]. 2024. URL: https://en.wikipedia.org/wiki/Standard_Model.

[8] R. L. Workman et al. "Review of Particle Physics". *PTEP* 2022 (2022). DOI: 10.1093/ptep/ptac097.

[9] H. David Politzer. "Reliable Perturbative Results for Strong Interactions?" *Phys. Rev. Lett.* 30 (1973). DOI: 10.1103/PhysRevLett.30.1346.

[10] "The ALICE experiment – A journey through QCD" (2022). arXiv: 2211.04384 [nucl-ex].

[11] John W. Harris and Berndt Müller. ""QGP Signatures" revisited". *Eur. Phys. J. C* 84 (2024). DOI: 10.1140/epjc/s10052-024-12533-y.

[12] Wit Busza, Krishna Rajagopal, and Wilke van der Schee. "Heavy Ion Collisions: The Big Picture, and the Big Questions". *Ann. Rev. Nucl. Part. Sci.* 68 (2018). DOI: 10.1146/annurev-nucl-101917-020852. arXiv: 1802.04801 [hep-ph].

[13] Johann Rafelski and Berndt Muller. "Strangeness Production in the Quark - Gluon Plasma". *Phys. Rev. Lett.* 48 (1982). [Erratum: Phys.Rev.Lett. 56, 2334 (1986)]. DOI: 10.1103/PhysRevLett.48.1066.

[14] P. Koch, Berndt Muller, and Johann Rafelski. "Strangeness Production and Evolution in Quark Gluon Plasma". *Z. Phys. A* 324 (1986).

[15] P. Koch, Berndt Muller, and Johann Rafelski. "Strangeness in Relativistic Heavy Ion Collisions". *Phys. Rept.* 142 (1986). DOI: 10.1016/0370-1573(86)90096-7.

[16] Johann Rafelski. "Strange anti-baryons from quark - gluon plasma". *Phys. Lett. B* 262 (1991). DOI: 10.1016/0370-2693(91)91576-H.

[17] Betty Abelev et al. "Multi-strange baryon production in pp collisions at $\sqrt{s} = 7$ TeV with ALICE". *Phys. Lett. B* 712 (2012). DOI: 10.1016/j.physletb.2012.05.011. arXiv: 1204.0282 [nucl-ex].

[18] Betty Abelev et al. "Centrality dependence of π, K, p production in Pb-Pb collisions at $\sqrt{s_{NN}} = 2.76$ TeV". *Phys. Rev. C* 88 (2013). DOI: 10.1103/PhysRevC.88.044910. arXiv: 1303.0737 [hep-ex].

[19] K. Aamodt et al. "Strange particle production in proton-proton collisions at $\sqrt{s}$ = 0.9 TeV with ALICE at the LHC". *Eur. Phys. J. C* 71 (2011). DOI: 10.1140/epjc/s10052-011-1594-5. arXiv: 1012.3257 [hep-ex].

[20] K. Aamodt et al. "Production of pions, kaons and protons in pp collisions at $\sqrt{s} = 900$ GeV with ALICE at the LHC". *Eur. Phys. J. C* 71 (2011). DOI: 10.1140/epjc/s10052-011-1655-9. arXiv: 1101.4110 [hep-ex].

[21] Betty Bezverkhny Abelev et al. "Multi-strange baryon production at mid-rapidity in Pb-Pb collisions at $\sqrt{s_{NN}} = 2.76$ TeV". *Phys. Lett. B* 728 (2014). [Erratum: Phys.Lett.B 734, 409–410 (2014)]. DOI: 10.1016/j.physletb.2014.05.052. arXiv: 1307.5543 [nucl-ex].

[22] J. Adams et al. "Scaling Properties of Hyperon Production in Au+Au Collisions at $\sqrt{s} = 200$ GeV". *Phys. Rev. Lett.* 98 (2007). DOI: 10.1103/PhysRevLett.98.062301. arXiv: nucl-ex/0606014.

[23] B. I. Abelev et al. "Systematic Measurements of Identified Particle Spectra in pp, d^+ Au and Au+Au Collisions from STAR". *Phys. Rev. C* 79 (2009). DOI: 10.1103/PhysRevC.79.034909. arXiv: 0808.2041 [nucl-ex].

[24] B. I. Abelev et al. "Strange particle production in p+p collisions at $\sqrt{s} = 200$ GeV". *Phys. Rev. C* 75 (2007). DOI: 10.1103/PhysRevC.75.064901. arXiv: nucl-ex/0607033.

[25] J. D. Bjorken. "Energy Loss of Energetic Partons in Quark - Gluon Plasma: Possible Extinction of High p(t) Jets in Hadron - Hadron Collisions" (1982).

[26] Miklos Gyulassy and Michael Plumer. "Jet Quenching in Dense Matter". *Phys. Lett. B* 243 (1990). DOI: 10.1016/0370-2693(90)91409-5.

[27] R. Baier et al. "Radiative energy loss of high-energy quarks and gluons in a finite volume quark - gluon plasma". *Nucl. Phys. B* 483 (1997). DOI: 10.1016/S0550-3213(96)00553-6. arXiv: hep-ph/9607355.

[28] R. Baier et al. "Radiative energy loss and p(T) broadening of high-energy partons in nuclei". *Nucl. Phys. B* 484 (1997). DOI: 10.1016/S0550-3213(96)00581-0. arXiv: hep-ph/9608322.

[29] Leticia Cunqueiro and Anne M. Sickles. "Studying the QGP with Jets at the LHC and RHIC". *Prog. Part. Nucl. Phys.* 124 (2022). DOI: 10.1016/j.ppnp.2022.103940. arXiv: 2110.14490 [nucl-ex].

[30] Shreyasi Acharya et al. "Measurements of inclusive jet spectra in pp and central Pb–Pb collisions at $\sqrt{s_{\mathrm{NN}}} = 5.02$ TeV". *Phys. Rev. C* 101 (2020). DOI: 10.1103/PhysRevC.101.034911. arXiv: 1909.09718 [nucl-ex].

[31] T. Matsui and H. Satz. "J/ψ Suppression by Quark-Gluon Plasma Formation". *Phys. Lett. B* 178 (1986). DOI: 10.1016/0370-2693(86)91404-8.

[32] Jaroslav Adam et al. "J/ψ suppression at forward rapidity in Pb-Pb collisions at $\sqrt{s_{\mathrm{NN}} = 5.02}$ TeV". *Phys. Lett. B* 766 (2017). DOI: 10.1016/j.physletb.2016.12.064. arXiv: 1606.08197 [nucl-ex].

[33] Robert L. Thews, Martin Schroedter, and Johann Rafelski. "Enhanced J/ψ production in deconfined quark matter". *Phys. Rev. C* 63 (2001). DOI: 10.1103/PhysRevC.63.054905. arXiv: hep-ph/0007323.

[34] R. Vogt. "Shadowing effects on J/ψ and Υ production at energies available at the CERN Large Hadron Collider". *Phys. Rev. C* 92 (2015). DOI: 10.1103/PhysRevC.92.034909. arXiv: 1507.04418 [hep-ph].

[35] S. Voloshin and Y. Zhang. "Flow study in relativistic nuclear collisions by Fourier expansion of Azimuthal particle distributions". *Z. Phys. C* 70 (1996). DOI: 10.1007/s002880050141. arXiv: hep-ph/9407282.

[36] Xiao-Mei Li et al. "Re-examination for the calculation of elliptic flow and other Fourier harmonics". *Mod. Phys. Lett. A* 25 (2010). DOI: 10.1142/S0217732310032470.

[37] Ulrich Heinz and Raimond Snellings. "Collective flow and viscosity in relativistic heavy-ion collisions". *Ann. Rev. Nucl. Part. Sci.* 63 (2013). DOI: 10.1146/annurev-nucl-102212-170540. arXiv: 1301.2826 [nucl-th].

[38] P. Kovtun, Dan T. Son, and Andrei O. Starinets. "Viscosity in strongly interacting quantum field theories from black hole physics". *Phys. Rev. Lett.* 94 (2005). DOI: 10.1103/PhysRevLett.94.111601. arXiv: hep-th/0405231.

[39] Jaroslav Adam et al. "Anisotropic flow of charged particles in Pb-Pb collisions at $\sqrt{s_{\mathrm{NN}}} = 5.02$ TeV". *Phys. Rev. Lett.* 116 (2016). DOI: 10.1103/PhysRevLett.116.132302. arXiv: 1602.01119 [nucl-ex].

[40] C. Adler et al. "Disappearance of back-to-back high p_T hadron correlations in central Au+Au collisions at $\sqrt{s_{NN}} = 200$-GeV". *Phys. Rev. Lett.* 90 (2003). DOI: 10.1103/PhysRevLett.90.082302. arXiv: nucl-ex/0210033.

[41] K. Aamodt et al. "Harmonic decomposition of two-particle angular correlations in Pb-Pb collisions at $\sqrt{s_{NN}} = 2.76$ TeV". *Phys. Lett. B* 708 (2012). DOI: 10.1016/j.physletb.2012.01.060. arXiv: 1109.2501 [nucl-ex].

[42] Rajan Gupta. "Introduction to lattice QCD: Course". *Les Houches Summer School in Theoretical Physics, Session 68: Probing the Standard Model of Particle Interactions*. 1997. arXiv: hep-lat/9807028.

[43] Shin Muroya et al. "Lattice QCD at finite density: An Introductory review". *Prog. Theor. Phys.* 110 (2003). DOI: 10.1143/PTP.110.615. arXiv: hep-lat/0306031.

[44] Claudia Ratti. "Lattice QCD and heavy ion collisions: a review of recent progress". *Rept. Prog. Phys.* 81 (2018). DOI: 10.1088/1361-6633/aabb97. arXiv: 1804.07810 [hep-lat].

[45] Michael L. Miller et al. "Glauber modeling in high energy nuclear collisions". *Ann. Rev. Nucl. Part. Sci.* 57 (2007). DOI: 10.1146/annurev.nucl.57.090506.123020. arXiv: nucl-ex/0701025.

[46] Dmitri Kharzeev, Eugene Levin, and Marzia Nardi. "The Onset of classical QCD dynamics in relativistic heavy ion collisions". *Phys. Rev. C* 71 (2005). DOI: 10.1103/PhysRevC.71.054903. arXiv: hep-ph/0111315.

[47] Dmitri Kharzeev, Eugene Levin, and Marzia Nardi. "QCD saturation and deuteron nucleus collisions". *Nucl. Phys. A* 730 (2004). [Erratum: Nucl.Phys.A 743, 329–331 (2004)]. DOI: 10.1016/j.nuclphysa.2004.06.022. arXiv: hep-ph/0212316.

[48] Dmitri Kharzeev, Eugene Levin, and Marzia Nardi. "Color glass condensate at the LHC: Hadron multiplicities in pp, pA and AA collisions". *Nucl. Phys. A* 747 (2005). DOI: 10.1016/j.nuclphysa.2004.10.018. arXiv: hep-ph/0408050.

[49] Bjoern Schenke, Prithwish Tribedy, and Raju Venugopalan. "Fluctuating Glasma initial conditions and flow in heavy ion collisions". *Phys. Rev. Lett.* 108 (2012). DOI: 10.1103/PhysRevLett.108.252301. arXiv: 1202.6646 [nucl-th].

[50] Bjoern Schenke, Chun Shen, and Prithwish Tribedy. "Running the gamut of high energy nuclear collisions". *Phys. Rev. C* 102 (2020). DOI: 10.1103/PhysRevC.102.044905. arXiv: 2005.14682 [nucl-th].

[51] Torbjörn Sjöstrand et al. "An introduction to PYTHIA 8.2". *Comput. Phys. Commun.* 191 (2015). DOI: 10.1016/j.cpc.2015.01.024. arXiv: 1410.3012 [hep-ph].

[52] Peter Skands, Stefano Carrazza, and Juan Rojo. "Tuning PYTHIA 8.1: the Monash 2013 Tune". *Eur. Phys. J. C* 74 (2014). DOI: 10.1140/epjc/s10052-014-3024-y. arXiv: 1404.5630 [hep-ph].

[53] G. Baym. "Thermal equilibration in ultrarelativistic heavy ion collisions". *Phys. Lett. B* 138 (1984). DOI: 10.1016/0370-2693(84)91863-X.

[54] Huichao Song, Steffen A. Bass, and Ulrich Heinz. "Viscous QCD matter in a hybrid hydrodynamic+Boltzmann approach". *Phys. Rev. C* 83 (2011). DOI: 10.1103/PhysRevC.83.024912. arXiv: 1012.0555 [nucl-th].

[55] S. A. Bass et al. "Microscopic models for ultrarelativistic heavy ion collisions". *Prog. Part. Nucl. Phys.* 41 (1998). DOI: 10.1016/S0146-6410(98)00058-1. arXiv: nucl-th/9803035.

[56] Bao-An Li and Che Ming Ko. "Formation of superdense hadronic matter in high-energy heavy ion collisions". *Phys. Rev. C* 52 (1995). DOI: 10.1103/PhysRevC.52.2037. arXiv: nucl-th/9505016.

[57] A. Bazavov et al. "Equation of state in (2+1)-flavor QCD". *Phys. Rev. D* 90 (2014). DOI: 10.1103/PhysRevD.90.094503. arXiv: 1407.6387 [hep-lat].

[58] Larry D. McLerran and Raju Venugopalan. "Computing quark and gluon distribution functions for very large nuclei". *Phys. Rev. D* 49 (1994). DOI: 10.1103/PhysRevD.49.2233. arXiv: hep-ph/9309289.

[59] J. Bartels, Krzysztof J. Golec-Biernat, and H. Kowalski. "A modification of the saturation model: DGLAP evolution". *Phys. Rev. D* 66 (2002). DOI: 10.1103/PhysRevD.66.014001. arXiv: hep-ph/0203258.

[60] Fred Cooper and Graham Frye. "Comment on the Single Particle Distribution in the Hydrodynamic and Statistical Thermodynamic Models of Multiparticle Production". *Phys. Rev. D* 10 (1974). DOI: 10.1103/PhysRevD.10.186.

[61] Zi-Wei Lin et al. "A Multi-phase transport model for relativistic heavy ion collisions". *Phys. Rev. C* 72 (2005). DOI: 10.1103/PhysRevC.72.064901. arXiv: nucl-th/0411110.

[62] Xin-Nian Wang. "Role of multiple mini - jets in high-energy hadronic reactions". *Phys. Rev. D* 43 (1991). DOI: 10.1103/PhysRevD.43.104.

[63] Bin Zhang. "ZPC 1.0.1: A Parton cascade for ultrarelativistic heavy ion collisions". *Comput. Phys. Commun.* 109 (1998). DOI: 10.1016/S0010-4655(98)00010-1. arXiv: nucl-th/9709009.

[64] T. S. Biro. "Quark coalescence and hadronic equilibrium" (2000). arXiv: hep-ph/0005067.

[65] An-Ke Lei et al. "Introduction to the parton and hadron cascade model PACIAE 3.0". *Phys. Rev. C* 108 (2023). DOI: 10.1103/PhysRevC.108.064909. arXiv: 2309.05110 [hep-ph].

[66] Torbjorn Sjostrand, Stephen Mrenna, and Peter Z. Skands. "PYTHIA 6.4 Physics and Manual". *JHEP* 05 (2006). DOI: 10.1088/1126-6708/2006/05/026. arXiv: hep-ph/0603175.

[67] Vardan Khachatryan et al. "Observation of Long-Range Near-Side Angular Correlations in Proton-Proton Collisions at the LHC". *JHEP* 09 (2010). DOI: 10.1007/JHEP09(2010)091. arXiv: 1009.4122 [hep-ex].

[68] Morad Aaboud et al. "Measurements of long-range azimuthal anisotropies and associated Fourier coefficients for *pp* collisions at $\sqrt{s} = 5.02$ and 13 TeV and p+Pb collisions at $\sqrt{s_{\mathrm{NN}}} = 5.02$ TeV with the ATLAS detector". *Phys. Rev. C* 96 (2017). DOI: 10.1103/PhysRevC.96.024908. arXiv: 1609.06213 [nucl-ex].

[69] Serguei Chatrchyan et al. "Observation of Long-Range Near-Side Angular Correlations in Proton-Lead Collisions at the LHC". *Phys. Lett. B* 718 (2013). DOI: 10.1016/j.physletb.2012.11.025. arXiv: 1210.5482 [nucl-ex].

[70] Betty Abelev et al. "Long-range angular correlations on the near and away side in p-Pb collisions at $\sqrt{s_{NN}} = 5.02$ TeV". *Phys. Lett. B* 719 (2013). DOI: 10.1016/j.physletb.2013.01.012. arXiv: 1212.2001 [nucl-ex].

[71] Serguei Chatrchyan et al. "Centrality Dependence of Dihadron Correlations and Azimuthal anisotropy Harmonics in PbPb Collisions at $\sqrt{s_{NN}} = 2.76$ TeV". *Eur. Phys. J. C* 72 (2012). DOI: 10.1140/epjc/s10052-012-2012-3. arXiv: 1201.3158 [nucl-ex].

[72] Shreyasi Acharya et al. "Investigations of Anisotropic Flow Using Multiparticle Azimuthal Correlations in pp, p-Pb, Xe-Xe, and Pb-Pb Collisions at the LHC". *Phys. Rev. Lett.* 123 (2019). DOI: 10.1103/PhysRevLett.123.142301. arXiv: 1903.01790 [nucl-ex].

[73] Albert M Sirunyan et al. "Pseudorapidity and transverse momentum dependence of flow harmonics in pPb and PbPb collisions". *Phys. Rev. C* 98 (2018). DOI: 10.1103/PhysRevC.98.044902. arXiv: 1710.07864 [nucl-ex].

[74] C. Aidala et al. "Creation of quark–gluon plasma droplets with three distinct geometries". *Nature Phys.* 15 (2019). DOI: 10.1038/s41567-018-0360-0. arXiv: 1805.02973 [nucl-ex].

[75] M. I. Abdulhamid et al. "Measurements of the Elliptic and Triangular Azimuthal Anisotropies in Central ^{3}He+Au, d+Au and p+Au Collisions at $\sqrt{s_{\mathrm{NN}}}$ = 200 GeV". *Phys. Rev. Lett.* 130 (2023). DOI: 10.1103/PhysRevLett.130.242301. arXiv: 2210.11352 [nucl-ex].

[76] Georges Aad et al. "Observation of Long-Range Elliptic Azimuthal Anisotropies in $\sqrt{s}$ =13 and 2.76 TeV *pp* Collisions with the ATLAS Detector". *Phys. Rev. Lett.* 116 (2016). DOI: 10.1103/PhysRevLett.116.172301. arXiv: 1509.04776 [hep-ex].

[77] Shreyasi Acharya et al. "Anisotropic flow and flow fluctuations of identified hadrons in Pb–Pb collisions at $\sqrt{s_{\mathrm{NN}}}$ = 5.02 TeV". *JHEP* 05 (2023). DOI: 10.1007/JHEP05(2023)243. arXiv: 2206.04587 [nucl-ex].

[78] Betty Bezverkhny Abelev et al. "Long-range angular correlations of π, K and p in p–Pb collisions at $\sqrt{s_{\mathrm{NN}}}$ = 5.02 TeV". *Phys. Lett. B* 726 (2013). DOI: 10.1016/j.physletb.2013.08.024. arXiv: 1307.3237 [nucl-ex].

[79] Michael J. Tannenbaum. "Latest Results from RHIC + Progress on Determining $\hat{q}L$ in RHI Collisions Using Di-Hadron Correlations". *Universe* 5 (2019). DOI: 10.3390/universe5060140. arXiv: 1904.08995 [nucl-ex].

[80] Vardan Khachatryan et al. "Evidence for collectivity in pp collisions at the LHC". *Phys. Lett. B* 765 (2017). DOI: 10.1016/j.physletb.2016.12.009. arXiv: 1606.06198 [nucl-ex].

[81] S. Acharya et al. "Energy dependence and fluctuations of anisotropic flow in Pb-Pb collisions at $\sqrt{s_{\mathrm{NN}}}$ = 5.02 and 2.76 TeV". *JHEP* 07 (2018). DOI: 10.1007/JHEP07(2018)103. arXiv: 1804.02944 [nucl-ex].

[82] Betty Bezverkhny Abelev et al. "Multiparticle azimuthal correlations in p -Pb and Pb-Pb collisions at the CERN Large Hadron Collider". *Phys. Rev. C* 90 (2014). DOI: 10.1103/PhysRevC.90.054901. arXiv: 1406.2474 [nucl-ex].

[83] Morad Aaboud et al. "Measurement of long-range multiparticle azimuthal correlations with the subevent cumulant method in *pp* and $p + Pb$ collisions with the ATLAS detector at the CERN Large Hadron Collider". *Phys. Rev. C* 97 (2018). DOI: 10.1103/PhysRevC.97.024904. arXiv: 1708.03559 [hep-ex].

[84] Morad Aaboud et al. "Measurement of multi-particle azimuthal correlations in *pp*, *p*+Pb and low-multiplicity Pb+Pb collisions with the ATLAS detector". *Eur. Phys. J. C* 77 (2017). DOI: 10.1140/epjc/s10052-017-4988-1. arXiv: 1705.04176 [hep-ex].

[85] Vardan Khachatryan et al. "Evidence for Collective Multiparticle Correlations in p-Pb Collisions". *Phys. Rev. Lett.* 115 (2015). DOI: 10.1103/PhysRevLett.115.012301. arXiv: 1502.05382 [nucl-ex].

[86] Albert M Sirunyan et al. "Multiparticle correlation studies in pPb collisions at $\sqrt{s_{\mathrm{NN}}} = 8.16$ TeV". *Phys. Rev. C* 101 (2020). DOI: 10.1103/PhysRevC.101.014912. arXiv: 1904.11519 [hep-ex].

[87] Shreyasi Acharya et al. "Searches for transverse momentum dependent flow vector fluctuations in Pb-Pb and p-Pb collisions at the LHC". *JHEP* 09 (2017). DOI: 10.1007/JHEP09(2017)032. arXiv: 1707.05690 [nucl-ex].

[88] Vardan Khachatryan et al. "Evidence for transverse momentum and pseudorapidity dependent event plane fluctuations in PbPb and pPb collisions". *Phys. Rev. C* 92 (2015). DOI: 10.1103/PhysRevC.92.034911. arXiv: 1503.01692 [nucl-ex].

[89] Shreyasi Acharya et al. "Observation of flow angle and flow magnitude fluctuations in Pb-Pb collisions at sNN=5.02TeV at the CERN Large Hadron Collider". *Phys. Rev. C* 107 (2023). DOI: 10.1103/PhysRevC.107.L051901. arXiv: 2206.04574 [nucl-ex].

[90] Georges Aad et al. "Longitudinal Flow Decorrelations in Xe+Xe Collisions at $\sqrt{s_{\mathrm{NN}}} = 5.44$ TeV with the ATLAS Detector". *Phys. Rev. Lett.* 126 (2021). DOI: 10.1103/PhysRevLett.126.122301. arXiv: 2001.04201 [nucl-ex].

[91] Morad Aaboud et al. "Measurement of longitudinal flow decorrelations in Pb+Pb collisions at $\sqrt{s_{\mathrm{NN}}} = 2.76$ and 5.02 TeV with the ATLAS detector". *Eur. Phys. J. C* 78 (2018). DOI: 10.1140/epjc/s10052-018-5605-7. arXiv: 1709.02301 [nucl-ex].

[92] "Measurements of longitudinal flow decorrelations in 5.02 TeV and 13 TeV *pp* collisions and 5.44 TeV Xe+Xe collisions with the ATLAS detector" (2022).

[93] Albert M Sirunyan et al. "Mixed higher-order anisotropic flow and nonlinear response coefficients of charged particles in PbPb collisions at $\sqrt{s_{\mathrm{NN}}} = 2.76$ and 5.02 TeV". *Eur. Phys. J. C* 80 (2020). DOI: 10.1140/epjc/s10052-020-7834-9. arXiv: 1910.08789 [hep-ex].

[94] Shreyasi Acharya et al. "Linear and non-linear flow modes in Pb-Pb collisions at $\sqrt{s_{\mathrm{NN}}} = 2.76$ TeV". *Phys. Lett. B* 773 (2017). DOI: 10.1016/j.physletb.2017.07.060. arXiv: 1705.04377 [nucl-ex].

[95] Bassam Aboona et al. "Beam energy dependence of the linear and mode-coupled flow harmonics in Au+Au collisions". *Phys. Lett. B* 839 (2023). DOI: 10.1016/j.physletb.2023.137755. arXiv: 2211.11637 [nucl-ex].

[96] Georges Aad et al. "Measurement of flow harmonics correlations with mean transverse momentum in lead-lead and proton-lead collisions at $\sqrt{s_{NN}} = 5.02$ TeV with the ATLAS detector". *Eur. Phys. J. C* 79 (2019). DOI: 10.1140/epjc/s10052-019-7489-6. arXiv: 1907.05176 [nucl-ex].

[97] Shreyasi Acharya et al. "Characterizing the initial conditions of heavy-ion collisions at the LHC with mean transverse momentum and anisotropic flow correlations". *Phys. Lett. B* 834 (2022). DOI: 10.1016/j.physletb.2022.137393. arXiv: 2111.06106 [nucl-ex].

[98] "Correlations between multiparticle cumulants and mean transverse momentum in small collision systems with the CMS detector" (2022).

[99] Morad Aaboud et al. "Correlated long-range mixed-harmonic fluctuations measured in *pp*, *p*+Pb and low-multiplicity Pb+Pb collisions with the ATLAS detector". *Phys. Lett. B* 789 (2019). DOI: 10.1016/j.physletb.2018.11.065. arXiv: 1807.02012 [nucl-ex].

[100] Albert M Sirunyan et al. "Observation of Correlated Azimuthal Anisotropy Fourier Harmonics in *pp* and $p + Pb$ Collisions at the LHC". *Phys. Rev. Lett.* 120 (2018). DOI: 10.1103/PhysRevLett.120.092301. arXiv: 1709.09189 [nucl-ex].

[101] Albert M Sirunyan et al. "Correlations of azimuthal anisotropy Fourier harmonics with subevent cumulants in *pPb* collisions at $\sqrt{s_{NN}}$ =8.16TeV". *Phys. Rev. C* 103 (2021). DOI: 10.1103/PhysRevC.103.014902. arXiv: 1905.09935 [hep-ex].

[102] Jaroslav Adam et al. "Correlated event-by-event fluctuations of flow harmonics in Pb-Pb collisions at $\sqrt{s_{\mathrm{NN}}} = 2.76$ TeV". *Phys. Rev. Lett.* 117 (2016). DOI: 10.1103/PhysRevLett.117.182301. arXiv: 1604.07663 [nucl-ex].

[103] Albert M Sirunyan et al. "Non-Gaussian elliptic-flow fluctuations in PbPb collisions at $\sqrt{s_{\mathrm{NN}}} = 5.02$ TeV". *Phys. Lett. B* 789 (2019). DOI: 10.1016/j.physletb.2018.11.063. arXiv: 1711.05594 [nucl-ex].

[104] Georges Aad et al. "Measurement of the distributions of event-by-event flow harmonics in lead-lead collisions at = 2.76 TeV with the ATLAS detector at the LHC". *JHEP* 11 (2013). DOI: 10.1007/JHEP11(2013)183. arXiv: 1305.2942 [hep-ex].

[105] Georges Aad et al. "Measurements of azimuthal anisotropies of jet production in Pb+Pb collisions at $\sqrt{s_{NN}} = 5.02$ TeV with the ATLAS detector". *Phys. Rev. C* 105 (2022). DOI: 10.1103/PhysRevC.105.064903. arXiv: 2111.06606 [nucl-ex].

[106] Serguei Chatrchyan et al. "Azimuthal Anisotropy of Charged Particles at High Transverse Momenta in PbPb Collisions at $\sqrt{s_{NN}} = 2.76$ TeV". *Phys. Rev. Lett.* 109 (2012). DOI: 10.1103/PhysRevLett.109.022301. arXiv: 1204.1850 [nucl-ex].

[107] Georges Aad et al. "Transverse momentum and process dependent azimuthal anisotropies in $\sqrt{s_{\mathrm{NN}}}$ = 8.16 TeV p+Pb collisions with the ATLAS detector". *Eur. Phys. J. C* 80 (2020). DOI: 10.1140/epjc/s10052-020-7624-4. arXiv: 1910.13978 [nucl-ex].

[108] "Azimuthal anisotropy of jet particles in p-Pb and Pb-Pb collisions at $\sqrt{s_{\mathrm{NN}}}$ = 5.02 TeV" (2022). arXiv: 2212.12609 [nucl-ex].

[109] Morad Aaboud et al. "Measurement of long-range two-particle azimuthal correlations in Z-boson tagged pp collisions at $\sqrt{s}$=8 and 13 TeV". *Eur. Phys. J. C* 80 (2020). DOI: 10.1140/epjc/s10052-020-7606-6. arXiv: 1906.08290 [nucl-ex].

[110] Georges Aad et al. "Measurement of the Sensitivity of Two-Particle Correlations in pp Collisions to the Presence of Hard Scatterings". *Phys. Rev. Lett.* 131 (2023). DOI: 10.1103/PhysRevLett.131.162301. arXiv: 2303.17357 [nucl-ex].

[111] Georges Aad et al. "Measurement of azimuthal anisotropy of muons from charm and bottom hadrons in Pb+Pb collisions at sNN=5.02 TeV with the ATLAS detector". *Phys. Lett. B* 807 (2020). DOI: 10.1016/j.physletb.2020.135595. arXiv: 2003.03565 [nucl-ex].

[112] Armen Tumasyan et al. "Probing Charm Quark Dynamics via Multiparticle Correlations in Pb-Pb Collisions at $\sqrt{s_{\mathrm{NN}}}$ =5.02 TeV". *Phys. Rev. Lett.* 129 (2022). DOI: 10.1103/PhysRevLett.129.022001. arXiv: 2112.12236 [hep-ex].

[113] Shreyasi Acharya et al. "J/ψ elliptic and triangular flow in Pb-Pb collisions at $\sqrt{s_{\mathrm{NN}}}$ = 5.02 TeV". *JHEP* 10 (2020). DOI: 10.1007/JHEP10(2020)141. arXiv: 2005.14518 [nucl-ex].

[114] L. Adamczyk et al. "Measurement of D^0 Azimuthal Anisotropy at Midrapidity in Au+Au Collisions at $\sqrt{s_{NN}}$=200 GeV". *Phys. Rev. Lett.* 118 (2017). DOI: 10.1103/PhysRevLett.118.212301. arXiv: 1701.06060 [nucl-ex].

[115] Albert M Sirunyan et al. "Studies of charm and beauty hadron long-range correlations in pp and pPb collisions at LHC energies". *Phys. Lett. B* 813 (2021). DOI: 10.1016/j.physletb.2020.136036. arXiv: 2009.07065 [hep-ex].

[116] Shreyasi Acharya et al. "Azimuthal Anisotropy of Heavy-Flavor Decay Electrons in p–Pb Collisions at $\sqrt{s_{\mathrm{NN}}}$ = 5.02 TeV". *Phys. Rev. Lett.* 122 (2019). DOI: 10.1103/PhysRevLett.122.072301. arXiv: 1805.04367 [nucl-ex].

[117] Georges Aad et al. "Measurement of azimuthal anisotropy of muons from charm and bottom hadrons in pp collisions at $\sqrt{s}$ = 13 TeV with the ATLAS detector". *Phys. Rev. Lett.* 124 (2020). DOI: 10.1103/PhysRevLett.124.082301. arXiv: 1909.01650 [nucl-ex].

[118] Shreyasi Acharya et al. "Measurement of Υ(1S) elliptic flow at forward rapidity in Pb-Pb collisions at $\sqrt{s_{\mathrm{NN}}} = 5.02$ TeV". *Phys. Rev. Lett.* 123 (2019). DOI: 10.1103/PhysRevLett.123.192301. arXiv: 1907.03169 [nucl-ex].

[119] "Azimuthal anisotropy of Υ(1S) mesons in pPb collisions at $\sqrt{\mathrm{s_{NN}}} = 8.16$ TeV" (2022).

[120] ALICE Public Preliminary Figures. *v_2 in central p–Pb collisions with π, K, p using improved template fit method compared to Hydro-coal-frag model*. [Online; accessed 20-Mar-2024]. 2020. URL: https://alice-figure.web.cern.ch/node/21596.

[121] Armen Tumasyan et al. "Two-particle azimuthal correlations in γp interactions using pPb collisions at sNN=8.16TeV". *Phys. Lett. B* 844 (2023). DOI: 10.1016/j.physletb.2023.137905. arXiv: 2204.13486 [nucl-ex].

[122] Georges Aad et al. "Two-particle azimuthal correlations in photonuclear ultraperipheral Pb+Pb collisions at 5.02 TeV with ATLAS". *Phys. Rev. C* 104 (2021). DOI: 10.1103/PhysRevC.104.014903. arXiv: 2101.10771 [nucl-ex].

[123] I. Abt et al. "Two-particle azimuthal correlations as a probe of collective behaviour in deep inelastic *ep* scattering at HERA". *JHEP* 04 (2020). DOI: 10.1007/JHEP04(2020)070. arXiv: 1912.07431 [hep-ex].

[124] I. Abt et al. "Azimuthal correlations in photoproduction and deep inelastic *ep* scattering at HERA". *JHEP* 12 (2021). DOI: 10.1007/JHEP12(2021)102. arXiv: 2106.12377 [hep-ex].

[125] Anthony Badea et al. "Measurements of two-particle correlations in e^+e^- collisions at 91 GeV with ALEPH archived data". *Phys. Rev. Lett.* 123 (2019). DOI: 10.1103/PhysRevLett.123.212002. arXiv: 1906.00489 [hep-ex].

[126] Jaroslav Adam et al. "Enhanced production of multi-strange hadrons in high-multiplicity proton-proton collisions". *Nature Phys.* 13 (2017). DOI: 10.1038/nphys4111. arXiv: 1606.07424 [nucl-ex].

[127] Christian Bierlich et al. "Strangeness enhancement across collision systems without a plasma". *Phys. Lett. B* 835 (2022). DOI: 10.1016/j.physletb.2022.137571. arXiv: 2205.11170 [hep-ph].

[128] Serguei Chatrchyan et al. "Event Activity Dependence of Υ(nS) Production in $\sqrt{s_{NN}}$=5.02 TeV pPb and $\sqrt{s}$=2.76 TeV pp Collisions". *JHEP* 04 (2014). DOI: 10.1007/JHEP04(2014)103. arXiv: 1312.6300 [nucl-ex].

[129] Helmut Satz. "Color deconfinement in nuclear collisions". *Rept. Prog. Phys.* 63 (2000). DOI: 10.1088/0034-4885/63/9/203. arXiv: hep-ph/0007069.

[130] S. S. Adler et al. "Absence of suppression in particle production at large transverse momentum in $\sqrt{s_{\mathrm{NN}}}$ = 200 GeV d + Au collisions". *Phys. Rev. Lett.* 91 (2003). DOI: 10.1103/PhysRevLett.91.072303. arXiv: nucl-ex/0306021.

[131] J. Adams et al. "Evidence from d + Au measurements for final state suppression of high p(T) hadrons in Au+Au collisions at RHIC". *Phys. Rev. Lett.* 91 (2003). DOI: 10.1103/PhysRevLett.91.072304. arXiv: nucl-ex/0306024.

[132] Georges Aad et al. "Centrality and rapidity dependence of inclusive jet production in $\sqrt{s_{\mathrm{NN}}}$ = 5.02 TeV proton-lead collisions with the ATLAS detector". *Phys. Lett. B* 748 (2015). DOI: 10.1016/j.physletb.2015.07.023. arXiv: 1412.4092 [hep-ex].

[133] A. Adare et al. "Centrality-dependent modification of jet-production rates in deuteron-gold collisions at $\sqrt{s_{\mathrm{NN}}}$=200 GeV". *Phys. Rev. Lett.* 116 (2016). DOI: 10.1103/PhysRevLett.116.122301. arXiv: 1509.04657 [nucl-ex].

[134] Jaroslav Adam et al. "Measurement of charged jet production cross sections and nuclear modification in p–Pb collisions at $\sqrt{s_{\mathrm{NN}}}$ = 5.02 TeV". *Phys. Lett. B* 749 (2015). DOI: 10.1016/j.physletb.2015.07.054. arXiv: 1503.00681 [nucl-ex].

[135] Vardan Khachatryan et al. "Charged-particle nuclear modification factors in PbPb and pPb collisions at $\sqrt{s_{\mathrm{NN}}}$ = 5.02 TeV". *JHEP* 04 (2017). DOI: 10.1007/JHEP04(2017)039. arXiv: 1611.01664 [nucl-ex].

[136] Björn Schenke, Chun Shen, and Prithwish Tribedy. "Features of the IP-Glasma". *Nucl. Phys. A* 982 (2019). DOI: 10.1016/j.nuclphysa.2018.08.015. arXiv: 1807.05205 [nucl-th].

[137] Ryan D. Weller and Paul Romatschke. "One fluid to rule them all: viscous hydrodynamic description of event-by-event central p+p, p+Pb and Pb+Pb collisions at $\sqrt{s}$ = 5.02 TeV". *Phys. Lett. B* 774 (2017). DOI: 10.1016/j.physletb.2017.09.077. arXiv: 1701.07145 [nucl-th].

[138] Wenbin Zhao et al. "Probing the Partonic Degrees of Freedom in High-Multiplicity $p-Pb$ collisions at $\sqrt{s_{NN}}$ = 5.02 TeV". *Phys. Rev. Lett.* 125 (2020). DOI: 10.1103/PhysRevLett.125.072301. arXiv: 1911.00826 [nucl-th].

[139] Xin-Li Zhao et al. "A transport model study of multiparticle cumulants in p + p collisions at 13 TeV". *Phys. Lett. B* 839 (2023). DOI: 10.1016/j.physletb.2023.137799. arXiv: 2112.01232 [nucl-th].

[140] Christian Bierlich, Torbjörn Sjöstrand, and Marius Utheim. "Hadronic rescattering in pA and AA collisions". *Eur. Phys. J. A* 57 (2021). DOI: 10.1140/epja/s10050-021-00543-3. arXiv: 2103.09665 [hep-ph].

[141] Sergei A. Voloshin et al. "Elliptic flow in the Gaussian model of eccentricity fluctuations". *Phys. Lett. B* 659 (2008). DOI: 10.1016/j.physletb.2007.11.043. arXiv: 0708.0800 [nucl-th].

[142] Jonah E. Bernhard, J. Scott Moreland, and Steffen A. Bass. "Bayesian estimation of the specific shear and bulk viscosity of quark–gluon plasma". *Nature Phys.* 15 (2019). DOI: 10.1038/s41567-019-0611-8.

[143] Ante Bilandzic, Raimond Snellings, and Sergei Voloshin. "Flow analysis with cumulants: Direct calculations". *Phys. Rev. C* 83 (2011). DOI: 10.1103/PhysRevC.83.044913. arXiv: 1010.0233 [nucl-ex].

[144] Nicolas Borghini, Phuong Mai Dinh, and Jean-Yves Ollitrault. "A New method for measuring azimuthal distributions in nucleus-nucleus collisions". *Phys. Rev. C* 63 (2001). DOI: 10.1103/PhysRevC.63.054906. arXiv: nucl-th/0007063.

[145] Ante Bilandzic et al. "Generic framework for anisotropic flow analyses with multiparticle azimuthal correlations". *Phys. Rev. C* 89 (2014). DOI: 10.1103/PhysRevC.89.064904. arXiv: 1312.3572 [nucl-ex].

[146] Xiangrong Zhu et al. "Investigating the correlations of flow harmonics in 2.76A TeV Pb–Pb collisions". *J. Phys. Conf. Ser.* 779 (2017). DOI: 10.1088/1742-6596/779/1/012062. arXiv: 1609.02628 [nucl-th].

[147] Giuliano Giacalone et al. "Symmetric cumulants and event-plane correlations in Pb + Pb collisions". *Phys. Rev. C* 94 (2016). DOI: 10.1103/PhysRevC.94.014906. arXiv: 1605.08303 [nucl-th].

[148] Piotr Bozek. "Transverse-momentum–flow correlations in relativistic heavy-ion collisions". *Phys. Rev. C* 93 (2016). DOI: 10.1103/PhysRevC.93.044908. arXiv: 1601.04513 [nucl-th].

[149] Chun, Shen. *DYNAMICAL MODELING OF THE COLLECTIVITY IN PO AND OO COLLISIONS*. [Online; accessed 20-Mar-2024]. 2021. URL: https://indico.cern.ch/event/975877/contributions/4118500/attachments/2185275/3692705/OO_and_pO.pdf.

[150] "LHC Machine". *JINST* 3 (2008). DOI: 10.1088/1748-0221/3/08/S08001.

[151] K. Aamodt et al. "The ALICE experiment at the CERN LHC". *JINST* 3 (2008). DOI: 10.1088/1748-0221/3/08/S08002.

[152] G. Dellacasa et al. "ALICE technical design report of the inner tracking system (ITS)" (1999).

[153] J. Alme et al. "The ALICE TPC, a large 3-dimensional tracking device with fast readout for ultra-high multiplicity events". *Nucl. Instrum. Meth. A* 622 (2010). DOI: 10.1016/j.nima.2010.04.042. arXiv: 1001.1950 [physics.ins-det].

[154] Francesca Carnesecchi. "Performance of the ALICE Time-Of-Flight detector at the LHC". *JINST* 14 (2019). DOI: 10.1088/1748-0221/14/06/C06023. arXiv: 1806.03825 [physics.ins-det].

[155] Shreyasi Acharya et al. "The ALICE Transition Radiation Detector: construction, operation, and performance". *Nucl. Instrum. Meth. A* 881 (2018). DOI: 10.1016/j.nima.2017.09.028. arXiv: 1709.02743 [physics.ins-det].

[156] T. V. Acconcia et al. "A Very High Momentum Particle Identification Detector". *Eur. Phys. J. Plus* 129 (2014). DOI: 10.1140/epjp/i2014-14091-5. arXiv: 1309.5880 [nucl-ex].

[157] D. C. Zhou. "PHOS, the ALICE-PHOton Spectrometer". *J. Phys. G* 34 (2007). DOI: 10.1088/0954-3899/34/8/S81.

[158] Terry C. Awes. "The ALICE electromagnetic calorimeter". *Nucl. Instrum. Meth. A* 617 (2010). DOI: 10.1016/j.nima.2009.10.010.

[159] J Allen et al. *ALICE DCal: An Addendum to the EMCal Technical Design Report Di-Jet and Hadron-Jet correlation measurements in ALICE*. Tech. rep. 2010. URL: https://cds.cern.ch/record/1272952.

[160] E. Abbas et al. "Performance of the ALICE VZERO system". *JINST* 8 (2013). DOI: 10.1088/1748-0221/8/10/P10016. arXiv: 1306.3130 [nucl-ex].

[161] M. Bondila et al. "ALICE T0 detector". *IEEE Trans. Nucl. Sci.* 52 (2005). DOI: 10.1109/TNS.2005.856900.

[162] S. C. Zugravel et al. "ALICE Zero Degree Calorimeters. The new readout system in LHC Run 3". *JINST* 18 (2023). DOI: 10.1088/1748-0221/18/02/C02009.

[163] K Aamodt et al. "Alignment of the ALICE Inner Tracking System with cosmic-ray tracks". *JINST* 5 (2010). DOI: 10.1088/1748-0221/5/03/P03003. arXiv: 1001.0502 [physics.ins-det].

[164] M. Krivda et al. "The ALICE trigger system performance for p-p and Pb-Pb collisions". *JINST* 7 (2012). DOI: 10.1088/1748-0221/7/01/C01057.

[165] Antonin Maire. "Track reconstruction principle in ALICE for LHC run I and run II. Principes de reconstruction de traces dans ALICE pour les runs I et II du LHC". General Photo. 2011. URL: https://cds.cern.ch/record/1984041.

[166] Pierre Billoir. "Progressive track recognition with a Kalman like fitting procedure". *Comput. Phys. Commun.* 57 (1989). DOI: 10.1016/0010-4655(89)90249-X.

[167] Stefan Roesler, Ralph Engel, and Johannes Ranft. "The Monte Carlo event generator DPMJET-III". *International Conference on Advanced Monte Carlo for Radiation Physics, Particle Transport Simulation and Applications (MC 2000)*. 2000. DOI: 10.1007/978-3-642-18211-2_166. arXiv: hep-ph/0012252.

[168] René Brun et al. "GEANT Detector Description and Simulation Tool" (1994). DOI: 10.17181/CERN.MUHF.DMJ1.

[169] B. Efron. "Bootstrap Methods: Another Look at the Jackknife". *The Annals of Statistics* 7 (1979). DOI: 10.1214/aos/1176344552. URL: https://doi.org/10.1214%2Faos%2F1176344552.

[170] Roger Barlow. "Systematic errors: Facts and fictions". *Conference on Advanced Statistical Techniques in Particle Physics*. 2002. arXiv: hep-ex/0207026.

[171] Bjoern Schenke, Prithwish Tribedy, and Raju Venugopalan. "Multiplicity distributions in p+p, p+A and A+A collisions from Yang-Mills dynamics". *Phys. Rev. C* 89 (2014). DOI: 10.1103/PhysRevC.89.024901. arXiv: 1311.3636 [hep-ph].

[172] Matthew Luzum. "Overview of Flow and Hydrodynamic Modeling of Nuclear Collisions". *J. Phys. Conf. Ser.* 446 (2013). DOI: 10.1088/1742-6596/446/1/012020.

[173] Sergei A. Voloshin, Arthur M. Poskanzer, and Raimond Snellings. "Collective phenomena in non-central nuclear collisions". *Landolt-Bornstein* 23 (2010). DOI: 10.1007/978-3-642-01539-7_10. arXiv: 0809.2949 [nucl-ex].

[174] Wenbin Zhao et al. "Hydrodynamic collectivity in proton–proton collisions at 13 TeV". *Phys. Lett. B* 780 (2018). DOI: 10.1016/j.physletb.2018.03.022. arXiv: 1801.00271 [nucl-th].

[175] H. J. Drescher and Y. Nara. "Effects of fluctuations on the initial eccentricity from the Color Glass Condensate in heavy ion collisions". *Phys. Rev. C* 75 (2007). DOI: 10.1103/PhysRevC.75.034905. arXiv: nucl-th/0611017.

[176] Zhi Qiu and Ulrich W. Heinz. "Event-by-event shape and flow fluctuations of relativistic heavy-ion collision fireballs". *Phys. Rev. C* 84 (2011). DOI: 10.1103/PhysRevC.84.024911. arXiv: 1104.0650 [nucl-th].

[177] Giuliano Giacalone et al. "Skewness of elliptic flow fluctuations". *Phys. Rev. C* 95 (2017). DOI: 10.1103/PhysRevC.95.014913. arXiv: 1608.01823 [nucl-th].

[178] D. Teaney and L. Yan. "Event-plane correlations and hydrodynamic simulations of heavy ion collisions". *Phys. Rev. C* 90 (2014). DOI: 10.1103/PhysRevC.90.024902. arXiv: 1312.3689 [nucl-th].

[179] S. H. Lim and J. L. Nagle. "Exploring origins for correlations between flow harmonics and transverse momentum in small collision systems". *Phys. Rev. C* 103 (2021). DOI: 10.1103/PhysRevC.103.064906. arXiv: 2103.01348 [nucl-th].

[180] Giuliano Giacalone, Björn Schenke, and Chun Shen. "Observable signatures of initial state momentum anisotropies in nuclear collisions". *Phys. Rev. Lett.* 125 (2020). DOI: 10.1103/PhysRevLett.125.192301. arXiv: 2006.15721 [nucl-th].

[181] Wojciech Broniowski, Mikolaj Chojnacki, and Lukasz Obara. "Size fluctuations of the initial source and the event-by-event transverse momentum fluctuations in relativistic heavy-ion collisions". *Phys. Rev. C* 80 (2009). DOI: 10.1103/PhysRevC.80.051902. arXiv: 0907.3216 [nucl-th].

[182] Betty Bezverkhny Abelev et al. "Event-by-event mean $p_{\mathbf{T}}$ fluctuations in pp and Pb-Pb collisions at the LHC". *Eur. Phys. J. C* 74 (2014). DOI: 10.1140/epjc/s10052-014-3077-y. arXiv: 1407.5530 [nucl-ex].

[183] ALICE collaboration. *Investigations of anisotropic flow using multiparticle azimuthal correlations*. [Online; accessed 20-Mar-2024]. 2022. URL: https://alice-figure.web.cern.ch/node/22085.

[184] ALICE collaboration. *v2-[pt] correlation in Pb–Pb, p–Pb and pp collisions*. [Online; accessed 20-Mar-2024]. 2023. URL: https://alice-figure.web.cern.ch/node/28069.

[185] Shreyasi Acharya et al. "$W^{\pm}$-boson production in p−Pb collisions at $\sqrt{s_{NN}} = 8.16$ TeV and PbPb collisions at $\sqrt{s_{NN}} = 5.02$ TeV". *JHEP* 05 (2023). DOI: 10.1007/JHEP05(2023)036. arXiv: 2204.10640 [nucl-ex].

[186] Matteo Cacciari, Mario Greco, and Paolo Nason. "The p_T spectrum in heavy-flavour hadroproduction." *JHEP* 05 (1998). DOI: 10.1088/1126-6708/1998/05/007. arXiv: hep-ph/9803400.

[187] John Campbell and Tobias Neumann. "Precision Phenomenology with MCFM". *JHEP* 12 (2019). DOI: 10.1007/JHEP12(2019)034. arXiv: 1909.09117 [hep-ph].

[188] Sayipjamal Dulat et al. "New parton distribution functions from a global analysis of quantum chromodynamics". *Phys. Rev. D* 93 (2016). DOI: 10.1103/PhysRevD.93.033006. arXiv: 1506.07443 [hep-ph].

[189] Constantin Loizides and Andreas Morsch. "Absence of jet quenching in peripheral nucleus–nucleus collisions". *Phys. Lett. B* 773 (2017). DOI: 10.1016/j.physletb.2017.09.002. arXiv: 1705.08856 [nucl-ex].

[190] Zhiyong Lu et al. "Probe nuclear structure using the anisotropic flow at the Large Hadron Collider". *Eur. Phys. J. A* 59 (2023). DOI: 10.1140/epja/s10050-023-01194-2. arXiv: 2309.09663 [nucl-th].

[191] Jiangyong Jia. "Probing triaxial deformation of atomic nuclei in high-energy heavy ion collisions". *Phys. Rev. C* 105 (2022). DOI: 10.1103/PhysRevC.105.044905. arXiv: 2109.00604 [nucl-th].

List of Figures

List of Tables